TESE DE DOUTORAMENTO

NEW INSIGHTS AND THERAPEUTIC APPROACHES OF POLYCYSTIC KIDNEY AND LIVER DISEASE

Adrián Cordido Eijo

ESCOLA DE DOUTORAMENTO INTERNACIONAL DA UNIVERSIDADE DE SANTIAGO DE COMPOSTELA

PROGRAMA DE DOUTORAMENTO EN MEDICINA MOLECULAR

SANTIAGO DE COMPOSTELA

2020

USC
UNIVERSIDADE
DE SANTIAGO
DE COMPOSTELA

AUTORIZACIÓN DO DIRECTOR/TITOR DA TESE

D./Dna. **Adrián Cordido Eijo**

Título da tese: **New insights and therapeutic approaches of Polycystic Kidney and Liver Disease**

Presento a miña tese, seguindo o procedemento axeitado ao Regulamento, e declaro que:

1) A tese abarca os resultados da elaboración do meu traballo.
2) De ser o caso, na tese faise referencia ás colaboracións que tivo este traballo.
3) Confirmo que a tese non incorre en ningún tipo de plaxio doutros autores nin de traballos presentados por min para a obtención doutros títulos.

E comprométome a presentar o Compromiso Documental de Supervisión no caso de que o orixinal non estea na Escola.

En **Santiago de Compostela**, **21 de Decembro de 2020**.

Fdo. Adrián Cordido Eijo

AUTORIZACIÓN DO DIRECTOR/TITOR DA TESE

D./Dna. **Miguel Ángel García González**

En condición de: **Director/a**

Título da tese: **New insights and therapeutic approaches of Polycystic Kidney and Liver Disease**

INFORMA:

Que a presente tese, correspóndese co traballo realizado por D/Dna Adrián Cordido Eljo, baixo a miña dirección/titorización, e autorizo a súa presentación, considerando que reúne os requisitos esixidos no Regulamento de Estudos de Doutoramento da USC, e que como director/titor desta non incorre nas causas de abstención establecidas na Lei 40/2015.

En Santiago de Compostela, 21 de Decembro de 2020

Fdo. Miguel Ángel García González

AUTORIZACIÓN DO DIRECTOR/TITOR DA TESE

D./Dna. **Ángel Carracedo Álvarez**

En condición de: **Titor/a**

Título da tese: **New insights and therapeutic approaches of Polycystic Kidney and Liver Disease**

INFORMA:

Que a presente tese, correspóndese co traballo realizado por D/Dna Adrián Cordido EIjo, baixo a miña dirección/titorización, e autorizo a súa presentación, considerando que reúne os requisitos esixidos no Regulamento de Estudos de Doutoramento da USC, e que como director/titor desta non incorre nas causas de abstención establecidas na Lei 40/2015.

En Santiago de Compostela, 21 de Decembro de 2020

Fdo. Ángel Carracedo Álvarez

Competing interests:

The intellectual property of the CystAnalyser (SC-208/19) was protected by a software registration: 2/3 USC (50% Eva Cernadas; 50% Manuel Fernández Delgado) and 1/3 FIDIS (50% Adrián Cordido; 50% Miguel Ángel García González).

The author has nothing to disclosure with the rest of content of the present thesis.

USC UNIVERSIDADE DE SANTIAGO DE COMPOSTELA

USC
UNIVERSIDADE
DE SANTIAGO
DE COMPOSTELA

En ciencia, unha constante é un valor que permanece invariable ao longo do tempo.

A Rebeca, a constante da miña vida.

USC
UNIVERSIDADE
DE SANTIAGO
DE COMPOSTELA

“Ciencia é crer na ignorancia dos científicos”.

Richard Phillips Feynman

“Odio aos indiferentes. Creo que vivir significa tomar partido (...). A indiferenza e a abulia son parasitismo, non vida. A indiferenza é o peso morta da historia (...). É a fatalidade (...). Vivo, son partisano, por iso odio a quen non toma partido. Odio aos indiferentes.”

Antonio Gramsci

Agradecementos

A pesar de que o último que se escribe dunha tese son os agradecementos, é o primeiro que aparece escrito. Xa que as persoas en agradecer son as que dan sentido ao traballo realizado. E como non pode ser doutra forma, non podía rematar todo isto sen agradecer a quen dalgunha forma fixo parte desta viaxe.

En primeiro lugar ao meu director de tese, Miguel por darme a oportunidade de traballar no laboratorio e realizar esta tese sobre un eido e unha enfermidade que dalgún xeito forman parte de min. Igualmente a Ángel, titor da mesma, grazas pola túa dilixencia cando o precisei.

Despois á xente do laboratorio onde pasei os meus últimos 5 anos, o Laboratorio 11 do IDIS ou "Nefro". A verdade é que sen vos todo sería moito peor, un traballo moito máis aburrido. As que xa non están coma: Olaya, quen foi a miña primeira mentora, Lisbeth, Patricia, Vanesa ou Julia. E ás que seguen ou sempre estiveron aí. Ana, a nosa técnico incansábel e resolve-todo, e Marta, a miña compi de mesa. Dous apoios fundamentais. Laura, a miña dobre no lab, Noa, María, Lara e Raquel. Grazas a todas por aguantarme durante este tempo, son mellor persoa despois de coñecervos.

Ao servizo de Nefroloxía do CHUS e ás súas profesionais, Cándido, Nis, Carmen etc que me deron outra visión do que é e debe ser a investigación.

Con respecto ao campo laboral, non podo rematar sen agradecer a toda a xente do Köttgen-Lab de Freiburg, Michael, Alexis, Natalia, Tillman, Simone, Hannah e Berenike por tres meses xeniais. Danke schön! Mención a parte merece Sebastià, amizade mallorquina que levei desde terras alemás. Temos pendente unha quedada, e a ser posíbel comendo polbo que non sexa conxelado.

Fora de NefroCHUS, non poido estar máis agradecido por toda a xente que coñecín e fixen amizade. Comezando desde a época de Mestrado: Raquel, Jeannette, Dopico e un longo etc pero sobre todo Luís e en especial Cris, grazas por estar aí. Facendo a tese foi moita a xente que dagún xeito me axudaron, a nivel científico como persoal. Gus, Lara, Jessi e Saul (Labs 4/12); Ángel e Marta (Labs 6 e 13); Marinela, Sonia, Cris, (Lab 6); Nerea (Lab 8); Lorena, Ángeles e Ángela (Lab 10); Sabela, Pablo etc (Lab 13); Raquel (Lab 14); Lorena, Alex, Alba etc (Lab 5/17); Miriam, Ana e María (Lab 18); Susana, Pilar e María (Proteómica); Alberto (Bioinformática); Patricia , María e María José (Anatomía patolóxica); Laura, Anas e David (CEBEGA); e finalmente, pero para nada menos importante, María Jesús, Clara e Alana. Neste apartado debo destacar a Eloi, por todos os momentos que pasamos xuntos e pola nosa amizade.
Ao meu segundo laboratorio, o Lab 3 do IDIS. Tamara e Nerea sodes dúas compañeiras e amigas máis. María, toda persoa necesita un espello ao que mirarse, eres unha verdadeira referente. Ás tres, grazas.

Aos camaradas, Julio, Vicente e Javi. Sen dúbida, "descubrirvos" e coñecervos é unha das mellores cousas que levo da miña etapa predoutoral. Sempre é agradábel coñecer xente coa túa mesma óptica e non sentirse coma un naufrago. Algún día brindaremos a fin desta trituradora de vida ¡Morte ao neoliberalismo!.

Dende que tiven oportunidade involucreime nas iniciativas populares e colectivas que xurdiron co obxectivo de mellorar as condicións laborais dxs investigadorxs en Galiza. E non podo pasar esta oportunidade en agradecer á xente coa que compartín, e continúo compartindo, esa loita. A Ezequiel, Mabel, Natalia, Carlos, José Luís, Eva, María e Alicia do Comité de Empresa da FIDIS e demais representantes sindicais de Coruña e Vigo coma Juan, Ana, Paula etc. Á xente que conformamos e demos inicio a InvestiGal: Javi, Zulema, Laura, Vanessa, Hugo, Andrés, David, Alejandro, María, Elena, Paula, Jose etc etc, unha rede de investigadorxs máis que necesaria e que agardo perdure moitos anos.

Do mesmo xeito non quero pasar esta oportunidade para recordar a bos amigos fora do ámbito científico. Mateo, Lago, Navedo e demais xente que me alegraron as noites dos venres nestes anos. Brais, Adrián, Marie e lobos en xeral, temos pendente unha quedada e a ser posible con concerto incluído.

No ámbito familiar quero agradecer a toda a miña familia e en especial a miña nai polo esforzo que hai detrás para que eu estea escribindo estas liñas. Sen o voso apoio e valores como o honradez e esforzo non chegaría nin a metade do camiño que recorrín.
Se cadra ven o máis difícil. Á persoa que máis lle debo, que máis coñezo e coa que comparto todo, é tamén da que custa máis escribir. Rebeca, grazas por todo. Do único que estou máis convencido, e máis que calquera resultado escrito nesta tese, é que sen ti todo sería moito máis difícil. Quérote.

De xeito simbólico, a Alexandra Elbakyan, a muller que creou e fundou Sci-Hub, a páxina que libera a diario miles de artigos científicos das multinacionais que privatizan e fan negocio co coñecemento científico. En palabras dela: “can knowledge be a property? do we need any property at all? Revolution! a mass protest against property striving for equality.”.

Foi un auténtico pracer pasar estes anos con todxs vós.

RESUMO

Introdución. A Enfermidade Poliquística Renal (PKD, polas súas siglas en inglés) é un grupo de enfermidades xenéticas que resultan no desenvolvemento de quistes renais. As formas máis común son, a enfermidade poliquística renal autosómica dominante (ADPKD) e enfermidade poliquística renal autosómica recesiva (ARPKD). A ADPKD ten unha prevalencia de 1:800, caracterízase pola formación e crecemento progresivo de múltiples quistes que levan á enfermidade renal en fase final (ESKD, polas súas siglas en inglés) e normalmente os síntomas aparecen na etapa adulta. A ARPKD ten unha prevalencia de 1:20.000, maniféstase perinatalmente ou na infancia e o curso clínico é grave e caracterízase pola combinación de enfermidade cística renal bilateral e fibrose hepática conxénita e a miúdo causa a morte neonatal. Na ADPKD, todos os quistes derivan das células renais epiteliais e de todos os segmentos renais. Non obstante, a ARPKD caracterízase pola dilatación dos condutos colectores das células epiteliais renais que irradian desde a medula ata a cortiza renal.

A enfermidade hepática poliquística (PLD) é un grupo heteroxéneo de enfermidades conxénitas caracterizadas pola dilatación do conduto biliar e o desenvolvemento de quistes derivados dos colanxiocitos (células epiteliais do conduto biliar). Os PLD hérdanse de forma dominante ou recesiva, e poden desenvolverse sos (enfermidade hepática poliquística illada ou PCLD) ou en asociación coa PKD, sendo a súa principal manifestación extrarenal.

ADPKD é xeneticamente heteroxénea con dous xenes identificados, *PKD1* e *PKD2*. A ARPKD é causada por mutacións en *PKHD1* e o recentemente descuberto, *DZIP1L*. A PCLD sempre ten herdanza dominante e é causada por mutacións en varios xenes: *PRKCSH*, *SEC63*, *LRP5*, *GANAβ*, *ALG8*, *SEC61B*, *PKHD1* (en heterozigosis) e *ALG9*.

PKD1 e *PKD2* codifican as proteínas Policistina-1/PC1 e Policistina-2/PC2 (tamén chamada TRPP2), respectivamente. Suxeriuse a PC1 como un suposto receptor para un ligando non identificado, e PC2 é unha canle de catión iónico non selectivo permeable ao Ca2+ e membro da familia potencial de receptor transitorio (TRP, polas súas siglas en inglés). PC1 e PC2 forman un complexo receptor de canle implicado na vía do Ca2+ e estas dúas proteínas están localizadas (entre outras localizacións celulares) no cilio primario das células epiteliais. Por outra banda, o produto proteico de *PKHD1* é a fibrocistina/poliductina/FPC, unha proteína de membrana situada no cilio primario das células epiteliais e con función indefinida.

Os pacientes con ADPKD e PLD normalmente son heterocigotos cunha mutación na liña xerminal nun xene PKD ou PLD (primeiro "*hit*"). A forza motriz que leva á cistoxénese e activa o fenotipo da enfermidade son as mutacións somáticas de segundo "*hit*". Este é o modelo de cistoxénese chamado "*two hit*", a teoría máis aceptada da formación de quistes en ADPKD e PCLD en humanos. Entón, segundo este modelo, un limiar crítico de proteína funcional delimita a formación de quistes e suxire que o momento de iniciación pode influír na gravidade da ADPKD. Non obstante, o mecanismo e o momento deste segundo "*hit*" son descoñecidos actualmente.

A formación e progresión dos quistes ocorre ao longo do tempo, os quistes aumentan en número e volume coa idade. A área acumulativa de quistes (índice quístico) é o biomarcador medible para cuantificar a cistoxénese, a expansión do quiste e rastrexar a gravidade e a progresión da enfermidade. O software actual que se usa para calcular o índice quístico é impreciso, polo que son necesarias ferramentas bioinformáticas máis precisas.

O enfoque clínico principal para os pacientes con PKD e PLD é reducir os seus síntomas clínicos porque, ata a data, non existe unha terapia específica e eficiente aprobada. O tratamento con PKD e PLD foi ineficaz e a única opción de tratamento é o transplante de ril e/ou fígado. En particular, as estratexias terapéuticas avanzaron aínda máis en ADPKD. Usando modelos de roedores *in vitro* e animais, propuxéronse

varios obxectivos e medicamentos para o tratamento da ADPKD que levou á aprobación do Tolvaptan (un inhibidor do receptor da vasopresina-2) como a primeira e única terapia para pacientes con ADPKD. Non obstante, non estamos nun punto final, este tratamento ten moitas limitacións e non está habilitado para todos os pacientes con ADPKD. Débense desenvolver novos e máis eficientes e seguros enfoques terapéuticos.

Dende que se describiron os xenes e as súas proteínas codificadas, desenvolvéronse varios modelos *in vitro* e animais para o estudo da PKD e descubríronse e caracterizáronse múltiples vías moleculares. Non obstante, o mecanismo molecular intrínseco chave da cistoxénese segue sendo descoñecido, o que provoca un aumento do interese por comprender as vías moleculares e desenvolver novas estratexias terapéuticas. Varias vías de sinalización e factores de transcrición están baixo o control da cistoxénese e da progresión da enfermidade: a vía cAMP regulada pola PKA quinasa e a AC6, vías pro-proliferativas como mTOR, RAS-RAF-ERK ou AKT, pro-inflamatorias e pro-fibróticas etc.

A fibrose é un mecanismo patolóxico caracterizado pola acumulación de matriz na rexión extracelular das células e está asociada á perda da función dos órganos. Na PKD e PLD, a expansión dos quistes e a perda da función renal e hepática asócianse con diferentes graos de fibrose intersticial progresiva e anomalías da matriz extracelular (ECM, polas súas siglas en inglés). As metaloproteasas da matriz (MMPs) son unha gran familia de proteasas implicadas na remodelación e degradación da ECM. A actividade das MMPs está regulada por varios mecanismos; un deles é a inhibición das metaloproteasas por parte dos inhibidores de tecidos endóxenos das metaloproteasas (TIMPs). As alteracións nas MMPs/TIMPs están implicadas na patoxénese humana e do rato e na progresión da PKD e PLD.

Por outra banda, a PKD e a PLD non son principalmente enfermidades inflamatorias; con todo, a inflamación intersticial promove a progresión do quiste a través do recrutamento de macrófagos e a regulación ascendente de citoquinas pro-inflamatorias, que tamén están presentes

en niveis elevados no fluído quístico renal e hepático. O indutor débil da apoptose (TWEAK, TNFSF12) semellante a un factor de necrose tumoral é unha glicoproteína transmembrana tipo II, que pertence á superfamilia TNF (TNFSF) das citoquinas e contribúe á inflamación renal que promove a secreción de quimioquinas polas células renais a proliferación de células renais e outras vías moleculares.

Material e métodos.

Métodos concisos do CystAnalyser. Para o estudo usáronse imaxes de tinguiduras de hematoxilina-eosina dos modelos animais C57/BL6 *Pkd1*$^{cond\ /cond}$*;Tam-Cre*$^{+}$ e C57/BL6 *Pkhd1*$^{del3-4/del3-4}$. Utilizáronse un total de 795 imaxes, clasificadas en "leve-quística", "quística" e "severamente-quística" acorde ao valor do seu índice cístico.

Proteómica. A biblioteca espectral créase cun grupo de cada grupo de mostras usando 4 µl (máis de 4 µg de proteína). As solucións peptídicas analizáronse mediante o método de "adquisición dependente dos datos de escopeta" (DDA, polas súas siglas en inglés) mediante micro-LC-MS/MS e o espectrómetro de masas acoplado era un espectrómetro de masa híbrido cuadrupolo-TOF, 6600 (SCIEX®). Corréronse un total de 4 µg de proteína por mostra e réplica técnica usando o método SWATH, e o aliñamento espectral e a extracción de datos realizouse mediante PeakView v.2.2.

Modelos de ratos. Na presente tese empregáronse as seguintes liñas PKD de rato: *Pkhd1*$^{del3-4/del3-4}$ ou *Pkhd1*-KO (un modelo animal *knockout* homocigoto para *Pkhd1* cos exóns 2 e 3 eliminados, que desenvolve unha enfermidade hepática poliquística progresiva pero non enfermidade renal) , *Pkd1*$^{del2-4/+}$ ou *Pkd1*-KO (modelo *knockout* de Pkd1 cos exóns 2 a 4 eliminados, que non presenta cistoxénese renal ou hepática en heterozigosis); e *Pkd1*$^{cond\ /cond}$*;Tam-Cre* ou *Pkd1*-CKO (un eliminatorio condicional homocigoto de *Pkd1* co sistema Cre-LoxP e un promotor dependente de tamoxifeno). Todos eles cruzado co fondo xenético C57BL/6 e co xenotipo confirmado por PCR. No caso de *Pkd1*$^{cond/cond}$*;Tam-Cre*, os ratos Cre- usáronse como *Wild Types* (tamén chamados WT) e Cre+ como mutantes (tamén chamados Mut ou KO).

Tratamentos. Marimastat (Sigma®) e Tolvaptan (Jinarc®) administráronse por vía intraperitoneal nunha dose de 1-10mg/kg/24h bid e 2mg/kg/24h bid respectivamente. Por outra banda, os ratos inxectáronse por vía intraperitoneal con TWEAK (30ng/g de rato/48h), neutralizado mAb anti-TWEAK (IgG1 BIIB023, clon P2D10) (10 mg/kg de rato/3 veces por semana) ou isotipo IgG (rato IgG2A) (10 mg/kg de rato/3 veces por semana) para grupos control, proporcionada xenerosamente por Biogen, Inc.
Histoloxía. O ril dereito e o lóbulo máis grande dos animais do fígado fixáronse sempre en paraformaldehido. Especificacións sobre tinguiduras, anticorpos e reactivos ollar a sección de Material e métodos.
Extracción de proteína e ARN. Os riles e o fígado esquerdo quedaron moídos en nitróxeno líquido e a metade do tecido está asignada á extracción de proteínas e a outra á extracción de ARN. A proteína e o ARN resultante empregáronse para a análises de RT-qPCR e *Western Blotting*. Especificacións sobre anticorpos, protocolos e reactivos ollar a sección de materiais e métodos.
Estatísticas. Para comparacións entre varios grupos, realizouse unha proba ANOVA coa proba posterior Tukey, mentres que a proba t de Student de dúas colas utilizouse para determinar a importancia das diferenzas entre dous grupos. Valores de P inferiores a 0,05 consideráronse estatisticamente significativos. Todos os conxuntos de datos analizáronse co software GraphPad Prism® (versión 5.0 ou 7.0).

Obxectivos. Neste contexto, o presente traballo ten os seguintes obxectivos: 1) desenvolver novas ferramentas máis fiables para a avaliación de enfermidades quísticas, coma a PKD e a PLD, que nos proporcionen o parámetro índice quístico; 2) realizar unha comparativa de proteómica cuantitativa de fígados de ratos *Wild Type* e poliquísticos para identificar novas posibles dianas terapéuticas e vías moleculares no campo da PLD; 3) testar o potencial terapéutico das metaloproteasas e as alteracións da matriz extracelular en modelos murinos ortólogos; 4) caracterizar o eixe FN14/TWEAK e probar o seu posible papel

terapéutico; 5) ampliar o coñecemento da interacción xenética de *Pkd1* e *Pkhd1* en modelos animais ortólogos de PKD.

Resultados e conclusións. En primeiro lugar, desenvolvemos un novo software, chamado CystAnalyser, que combina o procesamento automático de imaxes cunha interface gráfica de usuario (GUI polas súas siglas en inglés) que permite aos investigadores supervisar e corrixir facilmente o procesamento de imaxe antes da cuantificación. CystAnalyser é capaz de xerar un perfil quístico que inclúe o índice quístico, o número de quistes e o tamaño do quiste en imaxes de mostras histolóxicas nos eidos da PKD e PLD. CystAnalyser está escrito na linguaxe de programación C++ empregando a biblioteca GTK+ ("*GIMP Tool Kit*"), e os algoritmos empregados para recoñecer os quistes da imaxe son unha combinación de técnicas de visión computacionais validadas usando o núcleo dos módulos OpenCV e *imgproc*. Este software permite o recoñecemento automático de quistes e/ou ferramentas de post-procesamento supervisadas.
Para testar o software CystAnalyser, analizáronse 795 imaxes histolóxicas de ril cístico e fígado. Usando CystAnalyser non houbo diferenzas no cálculo do índice quístico de forma automática fronte á entrada do usuario, excepto en circunstancias específicas nas que era necesario que o usuario distinguise entre rexións lixeiramente quísticas das non quísticas. A sensibilidade e especificidade do número de quistes detectados pola cuantificación automática depende do tipo de órgano e gravidade quística, con valores 76,84-78,59% e 76,96-89,66% para o ril e 87,29-93,80% e 63,42-86,07% para o fígado. CystAnalyser, ademais, ofrece unha nova ferramenta para estimar o número de quistes e unha medida máis específica do índice quístico que o ImageJ, o software máis usado actualmente.
En conclusión, o noso grupo desenvolveu un software novidoso para a cuantificación de imaxes histolóxicas de ril de fígados císticos de modelos animais, chamado CystAnalyser. Ademais, CystAnalyser superou de forma sensible e fiable a cuantificación da área cística e do

número de quistes en comparación co software máis utilizado no eido da investigación de enfermidades císticas (ImageJ).

En segundo lugar, realizamos un estudo cuantitativo proteómico diferencial baseado na tecnoloxía SWATH MS na enfermidade do fígado poliquístico ou PLD. Usando a tecnoloxía SWATH MS, comparamos os proteomas *Wild Type* e dos fígados poliquísticos mutantes a partir dun modelo animal ortólogo de ADPKD (*Pkd1*$^{cond/cond}$*;Tam-Cre*$^{-/+}$). Obtivemos unha lista de proteínas con diferenzas estatísticas ($p \leq 0,05$) e un corte de máis de 2 veces de expresión (2 "*fold-change*"). Despois, realizamos análises GO e proteína-proteína identificando varias funcións biolóxicas chave nos fígados poliquísticos e dous grupos ou *clusters* importantes de proteínas. É destacable que o *cluster* máis enriquecido estivo centrado nos fibrinóxenos hepáticos abrindo novas liñas de investigación na fisiopatoloxía da PLD e novos posibles enfoques terapéuticos. Finalmente, validamos unha selección de posibles candidatos por RT-qPCR e *Western Blotting*, atopando unha alta correlación cos datos de proteómica cuantitativa (8 de 10 validados con RT-qPCR e 5 de 5 validados con *Western Blotting*).
Eu resumo, realizamos un estudo cuantitativo proteómico baseado na tecnoloxía SWATH MS que compara proteomas *Wild Types* e fígados poliquísticos. Identificamos novas vías moleculares e dianas no campo da PLD e da formación e crecemento cistoxénico hepático, e resaltamos o complexo dos fibrinóxenos como unha nova aproximación terapéutica, o cal deberá ser validado en estudos preclínicos futuros.

Continuando coa caracterización da proteómica cuantitativa diferencial, comparamos o patrón do proteoma entre *Wild Type* e riles (e fígados) mutantes de ratos na ADPKD. Despois do análise das vías moleculares, o noso estudo proteómico revelou a rexión extracelular como o compoñente celular máis enriquecedor nos riles e fígados poliquísticos, con importante relevancia das MMPs. Ademais, analizamos a expresión xenética (por RT-qPCR) de todas as MMPs e

TIMPs presentes en riles e fígados poliquísticos de rato en ADPKD e ARPKD atopando unha des-regulación xeral (regulación ascendente ou regulación descendente) da cistoxénese renal e hepática. As alteracións na ECM e a des-regulación da expresión de MMPs e TIMPs son características comúns do crecemento dos quistes renais e hepáticos, e contribúen á acumulación de fibrose intersticial e ao crecemento do quiste representado unha potencial opción terapéutica.

Con base nos nosos datos e na literatura, decidimos avaliar un inhibidor de MMPs chamado Marimastat como abordaxe terapéutica en dous modelos murinos ortólogos de PKD (*Pkd1*$^{cond/cond}$*;Tam-Cre*$^{-/+}$ e *Pkhd1*$^{del3\text{-}4/del3\text{-}4}$). O tratamento con Marimastat retardou a progresión da cistoxénese renal e inhibe de xeito específico os quistes derivados do conduto colector (quistes DBA+). Ademais, Marimastat inhibe significativamente a cistoxénese hepática ligada a ADPKD e ARPKD. Marimastat é unha nova posible aproximación terapéutica e as MMPs son unha boa diana terapéutica para a cistoxénese renal e hepática da PKD.

Ademais, Marimastat restaura a expresión das MMPs e TIMPs tanto no fenotipo renal coma no hepático. Importante destacar que estes efectos observáronse na cistoxénese renal e hepática e en ambos dous modelos murinos. Non obstante, varias MMPs e TIMPs non viron afectada a súa expresión despois do tratamento. Isto indica un equilibrio complicado e un control recíproco entre a expresión de diferentes MMPs e TIMPs. Do mesmo xeito, Marimastat mostrou un efecto na mellora da fibrose, con ata catro marcadores de fibrose que diminuíron significativamente nos modelos de ADPKD e ARPKD, e unha diminución significativa de *Cxcl1* (homólogo en rato da IL-8), o que pode suxerir control chave desta citoquina na expresión das MMPs na PKD e PLD.

Finalmente, probamos Marimastat en combinación con Tolvaptan. O Tolvaptan é un receptor selectivo de arginina vasopresina V2 (AVP V2R), e actualmente é a única terapia aprobada para pacientes con ADPKD. Demostramos un efecto sinérxico de Marimastat en combinación con Tolvaptan, xa que Marimastat máis Tolvaptan

atrasaron a cistoxénese renal e hepática en dous modelos murinos ortólogos de PKD.
En conclusión, o noso traballo resaltou o papel patóxeno da ECM e das MMPs na progresión da cistoxénese renal e hepática e avaliamos o seu potencial terapéutico empregando un inhibidor de MMPs, o Marimastat. Marimastat demostrou que diminúe a progresión do ciste renal e inhibe a cistoxénese hepática en modelos animais, e acompañado tamén dunha diminución significativa da fibrose renal e hepática. Finalmente, en combinación con Tolvaptan, Marimastat atrasou a enfermidade cística renal e hepática mostrando un efecto sinérxico beneficioso.

A continuación, describimos o rol do eixe TWEAK/Fn14 en ADPKD. En primeiro lugar, realizamos unha meta-análise de datos publicados de modelos animais de enfermidades quísticas que revelaron a regulación ascendente do ARNm de varios compoñentes da vía de sinalización de TWEAK. A continuación, avaliamos a expresión de Fn14 en humanos e nun modelo murino ortólogo de ADPKD. Observamos que TWEAK e Fn14 estaban sobre-expresados nos quistes renais de ADPKD de rato, mentres que TWEAK era significativamente alto en urina e fluído quístico en pacientes con ADPKD. O noso estudo revelou que o eixo Fn14/TWEAK está regulado á alza no ril poliquístico humano e de rato. En APDKD hai unha ventá de desenvolvemento crítica para a formación da cistoxénese. Os estudos de modelos de ADPKD de eliminación condicional (que nos permiten eliminar o xene *Pkd1* en diferentes puntos de desenvolvemento renal) demostraron que a eliminación de *Pkd1* en riles maduros (despois do día 14 posnatal, ventá non-quística) atrasou a formación de quistes en comparación coa eliminación antes do día 12 posnatal (ventá quística). Estudamos o papel de TWEAK en ADPKD en ambas ventás de desenvolvemento. TWEAK induciu e promoveu a formación de quistes na ventá non-quística, provocando unha cistoxénese renal focal e localizada. Do mesmo xeito, TWEAK acelerou o crecemento dos quistes renais na

ventá quística, empeorou a taxa de supervivencia e aumentou a cistoxénese e a insuficiencia renal.
Con base nestes resultados, probamos se TWEAK pode ser un obxectivo terapéutico usando anticorpos neutralizantes anti-TWEAK para tratar o noso modelo murino ADPKD. Anti-TWEAK retarda o crecemento do quiste mellorando a función renal e a taxa de supervivencia. A cistoxénese en ADPKD implica dúas etapas principais: a iniciación e a progresión do quiste. Os nosos resultados apoian que un mediador inflamatorio, TWEAK, xoga un papel no crecemento e progresión do quiste.
Anti-TWEAK restaura varias vías relacionadas con ADPKD. Descubrimos que o tratamento anti-TWEAK normalizaba a fosforilación de p38 e reducía o nivel total de proteína AKT e a súa fosforilación. Ademais, anti-TWEAK restaurou o compoñente canónico NF-κB p65, reduciu o marcador de macrófagos M1, *Mcp1*, e o marcador de macrófagos M2, Arg1, e causou unha lixeira redución da fibrose e da apoptose. Finalmente, analizamos o recrutamento de macrófagos avaliado polo recrutamento total de macrófagos F4/80, resultando nunha diminución significativa co tratamento anti-TWEAK.
En resumo, caracterizamos o eixe TWEAK/Fn14 en ADPKD achando unha sobre-regulación en mostras de humanos e ratos. Usando modelos murinos, demostramos que TWEAK empeorou a progresión do quiste renal, pero a terapia anti-TWEAK retardou o crecemento cístico diminuíndo marcadores pro-proliferativos, pro-inflamatorios e o recrutamento de macrófagos. Esta tese identifica a vía de sinalización TWEAK como un novo mecanismo de enfermidade implicado na cistoxénese e no crecemento quístico e pode levar a un novo enfoque terapéutico na ADPKD.

E finalmente, co obxecto de estudar a interacción xenética dos xenes *Pkd1* e *Pkhd1*, xeramos e caracterizamos dous novos e dobre *knockouts* para ambos xenes. Nun primeiro *knockout* dobre, cruzamos os seguintes modelos animais con alelos conxénitos e embrionarios, pero con ausencia de fenotipo quístico renal: $Pkhd1^{del3\text{-}4/del3\text{-}4}$ e $Pkd1^{del2\text{-}4/+}$. Estes

modelos animais non presentan fenotipo quístico renal, pero en combinación (rato DKO) atopamos un efecto sinérxico e aditivo. Do mesmo xeito, decidimos empregar un modelo condicional en heterozigosis de *Pkd1* (*Pkd1*$^{cond/+;}$*Tam-Cre*$^{+}$) e eliminámola en diferentes puntos da vida. A formación de quistes e a gravidade da enfermidade foron segundo o momento da eliminación do xene *Pkd1*. Estes resultados son consistentes coa idea de que *Pkd1*/PC1 ten un papel central na cistoxénese. Non obstante, o alelo *Pkhd1* en combinación cun alelo *Pkd1* condicionado e en homozigosis para adultos (*Pkd1*$^{cond/cond;}$*Tam-Cre*$^{+}$) (rato DcKO) presentou un fenotipo quístico renal inesperado máis leve con mellor función renal e diminución da cistoxénese. Por outra banda, o fenotipo hepático desenvolveu un efecto aditivo en ambos os dous dobre *knockout* (DKO e DcKO). Os nosos datos suxiren que a interacción xenética entre *Pkdh1* e *Pkd1* é indirecta e revela limiares distintos tanto para os xenes como para os riles e o fígado.

Como conclusión, xeramos e caracterizamos dous novos dobre *knockouts* de *Pkhd1* e *Pkd1* para ampliar o coñecemento da interacción xenética de ambos xenes e co fin de ampliar o coñecemento dos mecanismos moleculares subxacentes da enfermidade. O noso estudo fixo fincapé e destacou o papel central de *Pkd1*/PC1 na cistoxénese, a PKD como trastorno dependente da dose de proteínas funcionais e a posibilidade da existencia de diferentes limiares cistoxénicos tanto para ambos xenes como para ril e fígado.

En resumo, a presente tese amplía o coñecemento sobre novas ideas e enfoques terapéuticos nos campos das Enfermidades Poliquísticas Renal e Hepática.

Palabras chave:
PKD, PLD, ciste, aproximación terapéutica, *Pkd1*, *Pkhd1*

ABSTRACT

Introduction. Polycystic Kidney Disease (PKD) is a group of monogenic disorders that result in renal cyst development. The most common forms of disease are, Autosomal Dominant Polycystic Kidney Disease (ADPKD) and Autosomal Recessive Polycystic Kidney Disease (ARPKD). ADPKD has a prevalence of 1:800, is characterized by the formation and progressive growth of multiple cysts that lead to End Stage Kidney Disease (ESKD) and is normally an adult-onset. ARPKD has a prevalence of 1:20.000, manifests perinatally or in childhood and the clinical course is severe and characterized by the combination of bilateral renal cystic disease and congenital hepatic fibrosis and often causes neonatal death. In ADPKD, all cysts derive from epithelial renal cells and from all kidney segments. However, ARPKD is characterized by dilatation of the collecting ducts of renal epithelial cells that radiate from the medulla to the cortex.

Polycystic Liver Disease (PLD) is a heterogeneous group of congenital disorders characterized by bile duct dilatation and cyst development derived from cholangiocytes (epithelial cells from bile duct). PLDs are inherited in dominant or recessive form and can develop alone (Isolated Polycystic Liver Disease or PCLD) or in association with PKD, being its principal extrarenal manifestation.

ADPKD is genetically heterogeneous with two genes identified, *PKD1* and *PKD2*. ARPKD is caused by mutations in *PKHD1* ant the recent discovery, *DZIP1L*. PCLD is always with dominant inherited and is caused by mutation in several genes: *PRKCSH*, *SEC63*, *LRP5*, *GANAβ*, *ALG8*, *SEC61B*, *PKHD1* (in heterozygosis) and *ALG9*.

PKD1 and *PKD2* encode the proteins Polycystin-1/PC1 and Polycystic-2/PC2 (also called TRPP2), respectively. PC1 was suggested as a putative receptor for an unidentified ligand, and PC2 is a Ca2+-permeable non-selective ion cation channel and member of the transient receptor potential (TRP) family. PC1 and PC2 forms a receptor-channel complex implicated in Ca2+ pathway and these two proteins are located

(between other cellular localizations) in primary cilium of epithelial cells. On the other hand, the protein product of *PKHD1* is the fibrocystin/polyductin/FPC, a membrane protein located in the primary cilium of epithelial cells and with undefined function.

Patients with ADPKD and PLD are typically heterozygous with one germline mutation in one PKD or PLD gene ("first hit"). The driving force leading to cystogenesis and activate the disease phenotype are the somatic "second-hit" mutations. This is the called "two-hit" model of cystogenesis, the most widely accept theory of cyst formation in human ADPKD and PCLD. Then, according to this model a critical threshold of functional protein delimitates the cyst formation and suggests that timing can influences ADPKD severity. Nevertheless, the mechanism and timing of this second-hit are currently unknown.

Cyst formation and progression occurs along time, cysts increase in number and volume with age. The cumulative area of cysts (Cystic Index) is the measurable biomarker to quantify cystogenesis, cyst expansion and to track the severity and progression of the disease. The current software that used to calculate the cystic index are imprecise, so more precise bioinformatic tools are needed to and quantify cystic index.

The primary clinical approach for PKD and PLD patients is to reduce their clinical symptoms because, up to date, there is no approved specific and efficient therapy. PKD and PLD treatment has been ineffective and the only one curative option is kidney and/or liver transplantation. In particular, therapeutic strategies have advanced further in ADPKD. Using in vitro and animal rodent models, several targets and drugs were proposed for ADPKD treatment leading to the approbation of Tolvaptan (an inhibitor of vasopressin-2-receptor) as the first and unique therapy for ADPKD patients. However, we are not at endpoint, this treatment has many limitations and are not enabled for all ADPKD patients. Novel and more efficient and safety therapeutic approaches must be developed.

Since the genes and their encoded proteins were described, several *in vitro* and animal models were developed for the study of PKD and

multiple molecular pathways were discovered and characterized. However, the key intrinsic molecular mechanism of cystogenesis remains unknown, leading to an increased interest in understanding molecular pathways and developing new therapeutic strategies. Several signaling pathways and transcription factors are under the control of cystogenesis and the progression of the disease: cAMP pathway regulated by PKA kinase and AC6, pro-proliferative pathways as mTOR, RAS-RAF- ERK or AKT, pro-inflammatory and pro-fibrotic signaling pathways etc.

Fibrosis is a pathological mechanism characterized by the accumulation of matrix in the extracellular region of cells and is associated with loss of organs function. In PKD and PLD, expansion of cysts and loss of renal and hepatic function are associated with varying degrees of progressive interstitial fibrosis and abnormalities in extracellular matrix (ECM). Matrix metalloproteases (MMPs) are a large family of proteases involved in the remodeling and degradation of the ECM. The MMP activity is regulated by several mechanisms; one is the inhibition of metalloproteases by endogenous tissue inhibitors of metalloproteases (TIMPs). Alterations in MMPs/TIMPs are involved, both in human and mouse pathogenesis and in the progression of PKD and PLD.

On the other hand, PKD and PLD are not primarily an inflammatory disease; however, interstitial inflammation promotes cyst progression through macrophage recruitment and upregulation of pro-inflammatory cytokines, which also are present in high levels in renal and hepatic cystic fluid. Tumor Necrosis Factor-like Weak Inducer of Apoptosis (TWEAK, TNFSF12) is a type II transmembrane glycoprotein, which belongs to the TNF superfamily (TNFSF) of cytokines and contributes to kidney inflammation promoting chemokine secretion by renal cells kidney cell proliferation and other molecular pathways.

Material and methods.

CystAnalyser concise methods. Image from Hematoxylin-Eosin staining's of C57/BL6 *Pkd1*$^{cond/cond}$*;Tam-Cre*$^{+}$ and C57/BL6 *Pkhd1*$^{del3-4/del3-4}$ animal models were used for the study. A total of 795

image were used, classified in “Mild-Cystic”, “Cystic” and “Severely-Cystic” according to Cystic Index value.

Proteomics. Spectral library is created with a pool of each group of samples using 4 µl (over 4 µg of protein). The peptide solutions were analyzed by shotgun data-dependent acquisition (DDA) approach by micro-LC-MS/MS and the mass spectrometer coupled was a hybrid quadrupole-TOF mass spectrometer, 6600 (SCIEX®). Total of 4 micrograms of protein per sample and technical replicate were run using a SWATH method, and the spectral alignment and targeted data extraction were performed by PeakView v.2.2.

Mouse models. The following mouse PKD line were used in the present thesis: *Pkhd1*$^{del3\text{-}4/del3\text{-}4}$ or Pkhd1-KO (a homozygous *Pkhd1* knockout animal model with the exons 2 and 3 deleted that develops slowly progressive polycystic liver disease, but not kidney disease), *Pkd1*$^{del2\text{-}4/+}$ or *Pkd1*-KO (a *Pkd1* knockout with exons 2 to 4 deleted, which not present renal or hepatic cystogenesis in heterozygosity); and *Pkd1*$^{cond/cond}$*;Tam-Cre* or *Pkd1*-CKO (a homozygous *Pkd1* conditional knockout with the Cre-LoxP system and a tamoxifen dependent promoter). All of them are inbreed into the C57BL/6 strain and the genotype was confirmed by PCR. In the case of *Pkd1*$^{cond/cond}$*;Tam-Cre*, Cre- mice were used as *Wild Types* (also named WT) and Cre+ as mutants (also named Mut or KO).

Treatments. Marimastat (Sigma® #M2699) and Tolvaptan (Jinarc®) were administrated intraperitoneally in a dose of 1-10mg/kg/24h bid and 2mg/kg/24h bid respectively. On the other hand, mice were injected intraperitoneally with TWEAK (30 ng/g mouse/48h), neutralizing anti-TWEAK mAb (IgG1 BIIB023, clone P2D10) (10 mg/kg mouse/3 times weekly) or isotype IgG (mouse IgG2A) (10 mg/kg mouse/3 times weekly) for control groups, generously provided by Biogen, Inc.

Histology. The right kidney and the liver largest lobe of animals were always fixed in paraformaldehyde. Specifications about staining`s, antibodies and reagents in Material and methods section.

Protein and RNA extraction. Left kidneys and livers were ground in liquid nitrogen and half of the tissue is assigned to protein extraction

and the other one to RNA extraction. The protein and RNA resultant were used for RT-qPCR and *Western Blotting* analysis. Specification about antibodies, protocols and reagents in Material and Methods Section.
Statistics. For comparisons between multiple groups, a one-way ANOVA test with Tukey post-test was performed, whereas two-tailed Student's t test was used to determine significance of differences between two groups. P-values less than 0.05 were considered statistically significant. All data sets were analyzed with GraphPad Prism® Software (version 5.0 or 7.0).

Objectives. In this context, the present work has the following objectives: 1) develop new and more reliable tools for the assessment of cystic pathologies, as PKD and PLD, which provides us Cystic Index parameter; 2) perform a comparative of quantitative proteomic of *Wild Type* and polycystic mice livers in order to identify new possible novel therapeutic targets and molecular pathways on PLD field; 3) test the therapeutic potential of metalloproteases and extracellular matrix alterations in orthologous murine models; 4) characterize FN14/TWEAK axis and test its possible therapeutic role; 5) expand the knowledge of *Pkd1* and *Pkhd1* genetic interaction in PKD orthologous animal models.

Results and Conclusions. First, we have developed a new software, named CystAnalyser, that combines automatic image processing with a graphical user friendly interface (GUI) that allows investigators to oversee and easily correct the image processing before quantification. CystAnalyser was able to generate a cystic profile including cystic index, number of cysts and cyst size on histological images of samples in PKD and PLD field. CystAnalyser is written in the C++ programming language using the GTK+ ("GIMP Tool Kit") library, and the algorithms used to recognize the cysts on the image are a combination of computer vision techniques implemented using the

OpenCV modules *core* and *imgproc*. This software allows automatic cyst recognition and/or supervised post-processing tools.
In order to test the CystAnalyser software, 795 cystic kidney, and liver histological images were analyzed. Using CystAnalyser there were no differences calculating cystic index automatically versus user input, except in specific circumstances where it was necessary for the user to distinguish between mildly cystic from non-cystic regions. The sensitivity and specificity of the number of cysts detected by the automatic quantification depends on the type of organ and cystic severity, with values 76.84–78.59% and 76.96–89.66% for the kidney and 87.29–93.80% and 63.42–86.07% for the liver. CystAnalyser, in addition, provides a new tool for estimating the number of cysts and a more specific measure of the cystic index than ImageJ, the most widely used software today.
In conclusion, we have developed a new software toll for the quantification of histological images from cystic kidney and liver mice samples for routine biomedical research, called CystAnalyser. Besides, CystAnalyser overcome in sensitive and reliable quantifying the cystic area and the cyst number in comparison with the most used software in cystic disease research (ImageJ).

Second, we performed a differential proteomic quantitative study based on SWATH MS technology in polycystic liver disease or PLD. Using SWATH MS technology, we compared the proteomes of *Wild Type* and mutant polycystic livers from an ADPKD orthologous animal model ($Pkd1^{cond/cond};Tam\text{-}Cre^{-/+}$). We have obtained a list of proteins with statistical differences ($p \leq 0.05$) and more than 2 fold change cut off. Then, we performed a GO pathway and a protein-protein analysis identifying several main biological functions in polycystic livers and two important protein clusters. Importantly, the most enriched cluster was focused on hepatic fibrinogens opening new lines of research in PLD physiopathology and possible new therapeutic approaches. Finally, we validated a selection of possible candidates by RT-qPCR and *Western Blotting*, finding a high correlation with quantitative

proteomics data (8 to 10 validated with RT-qPCR, and 5 to 5 validated with *Western Blotting*).
In summary, we reported a proteomic quantitative study based on SWATH MS technology comparing proteomes of *Wild Type* and polycystic livers. We identified novel molecular pathway and targets in PLD field and we highlighted the fibrinogen-cluster as a new possible therapeutic target, which must be confirmed in future preclinical studies.

Continuing with the characterization of differential quantitative proteomics, we compared the proteome pattern between *Wild Types* and mutants mice kidneys (and livers) in ADPKD. After pathway analysis, our proteomic study revealed the extracellular region as the most enrichment cellular component in polycystic kidney and livers, with important relevance of the MMPs. Furthermore, we assed genetic expression (by RT-qPCR) of all MMPs and TIMPs present in mouse of polycystic kidney and livers in ADPKD and ARPKD finding a general deregulation (upregulation or downregulation) in renal and hepatic cystogenesis. Alterations in ECM and deregulation of MMPs and TIMPs expression are common features of renal and hepatic cyst growth, which contribute to accumulation of interstitial fibrosis and cyst growth and represent a potential therapeutic option.
Based in our data and the literature, we decide to evaluate an inhibitor of MMP called Marimastat as therapeutic approach in two PKD orthologous murine models ($Pkd1^{cond/cond};Tam\text{-}Cre^{-/+}$ and $Pkhd1^{del3\text{-}4/del3\text{-}4}$). Marimastat treatment slows renal cystogenesis progression and inhibits in a specific way collecting duct derived cysts (DBA^{+} cysts). Besides, Marimastat significantly inhibits hepatic cystogenesis related with ADPKD and ARPKD. Marimastat is a new possible therapeutic approximation and MMPs are a druggable target for renal and hepatic cystogenesis of PKD.
In addition, Marimastat restores MMPs and TIMPs expression in both renal and hepatic phenotypes. Significantly, these effects were observed in renal and hepatic cystogenesis and in both murine models. However,

several MMPs and TIMPs did not affect their expression after treatment. This indicates a complicate balance and reciprocal control between expression of different MMPs and TIMPs. In the same way, Marimastat have shown an effect in amelioration of fibrosis, with up to four fibrosis markers that decreased significantly in both ADPKD and ARPKD models, and a significant diminution of *Cxcl1* (IL-8 mouse homolog), which can suggest a key control of this cytokine in MMPs expression in PKD and PLD.
Finally, we tested Marimastat in combination with Tolvaptan. Tolvaptan is a selective arginine vasopressin V2 receptor (AVP V2R) and is currently the only approved therapy for ADPKD patients. We demonstrated a synergist effect of Marimastat in combination with Tolvaptan, Marimastat plus Tolvaptan delayed renal and hepatic cystogenesis in the two PKD orthologous murine models.
In brief, our work highlighted the pathogenic role of ECM and MMPs in the progression of renal and hepatic cystogenesis and we evaluated its potential therapeutic using a MMPs inhibitor, the Marimastat. Marimastat showed that ameliorates the renal cyst progression and inhibits the hepatic cystogenesis in animal models and accompanied with a significant decrease in renal and hepatic fibrosis. Finally, in combination with Tolvaptan, Marimastat delayed renal and hepatic cystic disease showing a mutual and beneficial synergist effect.

Next, we described the TWEAK/Fn14 axis in ADPKD. In first place, we performed a meta-analysis of published animal models data of cystic disease revealing mRNA upregulation of several components of TWEAK signaling pathway. Following, we evaluated Fn14 expression in human and in an orthologous murine model of ADPKD. We observed that TWEAK and Fn14 were overexpressed in mouse ADPKD kidney cysts, while TWEAK was significantly high in urine and cystic fluid from ADPKD patients. Our study revealed that Fn14/TWEAK axis is upregulated in human and mouse polycystic kidney.

In APDKD there is a critical developmental window for the formation of cystogenesis . Studies from ADPKD conditional knockout models (which allow us to delete *Pkd1* gene in different kidney development points) have demonstrated that *Pkd1* deletion in mature kidneys (after postnatal day 14, non-cystic window) delayed cyst formation compared with deletion before postnatal day 12 (cystic window). We studied the role of TWEAK in ADPKD in both developmental windows. TWEAK induced and promoted cyst formation in the non cystic window, causing a focal and located renal cystogenesis. In the same way, TWEAK accelerated renal cyst growth in the cystic window, worsened survival rate and increased cystogenesis and renal failure.

On the basis of these results, we tested whether TWEAK may be a therapeutic target using neutralizing anti-TWEAK antibodies for treats our ADPKD murine model. Anti-TWEAK slows cyst growth improving kidney function and survival rate. Cystogenesis in ADPKD involves two main stages: cyst initiation and cyst progression. Our results support that an inflammatory mediator, TWEAK, plays a role in cyst growth and progression.

Anti-TWEAK restores several ADPKD-related pathways. We found that anti-TWEAK treatment normalized p38 phosphorylation and reduced total AKT protein level and AKT phosphorylation. Also, anti-TWEAK restored the canonical NF-κB component p65, reduced the M1 macrophage marker, *Mcp1*, and the M2 macrophage marker, *Arg1* and caused a slight reduction of fibrosis and apoptosis. Finally, we analyzed macrophage recruitment assessed by the total macrophage recruitment F4/80 resulting in a significant decreased with anti-TWEAK treatment.

In sum, we characterized the TWEAK/Fn14 axis in ADPKD finding upregulation in human and mice samples. Using murine models, we demonstrated that TWEAK worsened the renal cyst progression but anti-TWEAK therapy effectively slows cyst growth decreasing pro-proliferative, pro-inflammatory markers and macrophage recruitment. This thesis identifies TWEAK signaling pathway as a new disease mechanism involved in cystogenesis and cystic growth and may lead to a new therapeutic approach in ADPKD.

And finally, in order to study the genetic interaction of *Pkd1* and *Pkhd1* genes we generated and characterized two new and double knockouts for both genes. In a first double knockout, we intercrossed the following animal models with congenic and embryonic alleles, but with absence of renal cystic phenotype: $Pkhd1^{del3\text{-}4/del3\text{-}4}$and $Pkd1^{del2\text{-}4/+}$. These single knockouts not present renal cystic phenotype, but in combination (DKO mice) we found a synergist and additive effect. In the same way, we decided to use a conditional knockout in heterozygosity of *Pkd1* ($Pkd1^{cond/+;}Tam\text{-}Cre^{+}$) and deleted it at different life points. Cyst formation and disease severity was according to timing of *Pkd1* gene inactivation. These results are consistent with the idea that Pkd1/PC1 has a central role in cystogenesis. However, *Pkhd1* allele in combination with an adult conditionate and homozygous *Pkd1* allele ($Pkd1^{cond/cond};Tam\text{-}Cre^{+}$) (DcKO mice) presented an unexpected milder renal cystic phenotype with better renal function and decreased of cystogenesis. By other hand, hepatic phenotype developed an additive effect in both double knockouts (DKO and DcKO). Our data suggest that genetic interaction between *Pkdh1* and *Pkd1* is indirect and reveal distinct thresholds for both genes and for both kidney and liver.
In conclusion, we generated and characterized two new double knockouts of *Pkhd1* and *Pkd1*. Our data emphasized the central role of *Pkd1*/PC1 for cystogenesis, the PKD as a gene-functional protein dosage-dependent disorder and the possibility of different thresholds for both genes and both kidney and liver.

In summary, the present thesis expands the knowledge about new insights and therapeutic approaches in the fields of Polycystic Kidney and Liver Diseases.

Key words:
PKD, PLD, cyst, therapeutic approach, *Pkd1*, *Pkhd1*

INDEX OF CONTENTS

ABBREVIATIONS 1
INTRODUCTION 4
1. POLYCYSTIC KIDNEY DISEASE 4
1.1. Autosomal Dominant Polycystic Kidney Disease 4
1.2. Autosomal Recessive Polycystic Kidney Disease 5
2. POLYCYSTIC LIVER DISEASE 7
3. PKD AND PLD GENES AND PROTEINS 8
3.1. PKD and PLD genetics 8
3.2. Proteins: structure and function 10
4. CYSTOGENESIS AND TWO-HIT MODEL 12
5. IMAGE TECHNIQUES FOR CYSTIC INDEX QUANTIFICATION 13
6. METHODS OF DIAGNOSIS AND TREATMENT OF PKD AND PLD 14
7. MOLECULAR PATHWAYS 16
7.1. Fibrosis in PKD and PLD 18
7.2. Inflammation and TWEAK 19
8. ROLE OF CILIA 21
9. THRESHOLD AND DOSAGE MODEL OF CYSTOGENESIS 23
OBJECTIVES 25
MATERIAL AND METHODS 27
1. CYSTANALYSER CONCISE METHODS 27
1.1. Animal models 27
1.2. Immunohistochemistry and image acquisition 27
1.3. Dataset description 27
1.4. Statistical analysis 28
1.5. Experts perception 29

2. PROTEOMICS 30
2.1. Protein digestion for proteomics 30
2.2. Generation of the references spectral library 30
2.3. Quantification by SWATH and data analysis 31
2.4. Data analysis 32
2.5. Signaling pathway analysis 33
3. MOUSE MODELS 34
4. TREATMENTS 35
4.1. Chapter 3: Marimastat and Tolvaptan 35
4.2. Chapter 4: TWEAK and Anti-TWEAK 36
5. HISTOLOGY 37
5.1. Histology Tissue Processing 37
5.2. Staining protocol 37
5.3. Image capture 38
5.4. Measurement of Cystic Index 38
5.5. Immunofluorescences and immunohistochemistry quantification 39
6. CLINICAL CHEMISTRY 39
7. PROTEIN AND RNA EXTRACTIONS 39
8. REAL-TIME QUANTITATIVE PCR 40
9. WESTERN BLOT 41
10. MOUSE TNFSF12/TWEAK ELISA 42
11. HUMAN ADPKD CYSTIC FLUID/HUMAN COHORT 42
12. *IN VITRO* EXPERIMENTS 42
13. STATISTICS 43
RESULTS 45

1. CHAPTER 1 45
1.1. Description and functionality of CystAnalyser 46
1.2. Development of algorithms for automatic cyst recognition 48
1.3. Cystic index, cyst number and size profile calculation 50
1.4. Comparison with ImageJ 56
2. CHAPTER 2 59
2.1. Liver proteome Characterization by SWATH analysis 60
2.2. Protein abundance changes in hepatic cystogenesis 62
2.3. Pathway analysis 67
2.4. Validations of target candidates 68
3. CHAPTER 3 71
3.1. Extracellular matrix and MMPs expression are deregulated in PKD 72
3.2. Marimastat reduces renal cyst growth in ADPKD and inhibits hepatic cystogenesis in PKD 73
3.3. Marimastat restores MMPs expression 78
3.4. Marimastat decreases interstitial fibrosis 78
3.5. Combination treatment: Marimastat plus Tolvaptan 83
4. CHAPTER 4 86
4.1. Data mining identification of Fn14 as overexpressed in polycystic kidney disease 87
4.2. Axis TWEAK/Fn14 are upregulated in ADPKD 89
4.3. TWEAK promotes cystogenesis and cyst progression in an orthologous model of ADPKD 91
4.4. Anti-TWEAK slows cyst growth and improves renal function in ADPKD mice 97
4.5. Anti-TWEAK decreases cell proliferation via inhibition of the AKT pathway 99

4.6. Anti-TWEAK treatment reduces inflammation and macrophage recruitment 100
5. CHAPTER 5 104
5.1. *Pkd1* and *Pkhd1* synergistic genetic interaction 105
5.2. *Pkd1* controls cyst progression in PKD 107
5.3. Novel genetic interaction in *Pkhd1* and *Pkd1* reveals possible key effectors in cyst formation 109
5.4. Additive effect in liver cystogenesis in *Pkhd1* and *Pkd1* genetic interaction 111
DISCUSSION 115
1. DISCUSSION CHAPTER 1 115
2. DISCUSSION CHAPTER 2 116
3. DISCUSSION CHAPTER 3 118
4. DISCUSSION CHAPTER 4 122
5. DISCUSSION CHAPTER 5 127
CONCLUSIONS 130
BIBLIOGRAPHY 133
SUPPLEMENTAL MATERIAL 154
1. SUPPLEMENTAL INFORMATION 154
1.1. Author contributions 154
1.2. Competing interests 154
2. SUPPLEMENTAL FIGURES 155
3. SUPPLEMENTAL TABLES 184
ANNEXS 194

ABBREVIATIONS

α-SMA:	Alpha-smooth muscle actin
ADPKD	Autosomal Dominant Polycystic Kidney Disease
AKT	Protein kinase B
ALT	Alanine Aminotransferase
ALP	Alkaline phosphatase
ANXA2	Annexin A2
Arg1	Arginase 1
ARPKD	Autosomal Recessive Polycystic Kidney Disease
BUN	Blood urea nitrogen
CKO	Conditional knockout
Col1a1	Collagen Type I Alpha 1 Chain
Ctgf	Connective tissue growth factor
Cxcl1	Chemokine (C-X-C motif) ligand 1
DAPI	4′,6-diamidino-2-phenylindole
DBA	Dolichos Biflorus Agglutinin
DcKO	$Pkhd1^{del3\text{-}4/del3\text{-}4}$; $Pkd1^{cond/cond}$;$Tam\text{-}Cre^{+}$ mouse
DKO	$Pkhd1^{del3\text{-}4/del3\text{-}4}$; $Pkd1^{del2\text{-}4/+}$ mouse
ECM	Extracellular matrix
ELISA	Enzyme-Linked ImmunoSorbent Assay
ERK	Extracellular-signal-regulated kinase
FIBA	Fibrinogen Alpha Chain

FIBB	Fibrinogen Beta Chain
FIGG	Fibrinogen Gamma Chain
FGL1	Fibrinogen-like protein 1
FN14	Fibroblast growth factor-inducible-14
FPC	Fibrocystin/polyductin
HAOX2	Hydroxyacid Oxidase 2
HEMO	Hemopexin
Hprt	Hipoxantina-guanina fosforribosiltransferasa
Gapdh	Glyceraldehyde-3-phosphate dehydrogenase
Il6	Interleukin-6
ILK	Integrin Linked Kinase
KO	Knockout/mutant
LTL	Lotus Tetragonolobus Lectin
Mcp1	Monocyte chemoattractant protein-1
MMP	Matrix metalloprotease
PC1	Polycystin-1
PC2	Polycystin-2
PCR	Polymerase chain reaction
PLD	Polycystic Liver Disease
PKD	Polycystic Kidney Disease
PKD1/*Pkd1*	Polycystic kidney disease 1
Pkd1-cKO	*Pkd1*$^{cond/cond}$;*Tam-Cre*$^{+}$ mouse

Pkd1-KO	*Pkd1*$^{del2\text{-}4/+}$ mouse
PKD2/*Pkd2*	Polycystic kidney disease 2
Pkhd1	Polycystic kidney and hepatic disease 1
Pkhd1-KO	*Pkhd1*$^{del3\text{-}4/del3\text{-}4}$ mouse
pX	Postnatal day X
RT-qPCR	Reverse-transcription quantitative PCR
S100A9	S100 Calcium Binding Protein A9
SAMP	Amyloid P Component, Serum
SEM	Standard error mean
SWATH-MS	Sequential Window Acquisition of all Theoretical fragment-ion spectra-Mass Spectrometry
TGFβ	Transforming growth factor beta
THP	Tamm-Horsfall protein
TIMP	Tissue inhibitors of metalloproteases
TWEAK	Tumor necrosis factor-like weak inducer of apoptosis
WB	*Western Blotting*
WT	*Wild Type*

USC
UNIVERSIDADE
DE SANTIAGO
DE COMPOSTELA

INTRODUCTION

INTRODUCTION

1. POLYCYSTIC KIDNEY DISEASE

Polycystic Kidney Disease (PKD) is a heterogeneous group of monogenic disorders characterized by the bilateral formation and progressive expansion of renal fluid-filled cyst that lead to end stage renal disease (ESRD). Several Mendelian diseases including Autosomal Dominant Polycystic Kidney Disease (ADPKD), Autosomal Recessive Polycystic Kidney Disease (ARPKD), and atypical forms of PKD can be grouped under this pathological entity[1]. The principal extrarenal manifestation of PKD is the Polycystic Liver Disease (PLD)[2].

1.1. Autosomal Dominant Polycystic Kidney Disease

Autosomal dominant polycystic kidney disease (ADPKD) is the most common renal genetic disorder, with an estimated prevalence of 1:800 individuals[3,4]. On the basis of this prevalence, ADPKD is predicted to affect more that 10 million people worldwide. ADPKD is characterized by the formation and progressive growth of multiple cysts that lead to End Stage Kidney Disease (ESKD) at the age of 50-60s years with gradual loss of renal function[5]. ADPKD is normally an adult-onset and is characterized by the progressively enlargement of cystic kidneys starting to develop in utero[6] (**Figure 1**). In ADPKD, all cysts derive from epithelial renal cells and from all kidney segments, but preferentially form the distal part of nephron and in the collecting duct[7].

The vast majority of patients develop the symptomatology of disease between the ages of 20-40s, but there have been sporadic cases that range in onset from late to childhood ("early onset", before 15 years old) or even *in utero* ("very early onset")[8]. Besides, ADPKD can be associated with several extrarenal manifestations including hypertension, symptomatic extrarenal cysts and subarachnoid hemorrhage from intracranial aneurysms[9,10]. **Figure 2** (upper panel) showed a representative macroscopic illustration and typical histologic

analysis of ADPKD kidneys, where innumerable cysts progresses along renal parenchyma[7].

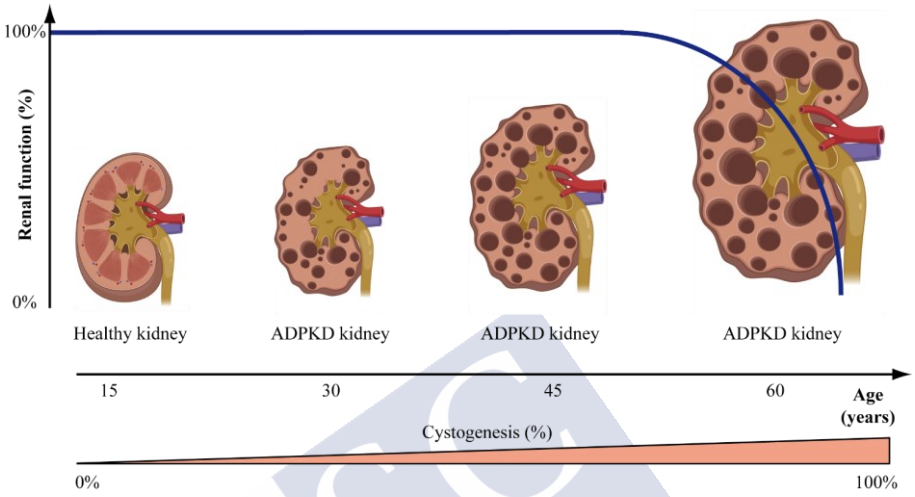

Figure 1. Typical pathogenesis of ADPKD. Cystogenesis and total kidney volume show a progressive growth along ADPKD patient life, which causes nephron compression and destruction. In early phases of disease, intact nephrons exhibit hyperfiltration compensatory function and GFR (blue line) is undamaged. However, with kidney volume increase, GRF decline leading to renal function loss and finally ESRD. Image of own elaboration.

1.2. Autosomal Recessive Polycystic Kidney Disease

On the other hand, Autosomal Recessive Polycystic Kidney Disease (ARPKD) is rarer than ADPKD (~1:20000 live births). ARPKD manifests perinatally or in childhood and the clinical course is severe and often causes neonatal death[7,11]. ARPKD constitutes one of the most important causes of renal replacement therapy and/or liver transplantation in childhood[12]. Other clinical manifestations of ARPKD in children and adults include systemic hypertension (56-70% of patients), growth retardation, urinary tract infection and hyponatremia[13].

ARPKD is characterized by the combination of bilateral renal cystic disease and congenital hepatic fibrosis. Fusiform dilatation of the collecting ducts of renal epithelial cells that radiate from the medulla to

the cortex characterizes the renal cystic disease[13] (**Figure 2**, lower panel), and the liver disease is characterized by hepatic fibrosis, consist in the abnormal development of biliary tree, increasing the number of tortuous interlobular bile ducts located in the periphery of the portal tract. There are varying degrees of portal fibrosis, hypoplasia of the small portal vein branches, and hepatic arteriolar prominence[14].

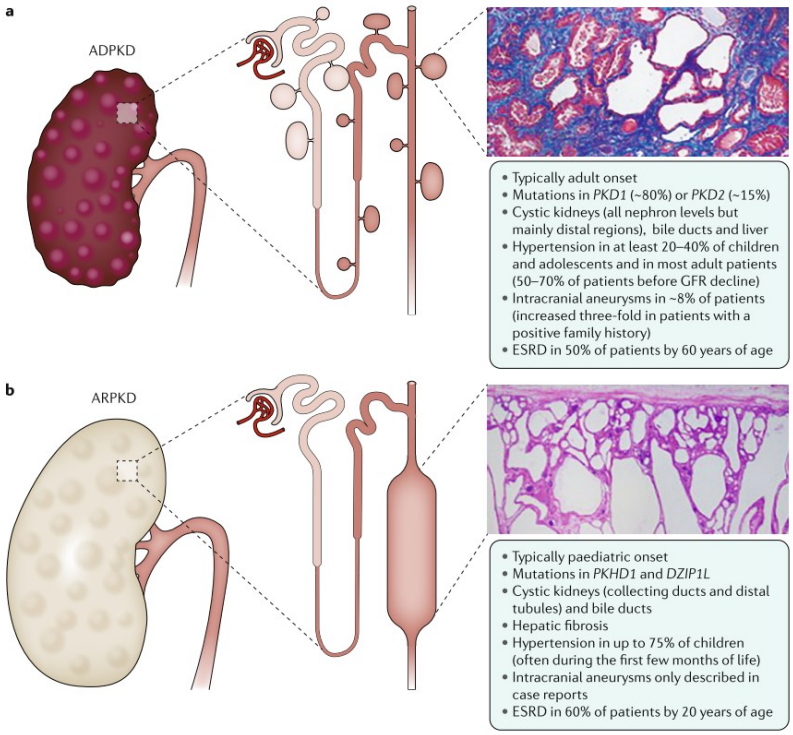

Figure 2. Principal manifestations of Polycystic Kidney Disease. (A) Autosomal Dominant Polycystic Kidney Disease is usually an adult-onset disease and it is characterized by the progressive formation and enlargement of renal cysts along parenchyma kidney (cystogenesis can occur in all nephron segments). The histology image is of the kidney (stained with Malloy trichrome stain) of a 49-year- old patient with end- stage ADPKD.(B) Autosomal Recessive Polycystic Kidney Disease usually presents in utero, perinatally or in infancy (pediatric-onset disease) that is characterized by the expansion and elongation of cysts in collecting ducts. Respective dilated collecting ducts run perpendicular to the renal capsule (renal section is stained with hematoxylin and eosin). Image taken from Bergman et al. 2017[7], allow by Springer Nature.

2. POLYCYSTIC LIVER DISEASE

Polycystic Liver Disease (PLD) is a heterogeneous group of congenital disorders characterized by bile duct dilatation and cyst development derived from cholangiocytes (epithelial cells from bile duct). The numerous cysts spread and progresses throughout the liver parenchyma[15]. PLDs are inherited in dominant or recessive form and can develop alone (Isolated Polycystic Liver Disease or PCLD) or in association with PKD, being its principal extrarenal manifestation. In ADPKD, the ~85% of patients develops liver cysts throughout hepatic parenchyma and the severity range from a few cysts or a severe hepatic cystogenesis[16]. Meanwhile, ARPKD liver cysts could be develop but the principal hepatic complications are defective remodeling of ductal plate with congenital hepatic fibrosis[7,16]. **Figure 3** represents the typical clinical manifestation of liver and kidney phenotype in ADPKD and ARPKD[17].

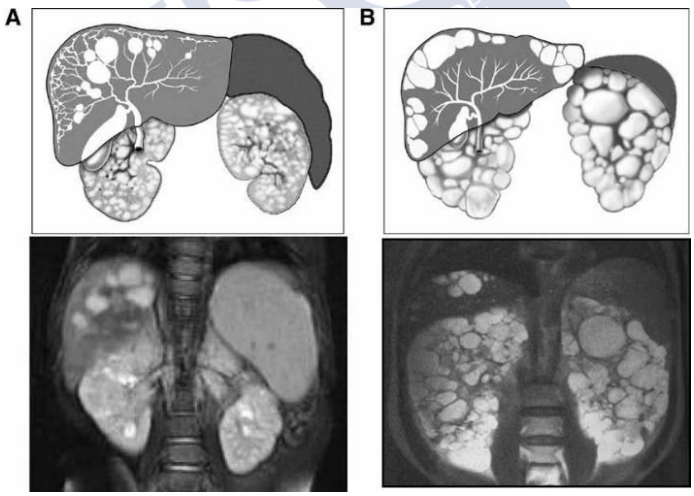

Figure 3. Schematic representation and MRI images of kidneys and livers in ADPKD and ARPKD patients. (A-B) Typical ARPKD (A) and ADPKD (B) clinical manifestation. ARPKD kidneys, usually, conserve their contour and form, but present several cysts in renal parenchyma. ARPKD livers have dilations in bile duct and presents liver cysts and prominent hepatic fibrosis. On the other hand, ADPKD liver often have deformed contours and enlarged size du to growth of innumerable macrocysts. Liver phenotype in ADPKD presents hepatic cysts but not adjoining with the biliary tree. Image taken from Gunay-Aygun et al. 2009[17], allow by John Wiley and Sons.

3. PKD AND PLD GENES AND PROTEINS

3.1. PKD and PLD genetics

ADPKD is associated with mutations in *PKD1* and *PKD2*. *PKD1* is a complex gene mapping to chromosome 16 (16p13.3)[18-20] and its genomic structure has a number of features important to mention: it is highly GC-rich wit a large number of CpG dinucleotides[21], 70% of the gene is duplicated multiple times in chromosome 16 (six pseudogenes)[22] and it contains a polypyrimidine tract in intron 21 of 2.5 kb (largest in human genome)[23]. *PKD2* is located in chromosome 4 (4q21) and has a simpler structure than *PKD1*[24] (**Figure 4** and **Table1**).

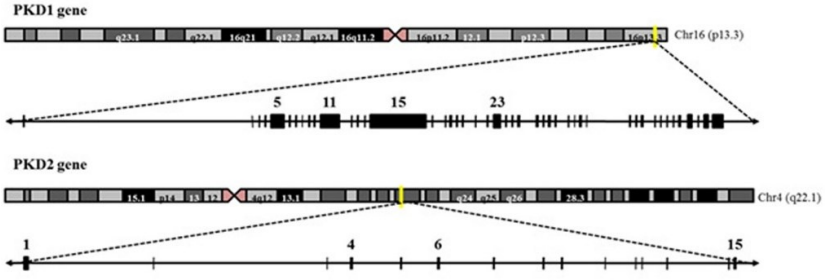

Figure 4. Chromosome localization and genomic structure of PKD1 and PKD2 genes. (A) Schematic representation of chromosomes and genomic structure for PKD1 and PKD2. Image taken from Cordido et al. 2017[5], an open-access article under the terms of the CC BY.

ARPKD is caused by mutations in *PKHD1*[25] ant the recently discovery, *DZIP1L*[26]. *PKHD1* gene, located in chromosome 6 (6p12.3-p12.2) (4,11–13) is one of the largest human genes with a genomic segment of ~500kb. It is predicted to have a minimum of 86 exons assembled in a complicated pattern of alternative splice variants, which transcribes a large full-length mRNA of approximately 8.5kb-13kb[27]. Using genome-wide analysis of SNPs, whole-exome sequencing and Sanger sequencing Lu and colleagues[26] establish *DZIP1L*, located on chromosome 3 (3q22.1- q23) and encodes a 767- amino acid protein, as a second gene involved in ARPKD pathogenesis. The authors identified mutations in seven patients, ~0.3% of cohort, and suggest that *DZIP1L* mutations are not a common cause of the disease[26,28] (**Table1**).

PCLD is caused by mutation in several genes, and always with dominant inherited. *PRKCSH*[29,30] and *SEC63*[31] were the first genes associated with PLD representing the ~20% and ~15% of patients, respectively. Next, *LRP5* were added to the lists of PLD genes[32]. Later, using whole exome sequencing in 327 genetically unresolved ADPKD families, *GANAβ* were identified as PCLD gene[33]. In the same way, in a second cohort of 102 genetically unresolved ADPLD patients, *GANAβ* (for the second time), *ALG8*, *SEC61B* and *PKHD1* (in heterozygosis) were associated in PLD genetic spectrum[34]. Finally, *ALG9* gene were associated with PCLD[35] (**Table1**). Mutations in these genes, together explain ~50% of PLD cases[36,37].

Table 1. Classification of PKD and PLD genes and proteins.

Disease	Gene	Protein	Reference
Polycystic Kidney Disease (PKD)			
Autosomal Dominant Polycystic Kidney Disease (ADPKD)	*PKD1*	Polycystin-1 (PC1)	18-20,38,39
	PKD2	Polycystin-2 (PC2)	24,38
Autosomal Recessive Polycystic Kidney Disease (ARPKD)	*PKHD1*	Fibrocystin/ Polyductin (FPC)	25,40,41
	DZIP1L	DAZ- interacting protein 1-like protein	26
Polycystic Liver Disease (PLD)			
N-linked glycosylation	*PRKCSH*	Glucosidase II Beta Subunit (GIIß)	29,30
	GANAB	Glucosidase II Alpha Subunit (GIIα)	33,34
	ALG8	Alpha-1,3-Glucosyltransferase	34
	ALG9	Alpha-1,2-mannosyltransferase	35
Endoplasmic reticulum translocation	*SEC63*	Translocation protein SEC63 (SEC63)	31
	SEC61B	Protein transport protein Sec61 subunit beta (SEC61ß)	34
Other functions	*LRP5*	LDL receptor-related protein 5	32
	PKHD1	Fibrocystin/ Polyductin (FPC)	34

3.2. Proteins: structure and function

PKD1 and *PKD2* encode the proteins Polycystin-1/PC1 and Polycystic-2/PC2 (also called TRPP2), respectively. PC1 was suggested as a putative receptor for an unidentified ligand which contains a long extracellular N-terminal domain, 11 transmembrane domain and a short C-terminal domain (**Figure 5** and **Table 1**)[38,39]. On the contrary, PC2 is a $Ca2^{+}$-permeable non-selective ion cation channel and member of the transient receptor potential (TRP) family. PC2 structure consists in six transmembrane segments, a pore loop domain (separating the first two membrane segments) and an N- and C- terminal domains[38,42] (**Figure 5** and **Table 1**). Localization of PC1 covers primary cilia, cytoplasmic vesicles, plasma membrane and cell adhesions. PC2 is found predominantly in endoplasmic reticulum, but also in plasma membrane, primary cilium and centrosome[43]. PC1 and PC2 forms a receptor-channel complex implicated in Ca^{2+} pathway[38,44]. Recent studies have reported that PC2 can function independently of PC1 in homomeric complexes formed by four PC2 in the primary cilium of renal epithelial cells to form a channel that is mainly permeant to monovalent cations. The heteromeric PC1-PC2 complex comprises one PC1 and three PC2 channel subunits[42,45]. However, the physiological function of polycystins remains unclear[46].

The protein product of PKHD1 is the fibrocystin/polyductin/FPC, a membrane protein with a long extracellular N-terminus, a single transmembrane segment and short cytoplasmic C-terminus tail[40,41]. FPC present a very complicated pattern of Notch-like proteolytic processing[47], and was found in the basolateral plasma membrane, primary cilia and in the centrosome in renal epithelial cells [48,49]. *DZIP1L* encodes the DAZ (Deleted in AZoospermia) interacting protein 1-like protein, a zinc- finger protein with several coiled-coil domains and one C2H2-type zinc finger domain near its N-terminus[26] (**Figure 5** and **Table 1**).

On the other hand, PLD proteins subdivided in three groups. First, the proteins involved in N-linked glycosylation and correct folding during the maturation of nascent proteins in endoplasmic reticulum (ER): glucosidase II beta subunit (GIIβ)[29,30], glucosidase II alpha subunit

(GIIα)[33,34], alpha-1,3-glucosyltransferase (ALG8)[34] and alpha-1,2-mannosyltransferase (ALG9)[35] encoded by *PRKCSH*, *GANAβ*, *ALG8* and *ALG9* respectively. Second, PLD proteins involved in ER translocation of precursor proteins: translocation protein SEC63 (SEC63)[31] and protein transport protein Sec61 subunit beta (SEC61β)[34], encoded by *SEC63* and *SEC61B*. These two groups are involved in the protein biogenesis pathway and Unfolded Protein Response (UPR) of polycystins at the ER (**Figure 6** and **Table 1**)[36]. Finally, the third group correspond to proteins with other functions (independently of ER): FPC(caused by mutations in *PKHD1* in heterozygosity)[34] and LRP5[32] (encoded by *LRP5*) which is a transmembrane coreceptor coupled with Frizzled receptor and playing a important role in Wnt signaling pathway (**Table 1**).

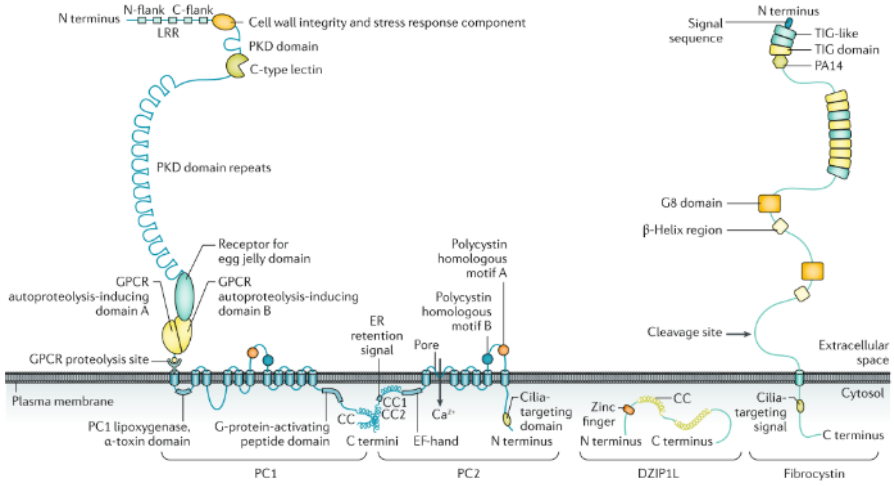

Figure 5. Structure of PKD proteins. Left to right, structure of Polycystin-1 (PC1), Polycystin (PC2), DAZ- interacting protein 1-like protein (DZIP1L) and fibrocystin/polyductin (FPC). PC1 and PC2 interacts through of their coiled-coil domains forming a complex that is located in several subcellular locations. DZIP1L is a soluble zin-finger protein located in centrioles and basal body at the ciliary transition zone. Finally, FPC is a receptor-like membrane protein located in primary cilium. Image taken from Bergman et al. 2017[7], allow by Springer Nature.

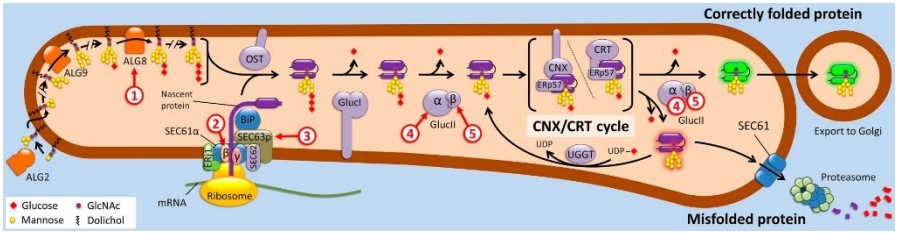

Figure 6. Scheme of ADPLD genes in endoplasmic reticulum (ER) protein biogenesis pathway. The ADPKD gene related with *N-linked glycosylation* and ER *translocation* of Unfold Protein Response (UPR) signaling pathway are represented in the scheme. (1) ALG8 and ALG9 catalyzes the addition of mannose and glucose residue. (2-3) SEC63 and SEC61ß facilitates the translocation of nascent proteins in ER. (4-5) GIIα and GIIß removes the second and primary glucose of unfolded protein to facilitates the CNX/CRT cycle and protein secretion, respectively. Image taken from Besse et al. 2017[34], allow by Robinson, George Canby.

4. CYSTOGENESIS AND TWO-HIT MODEL

Human kidney has approximately one million nephron, but an ADPKD patient will develop around 1000 cyst (1% of total)[50]. Also, ADPDK is highly variable between patients even in the same family[51]. The most widely accept theory of cyst formation in human ADPKD and PCLD is the "two-hit" model of cystogenesis[52]. Patients with ADPKD and PLD are typically heterozygous with one germline mutation in one PKD or PLD gene ("first hit"). Penetrant homozygous mutations in PKD genes result embryonically lethal[53–55]. The driving force leading to cystogenesis and activate the disease phenotype are the somatic "second-hit" mutations (**Figure 7**). This somatic mutation can be in the same germline mutated gene or in another different PKD/PLD gene. This fact was demonstrated in studies with renal and hepatic epithelial cysts from cystic fluid from patients, where loss of heterozygosity of *PKD1* or *PKD2* were found[54,56–60]. Nevertheless, the mechanism and timing of this second-hit are currently unknown[61].

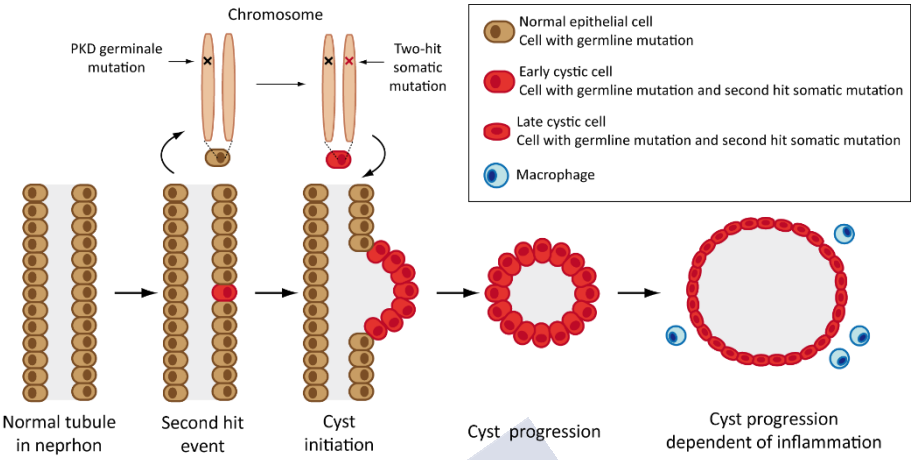

Figure 7. Mechanism of cyst formation and expansion in ADPKD. In ADPKD nephrons, all tubular epithelial cells contain one mutated (black cross) and one non-mutated copy of *PKD1* or *PKD2*. According to the "two-hit" model of cystogenesis, a second mutation (red cross) may eventually occur in the unaffected allele in an individual tubular epithelial cell. When the protein level of functional Polycystin-1 or Polycystin-2 fall below a critical threshold, cyst formation starts. Once cysts are formed, multiple molecular pathways are deregulated, and cysts progressively increase in size and number. During disease progression, the advanced stage is characterized by macrophage infiltration, fibrosis deposition, hyperproliferation, fluid transport and others pathological alterations. Image of own elaboration.

5. IMAGE TECHNIQUES FOR CYSTIC INDEX QUANTIFICATION

Cyst initiation or cystogenesis mostly occurs at embryonic stage, with increasing number of cysts and cystic volume expansion with the age [62,63], ultimately leading to renal and/or liver transplantation[9,64]. It has been established that the principal biomarker to provide a metric progression of the disease and monitor treatment efficacy is the measurement of total kidney and liver volume by imaging technologies [65,66]. We and other researchers have developed several *Pkd1*, *Pkd2* or *Pkhd1* animal models to study the pathological mechanisms undergoing cyst formation and progression including identifying genetic interactions and testing new therapeutic approaches [67–70]. Although magnetic resonance imaging (MRI) or sonographic images have been the standard methods for measuring the progression of PKD or PLD in humans, digital and histological microscopy images

have been the most commonly used in translational research. For these studies, it is well established that the analysis of the cumulative area of cysts within the total area of the kidney, liver or other organs (Cystic Index or CI) as a measurable biomarker to quantify cystogenesis, cyst expansion and to track the severity and progression of the disease.
The most commonly used tool to calculate the cystic index from histological samples is ImageJ, a multiplatform free software developed in the Java programming language[71,72,81–83,73–80] . This software develops an image thresholding which creates a binary image, where the cystic index is computed with the white regions defined as cysts and the black regions as tissue (background). However, it is known to researchers that this value is imprecise because many of the white regions in the image (lumen of arteries, veins, or non-cystic regions) are mistakenly considered to be cysts. In addition, ImageJ does not allow reviewing of the segmentation before the calculation process or the quantification of the cysts based on their profile. Therefore, a more precise tool is needed to quantify the cystic index in a reliable and accurate manner.

6. METHODS OF DIAGNOSIS AND TREATMENT OF PKD AND PLD

The diagnosis of ADPKD and PLD, when the disease in fully stablished, in clinically based on patient`s history and clinical parameters[5]. However, definitive diagnosis can be complicated and complementary approaches such as diagnostic imaging or genetic tests are necessary to confirm the diagnosis[10,15,84]. In ARPKD, ultrasound can detect the most severe by the findings of symmetrically enlarged, echogenic kidneys and medullary hyperechogenicity due to loss of corticomedullary differentiation[85]. However, as happens in ADPKD, the genetic test provide a accurate diagnosis for clinically un-diagnostic cases[86].
The primary clinical approach for PLD and PKD patients is to reduce their clinical symptoms because, up to date, there is no approved specific therapy. In general, management of vascular and bile duct

complication are the main clinical feature to control. However, the final treatment strategy usually is liver and kidney transplantation[7,15]. In particular, therapeutic strategies have advanced further in ADPKD. Using *in vitro* and animal rodent models, several targets and drugs were proposed for ADPKD treatment (**Figure 8**)[43]. Some of these therapeutic approaches have been tested in clinical trials in patients with ADPKD, resulting in the approbation of Tolvaptan, an inhibitor of vasopressin-2-receptor, as the first and unique therapy for ADPKD [61,87,88]. However, we are not at endpoint, this treatment has many limitations and are not enabled for all ADPKD patients[88,89]. In addition, there is no efficient treatment for ARPKD and PLD[7,16]. So, new and more efficient and safety therapeutic approaches must be developed.

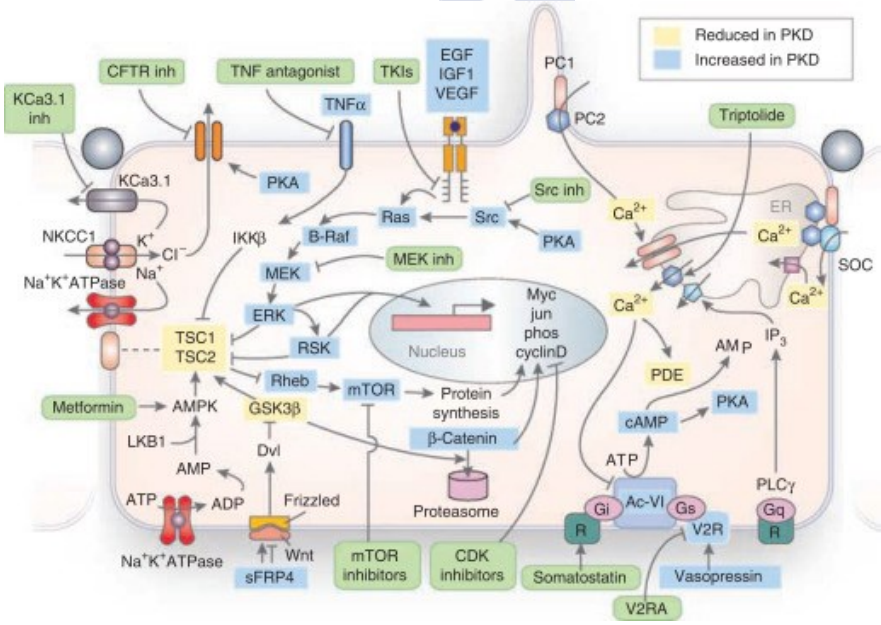

Figure 8. Illustration showing proposed treatments for PKD. Many treatments were proposed for PKD treatment in preclinical and clinical studies: V2 receptor antagonists, somatostatin, triptolide; tyrosine kinase, src, MEK, TNFα, mTOR, or CDK inhibitors; metformin, and CFTR or KCa3.1 inhibitors (green boxes). These possible treatments modulate deregulated pathway in PKD. At present, Tolvaptan (V2RA antagonist) is the only one approved for ADPKD patients. Image taken from Torres and Harris 2009[43], allow by Elsevier.

7. MOLECULAR PATHWAYS

Once PKD genes and their encoded proteins were identified, multiple *in vitro* and animal models were developed for the study of the disease[7,67]. This fact allowed characterizing many signaling pathways involved in the progression of the disease and the development of possible therapies[61,90,91]. In **Figure 12** and **Figure 9** represent several pathways related to PKD and PLD, respectively. It can be observe that a number of several signaling pathways and transcription factors are under the control of cystogenesis and the progression of the disease: cAMP pathway regulated by PKA kinase and AC6, pro-proliferative pathways as mTOR, RAS-RAF- ERK or AKT, pro-inflammatory and pro-fibrotic signaling pathways, secretory pathways etc[7,16]. Despite the big efforts of the scientific community in PKD and PLD fields, the main mechanism undergoing cystogenesis remains to be elucidated.

USC UNIVERSIDADE DE SANTIAGO DE COMPOSTELA

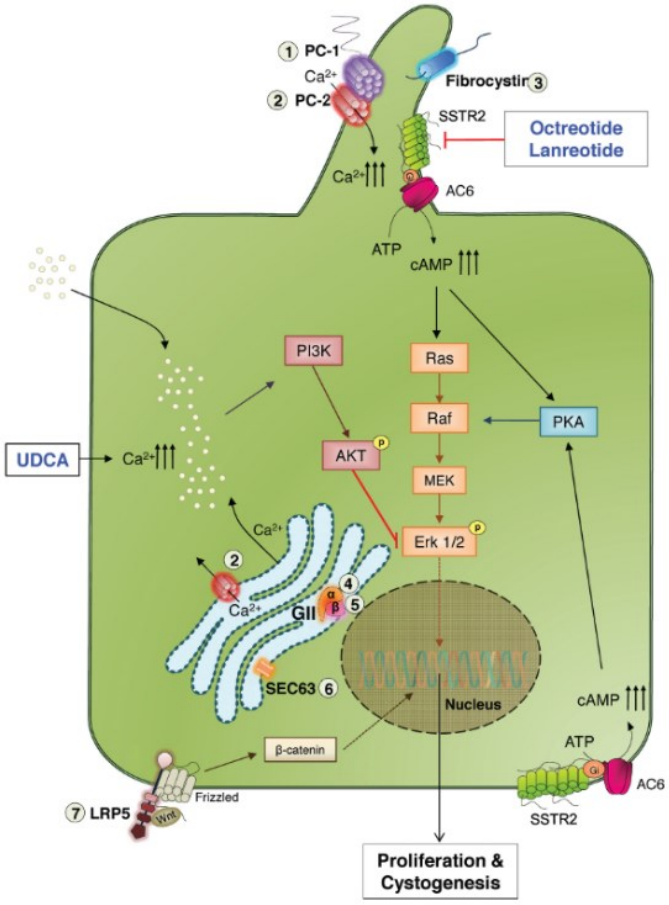

Figure 9. Cholangiocyte representation with principal molecular pathways involved in PLD. Proteins, and its subcellular localization, whose genes can be mutated in PLD and principal signaling pathways related to disease are shown in image. AC6, adenylate cyclase 6; ATP, adenosine triphosphate; Ca2þ,calcium; cAMP, cyclic adenosine monophosphate; GII, glucosidase II; Gi, G inhibitory protein; MEK, mitogen-activated protein kinase; pAKT, phosphorylated v-akt murine thymoma viral oncogene homolog 1; PC-1, polycystin 1; PC-2, polycystin 2; pERK ½, phosphorylated extracellular signal regulated kinase ½; PI3K, phosphatidylinositol 4,5-biphosphate 3-kinase; PKA, protein kinase A; SEC63, SEC63 homolog; UDCA, ursodeoxycholic acid. Image taken from Santos-Laso et al. 2017[16], allow by Georg Thieme Verlag KG.

7.1. Fibrosis in PKD and PLD

Fibrosis is a pathological mechanism characterized by the accumulation of matrix in the extracellular region of cells and is associated with loss of organs function[92]. In PKD, expansion of cysts and loss of renal and hepatic function are associated with varying degrees of progressive interstitial fibrosis[93,94]. Fibrosis in PKD has been studied as one of the first mechanism to promote PKD progression, after examination of human ADPKD kidneys and livers that showed abnormalities in extracellular matrix (ECM) deposition and increment of numbers of interstitial cells[93,95–99].

In this regard, matrix metalloproteases (MMPs) are a large family of proteases involved in the remodeling and degradation of the ECM, and in maintaining homeostasis and tissue remodeling[92,100] and kidney development[101,102]. MMP family groups more than 20 MMPs in humans and mice, which are classified in six groups according to their molecular structure and substrate preference in six groups: collagenases, gelatinases, stromelysins, matrilysins, membrane-type (MT) MMPs and others MMPs (**Figure 10**)[103–105]. The MMP activity is regulated by several mechanism, one is the inhibition of metalloproteases by endogenous tissue inhibitors of metalloproteases (TIMPs)[92,106]. Alterations in MMPs/TIMPs are involved, both in human and mouse pathogenesis and progression of PKD[107–111] and PLD[74,98,111,112]. To date, modulation of MMPs has not been studied as a potential therapeutic target for PKD.

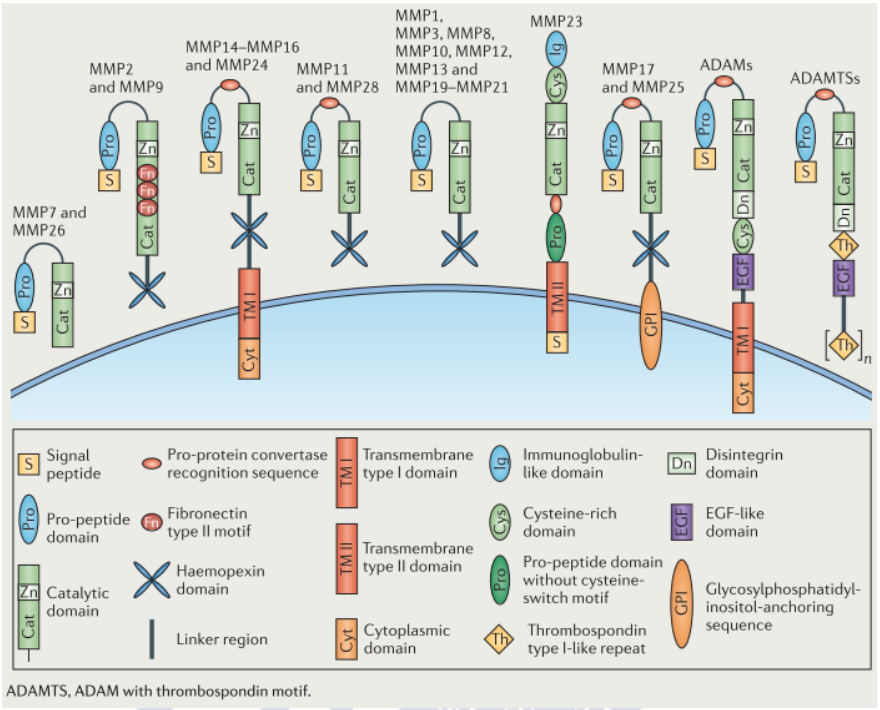

Figure 10. Matrix metalloproteinases (MMP) structure. MMPs typically consist in four domains: pro-peptide domain, catalytic domain, a linker region and the haemopexin domain. According to their biological effect and group of substrates, the MMP are classified into collagenases, gellatinases, stromelysins, matrilysins, membrane associated (transmembrane or GPI anchored) and others. According Disintegrin metalloproteinases (ADAMs) are part of adamalysin subfamily and its organization is similar to MMPs. Image taken from Khokha et al. 2013[101], allow by Springer Nature.

7.2. Inflammation and TWEAK

PKD and PLD are not primarily an inflammatory disease[113,114]; however, interstitial inflammation promote cyst progression through macrophage recruitment[115,116] and upregulation of pro-inflammatory cytokines, which also are present in high levels in renal[117,118] and hepatic[119,120] cystic fluid. Furthermore, several potential therapeutic targets were proposed in ADPKD field, showing amelioration in disease progression in preclinical animal models[82,121].

Tumor Necrosis Factor-like Weak Inducer of Apoptosis (TWEAK, TNFSF12) is a type II transmembrane glycoprotein that may be proteolytically processed, resulting in soluble TWEAK (sTWEAK). Both, full-length TWEAK (mTWEAK) and sTWEAK bind and activate the TWEAK receptor called fibroblast growth factor-inducible-14 (Fn14, TNFRSF12a). TWEAK belongs to the TNF superfamily (TNFSF) of cytokines, whose members modulate immune responses and inflammation[122]. TWEAK contributes to kidney inflammation promoting chemokine secretion by renal cells, and regulates kidney cell proliferation, apoptosis, differentiation and activation of nuclear factor κB (NF-κB) (**Figure 11**)[123–126]. Anti-TWEAK neutralizing antibodies were protective in experimental models of AKI and proteinuric and obstructive CKD[123,127], and have reached the clinical development stage[125].

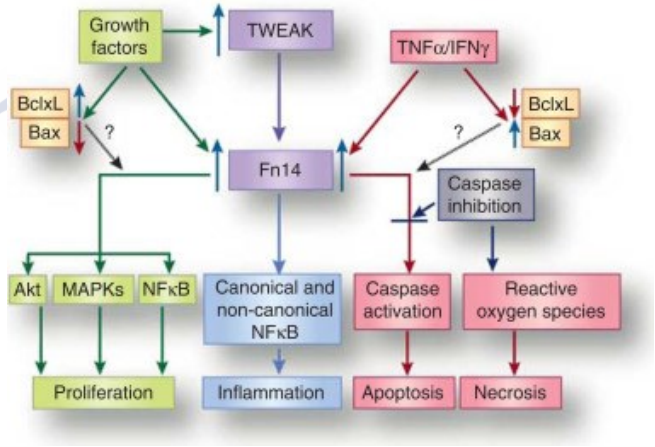

Figure 11. TWEAK signaling pathway scheme. TWEAK activates the FN14 receptor in renal epithelial cells. Growth factors increase TWEAK/Fn14 axis expression, leading an upregulation of proliferation and apoptotic effect of TWEAK. In the same way, the canonical activation contributes to proliferation increase and inflammatory status and cytokine secretion. Image taken from Sanz et al. 2011[121], allow by Elsevier.

8. ROLE OF CILIA

PKD are cilia-related disorders or ciliopathies[128]. All PKD proteins are localized, plus other cellular localizations, in primary cilium. PC1, PC2 and FPC are localized in apical and basal zones from primary cilium, while DZIP1L is located in the transition zone/basal body[7] (**Figure 12**). The primary cilium has a central role in cyst formation in kidney and liver[129]. Loss of cilia generate kidney cysts, but in a context of ADPKD with PC1 or PC2 deficiency loss of cilia suppresses cyst growth in kidney and liver[130]. Ma and colleagues[130] have demonstrated the universal mechanism of cilia in renal and hepatic cyst formation in ADPKD and PCLD. In the same way, the authors described the cilia dependent cyst activation (CDCA) signal and that targeting the CDCA pathway can slow cyst growth in animal models, highlighting its therapeutic potential[129].

By other hand, a mechanosensory role of cilium in ADPKD was suggested[131,132] and other studies supports the idea that PC2 is required for flow-mediated increase of cytosolic Ca^{2+} [133,134]. However, there have been controversial results reporting that mechanosensation does not occur via Ca^{2+} signaling in cilia[135], and open questions remains about the presence of others mechanosensitive elements in cilia[136].

For ARPKD, FPC deficiency does not affect polycystic biogenesis and cilia localization[34,137,138]. Besides, loss of cilia does not ameliorates or suppresses hepatic cyst growth in ARPKD[139]. These data suggests that cyst formation in *PKHD1* patient can involve a polycystin independent mechanism and that more functional studies are need to elucidate the exact role of cilia in ARPKD[129].

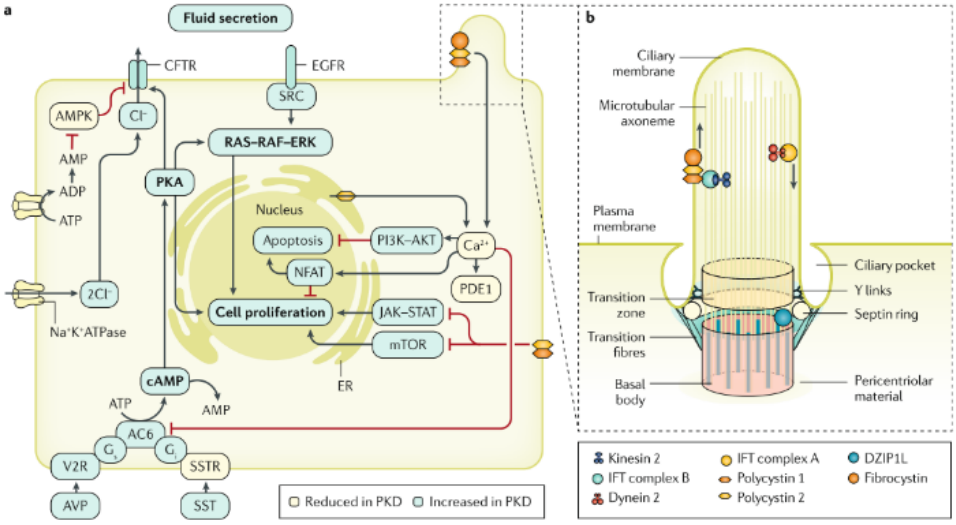

Figure 12. Mechanism involved and role of cilia in PKD. (A) PC1 and PC2 form a complex, that is localized in several cellular components including primary cilium in epithelial renal cells. In the last decades, it has been reported numerous signaling pathways related to cystogenesis and PKD progression and proposed as a possible mechanism regulating cyst growth: reduction of intracellular Ca^{2+}, increased cAMP levels (with AC6 mediation), activation of RAS-RAF-ERK and MAPK pathway, up-regulation of phosphoinositide 3-kinase (PI3K)–AKT, among others. (B) Primary cilium representation with PKD proteins localization. Other ciliary proteins, as Kinesin 2 or Dynesin 2, were bind to polycystins.AC6, adenylyl cyclase 6; AVP, arginine vasopressin; CFTR , cystic fibrosis transmembrane conductance regulator ; EGFR , epidermal growth factor receptor ; ER , endoplasmic reticulum; IFT, intraflagellar transport; PDE1, phosphodiesterase 1; PKA , protein kinase A ; PKD, polycystic kidney disease; SST, somatostatin; SSTR , somatostatin receptor ; V2R , vasopressin V2 receptor. Image taken from Bergman et al. 2017[7], allow by Springer Nature.

9. THRESHOLD AND DOSAGE MODEL OF CYSTOGENESIS

According to "two-hit" model, a second somatic mutation is necessary for cyst formation. This delimitates a critical threshold of functional protein that drives cystogenesis[140]. There are multiple observations that supports this idea. In human patients, mutations in *PKD1* have worse prognosis that those with mutations in *PKD2*[51,141], and the truncanting-*PKD1* mutations were associated with the most severe polycystic severe phenotype[142,143]. In animal models were reported that increase or decrease PC1 functional can worsened or rescues renal and hepatic phenotype, suggesting a central role of PC1 in cyst formation[144,145]. First, *Pkd1* incomplete penetrant alleles can influences disease severity[71]. Several genetic interactions between PKD and PCLD genes were reported showing that several mutated alleles together increased disease progression[69,137–139]. Next, rescuing PC1 dosage suppresses cyst formation in both kidney and liver[137]. The majority of identified PCLD genes are members of UPR and secretory protein biogenesis pathway, which mutations causes deficiency in PC1 maturation (with exception of *Pkdh1* and *Lrp5*)[33–35,129]. In relation with this, Cai and colleagues described the effect of several mutations in PC1 and PC2 trafficking and maturation, concluding that dysfunctional maturation of PC complex underlie PKD pathology[146]. Finally, a critical developmental window for cystogenesis has been identified suggesting that timing influences in ADPKD severity[70,147].

OBJECTIVES

OBJECTIVES

1. To develop new and more reliable tools for the assessment of cystic pathologies, as PKD and PLD, which provide us cystic index and number of cysts parameters.

2. Perform a comparative of *Wild Type* and polycystic mice livers proteomes using SWATH MS quantitative proteomics in order to identify new possible novel therapeutic targets and molecular pathways on PLD field.

3. To assess the therapeutic potential of metalloproteases and extracellular matrix alterations in PKD and PLD, testing the MMPs inhibitor Marimastat in orthologous murine models.

4. To characterize FN14/TWEAK axis in ADPKD and its role in cyst progression, as well as test a possible therapeutic approximation that module it.

5. To expand the knowledge of *Pkd1* and *Pkhd1* genetic interaction in PKD animal models, studying their renal and hepatic phenotypes and disease progression.

MATERIAL AND METHODS

MATERIAL AND METHODS

1. CystAnalyser concise methods

1.1. Animal models

C57/BL6 *Pkd1*$^{cond/cond}$*;Tam-Cre* and C57/BL6 *Pkhd1*$^{del3-4/del3-4}$ were used in the present study [68–70]. In the *Pkd1*$^{cond/cond}$*;Tam-Cre* model we induced Cre recombinase activity, in order to inactivate the *Pkd1* gene, in mice postnatal 10 and 11 days of age by intraperitoneally injecting nursing mothers with tamoxifen (10 mg/40 g) in corn oil (Sigma-Aldrich)[70]. Mice were sacrificed at postnatal day 30 (56 mice) or 45 (15 mice). The *Pkhd1*$^{del3-4/del3-4}$ mice were sacrificed with more than 8 months of age (14 mice). We used a total number of 85 mice in this study, performed using protocols approved by the Universidade de Santiago de Compostela Animal Care and Bioethical Committee (#15010/2020/002) and the mice were house in pathogen-free facility (SPF). For this chapter, we reutilized (according to 3Rs recommendations) animal tissues from other thesis chapters.

1.2. Immunohistochemistry and image acquisition

After mouse euthanasia, the kidneys and livers were washed in PBS 1X and fixed with 4% para- formaldehyde (pH 7.4) for at least 10 hours. Tissues were washed again with distilled water for 2 hours and rehydrated with 50% ethanol for 2h and finally kept in 70% ethanol at 4˚C. The organs, once processed, were embedded in paraffin and sectioned at 4.5µm thickness. Sagittal kidney sections and liver cross-sections were stained for Hematoxylin-Eosin using a standard protocol, which were then visualized under an Olympus BX51 microscope connected to an Olympus Camera DP70 using a magnification of 10X. The number of images acquired from each tissue range from three to ten images, and their size is 4080 × 3072 pixels.

1.3. Dataset description

The histological images of kidney and liver were grouped depending on their Cystic Index, according to value of CystAnalyser

Cystic Index Supervised or CIS, in: "Mild-Cystic", "Cystic" and "Severely-Cystic". In kidney, we considered a "Mild-Cystic" when its cystic index was between 0 to 35%, "Cystic" between 35% to 55% and "Severely-Cystic" greater than 55%. For liver, we considered a "Mild-Cystic" liver when its cystic index was lower than 5%, "Cystic" between 5% to 15% and "Severely-Cystic" greater than 15%. **Table 2** summarizes the number of images (795 in total) analyzed by CystAnalyser for each type of animal, Cystic Index and type of organ (kidney or liver).

Table 2. Number images used in Chapter 1 of Results. Number of kidney and liver images used in this work for each animal model and cystic phenotype, according to the classification used. p: postnatal day of sacrifice.

Animal model	Group			
	Mild Cystic (n)	Cystic (n)	Severely Cystic (n)	Total (n)
	Kidney			
Pkd1$^{cond/cond}$;*Tam-Cre* p30	67	126	33	226
p45	0	15	90	105
Total	67	141	123	331
	Liver			
Pkd1$^{cond/cond}$;*Tam-Cre* p30	187	56	2	245
p45	26	65	11	102
Pkhd1$^{del3-4/del3-4}$ p250	4	56	57	117
Total	217	177	70	464

1.4. Statistical analysis

For the statistical evaluation of the automatic recognition algorithms, we considered that a cyst was correctly recognized, a true positive (TP) hit, if the user did not modify the outline pro- vided by the recognition algorithm. A cyst was considered false positive (FP) whenever the user manually deleted the cyst, or it was modified by some "tools for supervision". A cyst was considered false negative (FN) whenever the user manually added one cyst, or it was added by some "tools for supervision". For example, when the user split a cyst, we counted it as one false positive (like deleted) and two false negatives

(like added). If the user performed the operation *Remove inner cyst*, all the cysts inside a manually added cyst were considered as FP. If the user uses the *Complete* tool, we counted one FP and one FN. If the user performed a *Merge* operation, we counted it as FP the number of cysts merged and one FN. When the user clicks the button *Run* after the label *Add smaller cyst*, all the cysts added were considered as FP. Once we counted the TP, FP and FN for an image, we defined the sensitivity (Se) and specificity (Sp), both in %, as:

$$Se = \frac{100TP}{FN+TP} \qquad Sp = (1 - \frac{FP}{NA}) * 100$$

Thus, the number of cysts in the image (after supervision) was NS = TP + FN and the number of cysts automatically recognized by the computer was NA = TP + FP.

The normality of the data was assessed using D'Agostino-Pearson, Kolmogorov-Smirnov and Shapiro-Wilk tests for all groups of data. Non-parametric methods were always required so, we calculated the statistical significance by Mann-Whitney non-parametric or Kruskal-Wallis non-parametric one-way ANOVA test with Dunn multiple pair-wise comparison post- test. We considered a value $p<0.05$ as significant. The statistical analysis was performed using Prism version 7.0 for Windows (GraphPad® software).

1.5. Experts perception

The System Usability Scale (SUS) is a free questionnaire to measure the learn ability and subjectively perceived usability of computer systems[148,149]. This questionnaire has 10 items with five-point scale ranging from 1 (strongly disagree) to 5 (strongly agree). The final system score was provided in a scale from 0 to 100. The score was calculated as following: for items 1, 3, 5, 7 and 9 (the positively worded items) subtract one from the user responses and for items 2, 4, 6, 8 and 10 (the negatively worded items) subtract the user responses from five. This scales all values from 0 to 4 (being 4 the most positive response).

The converted responses were added for each user and multiplied the total by 2.5 to convert the scale from 0 to 100 instead of from 0 to 40. The SUS score is translated to people's rating of systems and products in terms of adjectives in order to give a meaning to the SUS scores[150]. The criteria used was: SUS score below to 25 was a system worst imaginable; from 25 to 39 was from worst imaginable to poor; from 39 to 52 was from poor to ok; from 52 to 73 was ok to good; from 73 to 85 was good to excellent and from 85 to 100 was excellent to best imaginable. Thus, a small sample (8–12 users) was enough to give a good assessment of how people see your system or product. CystAnalyser was evaluated using SUS questionnaire by 10 researchers of Nephrology Lab with different expertise using it. The mean score achieved was 80.75, which means that CystAnalyser is from good to excellent. It is important to emphasize that half of the researchers scored CystAnalyser with more than 85 points, so they think that the software is from excellent to best imaginable.

2. PROTEOMICS

2.1. Protein digestion for proteomics

Protein aliquots of 100 µg were loaded on a 10% SDS-PAGE. The electrophoresis was stopped until the sample go into the resolving gel to concentrate the proteins in a single band. This band was stained using Coomassie, excised and cut into pieces to be washed with Milli-Q water and 50mM ammonium bicarbonate in 50% methanol and submitted to a manual digestion as describe elsewhere[151]. Finally, the peptides were dissolved in 0.1% formic acid for further analysis.

2.2. Generation of the references spectral library

A pool of each groups was performed using 4 µl (over 4 µg of protein) of each sample in order to obtain more representative protein identification in the spectral library. The peptide solutions were analyzed by shotgun data-dependent acquisition (DDA) approach by micro-LC-MS/MS. The samples were separated via micro- LC system

Ekspert nLC425 (Eksigen®) using a trap column YMC-TRIART C18 with a 3 mm particle size and 120 Å pore size (YMC Technologies, Teknokroma) and a column Chrom XP C18 150 mm × 0.30 mm, 3 mm particle size and 120 Å pore size (Eksigen®) at a flow rate of 10 µL/min. The solvents used were solvent A (water, 0.1% formic acid) and solvent B (ACN, 0.1% formic acid). The gradient was from 5% to 95% B for 30 min, 5 min at 90% B and, finally, other 5 min at 5% B for column equilibration, for a total time of 40 min. The mass spectrometer coupled was a hybrid quadrupole-TOF mass spectrometer, 6600 (SCIEX®) operating with data dependent acquisition system in positive ion mode. Using the mass spectrometer, a 250 ms survey scan was performed from 400 to 1250 m/z followed by MS/MS experiments from 100 to 1500 m/z (25 ms of acquisition time) for a total cycle time of 2.8 s. The fragmented precursors were added to the dynamic exclusion list for 15 s, any ion with charge +1 was excluded from the MS/MS analysis. The MS raw files and databases searches were combined and performed using ProteinPilot software v.5.0.1. (SCIEX®) using a UniProt Swiss-Prot database for Mouse. It is necessary to specify iodoacetamide cysteine-alkylation and trypsin digestion. The false discovery rate (FDR) was set to 1 for peptides and proteins with a confidence score above 99%[152].

2.3. Quantification by SWATH and data analysis

The SWATH–MS acquisition was performed using a DIA method. In Kidney we used 2 groups with 3 biological replicates per group and 3 technical replicates per sample, and in Liver we used 4 groups with 4 biological replicates per group and 3 technical replicates per sample (see **Supplemental Table 1** for more details). Tissues (kidney and liver) were analyzed and in all cases comparing *Wild Type* (from *Pkd1*$^{cond/cond}$*;Tam-Cre*$^{-}$ mouse) and Mutant (from *Pkd1*$^{cond/cond}$*;Tam-Cre*$^{+}$ mouse) conditions. A total of 4 micrograms of protein per sample and technical replicate were run using a SWATH method. This method is based in a cycle repetitions that consisted of the acquisition of 65 TOF MS/MS scans (400 to 1500 m/z, high sensitivity mode, 50 ms

acquisition time) of overlapping sequential precursor isolation windows of variable width (1 m/z overlap) covering the 400 to 1250 m/z mass range with a previous TOF MS scan (400 to 1500 m/z, 50 ms acquisition time) for each cycle. Total cycle time was 6.3 s. For each sample set, the width of the 100 variable windows was optimized according to the ion density found in the DDA runs using a SWATH variable window calculator worksheet from Sciex.

2.4. Data analysis

Once the individual samples are acquired in a SWATH mode, the spectral alignment and targeted data extraction were performed by PeakView v.2.2. (SCIEX®) matching the reference spectral library (Section 2.2.)[153–157] as described below. To obtain the areas in order to make a protein quantification, up to ten peptides per protein and seven fragments per peptide were selected, based on signal intensity; any shared and modified peptides were excluded from the processing. Five-minute windows and 30 ppm widths were used to extract the ion chromatograms; SWATH quantitation was attempted for all proteins in the ion library that were identified by ProteinPilot with an FDR below 1%. The retention times from the peptides that were selected for each protein were realigned in each run according to the iRT peptides spiked in each sample and eluted along the whole-time axis. The extracted ion chromatograms were then generated for each selected fragment ion; the peak areas for the peptides were obtained by summing the peak areas from the corresponding fragment ions. PeakView computed an FDR and a score for each assigned peptide according to the chromatographic and spectra components; only peptides with an FDR below 5% were used for protein quantitation. Protein quantitation was calculated by adding the peak areas of the corresponding peptides.

The integrated peak areas (processed ".mrkvw" files from PeakView) were directly exported to MarkerView software (AB SCIEX®) for relative quantitative analysis. The export generates three files containing quantitative information about individuals ions, the summed intensity of different ions for a particular peptide and the

summed intensity of different peptides for a particular protein. The data-independent method of quantification MarkerView has been used for analysis of SWATH MS data[158–161].MakerView uses processing algorithms that accurately find chromatographic and spectral peaks direct from the raw SWATH data. Data alignment by MarkerView compensates for minor variations in both mass and retention time values, ensuring that identical compounds in different samples are accurately compared to one another. To control possible uneven samples loss across the different samples during the sample preparation process, we performed a TAS normalization (Total Area Sum)[162–164]. For the analysis. the R 3.6.2 version and a set of packages has been used[165].

Finally, a Student's t-test (using MarkerView software) was performed to compare the groups in pairs in order to identify proteins which were significantly differentially represented, using adjusted p-value < 0.05 (multiple correction FDR method) and fold change > 2 as cut-off. Unsupervised multivariate statistical analysis using Principal Component Analysis (PCA) was performed to compare the data across the samples.

Volcano plots were used to graphically visualized the results, which were generated by plotting the log (2)-fold changes for all proteins identified against their log (10) p-value. Heatmap figure of unsupervised cluster analysis of proteins with significant differences according to SWATH MS analysis were generated to detect different cluster of proteins in different studied groups. Unsupervised multivariate statistical analysis using Principal Component Analysis (PCA) was performed to compare the data across the samples.

2.5. Signaling pathway analysis

Different functional analysis was performed using differentially expressed proteins with the aim to evaluate the most relevant interaction networks, related pathways or cellular components and other associated proteins or pathways. UniProt (https://www.uniprot.org/) protein accession number were used. Proteins with differences in protein

abundance were subjected to: String® (https://string-db.org/) and Panther® (http://pantherdb.org/) using Gene Ontology (GO) terms for study protein networks and biological association between proteins; and to Reactome® (https://reactome.org/) for study involved pathways and subpathways in relation or interaction with our significantly expressed proteins.

3. MOUSE MODELS

The following mouse PKD line were used in the present thesis: *Pkhd1*$^{del3\text{-}4/del3\text{-}4}$ or *Pkhd1*-KO (a homozygous *Pkhd1* knockout animal model with the exons 2 and 3 deleted that develops slowly progressive polycystic liver disease, but not kidney disease)[69], *Pkd1d*$^{el2\text{-}4/+}$ or *Pkd1*-KO (a *Pkd1* knockout with exons 2 to 4 deleted, which not present renal or hepatic cystogenesis in heterozygosity)[68]; and *Pkd1*$^{cond/cond}$*;Tam-Cre* or *Pkd1*-CKO (a homozygous *Pkd1* conditional knockout with the Cre-LoxP system and a tamoxifen dependent promoter)[68,70]. In genetic interaction study (Chapter 5), the *Pkhd1*$^{del3\text{-}4/del3\text{-}4}$*; Pkd1*$^{del2\text{-}4/+}$ mouse is also called DKO, and the *Pkhd1*$^{del3\text{-}4/del3\text{-}4}$; *Pkd1*$^{cond/cond}$*;Tam-Cre* is also named DcKO in order to facilitate their nomenclature. All of them are inbreed into the C57BL/6 strain and the genotype was confirmed by PCR. In the case of *Pkd1*$^{cond/cond}$*;Tam-Cre*, Cre- mice were used as *Wild Types* (also named WT) and Cre+ as mutants (also named Mut or KO). Deletion of *Pkd1* was always at postnatal days 10 and 11 with a single intraperitoneal injection of tamoxifen (10 mg/40g) (Sigma® #T5648), diluted in corn oil (Sigma-Aldrich® #C8267), each day for the mother of the litters to induce. In studies where we used *Pkhd1*$^{del3\text{-}4/del3\text{-}4}$ model, *Wild Type* C57BL/6 mice were used for *Wild Type*/control group. The experimental unit for all cases are the mutant (with mutations induced with tamoxifen or germline mutation) and *Wild Type* individuals. The groups were stablished by different individuals and organized in a random way (randomization) and trying 1:1 ratio between males and females in all groups. Anatomic features were used to identify the sex of animals. Mice were house in pathogen-free facility (SPF) according to University of Santiago stabling conditions. The full of experiments were performed for the author of thesis. In Supplemental material are

additional information about the specific number of mice and litters used in the different characters.

In Chapter 4, we used other mouse lines specified below. Kidney samples of slowly progressive C57/BL6 *Pkd1*$^{cond/cond}$*;Tam-Cre* mice[68,70] (*Pkd1* deletion on p45, sacrifice >14 weeks) were generated as previously described[79]. The C57/BL6 *Pkd1*$^{cond/cond}$*Tam-KSP-Cre* mice were generated using the same floxable allele[79] intercrossed with the Tm-KspCreER^{T2} (kindly provided by Dr. Peter Igarashi, University of Texas Southwestern Medical Centre)[166] Cre recombinase activity was induced by a single injection of Tamoxifen at P45 for the first line or at P10-11 for the second line and the animals were harvested at P175 or P38-39 respectively. Tamoxifen (Sigma® #T5648) freshly prepared and dissolved in corn oil (Sigma-Aldrich® #C8267) by continuous shaking at 37°C for 8 hours was injected intraperitoneally. In the same way, kidney samples of C57/BL6 *Pkd1*^{cond}*;Pax8;TET-OCre* mice[70,167] (*Pkd1* deletion on p27, sacrifice p150-160) were obtained from PO and TW (University of Maryland School of Medicine and Baltimore PKD centre). *Pkd1* inactivation was induced by a single injection of Doxycycline at postnatal day 27.

Training for the use of experimental animals was obtained based on the provided in galician "Decreto" 52/2018 (5th April), spanish law Orden ECC/566/2015 (BOE number 78, 01/04/2015) and Union Europe law 20/2013 (9th December). **Annexes 2** and **3** correspond to functions B, C and D of experimental animal according galician-spanish-european legislation. The experiments were conducted strictly following the protocols approved by the Ethical Committee of University of Santiago de Compostela, in the center CEBEGA (code: #15010/2020/002).

4. TREATMENTS

4.1. Chapter 3: Marimastat and Tolvaptan

Marimastat (Sigma® #M2699) and Tolvaptan (Jinarc®) were administrated intraperitoneally in a dose of 1-10mg/kg/24h bid and 2mg/kg/24h bid respectively (0.5ml 0.33mm(27G)x12.7mm syringe).

Animals were euthanized by oral isoflurane treatment (1,5%) and blood, after intravascular puncture, and tissues were collected. For all experiments we used two litters at least. With respect to genre of mice in treatment groups, in *Pkd1-CKO* we did not see any phenotypical difference in renal and hepatic cystogenesis. But in *Pkhd1-KO* model the females present more severe phenotype than males (data not shown), and bearing mind this, we used only males for single-Marimastat treatment and females for Marimastat plus Tolvaptan treatment. For more specifications about treatment model design and points of sacrifice see Results section (**Figure 28A** and **Figure 29H**) and about number of animal and litter for each treatment see Supplemental Tables section (**Supplemental Table 2** and **Supplemental Table 3**).

4.2. Chapter 4: TWEAK and Anti-TWEAK

Mice were injected intraperitoneally with TWEAK (30 ng/g mouse/48h), neutralizing anti-TWEAK mAb (IgG1 BIIB023, clone P2D10)[127] (10 mg/kg mouse/3 times weekly) or isotype IgG (mouse IgG2A) (10 mg/kg mouse/3 times weekly) for control groups (0.5ml 0.33mm(27G)x12.7mm syringe), generously provided by Biogen, Inc. Doses were chosen based on prior experience assessing the impact of TWEAK and anti-TWEAK antibodies in experimental murine kidney disease in which in vivo tested doses were in turn derived from cell culture studies[168–173]. All mice were euthanized using isoflurane (1.5%) and blood (by intravascular puncture) and tissues were collected. Animals were sacrificed at different time points (**Supplemental Figure 17**). At least, two litters and four animals and 1:1 ratio of males and females (no differences between males and females were found) were used for each treatment.

5. HISTOLOGY

5.1. Histology Tissue Processing

The right kidney and the liver largest lobe of animals were always fixed in paraformaldehyde (4% paraformaldehyde buffered solution, pH=7: Labbox® #FORM-D0P-10K) overnight at 4°C. Then, kidneys were bisected and dehydrated through xylene and ethanol and finally embedded in paraffin. To finish, cross sections of 4,5µm were collected.

5.2. Staining protocol

For Hematoxylin-Eosin (HE) and Masson-Trichrome staining's standard protocols was used. For immunohistochemistry and immunofluorescence, sodium citrate buffer pH=6 (Agilent Dako® #S2369) was used for antigen retrieval and tissue was blocked with antibody diluent (Agilent Dako® #K8006). The antibodies used for immunohistochemistry analysis included fibronectin (Agilent Dako® #A0245), actin smooth muscle (α-SMA/AML, Agilent Dako® #GA611-clone 1A4), cytokeratin 19 (CK19, Agilent Dako® #GA615-clone RCK108); for the immunodetection the HPR-conjugated detection system was used.

F4/80 and p65 Immunohistochemistry was performed using a PT-link device with a low pH solution. Sections were then washed with PBS for 5 minutes, blocked by incubation with 4% PBS/BSA + 6% serum and incubated with anti-F4/80 antibody (1:100; Bio-Rad® #MCA497GA), anti-p65 antibody (1:800, Santa Cruz Biotechnology Inc®, #sc-372 X). Sections were washed three times with PBS1x and incubated with biotin-conjugated anti-rat secondary antibody (1:200, Invitrogen) and with VECTASTAIN® Elite® ABC HRP Kit (Vector). Sections were counterstained with Carazzi`s hematoxylin. Images were captured with iScan Coreo Au™ (Ventana Medical Systems, Inc.).

On the other hand, LTL (Vector Laboratories® #FL-1321) and DBA (Vector Laboratories® # FL-1031) were used for direct immunofluorescence; and Tamm–Horsfall Protein (THP, Bio-Rad®

#8595-0054) was used for indirect immunofluorescence incubated with appropriated secondary antibody conjugated to rhodamine (Santa Cruz Biotechnology Inc® #sc-2367); and finally, tissues were incubated with DAPI (ThermoFisher Scientific® #D1306).

TUNEL was performed in 3-mm-thick sections of paraffin-embedded tissue with the In Situ Cell Death Detection Kit Fluorescein (Roche® #11684795910) according to the manufacturer's instructions. Nuclei were counterstained with DAPI and images were captured with fluorescence microscopy (Nikon E600). TUNEL positive were quantified in 15 randomly chosen fields (x400) in a blinded manner.

5.3. Image capture

Kidney and liver Images of longitudinal sections were captured with a loupe Leica DMD 108 (Leica®). By other part, Hematoxylin-Eosin and Masson-Trichrome staining's, immunohistochemistry's and immunofluorescences were visualized with a microscopy Zeiss Axio Vert.A1 (Carl Zeiss®). The pictures for the full kidney immunofluorescences were taken with a confocal spectral microscopy Leica TCS-SP8 (Leica®) and reconstruction was performed with Adobe Photoshop® Software.

5.4. Measurement of Cystic Index

Slides of longitudinal sections from the inner part of kidney (with papilla present) were always taken as representative images, which were used for measurement of cystic index and to count the number of total cysts of one individual. At least six microscopic images (both kidney and liver), which were visualized under an Olympus BX51 microscope connected to an Olympus Camera DP70, were used for quantification of cystic index and number of cysts. The quantification of both parameters was calculated with Automatic Cyst Recognition software tool called CystAnalyser as previously described[174]. Cyst size was assessed by the number of pixels and cysts classified into three size bins (cut-off points and how were these obtained: shorter cysts (<250 pixels), medium cysts (250-750 pixels) and largest cysts (>750 pixels).

5.5. Immunofluorescences and immunohistochemistry quantification

Immunofluorescences quantification were calculated using the manually tool of CystAnalyser software[174]. By other hand, immunohistochemistry's quantification was performed using "Split channels" function (green channel) and, specifically, Trichrome Masson staining quantifications using "Colour Deconvolution" function (H DAB vector and green channel) from Fiji-ImageJ® software. Finally, F4/80 positive macrophages in medulla or cortex were quantified in 25 randomly chosen fields (x20) in a blinded manner. At least, a n=3 was used for the histological experiments.

6. CLINICAL CHEMISTRY

Blood was collected before sacrifice and serum was obtained using SB vacutainer® SST II Advance tubes. Serum Blood Urean Nitrogen (BUN), Alanine transaminase (ALT) and alkaline phosphatase (ALP) was measured using the ADVIA 2400 Chemistry System (Siemens Healthineers®).

7. PROTEIN AND RNA EXTRACTIONS

At sacrifice points, left kidneys and livers were stored at -80ºC. Then, whole frozen kidney or liver were ground in liquid nitrogen and half of the tissue is assigned to protein extraction and the other one to RNA extraction.

On the one hand, protein extracts were prepared with RIPA lyses buffer (10Mm TRIS, 5mM EDTA, 150mM NaCl, 0.1%SDS, 1% TRITON X-100 and 1% sodium deoxycholate). 1% protease and phosphatase inhibitors (Sigma® #P8340 y #P0044) were added too. This tissue lysate suffered a centrifugation process (for 30 minutes at 4ºC and 14 000 rpm). After, the supernatant is recollected and quantified by Bradford protein assay (Bio-Rad® #5000001).

On the other hand, RNA was isolated using TRIzol protocol (TRI Reagent, Sigma® #T9424), in which Chloroform (Sigma® #C2432)

serves as denaturalization agent for the cells and Isopropanol (Sigma® #650447) is the RNA precipitating agent. The precipitate is diluted in DEPC water (Ambion® #AM9920), which also contains 1% SUPERaseIn RNase Inhibitor (Thermo Fisher® #AM2694).

8. REAL-TIME QUANTITATIVE PCR

One microgram of RNA was treated with DNase I (Invitrogen® #18068015) prior to reverse transcription by SuperScript® III First-Strand Synthesis System kit (Invitrogen®, #18080051). cDNA was employed for the gene expression analysis, using FastStart Universal SYBR GREEN Master (ROX) (Roche® #04913914001) in a Mx3005P system (Agilent Technologies®). The complete reactions were subjected to the following program: a denaturation step with 30 seconds at 95°C; 45 cycles of 30 seconds at 95°C, 1 minute at 60°C and 30 seconds at 72°C; followed by a cooling step. Each sample was run in triplicate in each experiment. Primers were designed with Primer 3 Plus (http://tiny.cc/pf928y) and they are based on the reference cDNA sequence published in Ensembl genome browser (http://www.ensembl.org/index.html), with the exception of *Fn14*, *Il-6* and RANTES primers in which the ThermoFisher® sequence (TaqMan probe) was used. Specific sequences can be found in **Supplemental Table 4**, **Supplemental Table 5** and **Supplemental Table 6**. The results were treated with the absolute quantification method. Therefore, a standard curve with known concentrations was used in the assay. Additionally, each sample is normalized to a constantly expressed gene: *Hprt* or *Gapdh*, used as housekeeping genes.

For in vitro experiments, 1 µg RNA was reverse transcribed with High Capacity cDNA Archive Kit (Applied Biosystems® #4368814). Quantitative PCR was performed in a 7500 Real Time PCR System with the Prism 7000 System SDS Software using predeveloped primers (Applied Biosystems®) and RNA expression of different genes was corrected for *Gapdh* expression.

9. WESTERN BLOT

Western-Blotting assays were performed on whole kidney lysates, described above. Total protein content was determined using Bradford protein assay (Bio-Rad® #5000001) and the same amount of each protein was boiled at 95°C for 5 minutes and separated in 10 to 12% SDS-PAGE under reducing conditions. Afterwards, proteins were transferred onto nitrocellulose membranes (Bio-Rad® #1620115). To avoid non-specific binding, membranes were blocked for 1 hour at room temperature using a 2.5% BSA solution (NZYTech® #MB046) for phosphorylated proteins, or SuperBlock Blocking Buffer (Thermo Fisher® #37515). Thereafter, membranes were incubated overnight at 4°C with primary antibodies and next washed in 0.3% Tween-20 in PBS. Lastly, the nitrocellulose membranes were incubated for 1 hour at room temperature with the HRP-linked secondary antibodies. Signals were developed with the SuperSignal™ West Pico PLUS Chemiluminescent Substrate kit (Thermo Fisher® #34580) or PierceTM ECL Western Blotting Substrate kit (Thermo Fisher® #32109) prior to visualization in the ChemiDoc™ Imaging System (Bio-Rad®). Protein bands were quantified using ImageJ® Lab software (v 4.0.1). Levels of the proteins were corrected for GAPDH, used as housekeeping.

The following primary antibodies were used for Western Blot: anti-ANXA2 (1:10000, Santa Cruz Biotechnology Inc® #sc-28385), anti-SAMP (1:5000, Santa Cruz Biotechnology Inc® #sc-393948), anti-FIBB (1:10000, Santa Cruz Biotechnology Inc® #sc-271035), anti-FIBA (1:5000, Santa Cruz Biotechnology Inc® #sc-398806), anti-FIBG (1:5000, Santa Cruz Biotechnology Inc® #sc-133157), anti-Fn14 (1:1000, Abcam® #Ab109365), anti-p-ERK (1:2000, Cell Signaling® #4370), anti-ERK (1:2000, Cell Signaling® #4695), anti-p-AKT (1:2000, Cell Signaling® #4060), anti-AKT (1:2000, Cell Signaling® #9272), anti-GAPDH (1:10000, Millipore®, #mab374) as well as the secondary antibody Goat anti-Rabbit IgG HRP (Thermo Fisher® #31460) or Goat anti-Mouse IgG HRP (Thermo Fisher® #31430).

10. MOUSE TNFSF12/TWEAK ELISA

Serum from *Wild Type* and Mutant *Pkd1*$^{cond/cond}$*;Tam-Cre* mice was used to assess TWEAK levels using the Mouse TNFSF12/TWEAK Sandwich High Sensitivity ELISA kit (Boster Biological Technology® #EK1176).

11. HUMAN ADPKD CYSTIC FLUID/HUMAN COHORT

The IIS-Foundation Jimenez Diaz Ethics Committee approved the protocol. Patients signed an informed consent according to the European Union Directive and Spanish law. Samples from patients were obtained from the IIS-Fundación Jimenez Diaz Biobank. Urine and plasma samples were centrifuged, divided into aliquots and stored at -80°C. Suppl table 1 provides clinical characteristics of patients. Controls included healthy individuals (2 female and 4 males with an age range of 25-63 years). Cyst fluids and cyst walls were obtained from 8 superficial clear cysts from 3 ADPKD kidneys (1 female and 2 males, with an age range of 45-54 years) from patients who underwent nephrectomy because of volume issues. Cyst fluid was snap frozen and stored at −80°C. TWEAK levels were determined with a commercially available enzyme-linked immunosorbent assay (ELISA) kit (Bender MedSystems® #BMS2006INST). Cyst walls were processed as for mice kidney tissue and studied by Fn14 immunohistochemistry. Details in **Supplemental Table 7**.

12. *IN VITRO* EXPERIMENTS

MCT cells are a proximal tubular epithelial cell line harvested originally from the renal cortex of SJL mice and have been extensively characterized[175]. They were cultured in RPMI 1640 (GIBCO® #10379144), 10% decomplemented fetal bovine serum (FBS), 2 mM glutamine, 100 U/mL penicillin and 100 µg/mL streptomycin, in 5% CO2 at 37 °C. Thereafter, subconfluent cells were rested in serum-free medium overnight and 100 ng/ml TWEAK was added for 3 hours, the concentration being based on prior dose-response curves[168].

Bone Marrow Derived Macrophages (BMDM) were obtained from 10-14-week-old WT mice. After sacrifice with CO2, bone marrow was extracted from the femur and tibia, and it was seeded with RPMI culture medium at 10% FBS, 100U/ml penicillin, 100 µg/ml streptomycin, 2mM L-glutamine and 5 ng/ml M-CSF (Macrophage Colony Stimulating Factor) (Biolegend® #574802)[176]. After 96h, macrophages were incubated with 100 ng/ml TWEAK for 3 hours.

13. STATISTICS

Data are presented as mean ± SEM for all cases (bar or point plots). First, normal distribution was confirmed by the Kolmogorov–Smirnov test. For comparisons between multiple groups, a one-way ANOVA test with Tukey post-test was performed, whereas two-tailed Student's t test was used to determine significance of differences between two groups. P-values less than 0.05 were considered statistically significant (*). Furthermore, ** corresponds to p-values < 0.01 and *** to p-values < 0.001. All data sets were analyzed with GraphPad Prism® Software (version 5.0 or 7.0).

USC
UNIVERSIDADE
DE SANTIAGO
DE COMPOSTELA

RESULTS

RESULTS

1. CHAPTER 1

CystAnalyser: A new software tool for the automatic detection and quantification of cysts in Polycystic Kidney and Liver Disease, and other cystic disorders

CystAnalyser: A new software tool for the automatic detection and quantification of cysts in Polycystic Kidney and Liver Disease, and other cystic disorders

Adrián Cordido[1,2.4, €], Eva Cernadas[5,€,*], Manuel Fernández-Delgado[5], Miguel A. García-González.[2.3.4, *]

[1] Grupo de Xenética e Bioloxía do Desenvolvemento das Enfermidades Renais, Laboratorio de Nefroloxía (No. 11), Instituto de Investigación Sanitaria de Santiago (IDIS), Complexo Hospitalario de Santiago de Compostela (CHUS), 15706, Santiago de Compostela, Spain.
[2] Grupo de Medicina Xenómica, Complexo Hospitalario de Santiago de Compostela (CHUS), 15706, Santiago de Compostela, Spain.
[3] Fundación Pública Galega de Medicina Xenómica-SERGAS, Complexo Hospitalario de Santiago de Compostela (CHUS), 15706, Santiago de Compostela, Spain.
[4] RedInRen RETIC, ISCIII, Spain.
[5] Centro Singular de Investigación en Tecnoloxías Intelixentes da USC (CiTIUS) Universidade de Santiago de Compostela, Rúa Xenaro de la Fuente Domínguez, 15782, Santiago de Compostela, Spain.

€ These authors contributed equally to this work.
* Corresponding authors

Cordido A, Cernadas E, Fernandez- Delgado M, Garcıa-Gonzalez MA. (2020). CystAnalyser: A new software tool for the automatic detection and quantification of cysts in Polycystic Kidney and Liver Disease, and other cystic disorders. PLoS Comput Biol 16(10): e1008337. https://doi.org/10.1371/journal. pcbi.1008337. (**Annex 1**).

PLoS Comput Biol: Impact Factor 4.428 (2018). Decil 1.

1.1. Description and functionality of CystAnalyser

CystAnalyser is written in the C++ programming language using the GTK+ ("GIMP Tool Kit") library (https://www.gtk.org) to develop the GUI, and the C++ interface of the OpenCV library (https://opencv.org) to process and recognize cysts in the image. **Figure 13** shows the main window of CystAnalyser with the lateral panel and a flowchart describing the main functionality for the user. CystAnalyser can work with default or preset configurations, allowing to set image preferences like image/ file paths, calibration, working colors, shapes drawn on the image and the type of tissue to be analyzed (liver or kidney) and saved for future analysis. The side panel contains all these settings as well as *Automatic cyst recognition*, *Supervised post-processing* and *Visualization of Results* tools. By clicking the *Run* button at the *Automatic cyst recognition* tool, cysts are recognized and drawn on the image. The user can review or modify the automatic cyst detection by using the following setup from the *Supervised post-processing* tool: 1) *Remove inner cyst* button: click on the button *Run* after the label *Remove inner cyst* to remove the automatically detected cysts, which fall into some cysts manually drawn by the user; 2) *Add smaller cysts* button: click on the *Run* button to automatically add smaller cysts, this functionality is oriented only to use with very small cysts that are not recognized by the *Automatic cyst recognition* tool. *Undo/Redo* can be used to include or exclude this analysis; 3) *Selected cyst* button: several cysts incorrectly recognized by the *Automatic cyst recognition* tool as only one cyst can be split consecutively by using the *Split* button. On the contrary, when one cyst is incorrectly recognized by *Automatic cyst recognition* as several cysts, they can be fused with the *Merge* tool. The zoom tool allows users to get very precise detail by magnifying a selected part of the image and manually draw a cyst or delete a selected cyst on the image.

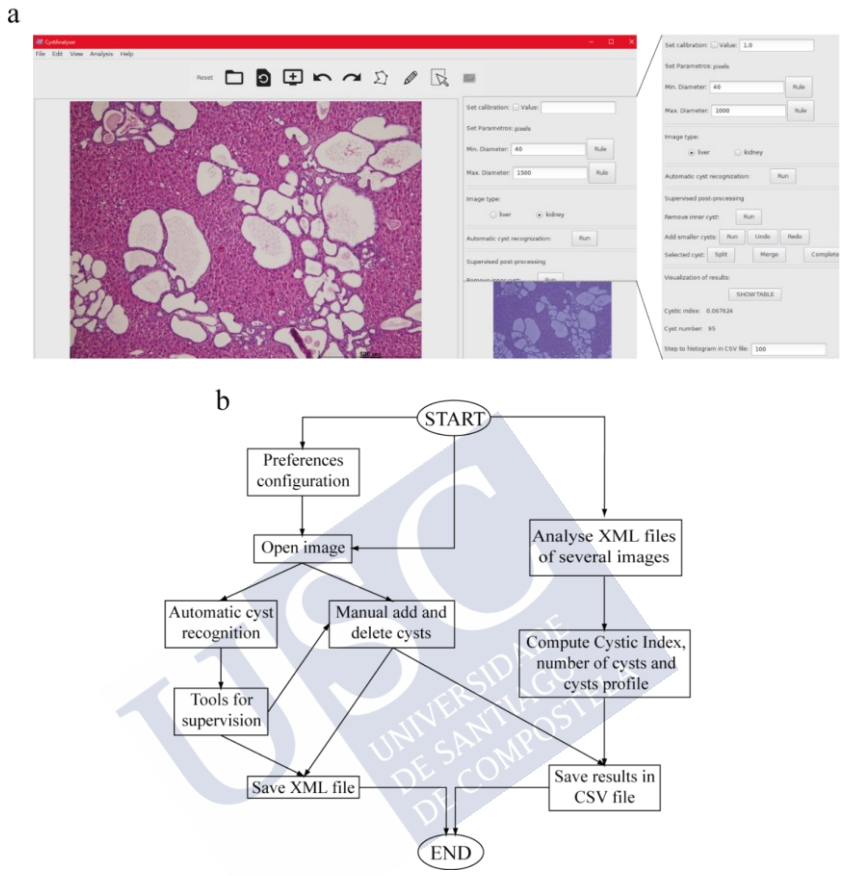

Figure 13. CystAnalyser overview. (a) Main window of CystAnalyser with a histological image of cystic liver (as example). On the right, we can see the full lateral panel showing the available Automatic cyst recognition, Supervised post-processing and Visualization of Results tools. (b) A flowchart containing the main tasks and functions of CystAnalyser. For more details and information see "Description and Functionality of CystAnalyser" sub-section.

The *Visualization of results* tool automatically shows the cystic index and number of cysts, allowing the user to explore the size of each drawn cyst in real time or to display a table with specific information for all cysts by clicking the *SHOW TABLE* tool (the cysts can be highlighted in the image by selecting them in the table). In addition, CystAnalyser allows the user to download and upload results in XML (eXtensible Markup Language) and CSV (Comma-Separated Values) format files.

The CVS file contains statistical information provided by quantitative analysis of the images: 1) spatial resolution, i.e., the relation between micrometers and pixels, at which the images were digitized, also known as calibration, which must be pre-specified by the user; 2) image size in pixels; 3) cystic index; 4) number of cysts; and 5) a profile of the cystic sizes, i.e. the number of cysts for each range of diameters or areas. A user guide has been provided for detailed description (see Online Supplemental Materials, Anexo 1).

1.2. Development of algorithms for automatic cyst recognition

The algorithms proposed to recognize the cysts on the image are a combination of known techniques in the computer vision field[177], implemented using the OpenCV modules *core* and *imgproc*. Firstly, the image has been segmented to transform it into a binary image, where white and black colors represent a cyst and the background, respectively. Secondly, this binary image was analyzed in order to extract the contours of the cysts. The main algorithmic steps are: 1) extract green channel (IG) from the original RGB image; 2) compute the average grey level (μG) from IG; 3) threshold the image IG using the level μG, resulting in a binary image IB; 4) apply the *kmeans* clustering algorithm[178], implemented by the OpenCV *kmeans*, to IG using as initialization the image IB and two clusters, resulting in a binary image Ik, which normally has spurious noise; 5) post-process the image Ik with mathematical morphology in order to remove the smaller regions with noise resulting in another binary image Io; and 6) extract the contour of the cysts from Io using the algorithm proposed by Suzuki and Be[179], which was implemented by the OpenCV function *findContours*. To provide the minimum and maximum cystic diameters (dmin and dmax), the user must manually specify the diameter or draw a diameter line on the image using the CystAnalyser graphical user interface. Finally, a size filter was applied to remove the regions with diameters outside the interested interval [dmin, dmax]. All the algorithmic steps were equal for both kidney and liver images, except in post-processing (step 5), where the mask size of the open morphological filter was constant and equal to three pixels for all liver images so as to remove noise in the binary image, I_k. This filter was

parametrized by d_{min} for kidney images, in order to remove the objects smaller than the desired cyst.

Using a preliminary version of CystAnalyser, the automatic algorithm showed difficulties distinguishing renal tubules from very small renal cysts. We updated CystAnalyser to include a supervised classifier in order to discriminate between true cysts and false positives by activating *Add smaller cysts* setup (click on the *Run* button to automatically add smaller cysts), this functionality was oriented only to use with very small cysts initially not recognized by the *Automatic cyst recognition* tool (see lateral panel **Figure 13A**). We used the Support Vector Machine (SVM) classifier[180], with radial basis function (RBF) kernel implemented by the LibSVM library[181] and accessed through its C binding. The SVM used the true data generated with the first version of the program. We used a total of 7535 small cysts (true cysts were annotated by an expert, and the false cysts were provided by CystAnalyser during the cyst recognition process), 50% of them devoted to training, 25% to validation and 25% to test. The experimental setting used 4-fold cross validation. The selection of values for the SVM tuning hyper-parameters (the regularization parameter C and the inverse γ of the RBF kernel spread) used the well-known grid search method, trying values {2i} from i = -5 to 15, step 2 for C and {2i} from i = -13 to with step 2 to γ. The combination of values that achieved the highest aver- age performance (measured by the Cohen kappa statistic) on the 4 validation sets were C = 2 and γ = 2−5. The average kappa and accuracy values over the test sets were 68.7% and 86.7%, respectively, although the performance of CystAnalyser working in a real laboratory environment was not evaluated. We developed experiments with different feature vectors in order to select the best trade-off of computational time and performance. Finally, the Local Binary Patterns (LBP)[182] of its grey-level version, were used as inputs of the classifier. This feature vector was calculated for each cyst using the pixels inside its area, similarly to previous software generated by us[183,184]. Specifically, we used the LBP uniform patterns in order to develop a feature vector of suitable dimension to be used by the classifier. The histogram of the patterns' labels accumulated over the cyst region was employed as texture

descriptor. The feature vector was constructed concatenating the histograms of the LBP uniform patterns considering the following values for the radius R and neighbors P pixels (R,P) = {(1,8), (2, 16), (3, 24)}, developing a vector with 54 features[181,182].

1.3. Cystic index, cyst number and size profile calculation

The *Automatic cyst recognition* and *Supervised post-processing* tools of CystAnalyser were tested in 464 liver and 331 kidney histological images. No differences were found between supervised and non-supervised Cystic Index (CIA versus CIS) and the number of cysts (NA and NS) in the kidney samples (**Figure 14A**). On the other hand, statistical significances were found in liver CI and N, indicating the necessity of supervision for *Automatic cyst recognition* (**Figure 14B**).

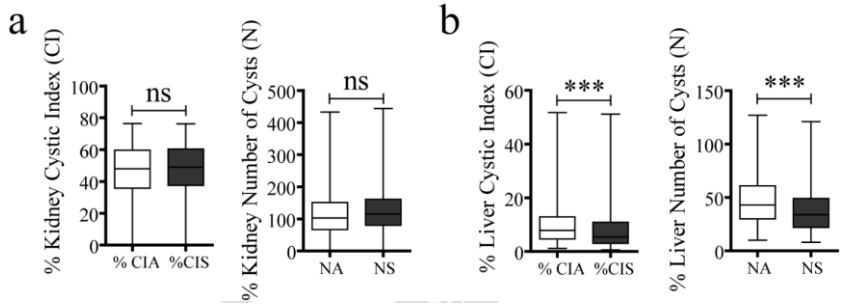

Figure 14. Cystic Index and Number of cysts analysis with supervised and non-supervised Automatic Cyst Recognition. Box plots show the comparison between Cystic Index Automated (CIA) versus Cystic Index Supervised (CIS) and between Number of cysts Automated (NA) versus Number of cysts Supervised (NS), respectively, for all kidney (a) and all liver (b) images. No significant differences were found between supervised and non-supervised Automatic Cyst Recognition in kidney images (a). However, supervise the Automatic Cyst Recognition significantly (***p<0,001) diminished the cystic index and number of cysts in liver samples (b). The lower and upper ends of the box define the 25% and 75% quantiles, respectively, the middle line in the box is the median of the values and the whiskers are the 0% and 100% quantiles. Mann-Whitney test was used for statistical analysis; ns: no significance; ***p<0,001.

In order to identify possible inaccuracies due to the variable phenotype across samples, we established varied degrees of liver and kidney disease phenotypes (mild-cystic, cystic and severely-cystic) according to the CI (see the Materials and methods section). **Figure 15** shows a representative example of the *Automatic cyst recognition*

interface for the different degrees of disease severity in cystic kidney and liver histological samples. The *Automatic cyst recognition* interface tool was robust calculating kidney cystic Index and the number of cysts (**Figure 16A**), with a sensitivity (Se) and specificity (Sp) range of 76.9–78.6 and 77–89.7, respectively for all degrees of disease phenotype (**Table 3**). Only in those scenarios where several big cysts become fused (severely-cystic phenotype) it was necessary to employ the Supervised post-processing tools by an expert user (**Table 3**, Severely Cystic NA vs. NS p>0.01).

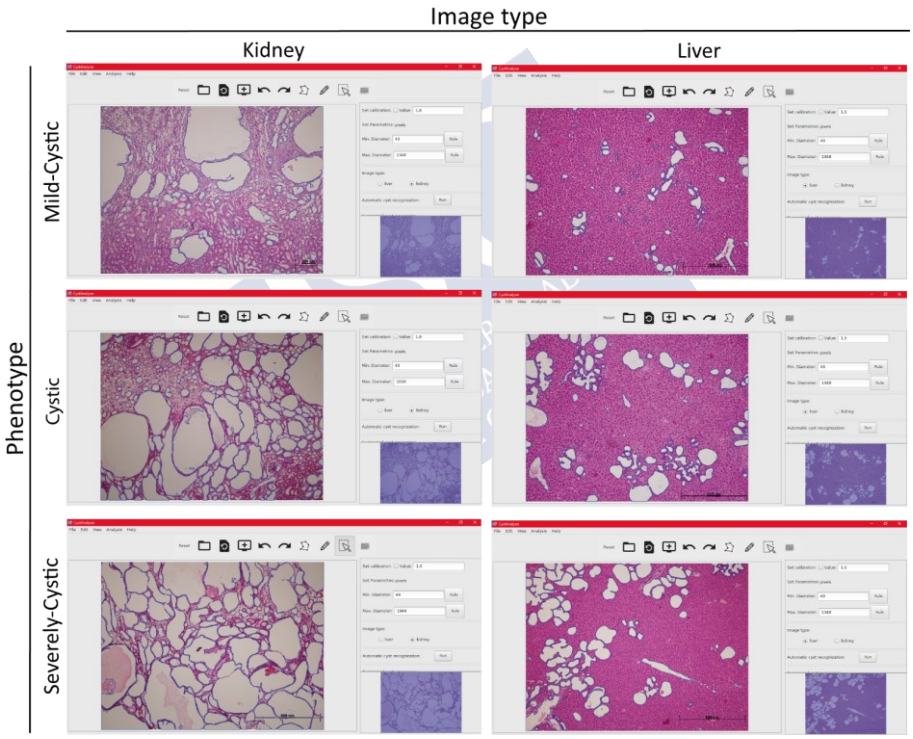

Figure 15. CystAnalyser Automatic Cyst Recognition in different group of severity of renal and hepatic cystic disease. Representative screenshots of CystAnalyser showing histological images of cystic liver and kidney after the application of the Automatic Cyst Recognition algorithms (cyst contour in blue). The left and right panels are respective histological images of kidney and liver. Upper panels show representative images of a mild-cystic phenotype, central panels are for cystic phenotype and bottom panels are for severely cystic phenotype.

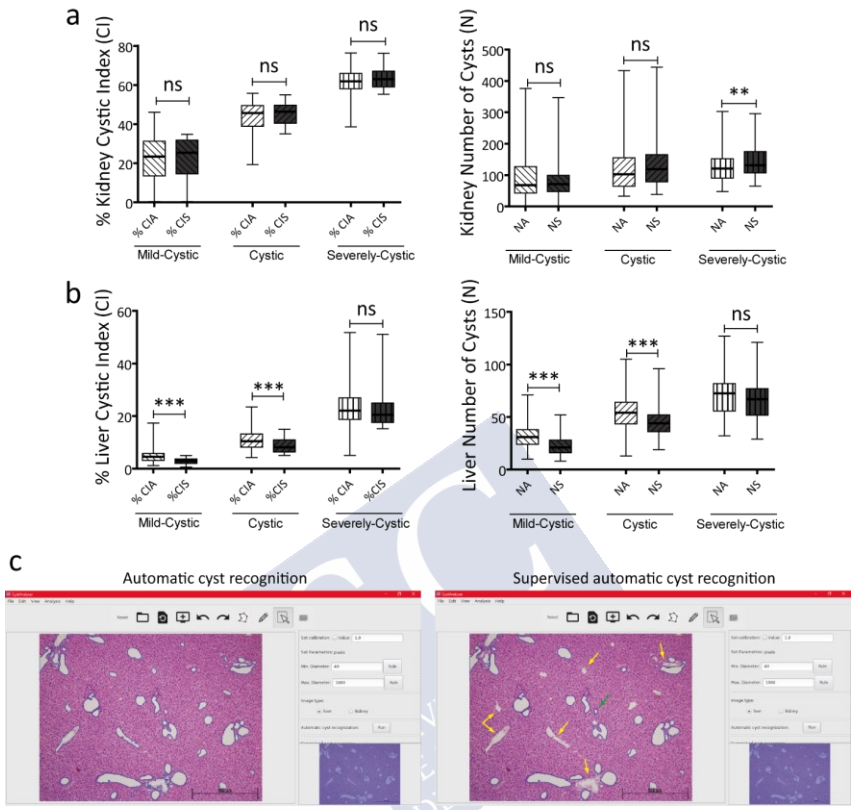

Figure 16. Comparison of supervised and non-supervised Automatic Cyst Recognition of CystAnalyser, according of cystic disease severity. (a-b) Box plots show the comparison between Cystic Index Automated (CIA) versus Cystic Index Supervised (CIS) and between Number of cysts Automated (NA) versus Number of cysts Supervised (NS), respectively, for kidney (a) and liver (b) images classified in mild-cystic, cystic and severely-cystic. No significant differences were found between supervised and non-supervised Automatic Cyst Recognition in kidney images (a) with the exception of the number of cysts in the renal severely-cystic phenotype. Nevertheless, in hepatic mild-mystic and mystic images we observed significant differences in Cystic Index and the Number of cysts (b). The lower and upper ends of the box define the 25% and 75% quantiles, respectively, the middle line in the box is the median of the values and the whiskers are the 0% and 100% quantiles. Mann-Whitney test was used for statistical analysis; ns: no significance; **p<0,01; ***p<0,001. (c) Representative example of mild-cystic liver with Automatic Cyst Recognition (left panel) and after Supervised Automatic Cyst Recognition (right panel). The yellow arrows show cysts erroneously recognized by the program or false positive, mostly bile ducts, hepatic vein and arteries. The green arrow shows a false negative or true cyst not detected by CystAnalyser. Bile ducts and hepatic vasculature represent an important part of hepatic cystic region recognized by CystAnalyser; which, when eliminated (with Supervised post- processing), implies a significant quantitative change in the cystic Index and number of cysts.

Group	CIA	CIS	p-value	Sig.	NA	NS	p-value	Sig.	PCD (%)	PCA (%)	Se (%)	Sp (%)
A						**Kidney**						
Mild cystic	22.25	21.76	>0.05	ns	82.97	96.46	>0.05	ns	23.04	21.92	77.94	76.96
Cystic	45.66	43.98	>0.05	ns	131.0	120.6	>0.05	ns	12.38	23.17	76.84	87.62
Severely cystic	63.26	61.85	>0.05	ns	142.3	126.6	<0.01	**	10.34	21.40	78.59	89.66
B						**Liver**						
Mild cystic	2.89	4.74	<0.001	***	22.79	32.30	<0.001	***	36.58	9.17	90.25	63.42
Cystic	8.90	10.98	<0.001	***	57.5	61.0	<0.001	***	20.63	12.38	87.29	79.38
Severely cystic	22.78	23.84	>0.05	ns	66.6	71.52	>0.05	ns	10.93	6.20	93.8	86.07

Table 3. Results of CystAnalyser® Automatic Cyst Recognition. Summary of results of the Automatic Cyst Recognition of kidney (a, upper panel) and liver images (b, down panel). The table reports the average value of the following parameters. The four first columns show comparison between Cystic Index Automated (CIA) versus Cystic Index Supervised (CIS); columns 5 to 8 show the results of compare Number of cysts Automated (NA) a Number of cysts Supervised (NS); finally, columns 9 to 12 represent the value for: Percentage of Cysts Deleted (PCD) and Percentage of Cysts Added (PCA) by the user in the supervision, the Sensitivity (Se) and Specificity (Sp) calculated by equation 1 (see Material and Methods section). Mann-Whitney test was used for statistical analysis; we considered a value $p < 0.01$ (**) or $p < 0.001$ (***) as significant and a value $p>0.05$ as non-significant (ns).

On the other hand, we observed that CI and N of mild-cystic and cystic livers needed to be calculated supervising the *Automatic cyst recognition*, using *Supervised post-processing* tools, due to non-specific recognition of extrahepatic bile ducts and vasculature structures (**Figure 16B** and **Table 3**). The sensitive range was 87.29–93.80 and the specificity range was 63.42–86.07, the lowest values corresponding to the mild-cystic phenotype (**Table 3**). **Figure 16C** shows an example of *Automatic cyst recognition* of a mild-cystic liver phenotype before (left panel) and after (right panel) user input by deletion of the extrahepatic bile ducts, hepatic veins and arteries in order to calculate the exact liver CI and N. Although it was an inconvenience, this result offered value to the plasticity of CystAnalyser providing both the supervised and non-super- vised tools according to the phenotype, organ and user needs.

As we can see in **Table 3** the Number of cysts after Supervision (NS) was higher for kidney images (except for mild-cystic images) than the Number of cysts Automated (NA). How- ever, this did not occur for liver images because NS is lower than NA (**Table 3**), owing to the necessity to delete hepatic vasculature and extrahepatic bile ducts (see **Figure 16, B and C**). In relation to this, the percentage of cysts recognized automatically by CystAnalyser and deleted by the user was lower in kidney than in liver (in **Table 3** column PCD). Nevertheless, the percent- age of cysts added by the user was higher in kidney than liver (in **Table 3** column PCA). This fact was also reported by sensitivity and specificity (in, columns Se and Sp respectively). The sensitivity was higher than 87.29% and 76.84% for all groups of liver and kidney respectively, and specificity range of 76.96–89.66% for kidney and 63.42–86.07% for liver images. These results of Sensitivity and Positive Predictive Value were very promising, taking into account the laborious way to count the recognition errors in this study (see subsection Statistical analysis, Chapter 1 - Materials and Methods), because when the expert used the Supervised post-processing tools, one action of the user on the GUI implied counting several errors (always more than two).

In order to analyze the behavior of CystAnalyser with the cyst profile, the size or diameter of each individual cyst was preset. **Figure 17** shows the Number of cysts Supervised (NS) and Cysts Automatically detected by CystAnalyser (NA) for all kidney (**Figure 17,** A–C) and liver (**Figure 17, D–F**) images featuring all the variable cystic phenotypes. In general, the cyst size profiles were quite similar. The main difference was the mild cystic images for the smaller cysts (diameter lower than 300 pixels) in the kidney (**Figure 17A**); specifically, for the cysts with diameters between 0 and 100 pixels the difference between NA vs NS is 12.01 points, and for the cysts with diameters between 100 and 200 pixels the difference was -10.56 points. The reason being the program had difficulty in recognizing the smallest renal cysts, with narrow lumens, which required marking or completing it manually. However, in the liver (lower panel) the main difference was for the bigger cysts (diameter higher than 500) in mildly cystic and cystic phenotypes, with a difference of1.75 points for both between NA vs NS. As mentioned and shown in **Figure 16C**, the extrahepatic bile ducts must be deleted from the recognized cysts and this generated a difference in the cystic index and cyst size profile, as it occupied an important part of the image.

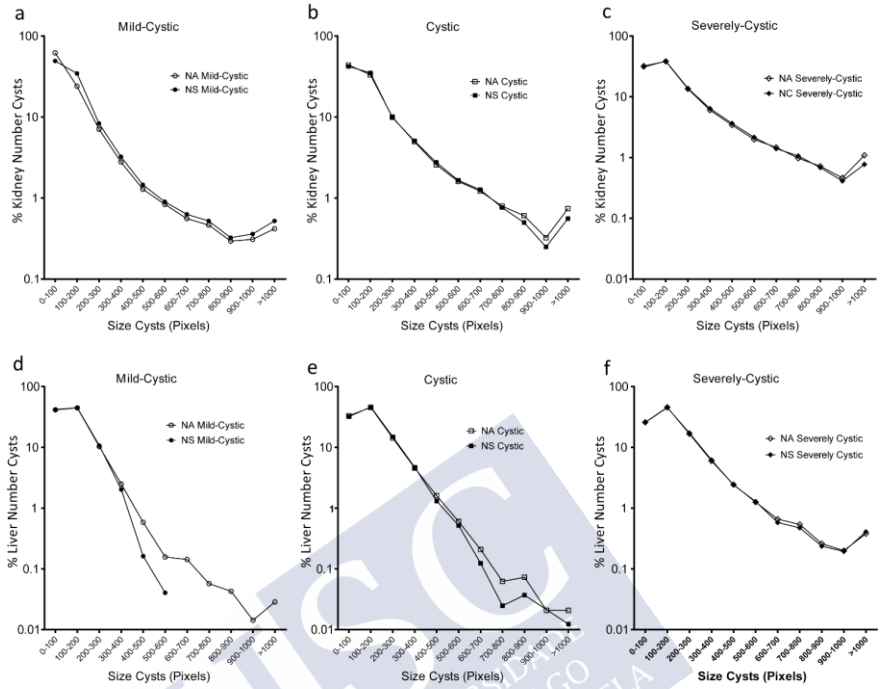

Figure 17. CystAnalyser allows studying the cystic profile, based on the size of the cysts. Logarithmic graph showing a profile of the cyst diameters automatically recognized by CystAnalyser (Number of cysts Automated, NA) versus the cysts reviewed (Number of cysts Supervised, NS) for kidney (a-c, upper row) and liver (d-f, lower row). In general, the cystic profiles were very similar except for the hepatic mild-cystic images (d); which after supervision of Automatic Cyst Recognition the biggest cysts disappeared due to deletion of bile ducts and hepatic vasculature (see Fig 4B and 4C). Kidney and liver images were classified in the different group according to severity of cystic disease. The cyst size is shown in pixels.

1.4. Comparison with ImageJ

Next, we compared the cystic index calculated by CystAnalyser (automated or CIA, and supervised or CIS) with ImageJ, which has been the software most used for this analysis. For the comparison study, we analyzed 128 images of kidney; 29 mild-cystic, 52 cystic and 47 severely- cystic and 287 images of liver; 111 mild-cystic, 115 cystic and 61 severely-cystic. Examples of the visual results of cystic kidney and liver images provided by CystAnalyser (before and after user supervision) and by ImageJ are shown in **Figure 18A**. We can see that ImageJ recognizes white parts as cysts, predominantly between cysts or zones in the renal medulla (near to renal papilla) in the case of kidney images, and hepatic parenchyma in the case of liver images. Besides,

given that ImageJ did not allow supervision after the automatic recognition of the cysts which increased likelihood of false positives (for example tubes and dilated tubes for kidney, extrahepatic bile ducts in the liver etc.) in the final result.

In order to perform a statistical comparison, **Figure 18B** and **C** show the cystic index calculated for all images, grouped by cystic phenotype for kidney (**Figure 18B**) and liver (**Figure 18C**), using: CystAnalyser without any user supervision (CIA), CystAnalyser after user supervision (CIS) and ImageJ. The difference between the cystic index calculated by CystAnalyser and ImageJ was significant for all cystic degrees except for the severely-cystic phenotype. ImageJ provided an overestimated result for both tissues, especially in kidney images since the difference between CIS (which is the most accurate value) and the cystic index of ImageJ was 38.07 points (mild-cystic), 22.45 points (cystic) and 7.28 points (severely-cystic). Consequently, CystAnalyser overcame ImageJ in precision. On the other hand, to do the quantitative analysis in ImageJ the segmentation threshold setting was required, a parameter which was implicit because it is meaning was not clear for the user, and its optimal value must be selected by trial and error, being different for each image. So, the cystic index calculated by ImageJ was subjective because it depended on the threshold selected by the expert, which may vary among experts. On the contrary, CystAnalyser only needed to set the range of cyst diameters to be recognized. This parameter was explicit (clearly understandable by the expert) and descriptive (it can be set in micrometers or pixels), and it was the same for all images, so the results of CystAnalyser were less subjective (or not subjective at all) with respect to the user who did the analysis.

In addition, CystAnalyser achieved a score of 80.75 in the System Usability Scale (SUS) questionnaire, used to measure the subjective perception of the system, which means that this software is considered good to excellent. CystAnalyser is fast enough to work online on a general-purpose personal computer in any biomedical laboratory, capable of developing automatic cyst recognition of an image almost instantaneously (approximately 3 seconds) and faster than ImageJ and requiring an average of approximately three minutes for manual expert supervision (ImageJ does not allow it), which could be avoided in program applications where automatic recognition is already accurate.

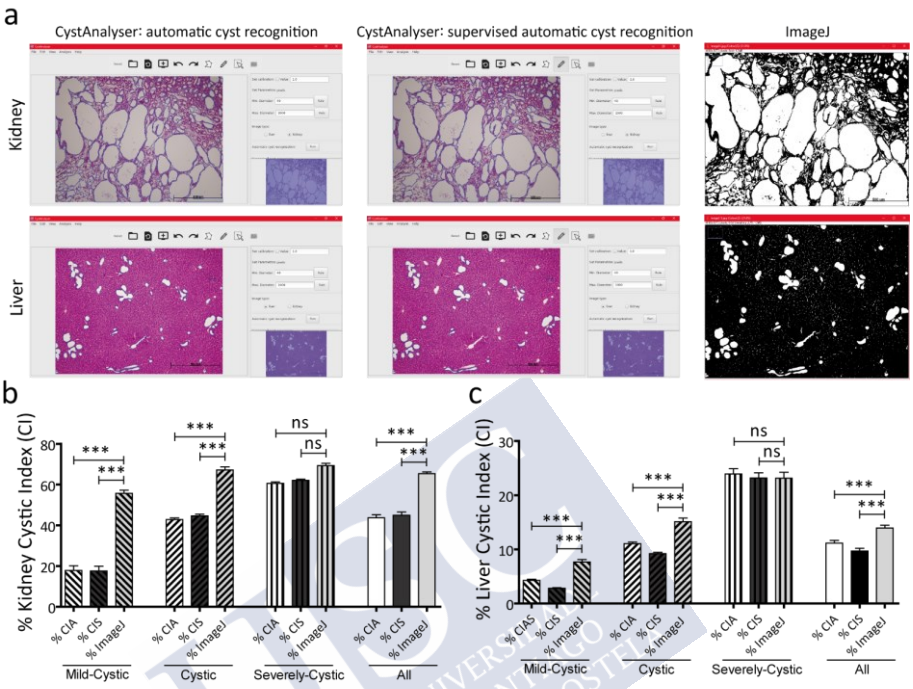

Figure 18. CystAnalyser provides a more reliable Cystic Index value than ImageJ. (a) Cyst recognition in a cystic kidney (upper panel) and liver (lower panel) images using CystAnalyser without supervision (left image), after user supervision (middle image) and using ImageJ. Cysts contours were overlapped to image for CystAnalyser (color blue); whereas for ImageJ the white regions were counted as cystic area. (b-c) Bar plots showing the cystic index of CystAnalyser (automated or supervised) versus Cystic Index provided by ImageJ for kidney (b) and liver (c). In general, we observed that CystAnalyser provided a more reliable and accurate Cystic Index than ImageJ; and in the same way, CystAnalyser discriminated better the different images according to severity of cystic disease. We found significant differences in Mild-Cystic and Cystic images (b-c). However, in severely-cystic images the cystic index provided by CystAnalyser and ImageJ were similar. CIA: Cystic Index Automated (provided by CystAnalyser). CIS: Cystic Index Supervised (provided by CystAnalyser). Bars represent mean + Standard Error (SE). Kruskal-Wallis test, with Dunn multiple pair-wise comparison post-test, was used for statistical analysis; ns: no significance; ***p<0,001.

2. CHAPTER 2

Quantitative proteomic study unmasks fibrinogen pathway in Polycystic Liver Disease

USC UNIVERSIDADE DE SANTIAGO DE COMPOSTELA

2.1. Liver proteome Characterization by SWATH analysis

Liquid chromatography coupled to tandem mass spectrometry (LC-MS/MS) it has been the most used and common technology for the characterization of proteomes, as well as biomarker researching or drug screening[185,186]. An emerging strategy named SWATH-MS (Sequential Window Acquisition of all THeoretical fragment-ion spectra-Mass Spectrometry) allows reproducibly, reliability and high-throughput quantification of up to thousands of proteins per biological sample and perform simultaneously a great quantity of assays[187]. So, the next-generation proteomics SWATH-MS technology allows to quantify proteome and to identify protein abundance. For SWATH-MS measurement, the samples are digested with trypsin and analyzed by liquid chromatography coupled to a tandem mass chromatography working in the so-called Data-Independent Acquisition (DIA) mode[186] (more details in Material and Methods).

In SWATH-MS, the total and final number of quantified proteins still depends on sample matrix and specifically in the good quality of a spectral library which is built with a pool mix of all samples (more details in Material and Methods). In our study, we have detected between ~1.300 and ~2.000 proteins at a critical false discovery rate (FDR) <1% in the liver libraries. We compare proteome pattern between *Wild Types* (WT) and mutants (KO) mice livers from an ADPKD orthologous murine model (*Pkd1*$^{cond/cond}$*;Tam-Cre* mouse) with the aim to identify new molecular pathways and therapeutic targets for hepatic cystogenesis (**Figure 19**).

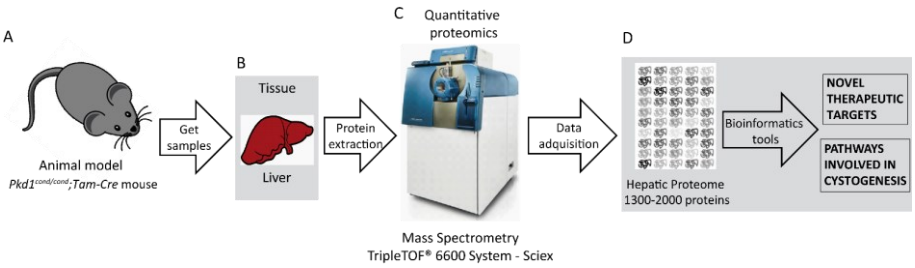

Figure 19. Illustrated Workflow scheme. (A) First, we use an ADPKD murine model (*Pkd1*$^{cond/cond}$*;Tam-Cre* mice) to get biological samples after sacrifice. (B) For this study, livers (cystic and non-cystic) were saved and frozen. (C) Next, the total protein was extracted and using quantitative proteomics (SWATH-MS analysis) the hepatic proteome of different samples was analyzed. (D) Finally, comparing cystic and non-cystic samples using a bioinformatics tools we could detect novel therapeutic targets and pathways involved in the process of cystogenesis.

We have induced *Pkd1* gene deletion in two different life time points, postnatal days 14 and 12 (p14 and p12, respectively), with the purpose of studying phenotypes with different severity in liver cystic growth (**Figure 20**). In this work, there are four study groups: *Wild Types* and Mutants with *Pkd1* gene deleted at p14 (named WT p14 and KO p14, respectively), and deleted at p12 (named WT p12 and KO p12, respectively). All cases were sacrificed at p30. A n of six was used for each group (24 samples in total). No differences were found between males and females, and the same number of males and females were used per each group (three males and three females in all cases). As we show in **Figure 20B**, the group of mutants p14 presented lower values of cystic index and number of cyst than mutants p12.

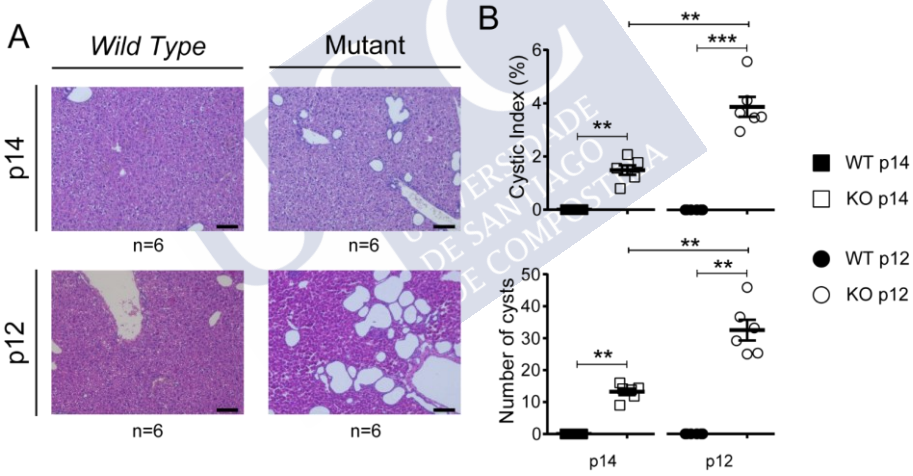

Figure 20. Cystogenesis characterization of phenotypes studied. (A) Representative images of Hematoxylin-Eosin (HE) stained from livers of *Pkd1*$^{cond/cond}$*;Tam-Cre* mouse *Wild Type* (WT, *Pkd1*$^{cond/cond}$*;Tam-Cre*$^{-}$) and Mutant (KO, *Pkd1*$^{cond/cond}$*;Tam-Cre*$^{+}$) with *Pkd1* gene deletion induced by tamoxifen at postnatal day 14 (p14) and 12 (p12). All mice were sacrificed at p30. Scale bar, 100μm. n represents the number of samples per group. (B) Hepatic cystic index (upper panel) and number of cysts (lower panel) of the different phenotypes. *Pkd1* deletion at p12 carries a more severe cystogenesis. Bars represent means±SEM in all cases. $p<0.05$ by T-student test (two tail) was considered as significative result. ** $p<0.01$, *** $p<0.001$.

2.2. Protein abundance changes in hepatic cystogenesis

First, we have performed TAS (Total Area Sum) normalization to evaluate that our samples followed a normal distribution pattern, as we show in **Supplemental Figure 1** and **Supplemental Figure 2**. Proteins showing a significant difference in abundance with a two-fold increase or decrease and an adjusted p-value significant (according to parametric Student`s t-test) between *Wild Type* and mutant samples are shown in **Table 4** and **Table 5**) with its respectively fold-changed and adjusted p-value observed. In total, 8 proteins showed a significant protein abundance (5 proteins increased or up-regulated and 3 proteins decreased or down-regulated) between p14 *Wild Type* and mutant groups (**Table 4**), and 26 proteins targets showed a significant protein abundance (20 proteins up-regulated and 6 proteins down-regulated) between p12 *Wild Type* and mutant groups (**Table 5**). Graphically, these variations can be observed through of volcano plots, which were generated by plotting the log(2)-fold changes for all proteins identified against their log(10) p-value (Figure 21). The lower number of proteins with significant difference at p14 can be explained by its milder cystogenic phenotype (Figure 20B). In the same way, our results suggest that the number of proteins and pathways increase with significant differences correlating with a severe phenotype and advanced stage of polycystic disease.

Table 4. Proteins list with two-fold increase or decrease abundance and an adjusted p-value (according to parametric Student`s t-test) comparing *Wild Type* and mutant polycystic livers with inactivation of the *Pkd1* gene at postnatal day 14.

Protein accession	Protein code	Gene name	Fold-change WT to mutant	p-value (Student`s t-test)
Pkd1 deletion at postnatal day 14 (p14)				
Q00898	A1AT5	*Serpina1e*	2,33	1,32E-03
P07356	ANXA2	*Anxa2*	2,27	3,72E-06
P12710	FABPL	*Fabp1*	2,20	6,58E-07
Q8BWU5	OSGEP	*Osgep*	2,19	4,45E-03
Q05816	FABP5	*Fabp5*	2,04	3,76E-04
Q8VED5	K2C79	*Krt79*	0,43	2,82E-03
Q6IFZ6	K2C1B	*Krt77*	0,47	2,42E-03
Q9Z2T6	KRT85	*Krt85*	0,37	7,16E-03

Table 5. List of proteins that presented an abundance with two-fold increase or decrease and an adjusted p-value (according to parametric Student`s t-test) comparing *Wild Type* and mutant polycystic livers. Table shows the list corresponding to the results with inactivation of the *Pkd1* gene at postnatal day 12.

Protein accession	Protein code	Gene name	Fold-change WT to mutant	p-value (Student`s t-test)
Pkd1 deletion at postnatal day 12 (p12)				
P12246	SAMP	*Apcs*	4,37	4,79E-07
Q71KU9	FGL1	*Fgl1*	3,52	5,02E-16
Q60590	A1AG1	*Orm1*	3,33	2,99E-09
Q9JHU9	INO1	*Isyna1*	3,32	8,19E-09
Q6P8J7	KCRS	*Ckmt2*	2,71	3,01E-02
O55222	ILK	*Ilk*	2,67	7,46E-04
P07310	KCRM	*Ckm*	2,67	1,13E-02
Q61024	ASNS	*Asns*	2,58	1,21E-09
Q05816	FABP5	*Fabp5*	2,51	2,28E-06
P31725	S10A9	*S100a9*	2,39	1,45E-06
Q8K0E8	FIBB	*Fgb*	2,33	1,21E-14
Q64464	CP3AD	*Cyp3a13*	2,18	3,77E-16
Q91X72	HEMO	*Hpx*	2,16	1,08E-13
Q8R429	AT2A1	*Atp2a1*	2,15	2,20E-02
P70697	DCUP	*Urod*	2,15	3,57E-06
E9PV24	FIBA	*Fga*	2,14	4,78E-11
Q8VCM7	FIBG	*Fgg*	2,09	2,84E-12
P01029	CO4B	*C4b*	2,08	1,51E-14
O09012	PEX5	*Pex5*	2,01	8,43E-03
P00405	COX2	*Mtco2*	2,01	1,35E-04
P05208	CEL2A	*Cela2a*	0,35	2,37E-02
Q63836	SBP2	*Selenbp2*	0,39	3,27E-05
Q9NYQ2	HAOX2	*Hao2*	0,42	2,40E-11
Q9D1L0	CHCH2	*Chchd2*	0,45	1,79E-07
P16015	CAH3	*Ca3*	0,47	1,19E-04
Q8R1F5	HYI	*Hyi*	0,49	5,79E-03

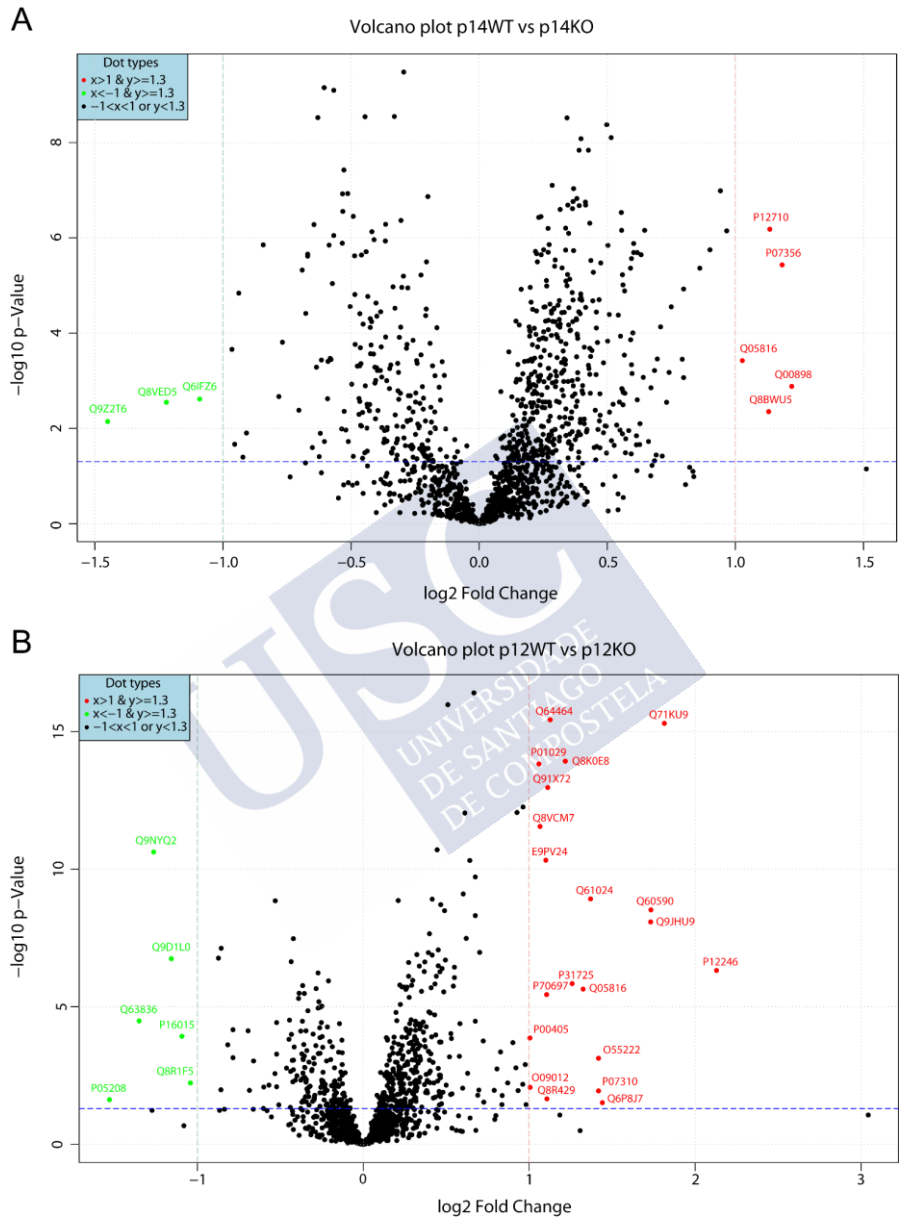

Figure 21. Volcanos plots comparing *Wild Type* and mutant samples. (A-B) Volcano plots of the SWATH MS analysis showing proteins with significance differences in increase (red points) or decrease (green points) protein abundance at p14 (A) and p12 (B). X-axis shows log(2)-fold change (red and green lines shows the increase and decrease 2-fold cut-off, respectively) and axis shows -log(10)-p-value (blue lines shows the cut-off of p value <0.05).

Next, the differences in protein abundance levels of significant protein were visualized in a cluster heatmap analysis, which show how different proteins are grouped (**Figure 22**). In the same way, clustering all proteins detected by SWATH MS analysis we can appreciate samples separate according to its quantitative proteome (**Supplemental Figure 3**).

Unsupervised multivariate statistical analysis using Principal Component Analysis (PCA) was performed to compare the data across the samples (**Figure 23**). Heatmap and PCA data demonstrated reproducibility among the sample triplicates as the three replicates clustered closely in both analyses. By other hand, we can observe both in the PCA and in the heatmap cluster analysis how some sample is not grouped correctly and overlap between the two clusters (**Figure 23** and **Supplemental Figure 3**). Nonetheless, we can see the tendency to separate data in two big groups corresponding to *Wild Type* and Mutant clusters.

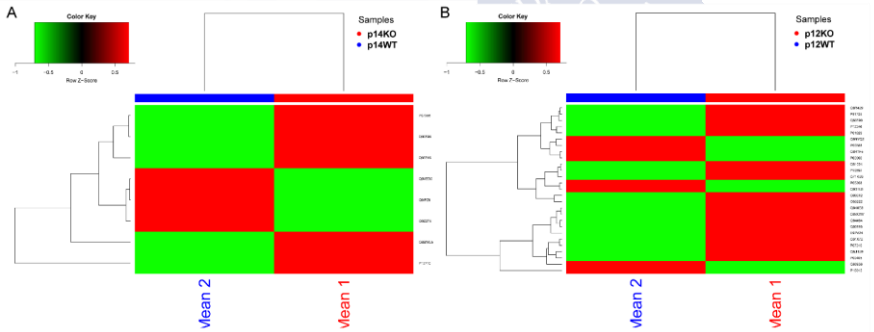

Figure 22. Heatmap figure of unsupervised cluster analysis of proteins with significant differences according to SWATH MS analysis. (A-B) Cluster of results corresponding to postnatal day 14 (A) and postnatal day 12 (B). Samples from the *Wild Types* (WT p12 and WT p14) and mutant (KO p12 and KO p14) groups are shown in blue and red, respectively. Color gradient is determined by the RowZ-score, where red and green represent increase and decrease, respectively, of protein abundance.

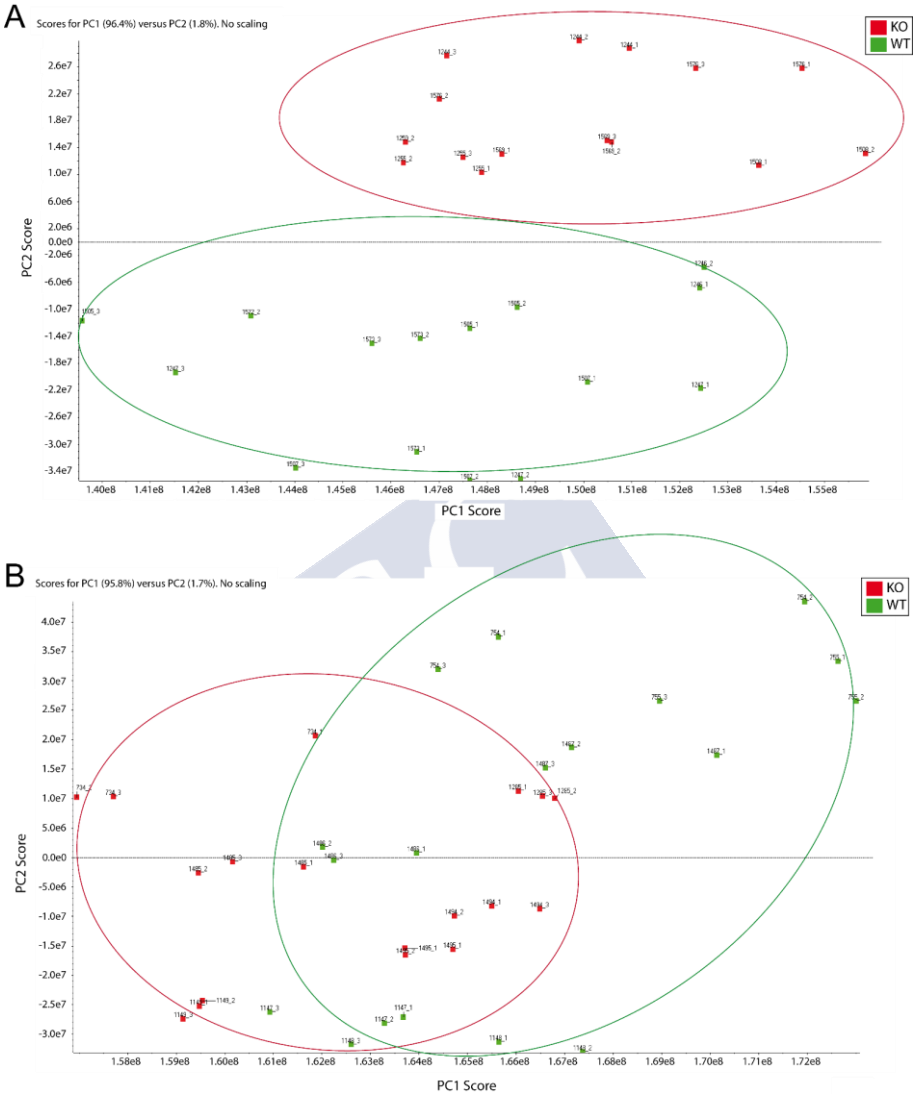

Figure 23. Unsupervised PCAs from SWATH MS data. (A-B) PCA multivariate statistical analysis of p14 (A) and p12 (B) data. Red and green circles represent KO and WT samples clusters, respectively. In p14 data, PCA has successfully separate the two clusters, however in P12 data we could observed overlap in part of samples (but we observed a separation tendency). In addition, PCA showed that the three technical replicates of each sample we clustered closely.

2.3. Pathway analysis

To evaluate the function of differentially expressed proteins by SWATH MS we used several bioinformatic tools and analysis. GO (Gene Ontology) terms and pathways analyses were performed using Panther[188], String[189] and Reactome[190]. The proteins were classified into GO categories, according to Panther, therefore the most enriched items were "cell communication", "cell adhesion" and "metabolic process" (**Supplemental Figure 4**). Besides, all proteins with significant differences were submitted to Reactome pathway analysis finding that metabolism and immune system were the most enrichment pathways (**Supplemental Figure 5**). Finally, the most significant terms GO (biological process) found on String were related to response to stress, metabolic process and protein complex biogenesis and assembly (**Supplemental Figure 6**).

Cluster analysis based on String was also performed to investigate the protein-protein interactions (interactions with experimental evidence). Overall, our quantitative proteomic data showed numerous interactions and proteins were clustered in different groups (**Supplemental Figure 7**). But focusing on two most representative and important clusters we can describe the majority of interactions in our data (**Figure 24**). Specifically, in cluster of p14 data we could find two proteins involved in the intracellular lipid transport (FABP1_P12710 and FABP5_Q05816), which interacts with Annexin A2 (ANXA2_P07356) a protein associated with diverse cellular functions such as cell motility (in epithelial cells), protein related to cytoskeleton and cell matrix interactions[191]. On the other hand, in p12 data we found a very strong protein-protein interaction cluster between different fibrinogens (FGL1_Q71KU9, FIBB_ Q8K0E8, FIBA_ E9PV24 and FIBGG_ Q8VCM7). Fibrinogens are involved in hepatocytes growth, mediates blood platelet spreading and interstitial collagen and fibrotic lesions[192]. Furthermore, additional proteins were found to interact with fibrinogens in the analysis such as Serum amyloid P-component (SAMP_P12246), hemopexin (HEMO_Q91X72) or hydroxyacid oxidase 2 (HAOX2_ Q9NYQ2).

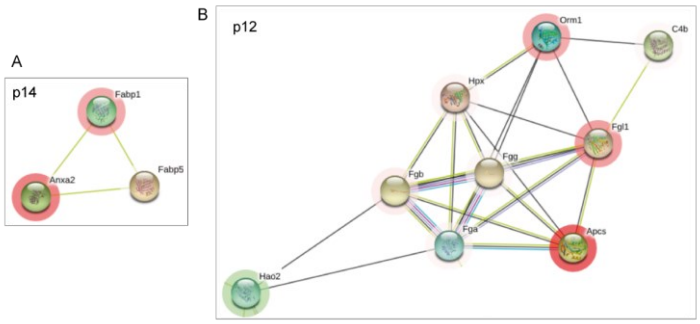

Figure 24. Protein-protein interaction map of selected clusters according to String. Proteins with significant increase and decrease protein abundance were submitted to String analysis. (A) and (B) represents protein-protein analysis of selected and most important clusters of p14 and p12 data, respectively. Proteins are represented as nodules, which are colored red or green imply increase or decrease in protein abundance respectively.

2.4. Validations of target candidates

Several proteins targets were selected for RT-qPCR and *Western Blotting* validation using other independent groups of six samples at p14 and p12. These target candidate proteins were selected based on involvement in protein-protein interaction clusters, its function and possible role in hepatic cystogenesis. The protein abundance from SWATH MS data of selected proteins is shown in **Supplemental Figure 8**. For RT-qPCR validation we selected, one up-regulated candidate protein of p14 data (ANXA2), eight up-regulated proteins of p12 data (SAMP, FGL1, ILK, S10A9, FIBB, HEMO, FIBA and FIBG) and one down-regulated protein of p12 data (HAOX2) were selected. Eight of ten of these selected proteins were validated at mRNA level by RT-qPCR (**Figure 25**). Interestingly, the two proteins that did not belong to the most enriched cluster (**Figure 24**), ILK and S10A9, did not present significant differences in genetic expression levels (**Figure 25C**). Finally, we have developed *Western Blotting* (WB) analysis in order to validate five selected proteins and we obtained statistical differences for all of them (**Figure 26** and **Supplemental Figure 9**). Overall, gene expression and WB analysis were very consistent with SWATH MS proteomic data and provided us interesting new targets and molecular pathways for future works and possible new therapeutic approaches for PLD.

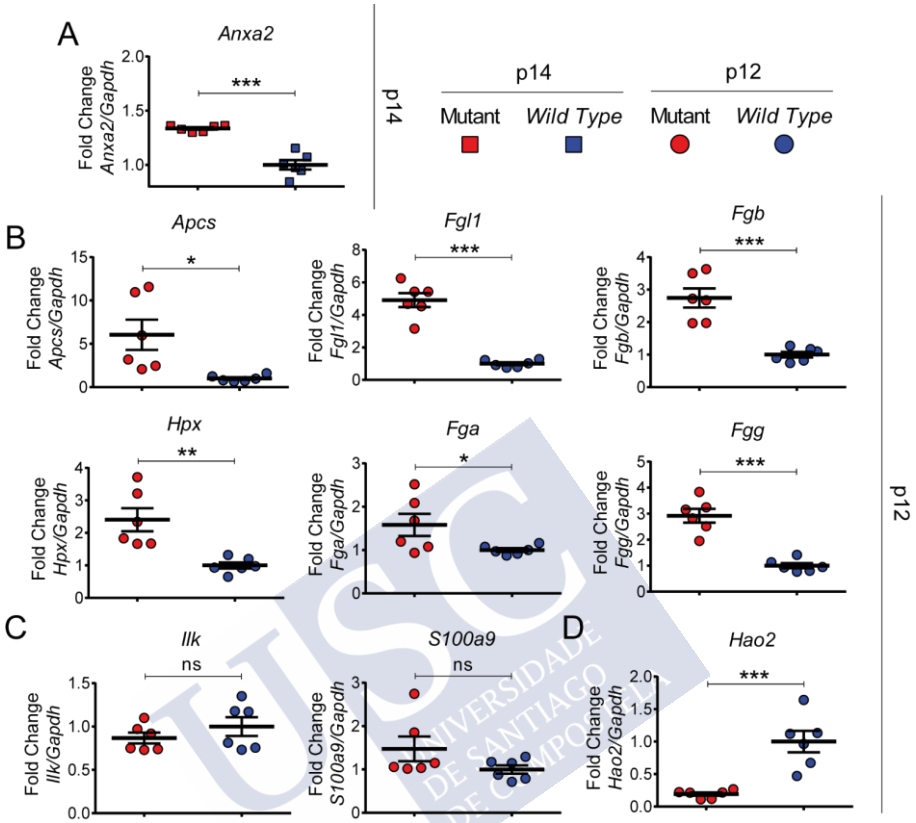

Figure 25. Validation of possible targets by RT-qPCR. Gene expression of eight to ten selected targets corelated with SWATH MS data. RT-qPCRs of up-regulated selected p14 target annexin A2 (*Anxa2*) (A); up-regulated p12 targets amyloid P Component, Serum (*Apcs*, SAMP gene), Fibrinogen Like 1 (*Fgl1*), Fibrinogen Beta Chain (*Fgb*), hemopexin (*Hpx*), Fibrinogen Alpha Chain (*Fga*), Fibrinogen Gamma Chain (*Fgg*) (B), Integrin Linked Kinase (*Ilk*) and S100 Calcium Binding Protein A9 (*S100a9*) (C); and down-regulated p12 target Hydroxyacid Oxidase 2 (*Hao2*). A n=6 was used for each protein group. *Gapdh* was used as housekeeping. Bars represent means±SEM. Student`s t-test with two-tail was used and a value of $P<0.05$ was considered significant. ns: not significant ($p\geq0.05$), * $p<0.05$, ** $p<0.01$, *** $p<0.001$.

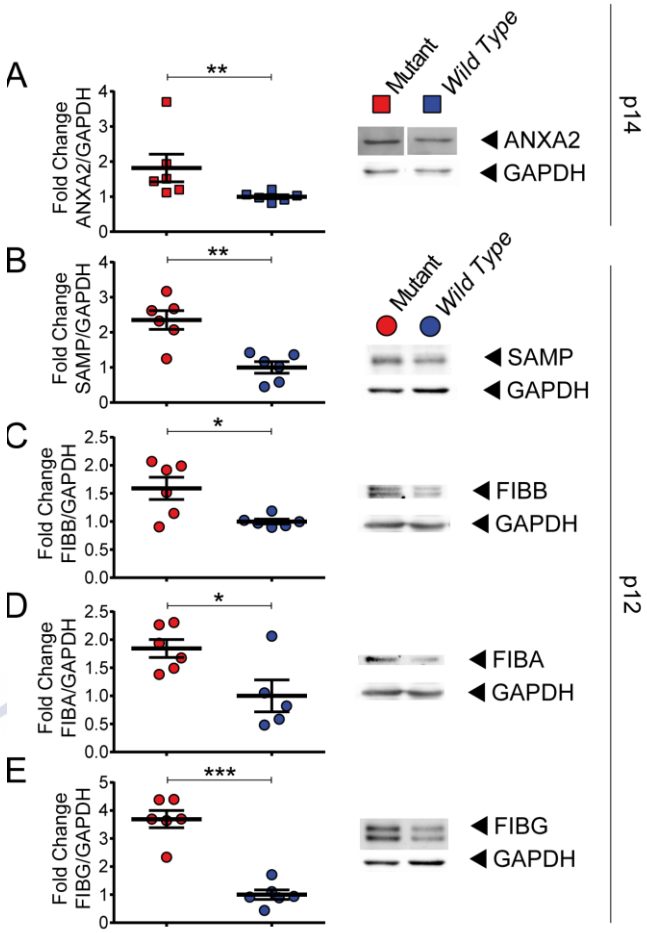

Figure 26. Validation of possible targets by *Western Blotting*. The protein abundance of five possible targets of our quantitative proteomic SWATH MS data were validated by *Western Blotting* (WB) analysis. WB of up-regulated selected p14 target annexin A2 (ANXA2) (A); up-regulated p12 targets amyloid P Component, Serum (SAMP) (B), Fibrinogen Beta Chain (FIBB) (C), Fibrinogen Alpha Chain (FIBA) (D), Fibrinogen Gamma Chain (FGG) (E). A n=6 was used for each protein group. GAPDH was used as housekeeping. Bars represent means±SEM. Student`s t-test with two-tail was used and a value of $P<0.05$ was considered significant. * $p<0.05$, ** $p<0.01$, *** $p<0.001$. Full WBs are shown in **Supplemental Figure 9**.

3. CHAPTER 3

Marimastat, a new therapeutic approach based in inhibition of metalloproteases in Polycystic Kidney and Liver Disease

USC UNIVERSIDADE DE SANTIAGO DE COMPOSTELA

3.1. Extracellular matrix and MMPs expression are deregulated in PKD

We used differential proteomics by mass spectrometry LC-MS/MS by SWATH-MS analysis to compare the proteome pattern between *Wild Types* and mutants (*Pkd1-CKO*) mice kidneys and livers. The goal is the study of key pathways and cellular components in ADPKD renal and hepatic phenotype (additional information in Material and Methods section) (**Figure 27A**). Mice were sacrifice at postnatal day 30 of age, at this point our orthologous murine model of ADPKD present a well-set polycystic kidney and liver disease with cysts in both the liver and kidney parenchyma. A set of proteins were differentially represented, with p-value < 0.05 and fold change > 2 as cut-off, for both renal and hepatic differential proteomics were obtained. Next, a functional study using String®[189] was performed unmask the extracellular space and extracellular matrix as two of the twenty cellular components more enrichment in our differential proteomics study (**Figure 27B**). In the same way, using Reactome®[190] we found that "Extracellular matrix organization" pathway and specifically " Degradation of the extracellular matrix" was the subpathway with most entities found and total interactors of our significantly differentially proteins set. Interestingly, several MMPs and Fibronectin were direct matches (**Supplemental Figure 10**). Our proteomic study revealed the extracellular region as the most enrichment cellular component in polycystic kidney and livers. Furthermore, genetic expression of MMP is deregulated in renal and hepatic cystogenesis of PKD. Thus, the deregulation of extracellular component is a common feature in ADPKD.

Based on the results of our differential proteomics study, the accumulative percent of extracellular region (extracellular space and extracellular matrix) is >38% and >47% of cellular components in renal and hepatic proteomics, respectively. Thus, we focused on the extracellular region because it contributed most substantially to the total differential proteome in our ADPKD model and we decide to study the role of extracellular matrix in PKD in greater detail. Therefore, we determined whether all MMPs and TIMPs present in mouse are deregulated in orthologous murine models of PKD by real-time quantitative PCR. Gene expression by RT-qPCR of MMPs and their natural inhibitors TIMPs validated the extracellular region deregulation in ADPKD. We have found a global deregulation (upregulation or

downregulation) of MMPs and TIMPs in mutant ADPKD kidney and livers compared to *Wild Type* tissues (**Figure 27C** and **E**). Besides, we also wanted to validate these results in ARPKD, for this propose we use the orthologous murine model *Pkhd1-KO* (*Pkhd1*$^{del3\text{-}4/del3\text{-}4}$) which develops slowly progressive polycystic liver disease. In the same way, expression levels of MMPs and TIMPs were deregulated in polycystic livers compared to *Wild Types* (**Figure 27D** and **F**).

3.2. Marimastat reduces renal cyst growth in ADPKD and inhibits hepatic cystogenesis in PKD

Deregulation of extracellular matrix and MMPs expression may be either functionally significant, and hence a possible therapeutic target, or simply represent an innocuous association of cyst progression. In order to discriminate between the two options, we have studied Marimastat, an MMP inhibitor[193,194], in pre-clinical studies on our orthologous models of PKD as a new possible therapeutic approach.

Firstly, we have administrated Marimastat in different doses (1 to 10 mg/kg) in *Pkd1-CKO* mice for two weeks in order to evaluate the therapeutic efficiency of a MMPs inhibitor in renal and hepatics cystogenesis of ADPKD (**Figure 28A**). Macroscopically we could see a modest effect of Marimastat in total renal volume compared with untreated group mice (**Figure 28B**). In the same way, kidney-weight to body-weight ratio, BUN level and cystic index were reduced in treated groups, but without significant differences (**Figure 28**, **C-E**). However, number of cysts was significant reduced in treated groups (**Figure 28F**). In order to further delve into our data, we have realized a study of origin cystic through specific markers of different parts of nephron by immunofluorescence. Interestingly, we have found that Marimastat causes a specific inhibition of cyst deriving from collecting ducts (DBA positive cysts). In the lowest doses the inhibition is not complete but from the 5 mg/kg and in increasing doses the effect is clear, reaching almost complete inhibition using the 10 mg/kg dose (**Figure 28**, **G** and **H**). In **Figure 28G** we show a total reconstruction of control and treated kidneys where we can see how DBA^{+} cysts turn in “normal tubes” with the Marimastat treatment. Furthermore, we have ruled out a possible effect of Marimastat on the DBA receptor expression by checking its presence treated *Wild Type* with the highest doses (**Figure 28H**). We have not seen any reduction in cysts derived from proximal tubules

(LTL^+) or thick ascending limb of the loop of Henle (THP+) (**Figure 28H** and **Supplemental Figure 11**).

By other hand, we have checked the possible benefit of Marimastat treatment in liver cystogenesis. In *Pkd1-CKO* mouse (experiment design in **Figure 28A**), treated group showed a decrease of hepatic cystogenesis with respect to control group, both in hepatic parenchyma and in cystic bile duct malformations (**Figure 29A**). With respect to liver function, at this age our model not present alterations in ALP and ALT serum levels so we could not observe differences with Marimastat (**Figure 29B**). Instead, the liver to body weight ratio was slightly decreased after Marimastat administration (**Figure 29C**) and, the cystic index and number of cysts were significant reduced in treated group (**Figure 29D**). Based on these results, we wanted to test the effect of Marimastat in *Pkhd1-KO* and ARPKD model for two weeks (**Figure 29E**). After treatment, the livers appeared smaller and with a significant reduction of hepatic biliary and parenchyma cystogenesis (**Figure 29F**). Significantly, ALP serum levels were decreased in treated group in comparison with control one, but not the ALT levels (**Figure 29G**), as well as the liver weight over body weight and hepatic cystic index and number of cysts (**Figure 29I**). Our data suggest that Marimastat causes a marked decrease in the expansion, progression and number of hepatic cysts both in ADPKD and ARPKD.

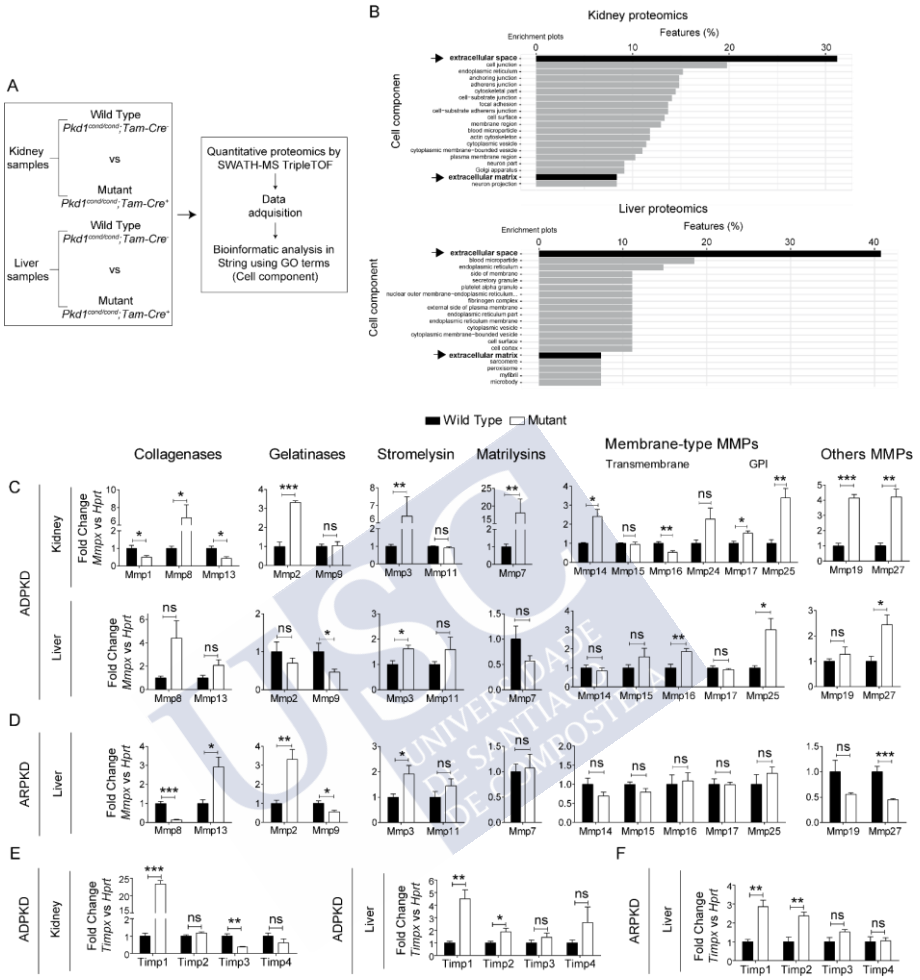

Figure 27. Extracellular matrix organization and MMPs and TIMPs expression is altered in PKD. (A) Representative workflow scheme is showed. A total of three *Wild Type* (*Pkd1*$^{cond/cond}$*;Tam-Cre*$^{-}$) and mutant (*Pkd1*$^{cond/cond}$*;Tam-Cre*$^{+}$) *Pkd1-CKO* mice samples of kidney and liver were analyzed by SWATH-MS. After comparison, we obtained a list of proteins with statistically significant and with two-folds of change. Finally, bioinformatic analysis was performed in String® software using GO terms-cellular component with the lists of significant proteins (B). Graphs represent the twenty enrichment plots of cellular component (based GO terms) for kidney (Up) and liver (Down) proteomics. The plots extracellular space and extracellular matrix are highlighted with black graphs and black arrows. (C-F) RT-qPCRs of all MMPs (C) and TIMPs (E) present in mouse in kidney and liver in ADPKD: Wild Types (n=4) and mutants (n=5) mice; and of all MMPs (D) and TIMPs (F) present in mouse in liver in ARPKD: Wild Types (C57BL/6 mouse n=5) and mutants (*Pkhd1*$^{del3\text{-}4/del3\text{-}4}$ n=6). Metalloproteinases were classified in families according to their biological effect and group of substrates. *Hprt* was used as housekeeping. Bars represent means±SEM. Two tail T-student; not significant($p \geq 0.05$), *$p<0.05$, **$p<0.01$, *** $p<0.001$.

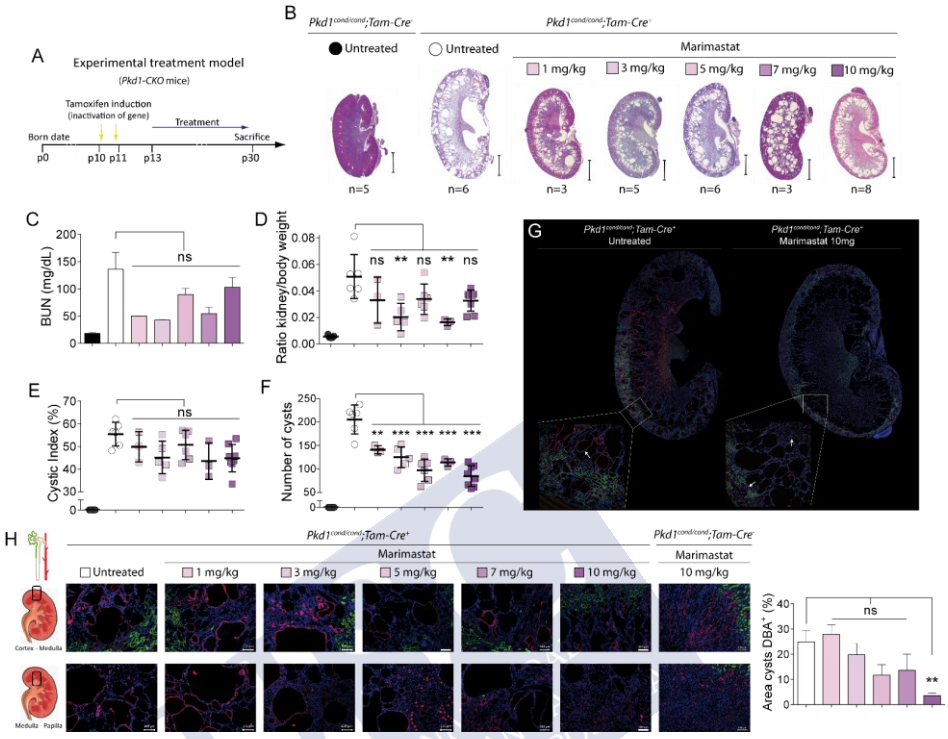

Figure 28. Marimastat improves moderately cystic renal phenotype and specifically inhibits cysts from collecting ducts of nephron. (A) Schematic view of the experimental design. *Pkd1-CKO* mice were injected with a single dose of Tamoxifen in two consecutive days (p10 and p11 consecutively), treatment started at p13 and finished in the sacrifice point (p30) where tissues, samples and data were recollected. p(x): postnatal day. (B) Representative images of sagittal kidney slides control and treated groups. Scale bar, 2mm. The n listed under kidney slides represents the number of mice analyzed for group. (C-D) Values of renal function based on BUN (C) and kidney weight-to-body weight ratio (D). (E-F) Cystic index (E) and total number of cysts (D) of all groups. (G) Reconstruction of immunofluorescence of full kidneys, untreated and treated Marimastat 10 mg/kg, marking proximal tubules in green (LTL) and collecting ducts (DBA) in red. Marimastat inhibits cystogenesis deriving from collecting duct (cysts DBA^+, marked in red). White boxes represent a magnification of representative zones. Arrows indicates DBA^+ cysts in untreated sample (left) and DBA^+ tubes in Marimastat treated kidney (right). (H) Left: immunofluorescences in renal cortex-medulla (up) and medulla-papilla (down). Green marks the cysts from proximal tubules and red marks cyst that derived from collecting ducts. Right: quantification of immunofluorescence DBA^+ cysts. Marimastat reduces DBA^+ cysts from 5mg dose and significantly with 10mg dose. Scale bar, 100µm. Bars represent means±SEM in all cases. $P<0.05$ by two-way ANOVA was considered as significative result. ns: not significant ($p\geq0.05$), * $p<0.05$, ** $p<0.01$, *** $p<0.001$.

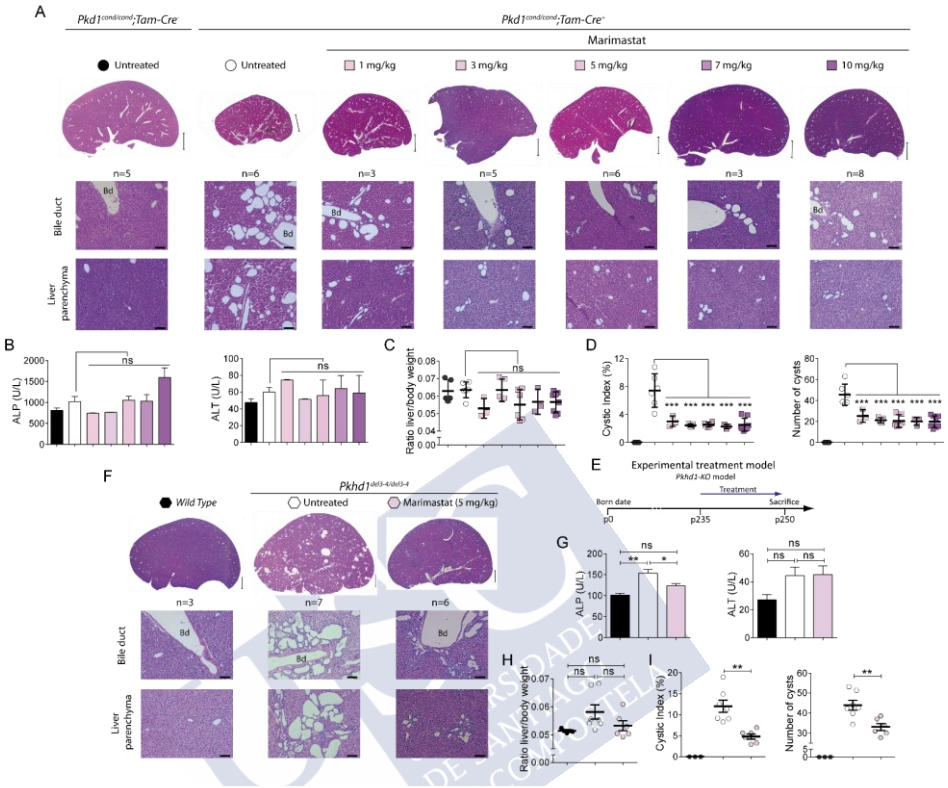

Figure 29. Marimastat inhibits hepatic cystogenesis in PKD. (A) Representative images of Hematoxylin-Eosin (HE) stained from livers of *Pkd1-CKO* mouse untreated and treated. Images of biggest lobule slide (upper panel), and cysts from hepatic parenchyma and bile duct (lower panel) are exposed, showing that Marimastat treatment inhibits hepatic cystogenesis in ADPKD. Scale bars, 2mm (A) 50µm (B). (B) ALP (left) and ALT (right) values of serum hepatic function. (E) Ratio of liver weight to total body weight. (D) Hepatic cystic index (left) and number of cysts (right) are decreased with Marimastat treatment. (E) Scheme of treatment model in *Pkhd1-KO model*. Mice are growing until postnatal day 235, when Marimastat treatment starts for two weeks. The sacrifice point was p250. p(x): postnatal day. (F) Representative images of macroscopic liver lobule (upper panel) and microscopic images of cyst from hepatic parenchyma and bile duct (lower panel). Livers were stained with hematoxylin-eosin. Scale bars, 2mm (upper panel) 50µm (lower panel). (G) ALP (left) and ALT (right) values of serum hepatic function. (H) Ratio of liver weight to total body weight. (I) Cystic index (left) was significant decreased in treated group, as well as number of cysts (right). Bars represent means±SEM in all cases. Two-way ANOVA was used and a value of $P<0.05$ was considered as significative result. ns: not significant ($p\geq0.05$), * $p<0.05$, ** $p<0.01$, *** $p<0.001$.

3.3. Marimastat restores MMPs expression

As we have seen, in polycystic kidney and liver disease gene expression of MMPs is deregulated and can be a new possible therapeutic approach. To further evaluate the effect of Marimastat MMPs signaling pathway, quantitative PCR was realized to evaluate gene expression of all MMPs and their endogenous natural inhibitors, TIMPs. In ADPKD, Marimastat restores gene expression of *Mmp8*, *Mmp2*, *Mmp3*, *Mmp17*, *Mmp25* and *Mmp19* in kidney, while in liver restores expression of *Mmp9*, *Mmp7*, *Mmp16*, *Mmp25* and *Mm27* (**Figure 30A**). With respect hepatic cystogenesis in ARPKD, *Mmp13*, *Mmp2*, *Mmp9* and *Mmp27* were restored after Marimastat treatment (**Figure 30B**). In our study we have not found deregulation of several MMPs in PKD (**Figure 27**, **C** and **D**), which does not change with treatment either. In that point, it must be important to point that the most of dysregulated MMPs restored their expression to normal levels with Marimastat treatment, an in some cases a trend towards restoration. On the other hand, Marimastat inhibits *Timp1* and *Timp2* upregulation in ADPKD kidneys and ARPKD livers, respectively. Interestingly, we have not observed any transcriptional changes in hepatic cystogenesis in ADPKD (**Figure 30C**).

3.4. Marimastat decreases interstitial fibrosis

We next investigated the effects of Marimastat, and restoration of MMPs expression, in fibrosis rated to PKD. The role of fibrosis in progression of PKD, as well as its therapeutic potential, was widely studied[93,100,195]. Our data showed that treatment with Marimastat significantly reduced the markers of fibrosis α-SMA and fibronectin by immunohistochemistry and collagen levels by Masson's trichrome staining in ADPKD kidneys (**Figure 31**, **A** and **B**). In the same way, mutant kidneys treated with Marimastat presented lower *Ctgf* expression compared whit matched controls (**Figure 31C**). By contrast, we have not found changes in *Tgfβ* and *Col1a1* gene expression (**Supplemental Figure 12A**). Several cytokines, such as interleukin-6 and -8 (IL-6 and IL-8) are present in high levels in renal[117,118] and hepatic[119,120] cystic fluids. Besides, in cell cultures the presence of inhibitor for IL-6 and IL-8 reduced baseline MMP hyperactivity in polycystic cholangiocytes[74]. Our data showed that *Il6* and *Cxcl1* (*Il-8* homolog in mouse) are upregulated in polycystic kidneys. Furthermore,

with Marimastat treatment the expression of *Cxcl1* was decreased, but no changes in expression of *Il6* were observed (**Figure 31D**).

In the same way, we also assed the hepatic fibrosis related to cystogenesis in ADPKD and ARPKD treated with Marimastat. Firstly, we could observe a significant reduction of α-SMA, fibronectin and a reduction of Masson's trichrome stain with Marimastat treatment in ADPKD orthologous mouse model (**Figure 32**, **A** and **B**). Expression of *Ctgf* was lower in treated mutant group but not significantly (**Figure 32C**). Contrary to the kidney, *Cxcl1* and *Il6* expression was not affected by treatment (**Figure 32D**). Finally, the hepatic fibrosis related to ARPKD cystogenesis was significant lower immunohistochemistry of α-SMA and fibronectin, and Masson's trichrome staining in treated group in comparison with its control (**Figure 32**, **E** and **F**). Additionally, the levels of *Ctgf* by RT-qPCR decreased with treatment (**Figure 32G**). Same that in kidney, expression levels of *Col1a1* and *Tgfβ* were not altered (**Supplemental Figure 12**, **A** and **B**). Interestingly, our data indicate a downregulation of *Cxcl1* and *Il-6* in our ARPKD model, and a modulation of *Cxcl1* expression by Marimastat treatment (**Figure 32H**).

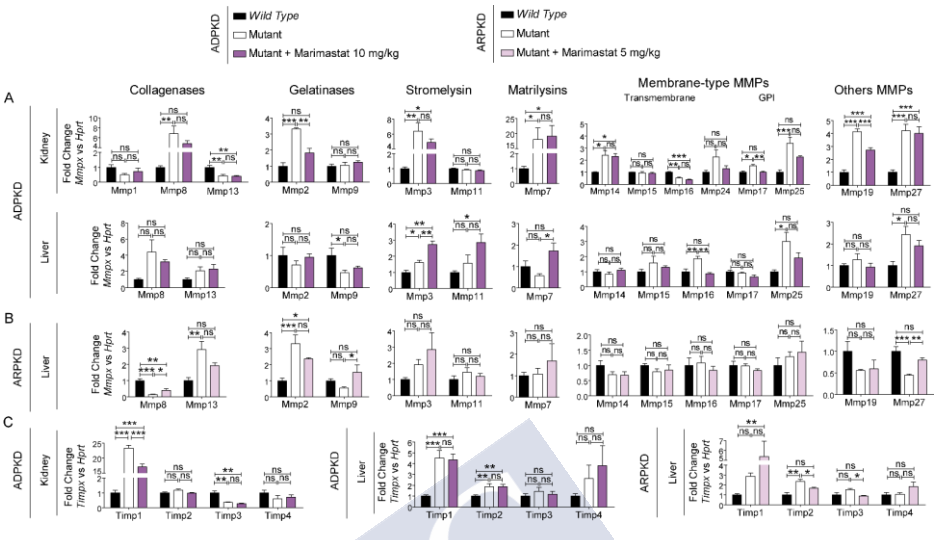

Figure 30. MMPs expression deregulation is restored with Marimastat. Genetic expression of all MMPs and TIMPs present in mice were checked in control and treated groups. RT-PCRs of MMPs (A) and TIMPs (C) in ADPKD kidney (up and left, respectively) and liver (down and right, respectively): *Wild Types* (*Pkd1*$^{cond/cond}$*;Tam-Cre*$^{-}$ n=4), mutants (*Pkd1*$^{cond/cond}$*;Tam-Cre*$^{+}$ n=5) and mutants treated (*Pkd1*$^{cond/cond}$*;Tam-Cre*$^{+}$ n=5); and RT-qPCRs of MMPs (B) and TIMPs (D) in ARPKD liver: *Wild Types* (C57BL/6 mouse; n=5), mutants (*Pkhd1*$^{del3\text{-}4/del\text{-}4}$ n=6) and mutants treated (*Pkhd1*$^{del3\text{-}4/del3\text{-}4}$ n=6). Metalloproteinases were classified in families according to their biological effect and group of substrates into collagenases, gellatinases, stromelysins, matrilysins, membrane associated (transmembrane or GPI anchored) and others. *Hprt* gene was used as housekeeping. All results are represented as means±SEM. Two-way ANOVA was used and a value of P<0.05 was considered significant. ns: not significant (p≥0.05), * p<0.05, ** p<0.01, *** p<0.001.

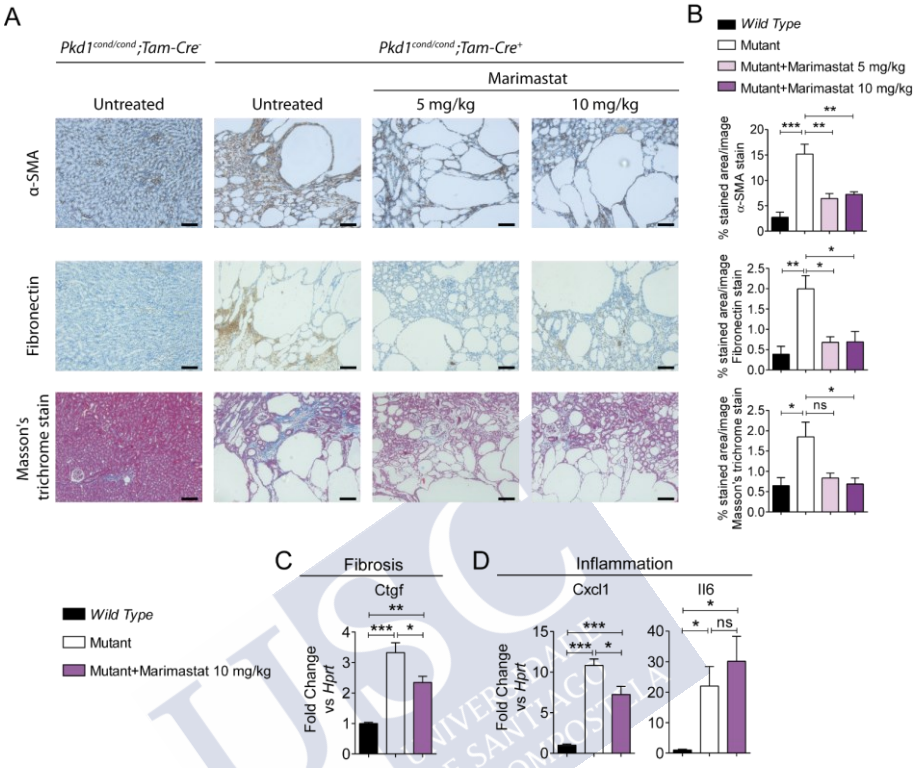

Figure 31. Marimastat slows renal fibrotic progression in ADPKD. (A-B) Immunocytochemical analysis (A) and staining area quantification (B) of α-SMA (up), fibronectin (center) and Masson trichrome stain (down) in kidney slides of *Wild Type* (*Pkd1*$^{cond/cond}$*;Tam-Cre*$^{-}$), mutant (*Pkd1*$^{cond/cond}$*;Tam-Cre*$^{+}$) and treated mutant (5 and 10 mg/kg) groups. N=3 slides were used per group. Scale bars: 100μm. (C-D) RT-qPCR of fibrotic marker Connective tissue growth factor (*Ctgf*) (C), and Chemokine (C-X-C motif) ligand 1 (*Cxcl1*; Interleukin-8 mice homolog) and interleukin 6 (*Il-6*) (D), two markers of inflammation, in *Wild Types* (*Pkd1*$^{cond/cond}$*;Tam-Cre*$^{-}$ n=4), Mutants (*Pkd1*$^{cond/cond}$*;Tam-Cre*$^{-}$ n=5) and Mutants treated with Marimastat 10mg/kg (*Pkd1*$^{cond/cond}$*;Tam-Cre*$^{+}$ n=5). *Hprt* gene was used as housekeeping. Bars represent means±SEM. Two-way ANOVA was used and a value of P<0.05 was considered significant. ns: not significant (p≥0.05), * p<0.05, ** p<0.01, *** p<0.001.

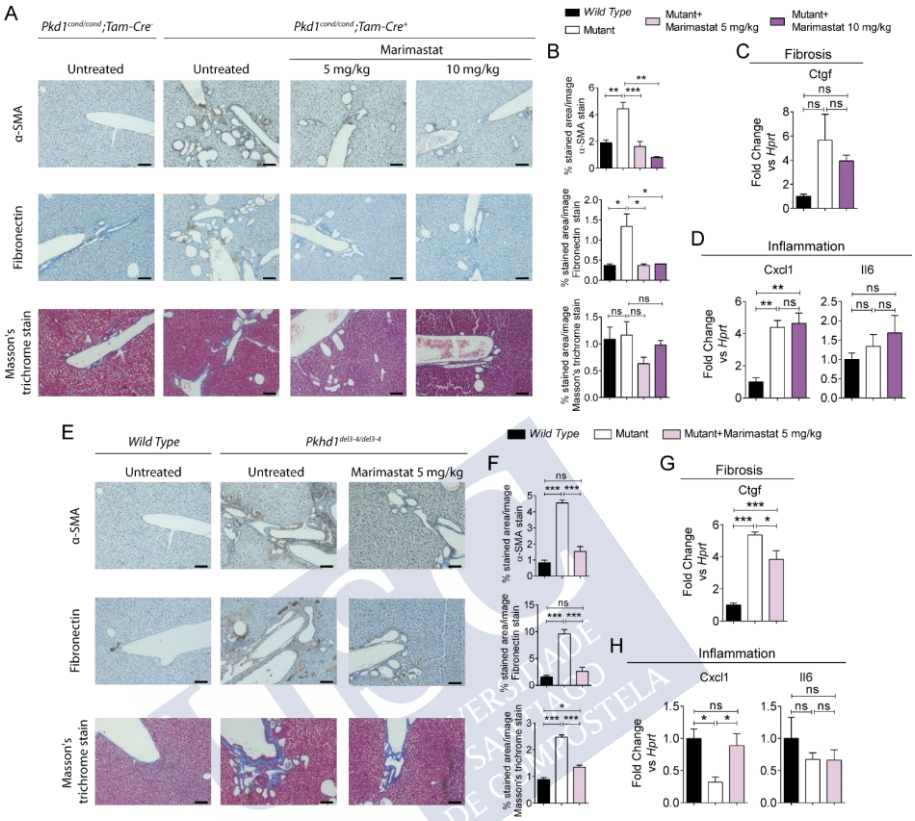

Figure 32. Marimastat ameliorates hepatic fibrosis in PKD. (A-B) Immunocytochemical analysis (A) and staining area quantification (B) of α-SMA (up), fibronectin (center) and Masson trichrome stain (down) in liver slides of *Wild Type* (*Pkd1*$^{cond/cond}$*;Tam-Cre*$^{-}$), mutant (*Pkd1*$^{cond/cond}$*;Tam-Cre*$^{+}$) and treated mutant (5 and 10 mg/kg) groups. (C-D) RT-qPCR of connective tissue growth factor (*Ctgf*) (C), a marker of fibrosis, and the two inflammation markers Chemokine (C-X-C motif) ligand 1 (*Cxcl1*; Interleukin-8 mice homolog) and interleukin-6 (*Il-6*) (D), in *Wild Types* (*Pkd1*$^{cond/con}$*; Tam-Cre*$^{-}$ n=4), Mutants (*Pkd1*$^{cond/cond}$*;Tam-Cre*$^{+}$ n=5) and Mutants treated with Marimastat 10mg/kg (n=5). (E-F) Immunohistochemistry (E) and staining area quantification (F) of α-SMA (up), fibronectin (center) and Masson trichrome stain (down) in liver slides of *Wild Type* (C57BL/6 mouse), mutant (*Pkhd1*$^{del3-4/del3-4}$) and treated mutant (5 mg/kg) groups. (G-H) Gene expression analysis by RT-qPCR of *Ctgf* (G), and *Cxcl1* and *Il-6* (H), in C57BL/6 mouse (n=5), mutant (*Pkhd1*$^{del3-4/del3-4}$ n=6) and Marimastat 5mg/kg mutant (n=6). For immunohistochemistry's: n=3 slides were used per group and scale bars represents 100μm. For RT-qPCRs: *Hprt* gene was used as housekeeping. Bars represent means±SEM. Two-way ANOVA was used and a value of P<0.05 was considered significant. ns: not significant (p≥0.05), * p<0.05, ** p<0.01, *** p<0.001.

3.5. Combination treatment: Marimastat plus Tolvaptan

Tolvaptan is the only approved treatment up to date for ADPKD due to its beneficial effect in slowing the progression of disease[196,197]. Therefore, we also realized a preclinical study in our *Pkd1-CKO* mice combining Marimastat and Tolvaptan to evaluate the additive benefit of both therapies together. The experimental design is the same performed to Marimastat-single study (**Figure 28A**). As we have previously pointed out, kidneys treated with Marimastat exhibited an improvement in kidney volume progression but Marimastat plus Tolvaptan treated mice showed a clear and strong reduction of progression of polycystic disease and restoration of renal function (**Figure 33**, **A** and **B**). In relation with the macroscopic observation, the ratio of kidney weight to body weight were significant reduced with combined therapy, as well as hepatic cystic index and number of cysts (**Figure 33**, **C** and **D**). Interestingly, Marimastat plus Tolvaptan showed a synergist effect by reducing number of renal cysts (**Figure 33D**).

Our data demonstrates the effectiveness of Marimastat to inhibit the hepatic cystogenesis in PKD. Next, we wanted to evaluate this efficacy also in combination with Tolvaptan. In liver cystogenesis related to ADPKD, our data have showed a protective effect of combination between Marimastat and Tolvaptan (**Figure 34A**). Nonetheless, we did not see any differences in hepatic function and liver weight to body weight ratio (**Figure 34**, **B** and **C**). It is important to keep in mind that we did not found differences between *Wild Type* and mutant groups, mainly due to mild phenotype of the model at the sacrifice point. On the contrary, cystic index and the number of cysts were significantly reduced with Marimastat plus Tolvaptan (**Figure 34D**). Due to the presence of V2R receptors (Tolvaptan target) in liver[198], we would want to test the possible effect of Tolvaptan in liver. Our data did not show significant differences, with exception of number of cysts, between mutant group and Tolvaptan treated group. Interestingly, a modest restoration of hepatic function and cystic index parameters was appreciated (**Supplemental Figure 13**). In the same way, Marimastat plus Tolvaptan treatment group showed a clear reduction in hepatic cystogenesis in *Pkhd1-KO* mice model (**Figure 34E**). However, our data did not show improvement in liver function after treatment (**Figure 34F**). Furthermore, we could observe lower ratio of liver to body weight and hepatic cystic index (**Figure 34**, **G** and **H**). With respect to number of cysts, our data have showed a reduction

but without significant differences (**Figure 34H**, right panel). Finally, the different treatments did not have a macroscopic damage or effect in the *Wild Type* individuals (**Supplemental Figure 15**).

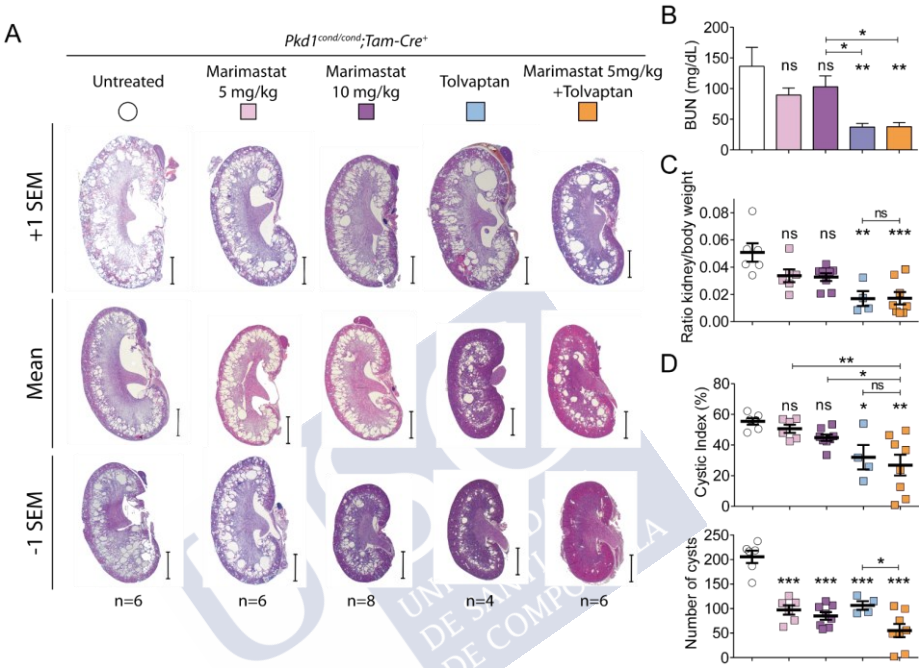

Figure 33. Tolvaptan in combination with Marimastat inhibits renal and hepatic cystogenesis and restores renal function. (A) HE sagittal cross-sections of kidneys from un- and treated groups of *Pkd1*$^{cond/cond}$*;Tam-Cre* mouse. Three kidneys, -1SEM, mean and +1SEM, are shown per group. Marimastat plus Tolvaptan showed a synergistic effect reducing cyst growth of kidney. (B-E) Furthermore, BUN (B), the ratio of kidney weight versus body weight (C), renal cystic index and total number of cysts (D) were reduced with both treatments. Scale bar, 2mm (magnification images) and 100µm (microscopic sections). The n listed under kidney and liver slides represents the number of mice analyzed for group. For all cases: bars represent means±SEM and two-way ANOVA was used and a value of $P<0.05$ was considered significant. ns: not significant ($p\geq0.05$), * $p<0.05$, ** $p<0.01$, *** $p<0.001$.

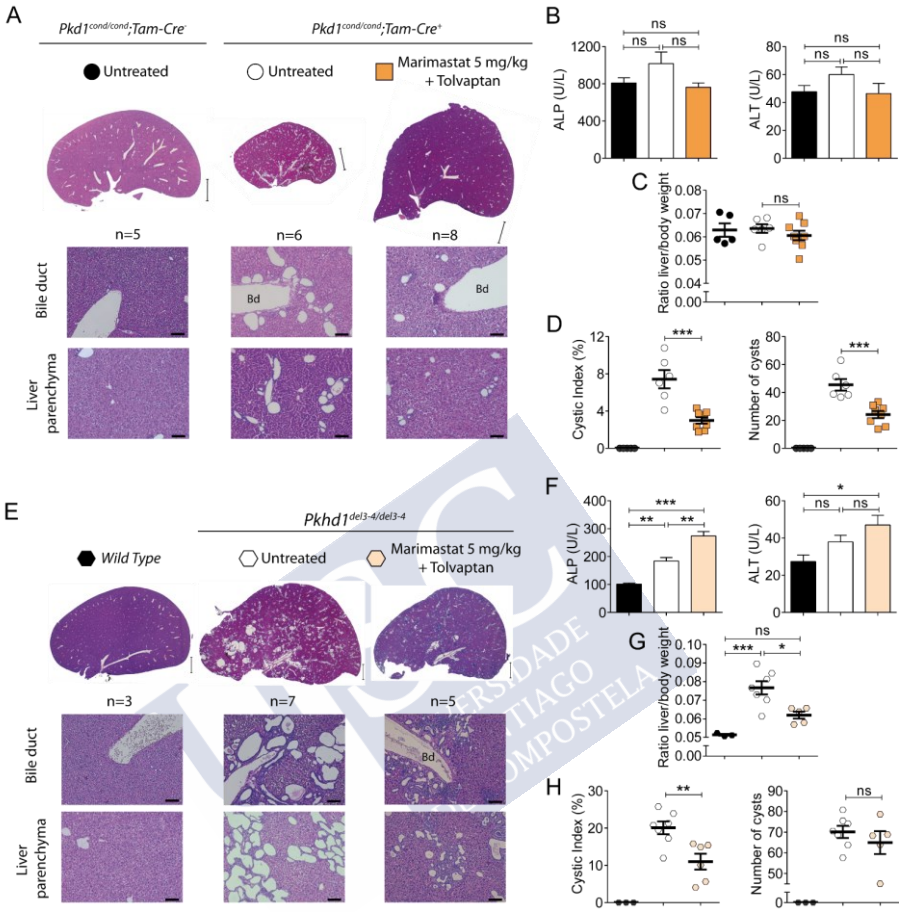

Figure 34. Marimastat plus Tolvaptan showed efficacy inhibiting hepatic cystogenesis in two orthologous PKD models. (A) Representative HE liver slides (upper panel) in ADPKD model *Pkd1*$^{cond/cond}$*;Tam-Cre* and representative sections of bile duct and hepatic parenchyma cysts (lower panel); most representative *Wild Type* (*Pkd1*$^{cond/cond}$*;Tam-Cre*$^{-}$) and mutant (*Pkd1*$^{cond/cond}$*;Tam-Cre*$^{+}$) untreated, and Marimastat plus Tolvaptan treated mutant are shown. (B) Hepatic serum values of ALP (left) and ALT (right). (C) Ratio of liver weight to body weight. (D) Cystic index (left) and total number of cysts (right). (E) Representative macroscopic images from livers *Wild types* (C57BL/6 mouse) and mutant (*Pkhd1*$^{del3-4/del3-4}$) untreated and Marimastat plus Tolvaptan treated mutant groups (upper panel). Images of representative sections of bile duct and parenchyma cysts (lower panel). (F) Hepatic function based in serum values of ALP (left) and ALT (right). (G) Ratio of live to body weight. (H) Cystic index (left) and total number of cysts (right). Scale bar, 2mm (magnification images) and 100µm (microscopic sections). The n listed under kidney and liver slides represents the number of mice analyzed for group. For all cases: bars represent means±SEM and two-way ANOVA was used and a value of P<0.05 was considered significant. ns: not significant (p≥0.05), * p<0.05, ** p<0.01, *** p<0.001.

4. CHAPTER 4

TWEAK signaling pathway blockade slows cyst growth and disease progression in Autosomal Dominant Polycystic Kidney Disease

4.1. Data mining identification of Fn14 as overexpressed in polycystic kidney disease

Since TNF superfamily members and their receptors are key mediators of inflammation that also regulate cell proliferation and cell death, polycystic kidney disease transcriptomics databases were searched for TNFSF and TNFRSF members which were differentially expressed and their expression increased in polycystic kidney disease. In available microarray datasets of ADPKD in mouse, rats, humans we found that Fn14 (TNFRSF12a) and/or TWEAK (TNFSF12) are the only genes of the TNF superfamily encoding a cytokine/ligand pair that were differentially expressed and increased in the three species (**Table 6**)[199–203]. Polycystic kidney disease transcriptomics databases were searched for TNFSF and TNFRSF members which were differentially expressed, and their expression increased in polycystic kidney disease through a search of GEO and PubMed. A p value of $p<0.05$ was considered significant for screening purposes since a high sensitivity was desired. Thus, Fn14 (5 datasets) and/or TWEAK (3 datasets) were increased in 6 datasets, while TNFR1 or TNFR2 were increased in 4 datasets from the 3 species, but the gene encoding the cytokine TNF was not overexpressed. Interestingly, a role for TNF in polycystic kidney disease has already been characterized[204]. No other TNFRSF/TNFSF gene was upregulated in two different species. These findings suggest that TWEAK/Fn14 axis could play a role in ADPKD.

Table 6. Table 1. Differentially expressed TNFSF and TNFRSF genes with increased expression in polycystic kidney disease. Transcriptomics databases were searched in PUBMED.

Species	Model	Gene	FC	p-value	Ref. (PMID)
Mouse	PKD1 -/- embryonic kidneys at days 14.5 vs days 17.5 (GSE24352)	***Fn14***	**2.85**	**0.0008**	21518438[199]
	L3-/L3- (PKD mice) vs WT littermates. 3 weeks old	***Fn14***	**3.08**	**0.00**	19099603[200]
		Tnfrsf11B	2.29	0.04	
		Tnfrsf19	1.95	0.04	
	L3-/L3- (PKD mice) vs WT littermates. 3.5 weeks old	***Fn14***	**1.95**	**0.01**	19099603[200]
		Tnfrsf11B	1.77	0.09	
		Tnfrsf19	1.56	0.03	
		Tnfr1	1.55	0.02	
Rat	Homozygous unaffected (+/+) and heterozygous affected (cy/+) Han:SPRD rats. 36 days old	***Fn14***	**2.32**	**0.0001**	23326503[201]
		Tnfr1	1.59	0.00	
		Tnfrsf9	1.40	0.0000	
		Tweak	**1.22**	**0.0000**	
		Tnfr2	1.11	0.0049	
	Homozygous unaffected (+/+) and heterozygous affected (cy/+) Han:SPRD rats. 36 days old	***Fn14***	**3.07**	**0.0018**	19102782[202]
		Tnfr1	1.99	0.00	
		Tweak	**1.32**	**0.0005**	
Human	Healthy tissue from PKD patients vs samples with small cysts (GSE7869)	*TNFR2*	2.28	3.07E-03	31907669[203]
		TNFSF13B	2.22	7.40E-03	
		TNFR1	2.07	2.29E-03	
		TNFRSF10B	1.99	4.27E-03	
		TWEAK	**1.79**	**1.51E-03**	
		TNFSF14	1.40	4.81E-02	
		TNFSF9	1.36	2.43E-02	

4.2. Axis TWEAK/Fn14 are upregulated in ADPKD

Using an orthologous model of ADPKD (*Pkd1*$^{cond/cond}$*;Tam-Cre*[68,70]), we analyzed the gene expression and protein levels of Fn14 (TWEAK receptor) at two different time points (postnatal days 30 and 45). Mutant kidney had higher Fn14 gene expression (15-fold) than corresponding controls, as assessed by real-time quantitative PCR (**Figure 35A**). In the same way, Fn14 protein levels were also upregulated in ADPKD mutant kidney (**Figure 35B**, **Supplemental Figure 14**, **A** and **B**) and Fn14 staining located along the cyst epithelium (**Figure 35D**). In addition, Fn14 was analyzed in there further models to strengthen this concept. Gene expression and protein levels of Fn14 were higher in mutant *Pkd1*$^{cond/cond}$*Tam-Cre* mice with slowly progressive ADPKD (**Supplemental Figure 16**, **A** and **B**), in *Pkd1*$^{cond/cond}$*Tam-KSP-Cre* ADPKD mice with a kidney epithelial cell promoter (**Supplemental Figure 16**, **C** and **D**) and in *Pkd1*^{cond}*;Pax8;TET-OCre+* ADPKD mice with a tubular-cell-specific promoter (**Supplemental Figure 16**, **E** and **F**). Serum murine TWEAK levels we assessed by ELISA. As was the case for human ADPKD, no statistically significant differences were observed in serum in mutant mice (**Figure 15C**). Thus, we have found overexpression of Fn14 receptor in cystic kidneys of several animal models of ADPKD and it was specifically located in renal cyst epithelium.

Next, we determined status of the Fn14/TWEAK axis in human ADPKD. TWEAK was assessed by ELISA in cystic fluid, urine and plasma. Cystic fluid TWEAK levels were higher than in plasma, suggesting local production or secretion in multiple cysts from three patients with ADPKD (Figure 1E). Thus, although cystic fluid contents were heterogeneous, 16/22 (72.72%) cysts had TWEAK levels above the mean level of TWEAK in plasma of healthy subjects. Similarly, urinary TWEAK levels were higher in urine from ADPKD patients than from controls (**Figure 35F**). By contrast, no statistically significant differences were observed in plasma TWEAK, suggesting local TWEAK production in the kidneys (**Figure 35G**). Immunohistochemistry disclosed Fn14 staining along the cyst epithelium (located in a perinuclear region), thus placing receptor

expression at the site of TWEAK presence (**Figure 35H**, **Supplemental Figure 14C**).

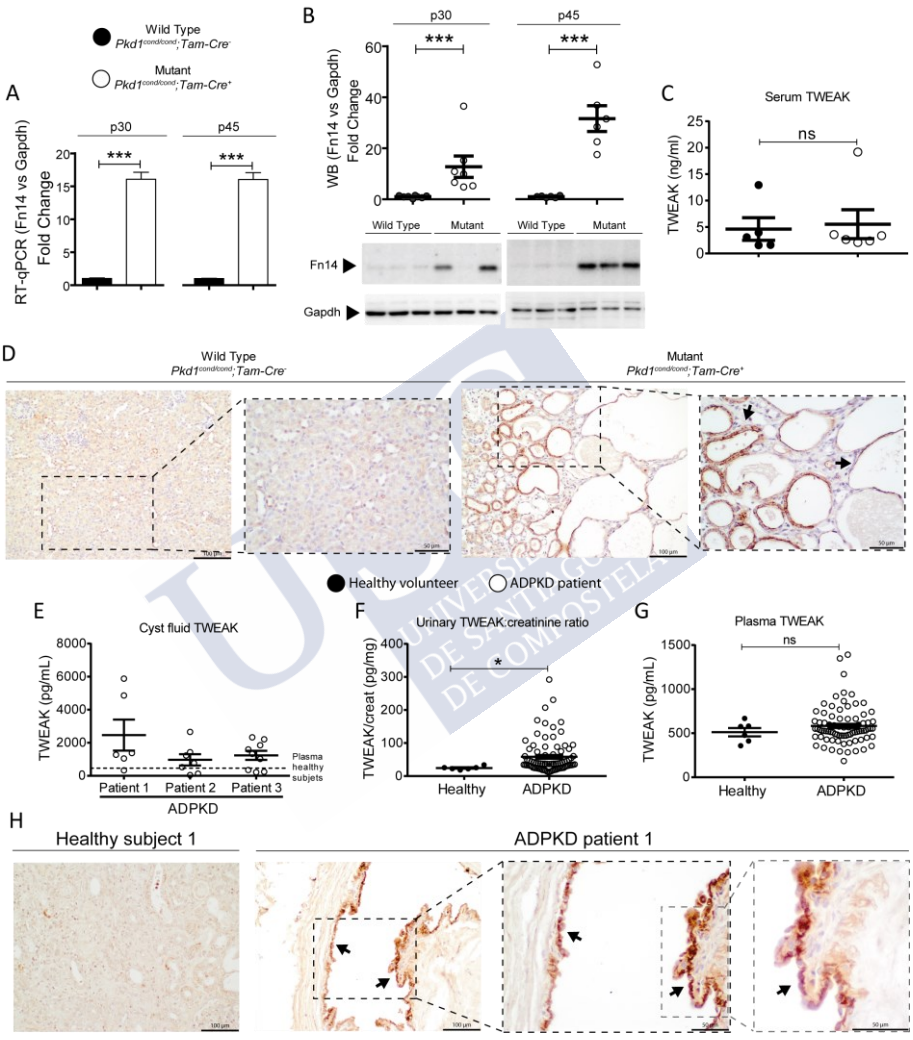

Figure 35. TWEAK and its receptor Fn14 are upregulated in ADPKD. Fn14 is upregulated in *Pkd1*$^{cond/cond}$*Tam-Cre* ADPKD orthologous mice (mutant), *Pkd1* inactivated on postnatal day 10-11. (A) *Fn14* gene expression assessed by real-time quantitative PCR (RT-qPCR) in *Wild Type* (n=6) and Mutant samples (n=6) of kidney at two different time points, postnatal days 30 and 45 (p30 and p45). *Gapdh* was used as housekeeping control. (B) Protein level assessed by Western Blot in Wild Type (n=6) and Mutant samples (n=6) of kidney at two different time points, postnatal days 30 and 45 (p30 and p45). Upper panel; densitometry represented as fold change (*Wild Type* versus Mutant) and normalized with the housekeeping protein GAPDH. Lower panel; representative blots (additional information in Supplemental Figure 1). (C) No significant differences TWEAK cytokine levels were observed in PKD mouse serum by ELISA (D) Fn14 immunohistochemistry in mouse samples at p45 shown a specific staining in cyst epithelium (black arrows). (E-G) TWEAK was assessed by ELISA in renal cyst fluid, urine and plasma from ADPKD patients and healthy volunteers. (E) TWEAK concentration was higher in most individual cyst fluids from ADPKD patient than in plasma of healthy volunteers. (F) The urinary TWEAK: creatinine ratio is higher in ADPKD patients than in healthy volunteers. (G) No significant differences were observed in plasma TWEAK between ADPKD patients and healthy volunteers. (H) FN14 immunohistochemistry in human ADPKD (n=3) (x200 magnification) disclosed staining of the cyst epithelium (black arrows). pX: postnatal day X. Bars represent means ± SEM. ns: not significant ($p \geq 0.05$), * $p<0.05$, ** $p<0.01$, *** $p<0.001$.

4.3. TWEAK promotes cystogenesis and cyst progression in an orthologous model of ADPKD

Previous studies have shown that early inactivation of the *Pkd1* gene (before p14) triggers a prominent polycystic disease (cystic window), while inactivation after p14 does not show cyst formation until 5 months after inactivation, with a mild phenotype (non-cystic window). [70,147]. Thus, in APDKD there is a critical developmental window for the formation of cystogenesis. We studied the role of TWEAK in ADPKD in both developmental windows, cystic and non-cystic windows, by administering tamoxifen to inactive *Pkd1* at different time points in order to study the role of TWEAK in ADPKD (**Supplemental Figure 17**).

4.3.1. TWEAK induces cystogenesis in the non-cystic window in *Pkd1* deficient mice.

In a first study, we have administered TWEAK in the non-cystic window for two weeks (Supplemental Figure 3A). Interestingly, in mutant mice (*Pkd1*$^{cond/cond}$*;Tam-Cre*$^{+}$) TWEAK treatment induced cystogenesis (**Figure 36A**). This cystogenesis is focal and does not appear throughout the parenchyma, so it is not associated with increased kidney volume. In this regard, renal function and the kidney to body weight ratio were similar in control and TWEAK-treated group (**Figure 36**, **B** and **C**). However, TWEAK significantly increased the cystic index and the total of number of cysts (**Figure 36**, **D** and **E**). Using immunofluorescence for specific nephron markers, we characterized the location of TWEAK-induced focal cystogenesis. Most cysts had collecting duct origin (DBA^{+}) (**Figure 36F**, Lower panel). Cysts also originated from the thick ascending limb of the loop of Henle (THP^{+}) (**Figure 36F**, Center), as well as from dilated proximal tubules (LTL^{+}) (**Figure 36F**, Upper panel). Our results have demonstrated that in a context of *Pkd1* loss, but without a spontaneous cystic phenotype, it is possible to induce cystogenesis by a pro-inflammatory environment resulting from TWEAK administration.

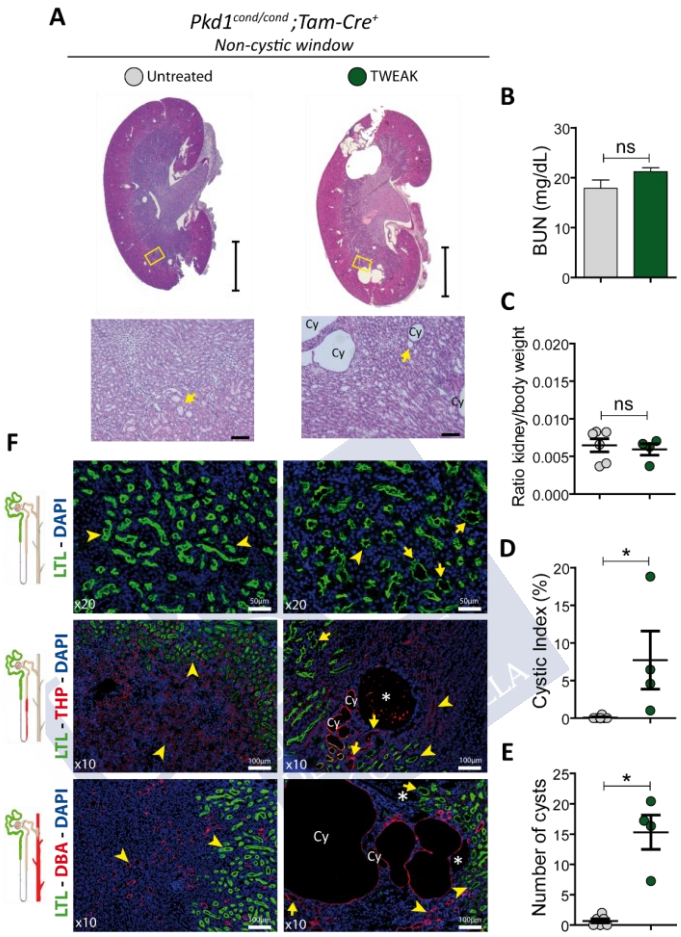

Figure 36. TWEAK induces cyst formation in the non-cystic developmental window of *Pkd1* deficiency. (A) Representative Hematoxylin-Eosin stained kidney sections from TWEAK (n=4) and control (n=6) mice at p30, schematic representation of the experimental design in **Supplemental Figure 17A.** Several cysts with a focal distribution are observed in TWEAK-stimulated kidney (Cy). Arrows represent dilated tubules. Scale bars: 2 mm (upper panel); 100 µm (lower panel). In this developmental window, renal function assessed as Blood Urea Nitrogen (BUN) (B) and the kidney/body weight ratio (C) do not change significantly. By contrast, TWEAK increased the cystic index (D) and the number of cysts (E). (F) Immunofluorescence of specific nephron markers from proximal tubule (LTL, Lotus Tetragonolobus Lectin. Green, upper panel), ascending limb of the loop of Henle (THP, Tamm-Horsfall Protein. Red, center) and collecting duct (DBA, Dolichos Biflorus Agglutinin. Red, lower panel). Cy: cyst; * cyst without specific marking; yellow arrow: dilated tubule; yellow arrowhead: tubule. Scale bars: 50 µm (upper panel) and 100 µm (center and lower panel). pX: postnatal day X. Bars represent means±SEM. ns: not significant; * $p<0.05$.

4.3.2. TWEAK promotes cystogenesis in the cystic window in *Pkd1* deficient mice.

Next, we tested the impact of TWEAK in short-, medium- and long-term models. In the short-term model, TWEAK was administered before (p8-p10) inducing *Pkd1* deletion by tamoxifen in the cystic window (p10-p11) (**Supplemental Figure 17B**). This model is characterized by the spontaneous development of kidney cysts in mutant mice. Kidneys from TWEAK-exposed mice appeared larger macroscopically than control kidneys (**Figure 37A**). We have not found significant difference in renal function (**Figure 37B**), either in kidney to body weight ratio or number of cysts, although there was a slight numerical increase of the two later parameters (**Figure 37, C** and **E**). Importantly, the cystic index was significantly higher in TWEAK-group mice (**Figure 37D**). No differences in cyst origin were observed between control and TWEAK group (**Supplemental Figure 18**).

These results suggest a possible pro-cystogenesis role of TWEAK that may have not become fully evident because of a short follow-up. To confirm the pro-cystogenesis role of TWEAK, we developed two longer models of TWEAK administration in the context of *Pkd1* loss during the cystic window, with readout at p30 (medium-term) or p45 (long-term) (**Supplemental Figure 17C**). The kidney cyst readout at postnatal day p30, results were not conclusive (data not shown) so this was considered an early time point and used to explore cellular and molecular mechanisms involved (see below). By contrast at postnatal day 45 TWEAK aggravates cyst progression (**Figure 38A**), resulting in decreased renal function characterized by higher BUN levels (**Figure 38B**), and increased the kidney to body weight ratio (**Figure 38C**). Although macroscopically the kidneys from control and TWEAK-treated mice appeared to be the same size (**Figure 38A**), it is important note that the total weight of TWEAK mice was significantly lower (**Figure 38G**, **Supplemental Figure 19**). Additionally, TWEAK also increased the renal cystic index and number of cysts (**Figure 38**, **D** and **E**). Finally, TWEAK-exposed mice had lower survival than controls (67% vs 75%, scarified at p45) (**Figure 38F**). By contrast to *Pkd1* deficient mice, no apparent kidney damage was observed in TWEAK-exposed *Wild Type* mice (**Supplemental Figure 20**).

4.3.3. TWEAK promotes inflammation in macrophages and epithelial cells.

To complete our *in vivo* findings, we performed cell culture experiments to strengthen the concept that TWEAK promotes an inflammatory response in cell types relevant for ADPKD. Cultured *Wild Type* macrophages (BMDM) and tubular epithelial cells (MCT) were stimulated with TWEAK for 3h. TWEAK promoted an inflammatory response in both cellular types, as assessed by *Mcp1*, RANTES and *Il-6* gene expression (**Supplemental Figure 21**).

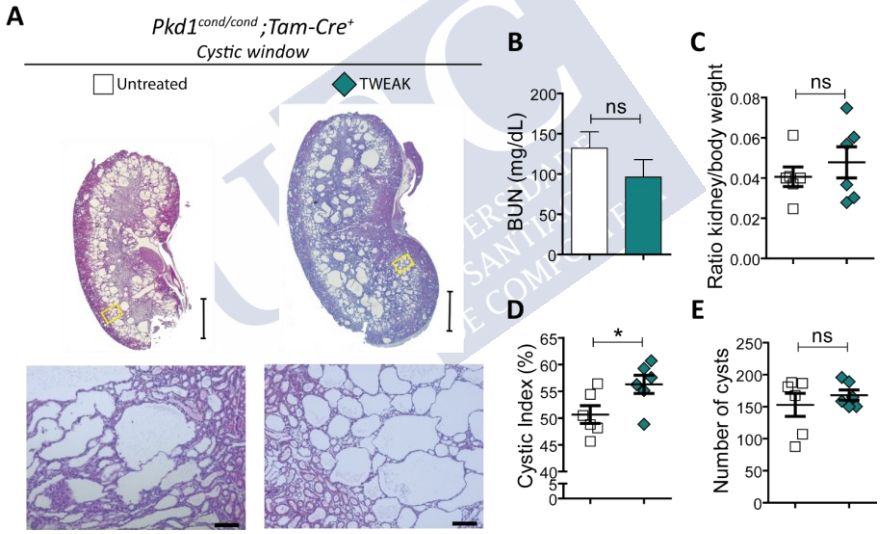

Figure 37. Short-term TWEAK administration increases the severity of cystic disease in the cystic window. Only two TWEAK doses were administered before *Pkd1* inactivation. Representative images of kidney histology at p30 of control (n=6) and TWEAK-exposed (n=6) mice (A), additional information in **Supplemental Figure 17B**. Scale bars: 2 mm (upper panel); 100 µm (lower panel). Blood Urea Nitrogen (BUN) (B) and the ratio of kidney to body weight (C) of control and TWEAK-exposed mice did not change. TWEAK induced a significant increase of cystic index (D), but did not modify the number of cysts (E). p(x): postnatal day. Bars represent means±SEM. ns: not significant; * $p<0.05$.

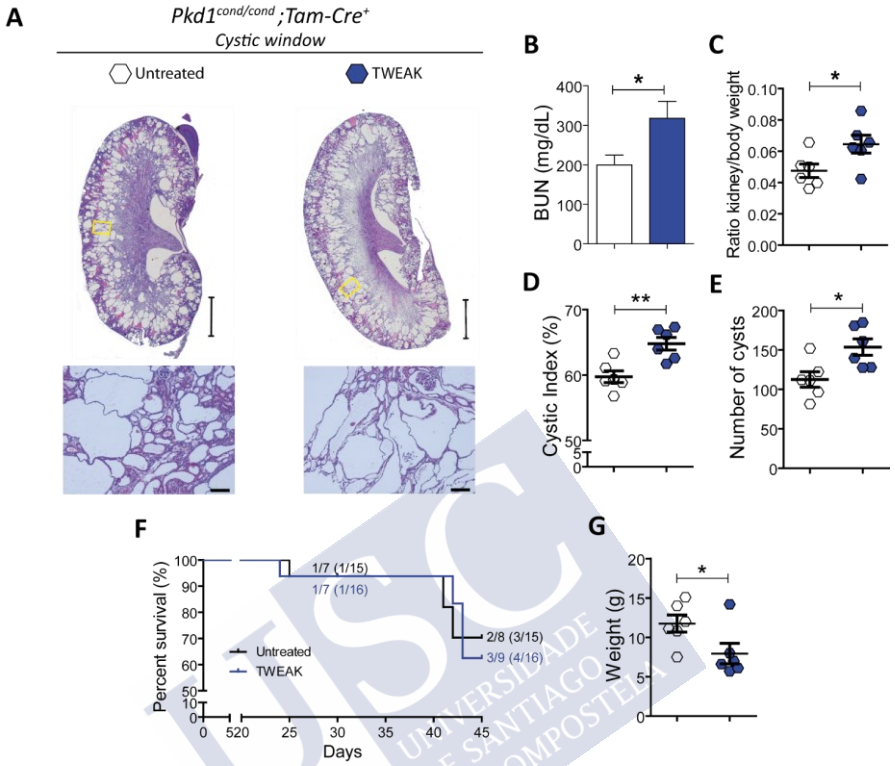

Figure 38. Long-term TWEAK administration increases disease progression in ADPKD. (A) Representative images of the histologic analysis of kidneys at p45 in control (n=6) and TWEAK-exposed (n=6) groups, schematic representation of the experimental design in **Supplemental Figure 17C**. Scale bars: 2 mm (upper panel); 100 µm (lower panel). TWEAK increases Blood Urea Nitrogen (BUN) (B), the ratio of kidney to body weight (C), and renal cystic index (D) and number of cysts (E). (L) Kaplan-Meier survival plots over time. Mice exposed to TWEAK had lower survival than control mice. (M) Weight of control and TWEAK-exposed mice: TWEAK slowed mice growth. p(x): postnatal day. Bars represent means±SEM. ns: not significant; * $p<0.05$; ** $p<0.01$.

4.4. Anti-TWEAK slows cyst growth and improves renal function in ADPKD mice

Our results demonstrate that Fn14/TWEAK axis is upregulated and promotes cyst progression in ADPKD. On the basis of these results, we decided tested TWEAK as therapeutic target. For that, we administrated neutralizing anti-TWEAK antibodies in the cystic window of the orthologous mouse *Pkd1*$^{cond/cond}$*;Tam-Cre* for targeting TWEAK (**Supplemental Figure 17C**).

Anti-TWEAK treatment resulted in smaller kidneys than in untreated controls (**Figure 39A**). Importantly, kidney function (assessed as BUN) was better preserved and the kidney to body weight ratio and cystic index were remarkably lower in anti-TWEAK treated mice (**Figure 39**, **B-D**). In the histological analysis, we did not observe significant differences in the total number of cysts (**Figure 39E**). We next wanted to do a more refined analysis dividing cysts by size, we have found that anti-TWEAK reduced the number of larger cysts (**Figure 39F**). Bearing in mind that Fn14 is expressed both in proximal and distal-collecting tubules[171]; we found that anti-TWEAK mostly reduced the cysts in proximal (LTL$^+$) and collecting (DBA$^+$) tubules (**Figure 39, G** and **H**, **Supplemental Figure 22** upper panel), but not the size of cysts from the thick ascending limb of the loop of Henle (THP$^+$) (**Supplemental Figure 22** lower panel). Anti-TWEAK also increased the survival of mice over TWEAK-exposed or control untreated mice (**Figure 39I**). Anti-TWEAK therapy was further associated with a larger mice weight increase (**Supplemental Figure 19**). Finally, we did not find any apparent damage of anti-TWEAK treatment (**Supplemental Figure 20**).

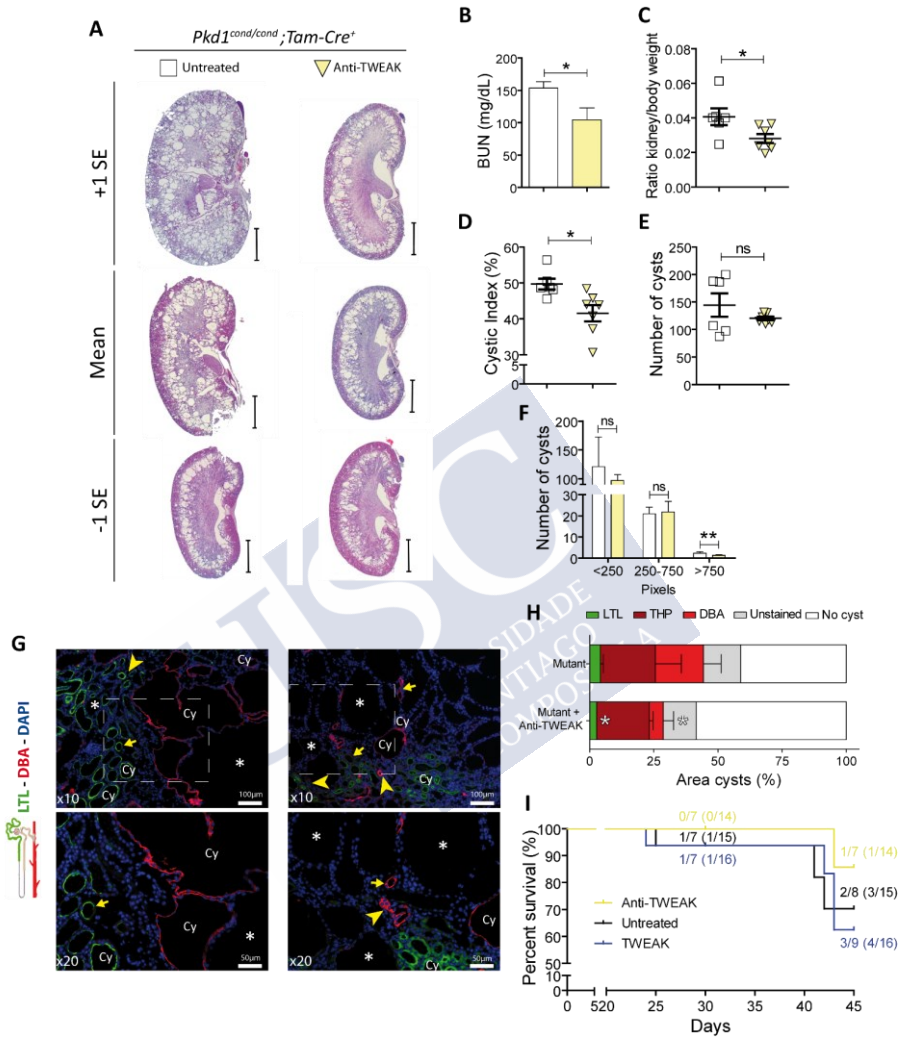
A
Pkd1cond/cond;Tam-Cre+
Untreated
Anti-TWEAK
+1 SE
Mean
-1 SE
B
BUN (mg/dL)
C
Ratio kidney/body weight
D
Cystic Index (%)
E
Number of cysts
ns
F
Number of cysts
<250
250-750
>750
Pixels
G
LTL - DBA - DAPI
Cy
x10
x20
H
LTL
THP
DBA
Unstained
No cyst
Mutant-
Mutant + Anti-TWEAK
Area cysts (%)
I
Percent survival (%)
Anti-TWEAK
Untreated
TWEAK
0/7 (0/14)
1/7 (1/15)
1/7 (1/16)
1/7 (1/14)
2/8 (3/15)
3/9 (4/16)
Days

Figure 39. Treatment with anti-TWEAK decreases renal cyst progression. (A) Hematoxylin-Eosin stained sagittal cross-sections of kidneys treated with anti-TWEAK (n=6) and control kidneys (n=6), sacrifice at postnatal day p30. Representative images with values within mean ±1xSE shown. Additional information about the experimental design in **Supplemental Figure 17C**. Scale bars: 2 mm (upper panel); 100 µm (lower panel). Blood Urea Nitrogen (BUN) (B), percentage of kidney weight to total body weight (C) and cystic index (D) were significantly reduced in anti-TWEAK treated mice at time p30. (E) No significant differences in cyst number were observed. However, classification of the number of cysts by size in three groups according the size estimated by number of pixels disclosed that the number of largest cysts (>750 pixels) was reduced with treatment (F). (G) Immunofluorescence of specific nephron markers from proximal tubule (LTL, Lotus Tetragonolobus Lectin, green) and collecting duct (DBA, Dolichos Biflorus Agglutinin, red). Representative images are shown, where it is observed that anti-TWEAK slows progression of LTL^+ and DBA^+ cysts. Cy: cyst; * cyst without specific marking; yellow arrow: dilated tubule; yellow arrowhead: tubule. Scale bars: 100 µm (upper panel) and 50 µm (lower panel). (H) Quantification of immunofluorescence cystic area. Anti-TWEAK treatment reduces cystic area of LTL^+ and DBA^+ cysts. (I) Kaplan-Meier survival plots of time. Treatment with anti-TWEAK increased survival (93% survival) over control and TWEAK-exposed mice. p(x): postnatal day. Bars represent means±SEM. ns: not significant; * $p<0.05$; ** $p<0.01$.

4.5. Anti-TWEAK decreases cell proliferation via inhibition of the AKT pathway

TWEAK activates the proliferative pathway driven by mitogen-activated protein kinases (MAPKs) such as extracellular signal-regulated kinase1/2 (ERK1/2) and MAPK p38, as well as PI3K/AKT in different cell types, including renal cells[169,205,206]. In the same way, the mammalian target of rapamycin (mTOR) and MAPK pathways are deregulated in ADPKD[54,207–209]. Thus, inhibition of mTOR was beneficial in preclinical studies with animal models of ADPKD[210–213]. We found that the pERK1/2 / ERK1/2 ratio was increased in untreated cystic kidneys, indicating ERK1/2 activation, and this was not modified by anti-TWEAK treatment at postnatal day 30 (**Figure 40A**; **Supplemental Figure 23**, **A** and **B**). By contrast, anti-TWEAK normalized p38 phosphorylation, which was increased, evidencing increased p38 MAPK activation, in untreated cystic kidneys (**Figure 40B**; **Supplemental Figure 23**, **C** and **D**). Furthermore, our results show that anti-TWEAK also reduced total AKT protein levels and AKT phosphorylation, which were also increased in untreated cystic kidneys (**Figure 40C**; **Supplemental Figure 23**, **E** and **F**). Changes in AKT

protein levels were not explained by changes in *Akt1* gene expression (**Figure 40D**).

In an inflammatory milieu, TWEAK induces mesangial and tubular cell apoptosis[205,214]. The number of apoptotic cells detected by TUNEL decreased with anti-TWEAK (**Figure 40E**). In addition, we evaluated fibrosis after anti-TWEAK treatment. We found a modest reduction of fibrosis with a reduction of fibronectin staining (**Figure 40F**). However, we did not find significant differences in α-SMA staining or *Tgfβ1* and *Ctgf* gene expression (**Supplemental Figure 24**).

4.6. Anti-TWEAK treatment reduces inflammation and macrophage recruitment

A major pathological feature of ADPKD is the development of interstitial inflammation[113]. Several studies reported that macrophage activation and infiltration are implicated in ADPKD cyst growth[115,116], as well as an increased expression of many pro-inflammatory markers and cytokines [82,121,204]. On the basis of these findings, we tested the gene expression of proinflammatory markers of alternative macrophage activation phenotypes, called M1 and M2, respectively. In summary, we studied four M1 macrophage markers (*Nos2*, *Il-12*, *Tnfα*, *Mcp1*) and four M2 markers (*Arg1*, *Mrc1*, *Csf1*, *Csf2*). At postnatal day 30, there was a mixed phenotype with an upregulated expression of two proinflammatory (*Tnfα*, *Mcp1*) and all alternative (*Arg1*, *Mrc1*, *Csf1*, *Csf2*) macrophage activation genes studied (**Supplemental Figure 25**, **A** and **B**). Importantly, the gene expression of two most upregulated markers in untreated *Pkd1* mutant mice, *Mcp1* and *Arg1*, were downregulated by anti-TWEAK treatment (**Figure 41**, **A** and **B**). *Fn14* expression was downregulated by anti-TWEAK, likely due to a lower inflammatory status and cyst progression (**Figure 41C**). However, TWEAK did not further increase *Fn14* expression (**Supplemental Figure 26**).

TWEAK activates the canonical and non-canonical NF-κB pathways[215]. In untreated ADPKD, we observed evidence of canonical NF-κB pathway activation, as *Mcp1* and *Cxcl16* were upregulated, and evidence of non-canonical NF-κB pathway downregulation, as *Ccl19* and *Ccl21* were downregulated (**Supplemental Figure 25**, **C** and **D**).

Anti-TWEAK, as noted above, decreased the expression of *Mcp1* (canonical pathway), however we have not found significant differences in the non-canonical pathway NF-κB markers (**Figure 41**, **D** and **E**). In the same way, staining for the canonical NF-κB component p65 showed a significant decrease of stained cells after anti-TWEAK treatment (**Figure 41F**).

Finally, using a specific marker of mouse monocytes/macrophages called F4/80[216], an increased macrophage recruitment was confirmed in untreated *Pkd1* deficient kidneys. F4/80 stained macrophages infiltration was significantly reduced by anti-TWEAK treatment (**Figure 41**, **G** and **Supplemental Figure 27**). We further studied macrophage infiltration in early disease stages to elucidate whether reduced macrophage recruitment could drive slower cyst progression in anti-TWEAK-treated mice. Anti-TWEAK decreased cyst progression in early stages of disease, but we did not find differences in F4/80 staining at this stage (**Supplemental Figure 28**). Our data suggest that a decrease of macrophage recruitment under TWEAK/Fn14 pathway is a direct cause of cystic disease reduction, and therefore, all physio-pathological consequences undergoing this pathway are directly related to cystic epithelia. Modulation of TWEAK/Fn14 axis has been unmasked as a ADPKD novel potential therapeutic target.

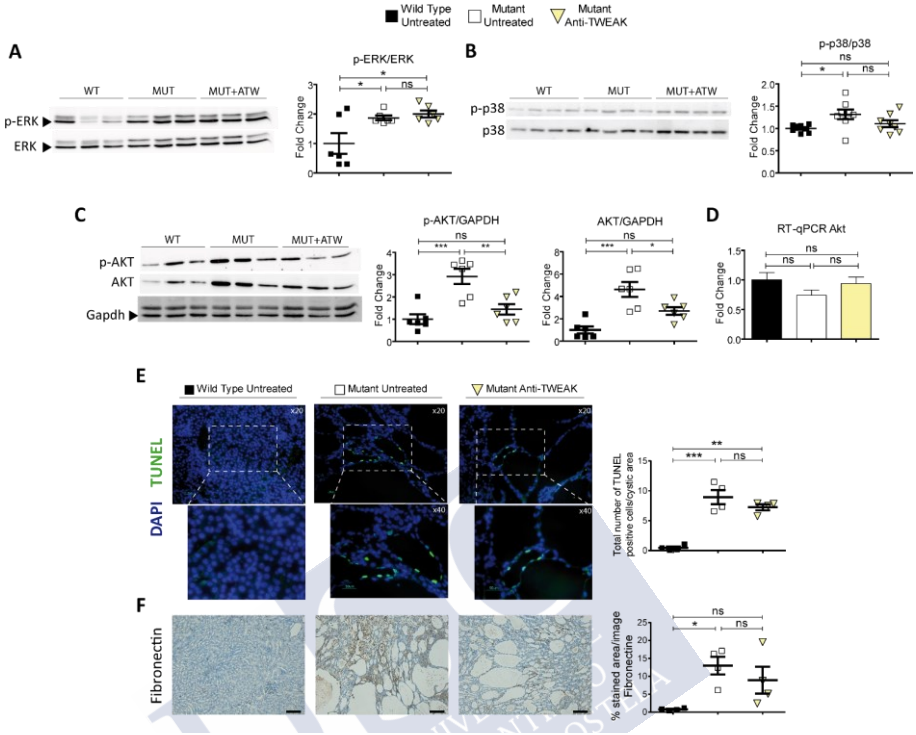

Figure 40. Molecular pathways related to proliferation and MAPK pathway and fibrosis in cystic kidney. Anti-TWEAK treatment reduces AKT and p-AKT but not p-ERK at postnatal day 30. (A) Western Blot analysis for p-ERK and ERK of total kidney protein lysates of Wild Type (n=6), Mutant (n=6) and Mutant anti-TWEAK mice (n=6). (B) p-ERK/ERK ratio. ERK was used as housekeeping. (C) Protein level by Western Blot for p-p38 and p38 of total kidney protein lysates of Wild Type (n=6), Mutant (n=6) and Mutant anti-TWEAK mice (n=6). (D) p-p38/p38 ratio. P38 was used as housekeeping. (E) Western Blot for p-AKT, AKT and GAPDH of total kidney protein lysates of Wild Type (n=6), Mutant (n=6) and Mutant anti-TWEAK mice (n=6). Ratios for p-AKT/GAPDH (F), and AKT/GAPDH (G). GAPDH was used as housekeeping, due to changes in AKT protein levels, precluding the use of AKT to normalize p-AKT levels. (H) RT-qPCR of *Akt1* gene for Wild Type (n=5), Mutant (n=5) and Mutant animals treated with anti-TWEAK (n=6). No significant differences in *Akt* mRNA were observed. (E) Anti-TWEAK decreases apoptosis in kidney treated anti-TWEAK group, as detected by TUNEL assay. Upper panel: representative images of apoptotic cells stained with TUNEL assay. Lower panel: nuclei stained with DAPI. (F) Immunohistochemically analysis of fibronectin (center) in kidney slides of *Wild Type*, mutant and anti-TWEAK groups. n=4 was used per group. Fibrosis, assed through fibronectin staining, was modest diminished with anti-TWEAK. Scale bars: 100µm. Mice were sacrificed at postnatal day p30, according of the scheme shown in **Supplemental Figure 17C** (medium-term model). p(x): postnatal day. Bars represent means±SEM. ns: not significant; * p<0.05; ** p<0.01. *** p<0.001.

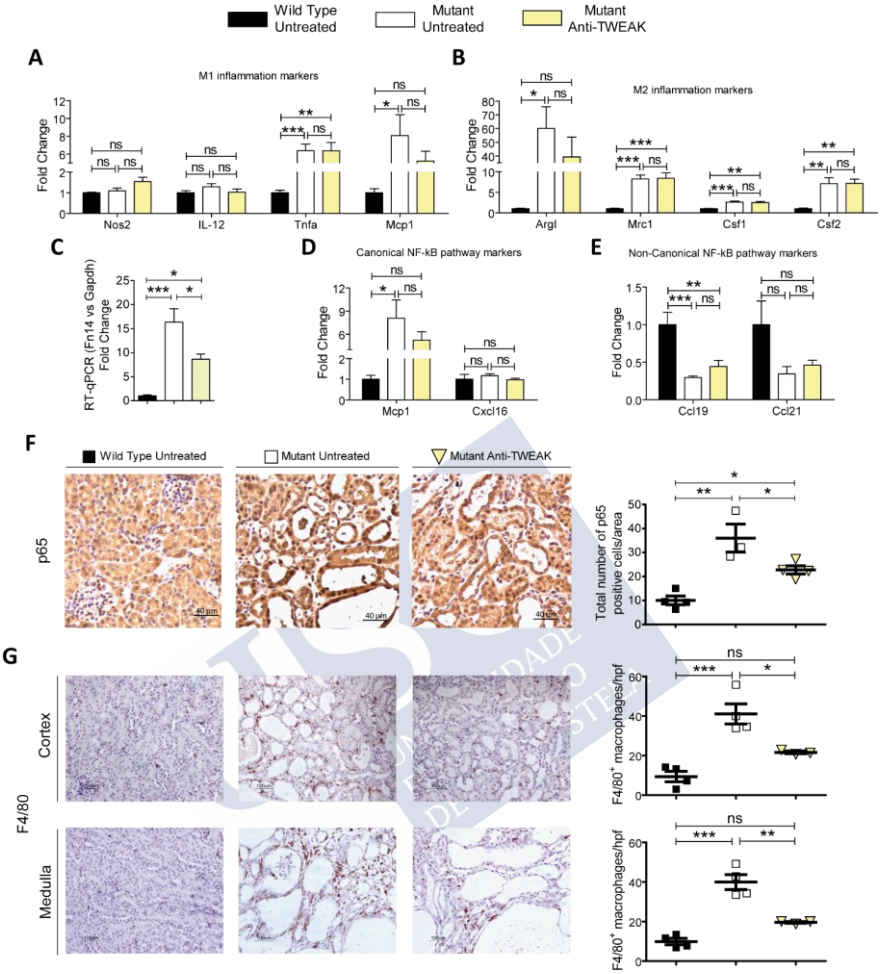

Figure 41. Characterization of proinflammatory (M1) and alternative (M2) macrophage gene expression. Anti-TWEAK decreased the expression of *Mcp1* and *Arg1* and reduces macrophage recruitment at postnatal day 30. RT-qPCR of *Nos2*, *Il-12*, *Tnfa* and *Mcp1* (M1 pathway markers) (A), *Arg1*, *Mrc1*, *Csf1* and *Csf2* (M2 pathway markers) (B) and *Fn14* (C). Gene expression by RT-qPCR of *Mcp1* and *Cxcl16* (D), and *Ccl19* and *Ccl21* (E), markers of canonical and non-canonical NF-κB pathway activation, respectively. *Wild Type* (n=5), Mutant (n=5) and Mutant mice treated with anti-TWEAK (n=6) were used for this experiment set. *Hprt* was used as housekeeping gene in all cases. Macrophage infiltration was reduced by anti-TWEAK treatment. Anti-TWEAK significantly decreases NF-κB pathway activation. (F) Nuclear p65 staining is decreased in anti-TWEAK treated group. Representative images are shown. N=4 was used per group. (G) F4/80 staining in kidney tissue. There were lower numbers of positive F4/80 macrophages in cortex and medulla (upper and lower panels, respectively) in mutant mice treated with anti-TWEAK (n=3) than in untreated mutant mice (n=4). Mice were sacrificed at postnatal day p30, according of the scheme shown in **Supplemental Figure 17C** (medium-term model). Bars represent means±SEM. ns: non-significant; * p<0.05; ** p<0.01; *** p<0.001.

5. CHAPTER 5

Genetic interactions of *Pkhd1* and *Pkd1* reveal new possible insights in cyst formation.

USC UNIVERSIDADE DE SANTIAGO DE COMPOSTELA

5.1. *Pkd1* and *Pkhd1* synergistic genetic interaction

With the purpose to study the genetic interaction between *Pkd1* and *Pkhd1*, as well as dosage and timing effect, we interbreed knockout $Pkd1^{del2\text{-}4/+}$ (*Pkd1*-KO) and conditional knockout $Pkd1^{cond/cond}$*;Tam-Cre* (*Pkd1*-cKO) mice[68,70] with knockout $Pkhd1^{del3\text{-}4/del3\text{-}4}$ (*Pkhd1*-KO) mice[69]. $Pkd1^{cond/cond}$*;Tam-Cre* mouse develops severe polycystic kidney and liver disease, however $Pkd1^{del2\text{-}4/+}$ mouse not present polycystic disease in heterozygosis and develop only focal renal cysts in embryonic stage and homozygosis. By other hand, $Pkhd1^{del3\text{-}4/del3\text{-}4}$ mice develop the progressive liver polycystic disease typical of ARPKD but without kidney cysts. All of them were intercrossed in C57BL/6 mouse background. Interestingly, $Pkhd1^{del3\text{-}4/del3\text{-}4}$*;*$Pkd1^{del2\text{-}4/+}$ (DKO) mice have presented renal cystogenesis. Mice were sacrificed in different life points confirming that single knockout mice (*Pkd1*-KO and *Pkhd1*-KO) not develop renal cystogenesis. However, the intercross of both alleles in a double knockout (DKO) have resulted in renal cyst formation and growth (**Figure 42A, Supplemental Figure 29A**). Cyst could be found in CKO mice from the earliest stages, at postnatal day 30, and from postnatal day 80 all mice (except one) presented renal cyst (**Figure 42B**). The area occupied by the cysts (cystic index) and the number of cysts increased over time (**Figure 42, C** and **D**). Cyst formation in DKO mice was confirmed using epithelial- specific markers for nephron segments. We have found renal cysts in proximal tubules (LTL^+), ascending limb of the loop of Henle (THP^+) and collecting ducts (DBA^+) (**Supplemental Figure 30**). These results suggest that cystogenesis in DKO mice was not confined to specific kidney region. Besides, these cystogenesis was mainly focal and located causing a significant growth of kidney weight in advanced stage of mice life (at postnatal day 250) (**Supplemental Figure 31A**). However, we did not find differences in the loss of renal function (**Supplemental Figure 31B**). Our results in show that animal models with PKD mutations that do not show a cystic phenotype, in combination can manifest disease phenotype. In the same way, these results reinforce the idea that *Pkhd1* and *Pkd1* interact genetically and that protein threshold is important for cystogenesis suggesting a possible common pathway for cyst formation in PKD.

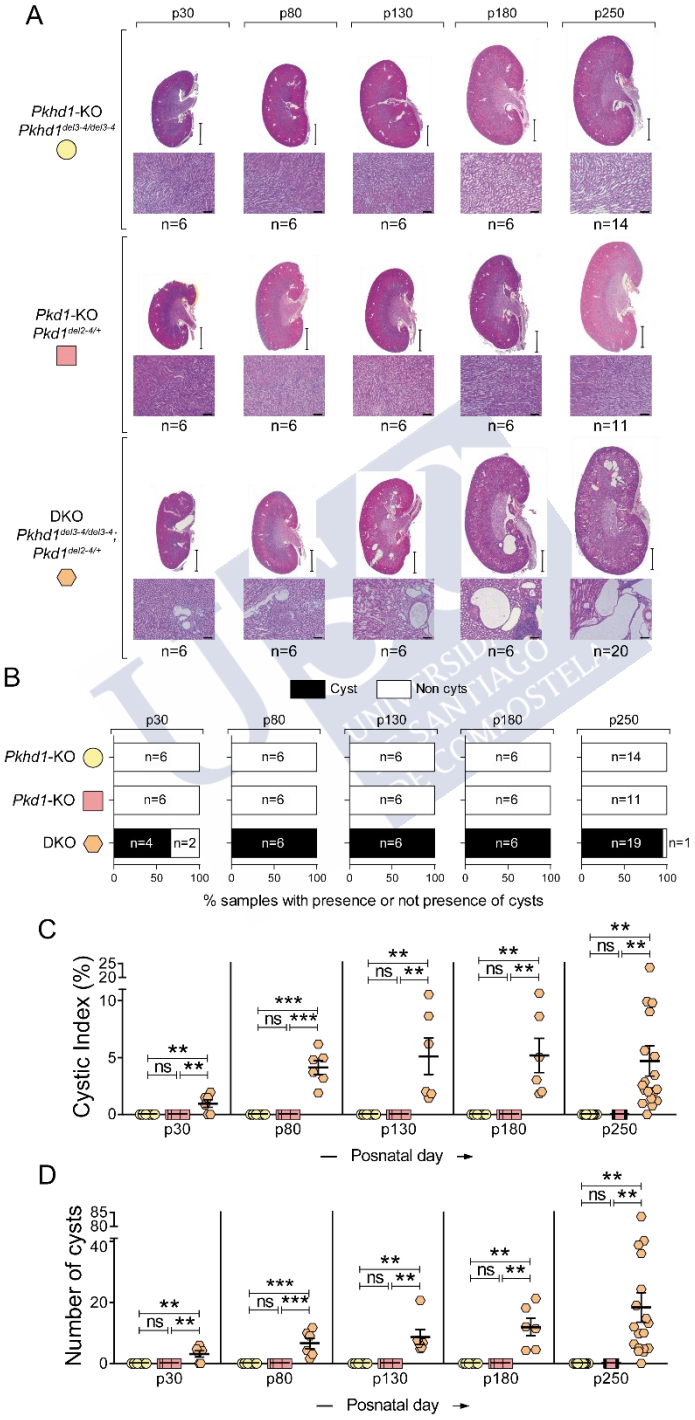
A
p30
p80
p130
p180
p250
Pkhd1-KO
Pkhd1del3-4/del3-4
n=6
n=6
n=6
n=6
n=14
Pkd1-KO
Pkd1del2-4/+
n=6
n=6
n=6
n=6
n=11
DKO
Pkhd1del3-4/del3-4;
Pkd1del2-4/+
n=6
n=6
n=6
n=6
n=20
B
Cyst
Non cyts
p30
p80
p130
p180
p250
Pkhd1-KO
Pkd1-KO
DKO
n=6
n=6
n=6
n=6
n=14
n=6
n=6
n=6
n=6
n=11
n=4
n=2
n=6
n=6
n=6
n=19
n=1
0
50
100
% samples with presence or not presence of cysts
C
Cystic Index (%)
25
20
10
5
0
**
ns
***
p30
p80
p130
p180
p250
Posnatal day
D
Number of cysts
85
80
40
20
0
Posnatal day

Figure 42. Synergistic effect of *Pkd1* and *Pkhd1* mutations in renal cystogenesis. Single knockouts of *Pkhd1* and *Pkd1* did not present renal cysts, but in combination have developed renal cystogenesis and cyst growth showing a synergist effect. (A) Representative images of the histologic analysis of kidneys in $Pkhd1^{del3\text{-}4/del3\text{-}4}$ (*Pkhd1*-KO), $Pkd1^{del2\text{-}4/+}$ (*Pkd1*-KO) and $Pkhd1^{del3\text{-}4/del3\text{-}4}$;$Pkd1^{del2\text{-}4/+}$ (DKO) mice groups. Schematic representation of the experimental design in **Supplemental Figure 29A**. The n listed under kidney slides represents the number of mice analyzed for group. Scale bars: 2 mm (upper panel); 100 µm (lower panel). (B) Graph representing the presence or absence of renal cysts. (C-D) Cystic index and total number of cysts. p(x): postnatal day. Bars represent means±SEM. ns: not significant; ** p<0.01; *** p<0.001.

5.2. *Pkd1* controls cyst progression in PKD

Several studies have shown evidences that PC1 dosage modifies and governs PKD severity[71,137,144,217]. Also, a previous study reported that differences in the timing and dosage of tamoxifen of *Pkd1* gene determine the severity of the disease[77]. So, we hypothesized that deletion timing and dosage of *Pkd1* gene (and PC1) is determinant in genetic interaction between *Pkhd1* and *Pkd1*. Next, we have generated a double knockout of *Pkhd1* with an inducible conditional *Pkd1* deletion in heterozygosis ($Pkhd1^{del3\text{-}4/del3\text{-}4}$;$Pkd1^{cond/+}$;*Tam-Cre*$^{+}$) in order to evaluate the impact of timing for *Pkd1* deletion in genetic interaction of both genes (**Supplemental Figure 29B**). First, $Pkhd1^{del3\text{-}4/del3\text{-}4}$;$Pkd1^{cond/+}$;*Tam-Cre*$^{+}$ mice have presented cyst formation (**Figure 43A**), reinforcing our previous data (**Figure 42A**). Giving the fact that cystogenesis present in these animal models is not severe (predominantly isolated and focal renal cysts), we have not found high values in serum BUN corresponding to loos of kidney function (**Figure 42B**). But we have observed a timing effect on kidney size and cyst formation (**Figure 43**, **C** and **D**). Cystogenesis (measured as cysts presence, cystic index and number of cysts) was higher on $Pkhd1^{del3\text{-}4/del3\text{-}4}$;$Pkd1^{del2\text{-}4/+}$;*Tam-Cre*$^{+}$ (DKO) mice than $Pkhd1^{del3\text{-}4/del3\text{-}4}$;$Pkd1^{cond/+}$;*Tam-Cre*$^{+}$ mice with *Pkd1* deletion at p1-2, and this last presented a higher cystogenesis than with *Pkd1* deletion at p10-11 (**Figure 43**, **D-F**). Our data demonstrated that a congenital and embryonic *Pkd1* mutation causes a worse prognosis and progression of polycystic disease, in a *Pkhd1* genetic interaction context, that a newborn (p1-2) or *a posteriori* deletion (p10-11) in murine orthologous models.

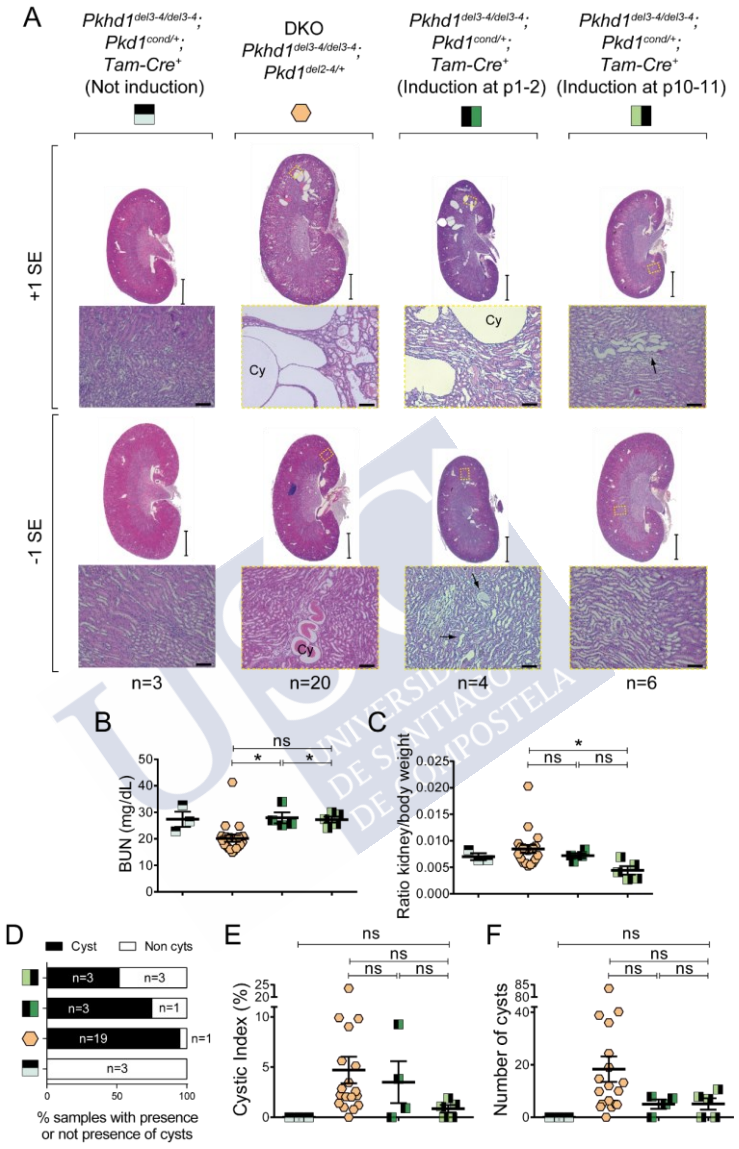

Figure 43. Timing in *Pkd1* deletion determines cyst progression in PKD. (A) Representative Hematoxylin-Eosin images of kidneys from *Pkhd1*$^{del3-4/del3-4}$;*Pkd1*$^{del2-4/+}$ (DKO) and *Pkhd1*$^{del3-4/del3-4}$;*Pkd1*$^{cond/+}$;*Tam-Cre*$^{+}$ (with *Pkd1* not or deletion at different life points, p1-2 and p10-11 respectively) mice groups. Schematic representation of the experimental design in **Supplemental Figure 29B**. The n listed under kidney slides represents the number of mice analyzed for group. Scale bars: 2 mm (upper panel); 100 µm (lower panel). (B-C) Ratio of kidney to body weight (B) and renal function based on BUN (C). (D) Graph representing the presence (black box) or absence (white box) of renal cysts. (E-F) Renal cystic index and number of cysts. p(x): postnatal day. Bars represent means±SEM. ns: not significant; * p<0.05.

5.3. Novel genetic interaction in *Pkhd1* and *Pkd1* reveals possible key effectors in cyst formation

With the aim of expand the study, we generated a new double knockout murine model intercrossed *Pkhd1*-KO (*Pkhd1*$^{del3\text{-}4/del3\text{-}4}$) mice and *Pkd1*-cKO (*Pkd1*$^{cond/cond}$*;Tam-Cre*) mice. *Pkd1*-cKO develops a rapid and severe renal polycystic phenotype when *Pkd1* is deleted before postnatal day 12 (p12)[70], and we supposed that in context with other mutation in other PKD gene (*Pkhd1*) would trigger a more severe cystogenic response. Surprisingly, *Pkhd1*$^{del3\text{-}4/del3\text{-}4}$*;Pkd1*$^{cond/cond}$*;Tam-Cre*$^{+}$ (DcKO, double conditional knockout) mice developed a milder renal polycystic disease in comparation with *Pkd1*-cKO (**Figure 44A**). Mice groups were sacrificed in three different times (p18, p30 and p45), after *Pkd1* deletion at p10-11, in order to analyze the disease progression (**Supplemental Figure 29C**). DcKO mice group presented an amelioration of renal cystic disease in kidney size/weight and an improvement in kidney function (**Figure 44**, **B** and **C**). Additionally, cystic index and number of cysts were also significantly reduced in DcKO mice from initial to end studied stage (**Figure 44**, **D** and **E**). Cystic origin characterization using nephron markers showed a general decrease of cyst growth and not confined to one specific nephron segments (**Supplemental Figure 32**). Next, we examined the genetic interaction between heterozygous mutations in *Pkdh1* in *Pkd1*-cKo mice to determine if *Pkhd1* can be a modifier of cystic disease. *Pkhd1*$^{del3\text{-}4/+}$*;Pkd1*$^{cond/cond}$*;Tam-Cre*$^{+}$ mice developed a similar cyst progression severity than *Pkd1*-cKO suggesting a not additive or synergistic effect of heterozygous *Pkhd1* allele (**Supplemental Figure 33**). Our data suggests that a germinal *Pkhd1* mutation with a deletion of *Pkd1* in adult context together (both, in homozygosity), ameliorates the renal ADPKD phenotype in murine models.

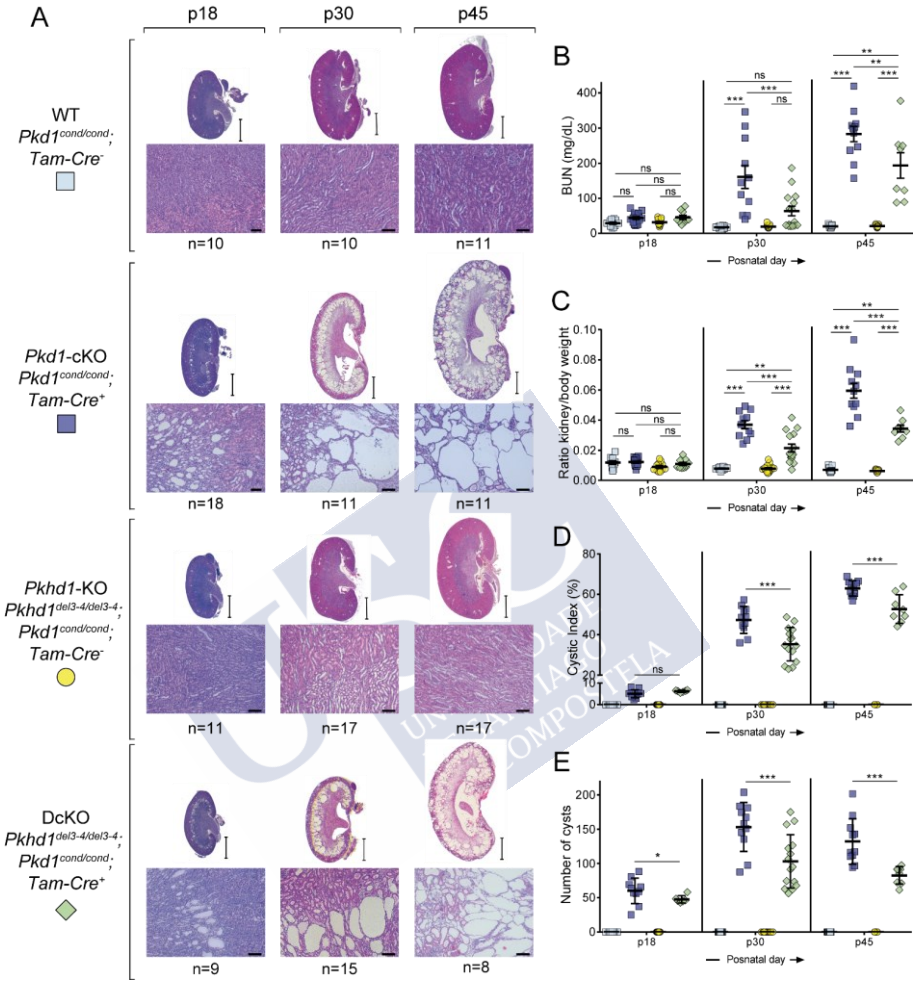

Figure 44. Double homozygous of *Pkhd1* knockout and *Pkd1* conditional knockout presented an amelioration of renal cystic disease. Homozygous mutation in *Pkhd1* and adult stage deletion of *Pkd1* causes an unexpected protective effect in cystic renal progression. (A) Representative Hematoxylin- Eosin images of the kidneys in *Pkd1*$^{cond/cond}$;*Tam-Cre*$^{-}$ (WT), *Pkd1*$^{cond/cond}$;*Tam-Cre*$^{+}$ (*Pkd1*-cKO), *Pkhd1*$^{del3-4/del3-4}$; *Pkd1*$^{cond/cond}$;*Tam-Cre*$^{-}$ (*Pkhd1*-KO) and *Pkhd1*$^{del3-4/del3-4}$; *Pkd1*$^{cond/cond}$;*Tam-Cre*$^{+}$ (DcKO) mice groups. Schematic representation of the experimental design in **Supplemental Figure 29C**. The n listed under kidney slides represents the number of mice analyzed for group. Scale bars: 2 mm (upper panel); 100 µm (lower panel). (B) Renal function based on BUN. (C) Ratio of kidney weight to body weight. (C-D) Renal cystic index and number of cysts, respectively. p(x): postnatal day. Bars represent means±SEM. ns: not significant; * p<0.05; ** p<0.01; *** p<0.001.

5.4. Additive effect in liver cystogenesis in *Pkhd1* and *Pkd1* genetic interaction

Analysis of the liver physiopathology at different life points in the same studied phenotypes showed an increase in severity in double knockouts mice. The digenic DKO (*Pkhd1*$^{del3\text{-}4/del3\text{-}4}$;*Pkd1*$^{del2\text{-}4/+}$) showed a worse progression of hepatic phenotype than single knockouts of *Pkhd1* and *Pkd1* (*Pkhd1*$^{del3\text{-}4/del3\text{-}4}$ and *Pkd1*$^{del2\text{-}4/+}$, respectively) (**Figure 45A**). Liver from DKO mice have presented higher liver weight, with respect body weight, and significant increase of ALT serum values after six months (at p180 and p250) (**Figure 45**, **B** and **C**). With respect to hepatic cystic index and number of cysts we did not found conclusive differences about the additive effect of genetic interaction of *Pkhd1* and *Pkd1* (**Supplemental Figure 34**).

The synergistic interaction between both genes was more consistent studying the homozygous double knockout (*Pkhd1*$^{del3\text{-}4/del3\text{-}4}$;*Pkd1*$^{cond/cond}$;*Tam-Cre*$^{+}$, DcKO). Contrary to kidney results, in DcKO mice have developed worse progression in hepatic cystogenesis showing an additive effect of *Pkhd1* and *Pkd1* genes in liver disease phenotype (**Figure 46A**). DcKO mice presented loss of hepatic function, according with high and aberrant ALP and ALT serum values in comparison with single *Pkd1*-cKO and *Pkhd1*-KO single knockout (**Figure 46**, **B** and **C**). With respect to ratio liver to body weight, we did not find significant differences suggesting not additive effect in hepatic volume (**Figure 46D**). However, hepatic cystic index and number of cysts increased in DcKO mice (**Figure 46**, **E** and **F**). Besides, DcKO mice showed a severity of enlargement/dilation of branches of the bile ducts (see bile ducts in macroscopic liver slides in **Figure 46A**, and **Supplemental Figure 35**). In conclusion, our data demonstrated that *Pkhd1* and *Pkd1* genes interact genetically aggravating hepatic disease in PKD.

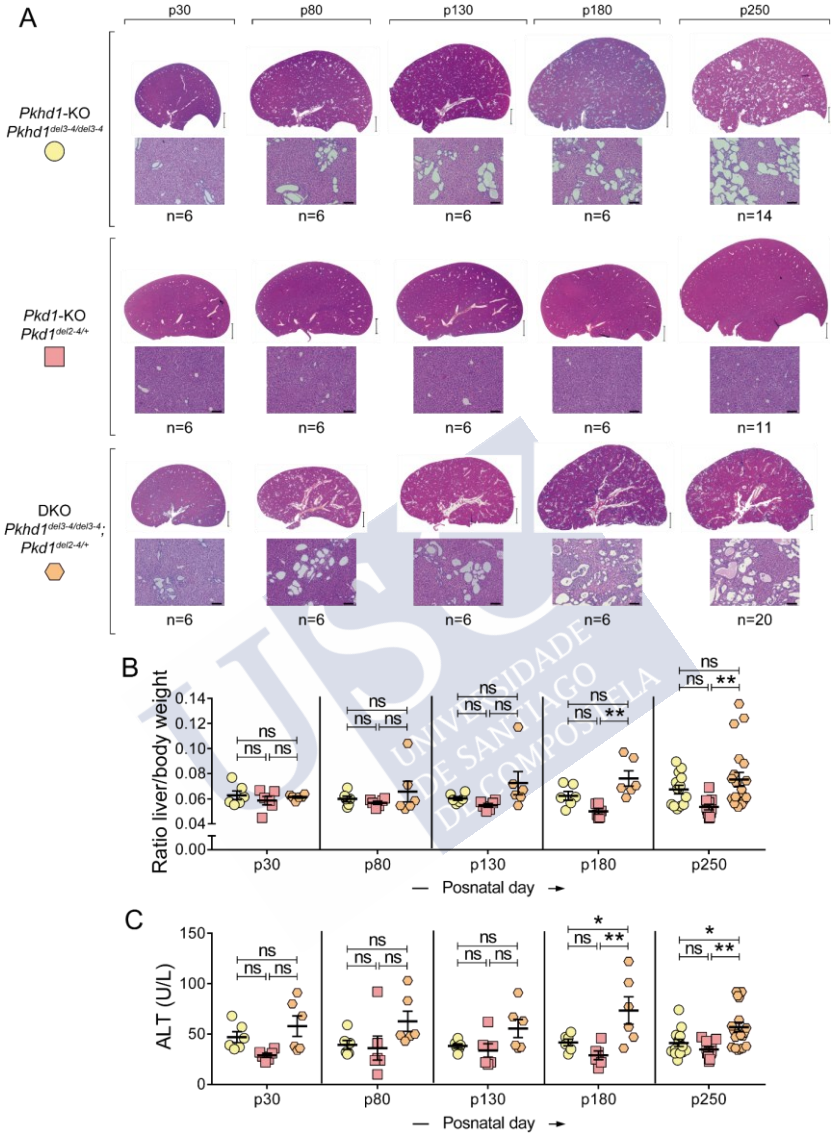

Figure 45. Characterization of liver phenotype in *Pkhd1* and *Pkd1* genetic interaction. (A) Hematoxylin-Eosin stain of representative liver sections from P*khd1*$^{del3-4/del3-4}$ (*Pkhd1*-KO), *Pkd1*$^{del2-4/+}$ (*Pkd1*-KO) and *Pkhd1*$^{del3-4/del3-4}$;*Pkd1*$^{del2-4/+}$ (DKO) animal groups. Schematic representation of the experimental design in **Supplemental Figure 29A**. The n listed under kidney slides represents the number of mice analyzed for group. Scale bars: 2 mm (upper panel); 100 µm (lower panel). (B) Ratio of liver weight to body weight. (C) Hepatic function according ALT serum values. (D-E) Cystic index and total number of cysts. p(x): postnatal day. Bars represent means±SEM. ns: not significant; *p<0.05; ** p<0.01; *** p<0.001.

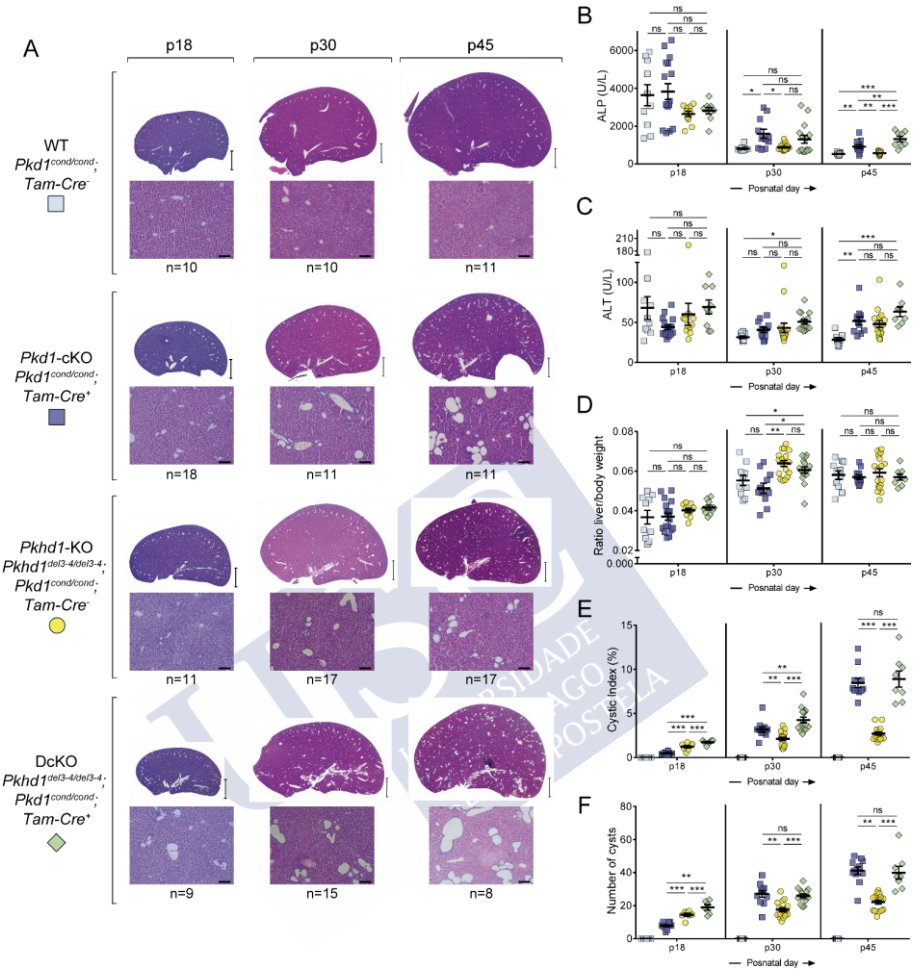

Figure 46. Double homozygous of *Pkhd1* knockout and *Pkd1* conditional knockout aggravates hepatic cyst progression. Liver disease was significantly worse in due to the loss of *Pkhd1* and *Pkd1*. (A) Representative images of liver Hematoxylin-Eosin sections of $Pkd1^{cond/cond}$;*Tam-Cre*$^{-}$ (WT), $Pkd1^{cond/cond}$;*Tam-Cre*$^{+}$ (*Pkd1*-cKO), $Pkhd1^{del3-4/del3-4}$; $Pkd1^{cond/cond}$;*Tam-Cre*$^{-}$ (*Pkhd1*-KO) and $Pkhd1^{del3-4/del3-4}$; $Pkd1^{cond/cond}$;*Tam-Cre*$^{+}$ (DcKO) mice groups. Schematic representation of the experimental design in **Supplemental Figure 29C**. The n listed under kidney slides represents the number of mice analyzed for group. Scale bars: 2 mm (upper panel); 100 µm (lower panel). (B-C) Hepatic function based on ALP (B) and ALT (C). (D) Ratio of liver to body weight. (E-F) Liver cystic index (E) and total number of cysts (F). p(x): postnatal day. Bars represent means±SEM. ns: not significant; * p<0.05; ** p<0.01; *** p<0.001.

DISCUSSION

DISCUSSION

1. DISCUSSION CHAPTER 1

This work proposes CystAnalyser as a new reliable and easy to use software tool to evaluate cystic pathologies, such as polycystic kidney disease (PKD) and polycystic liver disease (PLD). CystAnalyser combines the automatic recognition of the cysts in histological images with a friendly GUI which allows to supervise the recognition before quantification. CystAnalyser provides the cystic index (area of cysts within the total area of a tissue), the number of cysts and the cystic profile (based on individualized cystic size) of a histological image.

In order to test CystAnalyser, we compared the cystic index and the number of cysts provided by CystAnalyser with the automatic cyst recognition tool with or without user input. A collection of 795 images was quantified by CystAnalyser (see Materials and methods section), obtaining significant differences in the images of the liver but not the kidney. In order to make a more precise characterization to identify the cause of these differences and evaluate the reliability of the program, we classified the images into three groups according to the severity of the cystic phenotype (mild-cystic, cystic, and severely cystic; see the Materials and methods section). The main differences were identified in the processing of mild cystic and cystic hepatic images, where it was difficult to distinguish small cysts from the extrahepatic bile ducts and hepatic vasculature for a novice in the field. Therefore, in this scenario, the input of an expert was recommended since the software error in determining the cystic index in mild cystic and cystic liver images was 39.03% and 18.94%, respectively. On the other hand, in kidney images, in general, there were no differences between the recognition of automatic supervised and unsupervised cysts, except for the number of cysts within severe cystic phenotype. There were no significant differences between the cystic profiles according to the size of the cyst obtained with and without supervision for both tissues. Regarding the sensitivity and specificity of the software, the value ranges were 76.84–90.25% for the kidney and 63.4–89.66% for the liver, respectively. These values we are intentionally underestimated, because the software used a strict methodology to over count errors (dividing a cyst into two different counts as several errors and not as one). For this rea- son, CystAnalyser allowed users to monitor or supervise the default

quantification process to obtain results with greater precision and robustness.
With the aim of assessing the potential of this new software, we also compared CystAnalyser versus, the software most commonly used in scientific research, ImageJ. CystAnalyser was shown to outperform ImageJ in precision and reliability, being less subjective even without user supervision. In addition, CystAnalyser provided additional functionalities to calculate the number of cysts, the cystic profile based on their diameter and the possibility of monitoring and modifying the cysts identified by the software before quantification. The number of cysts and the cystic profile are necessary for the characterization of the phenotype and, therefore, the pathophysiology of the polycystic disease, complementing the cystic index, which is the most used biomarker in polycystic research (Manuscript under review).
Future work on this software will focused on the development of new functionalities in automated microscopes in order to perform an automatic quantitative analysis of serial images. Super- vised machine learning techniques will also be used to avoid post-processing of recognized cysts by decreasing the number of false positives, increasing the specificity of automatically detected results, and reducing the time and effort of expert supervision. Similarly, we would like to extend this automatic detection application to other techniques such as immunofluorescence (in order to specifically mark and quantify cysts from different parts of the nephron) and to other fields of nephrology such as glomerulopathies (automated quantification of the number and type of glomeruli).

2. DISCUSSION CHAPTER 2

Polycystic Liver Disease is characterized by progressive bile duct dilation and cyst progression, and current therapeutic strategies are based on surgical procedures and pharmacological management to ameliorate the disease symptoms. Therefore, PLD treatment has been ineffective and the only one curative option is liver transplantation[218]. Besides, the key intrinsic molecular mechanism of cystogenesis remains unknown. So, an emerging interest in understanding molecular pathways and developing new therapeutic strategies is increasing[16,94].

The purpose of present SWATH MS work was characterized the proteomic changes in polycystic livers and provided new insights and therapeutic targets into PLD issue.

Therefore, we used next generation quantitative proteomic approach SWATH MS to compare the proteomes of *Wild Type* and mutant (polycystic) livers from an ADPKD orthologous murine model. Using an ADPKD orthologous mouse model[68,70], we compared two different stages of polycystic liver disease progression finding several proteins with statistical differences and more than 2-fol-change cut-off. First, we identified a total of 26 and 8 proteins with changes in protein abundance in p12 and 14 data, respectively. Second, our pathway and GO analysis has identified as principal biological functions the metabolism, protein biogenesis and assembly processes and the response to stress. This opens new lines of research in PLD physiopathology and possible new therapeutic approaches of the disease. Third, our data suggest that in advanced stages of disease progression the number of pathways deregulated increased, probably due to secondary effects of the disease. In the same way, these results reinforce the idea of cyst growth passes with two big stages: cyst initiation and cyst progression[67]. Fourth, the protein-protein interaction analysis identified two important clusters, the most enriched and important focused on hepatic fibrinogens. And fifth, RT-qPCR and *Western Blotting* validations of selected candidates were consistent with SWATH MS quantitative proteomic data. Together, these results helped us to dig into the understanding and the targeting as possible therapies of cystogenesis and cystic progression/expansion. In addition, ANXA2 is a calcium-regulated membrane-binding protein related with hepatic fibrosis[219,220], which is a common feature in disease progression of PLD[94]. FIBA knockout mice present pancreatic cysts[221]. Furthermore, fibrinogens are associated with MAPK[222,223] and integrins[224], two pathways that have been shown to be effective as potential therapy for ADPKD in preclinical studies[75,211].

In summary, we identified several novel targets and pathways involved in physiopathology of PLD by quantitative proteomic SWATH MS technology. We emphasized the novel therapeutic opportunity presented by fibrinogens (and the other related identified proteins), mainly due the fact that all validations with significant differences carried out are related with fibrinogen-cluster. Nevertheless, this potential need to be confirmed in future preclinical studies, as well as

more functional studies to characterize the exact role of our target candidates in PLD. In conclusion, this thesis opens new future fields of research for the understanding and possible therapeutic targets for both PLD.

3. DISCUSSION CHAPTER 3

Extracellular matrix (ECM) alterations were identified decades ago in PKD and PLD patients, as well as in animal models[95,98,225]. In this study we identified ECM alterations as one of the main factors in cystogenesis, and we evaluated its therapeutic potential. First, quantitative differential proteomics of *Wild Types* and Mutant kidneys and livers from a murine model of ADPKD revealed the extracellular region as the most enrichment cellular component in polycystic kidney and liver disease. The accumulative percent of ECM in String® was >38% and >47% of cellular components in renal and hepatic quantitative differential proteomics, respectively. And, according to Reactome®, "Extracellular matrix organization" and "Degradation of the extracellular matrix" were some of the most enrichment molecular pathway and subpathway, respectively. In the same way, a transcriptomic study performed in kidneys of a rat model of PKD highlighted the ECM genes in PKD progression[225]. This important fact is due to a possible central role of interstitial fibrosis in the initiation and progression of cystogenesis. In addition, our proteomic study unmasked a list of targets that will be studied in future works and that will help us to identify new pathways and process related with cystogenesis, as well as possible new therapeutic approaches.

And second, our data showed that renal and hepatic cystogenesis in mouse occurs with a global deregulation of the expression of all MMPs groups. In the same way, we demonstrated that TIMPs, the natural and principal inhibitors of MMPs, are deregulated. In our results we can see that the usual alteration is the upregulation both MMPs (e.g., stromelysins) and TIMPs (e.g., TIMP1-2). However, some MMPs (e.g., MMP16 in kidney or MMP9 in liver) and TIMPs (e.g., TIMP3 in kidney) are deregulated in renal and hepatic cystogenesis. The role of MMPs and TIMPs in renal fibrosis was studied in knockout mice. *Mmp2*$^{-/-}$ and *Mmp7*$^{-/-}$ mice models have shown attenuation of renal fibrosis, as well as, in *Timp2*$^{-/-}$ mice[226–228]. Nevertheless, *Timp3*$^{-/-}$ mice has increased fibrosis suggesting a protective effect of *TIMP3*[228,229], and *Timp1*$^{-/-}$ mice not develop fibrosis due to a compensatory increase of

TIMP3[230]. These studies revealed a existence of a balance and complex patterns of expression with both up- and down-regulation between the different MMPs and TIMPs in fibrosis[92]. Our transcriptional study in polycystic kidney and liver disease goes in line with this idea. In summary, our data is consistent with the idea that polycystic kidney and liver disease progress with alterations in ECM and MMP activity, which contribute to accumulation of interstitial fibrosis and cyst growth and represent a potential therapeutic option.

Even though the potential for MMP inhibition as a therapeutic target for PKD remains unclear, future efforts should be directed to address this issue. Despite the amount of data about ECM and MMP alterations and fibrosis in PKD[93,106,195], hardly any specific therapeutic possibilities for this molecular pathways and processes were tested in *in vitro* and preclinical studies[74,231]. In a previous study, Urribarri *et al*.[74] describe metalloprotease hyperactivity in cystic cholangiocytes and the its inhibition with Marimastat inhibited hepatic cystogenesis in three-dimensional cultures and in a ARPKD rat model. Interestingly, the authors did not find significance differences in renal cystogenesis. Based in our data and the literature, we decide to evaluate Marimastat as therapeutic approach in our two PKD orthologous murine models. By contrast with Urribarri *et al*.[74], our results data shows an amelioration of the renal disease in an murine mouse model of ADPKD. In relation, other previous studies have speculated on the possibility of inhibiting MMPs as a therapeutic strategy in PKD[231,232]. Other important finding of the present work is that shows for the first time the specific inhibition of cysts derived from a specific nephron segment, renal collecting ducts. Future experiments in specific cell cultures from different nephron parts will be necessary to establish the molecular mechanisms downstream of this nephron segment specific phenotype. But our data is consistent in the reduction of hepatic cystogenesis finding a significant inhibition in both ADPKD and ARPKD orthologous murine models. In conclusion, our in vivo results showed that Marimastat decreases the severity of PKD and PLD, and we demonstrated that intervening abnormalities in ECM and MMP reduces renal and hepatic cystogenesis.

We also found that Marimastat treatment restores deregulation of MMPs and TIMPs expression. Significantly, these effects were observed in renal and hepatic cystogenesis and in both murine models. By contrast, some MMPs and TIMPs did not affect their expression

with treatment, and others were not deregulated in PKD or PLD, which again indicates the existence of a balance and reciprocal control between expression of different MMPs and TIMPs. Fibrosis parallels with the progression of the disease which was described as one of the major pathological features of PKD and PLD. ECM accumulation were found in PKD and PLD patients, as well as orthologous murine models[74,98,107–112], and also observed in early-stage of the disease in ADPKD patients[95]. Furthermore, MMPs alterations, TIMPs upregulation and increases of interstitial collagens are some of classical features of fibrosis[93,195] and are also supported by our data. So, we wanted to test the possible effect of Marimastat in fibrosis status in PKD and PLD. Our results show that Marimastat inhibited renal and hepatic fibrosis, with up to four fibrosis markers that decreased significantly in both ADPKD and ARPKD models. Our data indicates that Marimastat could be a new therapeutic approach to regulate renal and hepatic fibrosis in PKD and PLD. Next, we focused in upstream factors of MMPs such as the cytokine IL-6 and IL-8, as mentioned previously, are present in high levels in renal[117,118] and hepatic[119,120] cystic fluid and regulate MMP activity[74]. We found upregulation of *Il-6* and *Cxcl1* (IL-8 mouse homolog) in renal ADPKD but with respect to PLD we only find differences in *Cxcl1* expression. After Marimastat treatment, *Cxcl1* expression was restored but we did not observe differences in *Il-6* expression. Our data suggest the idea that IL-8 could be the central cytokine in regulate MMPs expression during cyst growth progression (**Figure 47**).

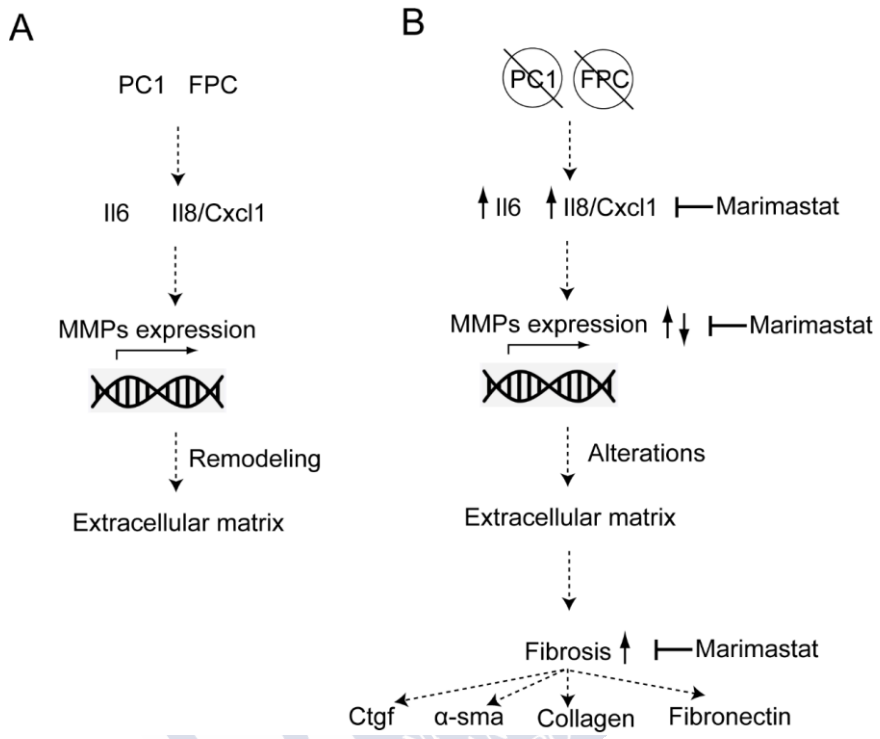

Figure 47. Schematic diagram of the working model proposed. (A) In healthy conditions, IL6 and Il8/Cxcl1 enhances the matrix metalloproteases (MMPs) expression, which remodeling the extracellular matrix (ECM). (B) *Pkd1* and *Pkhd1* mutations result in the absence or lack of functional PC1 and FPC, which triggers the renal and hepatic cystogenesis. In polycystic kidney and livers present significantly high levels of Il6 and Il8/Cxcl1, and this event is associated with a global deregulation (up or downregulation) of MMPs expression and consequently with alterations in ECM and an increase of fibrosis. Marimastat treatment decreases Il8/Cxcl1 and restores MMPs expression causing an amelioration of fibrosis and renal and hepatic cystogenesis. PC1: Polycystin-1; FPC: polyductin; Il6: interleukin-6; Il8: interleukin-8; Cxcl1: Chemokine (C-X-C motif) ligand 1; MMP: matrix metalloprotease; Ctgf: connective tissue growth factor; α-SMA: α -smooth muscle actin.

Finally, we tested Marimastat in combination with Tolvaptan. Tolvaptan is a highly potent and selective arginine vasopressin V2 receptor (AVP V2R) antagonist. Vasopressin is a hormone that induces reabsorption of water in the collecting duct by binding AVP V2R, which is upregulated in PKD patients[233,234] and also in cholangiocytes from ADPKD liver samples[198]. So, Tolvaptan blocks the reabsorption of water in collecting duct and in clinical trial its efficacy was demonstrated by reducing kidney volume in ADPKD patients[196,197].

Our study shows that Marimastat plus Tolvaptan delayed renal and hepatic cystogenesis in two PKD orthologous murine models. Considering that Marimastat and Tolvaptan function through different and independent mechanisms, combining both drugs produce synergistic beneficial effects on polycystic kidney and livers. These results reinforce the role of MMPs in PKD and PLD and its potential therapeutic.

4. DISCUSSION CHAPTER 4

Renal inflammation in ADPKD has been associated with the expression and accumulation of proinflammatory cytokines, including TNFα, IL-6, IL-8 or MCP1[116–118,204,235]. Our data show that the TWEAK/Fn14 axis is upregulated in *Pkd1* mutant kidneys of an orthologous murine mice model of ADPKD, both by RT-qPCR and Western Blot analysis. In the same way, ADPKD patients results are consistent with TWEAK/Fn14 axis activation since TWEAK was abundant in renal cyst fluid and urine and cyst epithelium expressed FN14. Finally, we provide functional in vivo evidence that the TWEAK/Fn14 axis contributes to ADPKD cyst progression, according to the "two-hit" model of cystogenesis, and that represent a potential therapeutic target (**Figure 48A**). Our findings of serum TWEAK levels similar to controls but high cyst fluid and urinary TWEAK in human ADPKD support a local origin of TWEAK, likely tubular epithelium, given that cyst fluid for analysis was clear. However, we cannot exclude a contribution by local leukocytes. In this regard, serum TWEAK is decreased in advanced CKD but may be increased in early CKD when this is due to inflammatory conditions such as systemic lupus erythematous[236,237]. The combined human and murine data in serum TWEAK suggests that ADPKD, per se, does not modulate serum TWEAK.

It has been debated whether inflammation is a driving force for cyst formation or a consequence of the pathology[113,195]. On the other hand, studies from ADPKD conditional knockout models (which allow us to delete *Pkd1* gene in different kidney development points) have demonstrated that *Pkd1* deletion in mature kidneys delayed cyst formation compared with deletion before postnatal day 12 or with germinal knockout in utero[70,147]. This lack of cystic disease in mature kidneys has provided an opportunity to determine what factors, or third

hits, might trigger cystogenesis in rodent models[61]; including ischemia[238,239], renal injury [240,241] or nephrotoxicity[242]. In this context of *Pkd1* loss without a cystic phenotype (the non-cystic window), TWEAK promotes cyst initiation or cystogenesis. In the same way, in the cystic disease context (cystic window, with *Pkd1* inactivation before p12), treatment with TWEAK accelerates kidney and cystic disease progression. These results suggest that inflammation and specifically, the inflammatory cytokine TWEAK, can play a key role in defining the rate of cyst initiation and development in ADPKD.

Therapeutic modulation of the Fn14/TWEAK axis has been successful in preclinical model of different kidney diseases as AKI, kidney fibrosis, lipid-induced kidney injury or lupus nephritis [124,168,171,206,243,244]. Furthermore, clinical trials targeting the Fn14/TWEAK axis were performed in rheumatoid arthritis[127] (NCT00771329), lupus nephritis (study ATLAS, NCT01499355), muscle atrophy (NCT01943513) and in patients with advanced solid tumors (NCT00738764)[125]. We have now modulated the Fn14/TWEAK axis in a murine orthologous mice ADPKD model by administering neutralizing anti-TWEAK antibodies. Our data shows that anti-TWEAK slows cystic disease progression and improves renal function in murine ADPKD animal model, without apparent signs of kidney toxicity. TWEAK caused a clear pro-cystogenic role in later stage (p45), and anti-TWEAK enhanced cyst progression in medium-term model (p30), these variances in the mice life-time can be explained by the differential effect of administrating a stimulus or a blocker, as well as the different inflammatory and disease status at different times.

Cyst growth in ADPKD involves two main stages: cyst initiation and cyst progression (**Figure 48A**). Initiation is induced by a deficiency in mature Polycystin-1 or -2 (PC1 and PC2) protein caused by pathogenic mutations in the *PKD1* and *PKD2* genes, respectively. Disease progression incorporates other players and interstitial inflammation was proposed as a key process in progressive cyst enlargement. Our results support that a single inflammatory mediator, TWEAK, plays a role in cyst progression or second step of cyst growth.

In support of this idea, we found that anti-TWEAK treatment restored proliferative and inflammation pathways related with ADPKD progression (**Figure 48B**). In kidney cells, TWEAK can activate MAPKs and the phosphoinositide 3-kinase/Akt pathway[123,169,245]. The ERK/MAPK and AKT/mTOR signaling pathways are upregulated in

ADPKD kidneys, and their inhibition slows ADPKD progression[211,246–248]. Similarly, we found upregulation of p-ERK/ERK and p-p38/p38, as well as of total-AKT and p-AKT in ADPKD kidneys. It has been reported that total-AKT protein level is elevated in mutant kidneys from several animal models of ADPKD [77,213,249,250], so our findings are in line with the literature. Furthermore, anti-TWEAK treatment restored p-p38/p38, total-AKT and p-AKT to control values. Our data favor the view that TWEAK has a pro-proliferative role on several signaling pathways in kidney tubules and that the therapeutic modulation of TWEAK can be an effective treatment in ADPKD. These results are in line with the pro-proliferative activity of TWEAK on kidney tubular cells and kidney fibroblasts, that was observed both in cultured cells and in vivo and contributed to kidney growth post-unilateral nephrectomy[169,172].

On the other hand, TWEAK induces renal tubulointerstitial inflammation, chemokine expression[168,169,205], macrophage recruitment[168] and NF-κB pathway activation[171,206]; signaling pathways also widely studied in ADPKD[195]. In this regard, TWEAK or Fn14 blockade reduced inflammatory gene expression in experimental lupus nephritis[244] and reduced pro-inflammatory chemokines and macrophage recruitment in experimental AKI[168]. We now observed that anti-TWEAK effectively decreased the gene expression of *Arg1*, *Mcp1*, and macrophage recruitment, assessed by the total mouse macrophage marker F4/80, again resulting in decreased cyst progression and improvement in BUN levels. Two different studies reported that inhibition of *Arg1* or *Mcp1* delays cyst growth, so it is biologically significant that anti-TWEAK treatment reduced their expression in our study[82,121]. M2 macrophages were reported to be abundant infiltrating cells in ADPKD and pharmacological inhibition of ARG1 slowed cyst progression and reduced proliferative indices [121]. Also, these authors enrich the characterization of macrophage population function in ADPKD kidneys. Our data are in line with these findings since macrophages in advanced ADPKD present mainly an M2-phenotype rather than an M1 phenotype. Furthermore, in a further study, treatment with VEGFC reduced *Arg1* expression and M2 macrophage infiltration and improved cystic disease[251]. Regarding MCP1, a double knockout of both *Mcp1* and *Pkd1,* resulted in suppressed macrophage accumulation and decreased cyst growth[82]. In this regard, high urinary

MCP1 was a biomarker of disease progression in ADPKD patients treated with Tolvaptan[252–254].

Some limitations should be acknowledged. Thus, human data were observational, and the murine immune system has several differences with the human system. However, the intervention studies in an orthologue model of the most common and severe form of human ADPKD, involving both activation and inactivation of the TWEAK/Fn14 axis and the study of both male and female animals, were consistent and aligned with the human data. Furthermore, a therapeutic tool already available and tested in humans was found effective in limiting cystogenesis and preserving kidney function, which may facilitate clinical translation.

USC UNIVERSIDADE DE SANTIAGO DE COMPOSTELA

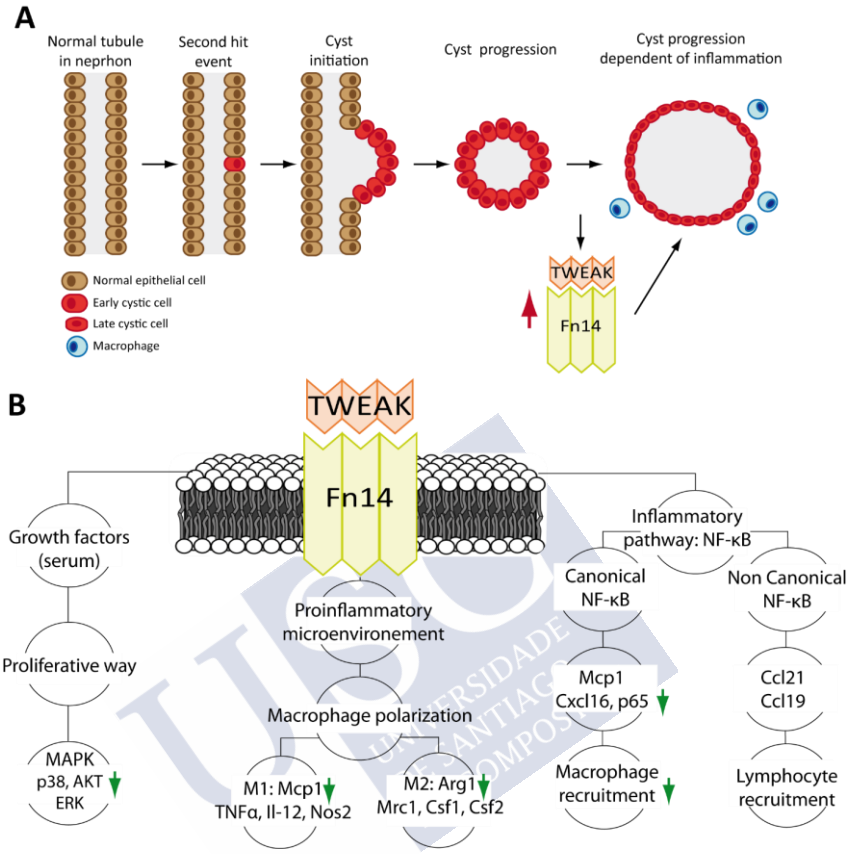

Figure 48. Proposed model of TWEAK in regulation of cyst progression in ADPKD. (A) Mechanism of cyst formation and expansion in ADPKD. In ADPKD nephrons, all tubular epithelial cells contain one mutated and one unaffected copy of *PKD1* or *PKD2*. According to the "two-hit" model of cystogenesis, a second mutation may eventually occur in the unaffected allele in an individual tubular epithelial cell. When the protein level of functional Polycystin-1 or Polycystin-2 (products of *PKD1* and *PKD2*, respectively) fall below a critical threshold, cyst formation starts. Once cysts are formed, multiple molecular pathways are deregulated, and cysts progressively increase in size. During disease progression, the advanced stage is characterized by macrophage infiltration, pro-inflammatory chemoattractants and inflammation-dependent injury. In this study, we reported that TWEAK and Fn14 are upregulated in ADPKD, and they contributed to cystogenesis in a murine ADPKD model. (B) TWEAK pathway. TNF-like weak inducer of apoptosis (TWEAK) is a trimeric cytokine that binds to the Fn14 receptor Fn14 after trimerization. TWEAK and Fn14 are present in epithelial renal cells and regulate cell proliferation, inflammation, NF-κB activation and other pathways. We report that targeting TWEAK with a specific treatment reduced the expression of key ADPKD -related protein markers like AKT and p38 (proliferative way), *Arg1* (M2 macrophage polarization), *Mcp1* (M1 macrophage polarization and canonical NF-κB activation), p65 (canonical NF-κB activation) and reduced macrophage infiltration. Our results suggest that the TWEAK/Fn14 axis is a new potential therapeutic target for ADPKD.

5. DISCUSSION CHAPTER 5

Genetic interaction between *Pkhd1* and *Pkd1*, the most common genes of ARPKD and ADPKD respectively, was previously described[69]. Following, the knowledge in this field been debated and expanded [34,137,138,144,255,256]. Orthologous murine *in vivo* models allow us to modulate the timing expression and combinate different gene alleles. Here, we reported two new murine double knockouts of *Pkhd1* and *Pkd1*. After phenotype characterization we found a synergist and additive effect combining embryonic and congenic alleles ($Pkhd1^{del3-4/del3-4}$ and $Pkd1^{del2-4/+}$ and $Pkd1^{cond/+}$;*Tam-Cre*$^{+}$). However, using adult conditionate and homozygous allele of *Pkd1* ($Pkd1^{cond/cond}$;*Tam-Cre*$^{+}$) we have discovered an unexpected milder renal cystic phenotype in combination with *Pkhd1*. Our study highlighted the central role of threshold and timing deletion of *Pkd1*/PC1 for cyst formation in PKD. Also, we generated two interesting and novel PKD models for future studies in order to investigate the possible key pathways of cystogenesis.

Different studies have reported genetic interaction between *Pkd1* and *Pkhd1* in rodent models. All of them described mild cystic disease phenotypes of *Pkd1* and/or *Pkhd1* enhanced their severity in combination[69,137,138]. First, we generated *Pkhd1* and *Pkd1* double knockout model (DKO) and we demonstrated that two not-pathological mutant alleles ($Pkhd1^{del3-4/del3-4}$ and $Pkd1^{del2-4/+}$) in combination developed cyst formation and cyst progression. Next, we decided to use a conditional knockout in heterozygosity of *Pkd1* ($Pkd1^{cond/+}$;*Tam-Cre*$^{+}$) and deleted it at different life points. Cyst formation and disease severity was according to timing of *Pkd1* gene inactivation. It is important to emphasize that both animal models present the same mutation, a complete deletion of exons 2 to 4 of *Pkd1* gene[68,70]. Likewise, we do not rule out a possible dose effect in PC1 in the phenotypes described and not only a *Pkd1* deletion timing effect, because the phenotype with more severe polycystic disease correspond with embryonic deletion and also with the model with a hypothetic less PC1 dose. Threshold and dosage model in ADPKD was first reported in *trans*-heterozygous[257,258] and after validated in *in vitro* and *in vivo* studies[34,71,137,143,259]. Specifically, some of these studies suggest that *Pkd1*/PC1 is the central determinant of cyst formation. Fedeles and colleagues showed that PC1 overexpression rescued PKD and ADPLD phenotypes[137]. In the same way, several ADPLD genes involved in PC1

biogenesis were reported[33–35,260]. Our data is consistent with the idea that *Pkd1*/PC1 has a central role in cystogenesis.

Interestingly, we found an improvement of renal cystic phenotype in DcKO mice (*Pkhd1*$^{del3\text{-}4/del3\text{-}4}$;*Pkd1*$^{cond/cond}$;*Tam-Cre*$^{+}$). Two different studies using *in vitro* models were reported that FPC loss not affect in PC1 biogenesis and location[34,138]. Our results showed that *Pkhd1* heterozygous not modulates the ADPKD disease severity. By other hand and contrary of renal cystic disease, hepatic phenotype developed an additive effect of both genes and in both double knockouts (DKO and DcKO). Our data and these previous studies suggest that genetic interaction between *Pkdh1* and *Pkd1* is indirect and reveal distinct thresholds for both genes.

Deletion of several related-cilia genes in animal models causes PKD, as well as *Kif3a*[130,261], *Ift88*[262], *Ift20*[263], *Ift140*[264], *Ift139*[265], *Arl13b*[266] and finally *Tulp3*[267]. These studies in mouse have identified the called ciliopathic PKD or cPKD, which is inherited recessively and developed renal cystogenesis (and other cilia structural defects and ciliopathy phenotypes), and its specific mechanism cilia-dependent cyst activation or CDCA. Interestingly, Ma et colleagues[130] have demonstrated that loss of cilia suppresses renal cyst growth suggesting that CDCA pathway is active in the absence of polycystins (PC1 and PC2) but needs an intact and complete functional cilium. Recently, Gallagher and Somlo[139] have reported that this loss of cilia not slow liver disease progression in ARPKD but can abrogate the *Pkd1* dosage-dependent worsened in a context of *Pkhd1* and *Pkd1* genetic interaction. These data suggest that genetic interaction between both *Pkhd1* and *Pkd1* is indirect and they do not function in a common CDCA-related pathway in liver cystogenesis. In our study, we observed an amelioration of renal cyst growth in DcKO mice but a worse polycystic hepatic phenotype. In the same way, cilia length was recently proposed as therapeutic target for renal and hepatic cyst formation[268].We hypothesize that the ciliogenesis-cilia length and/or CDCA pathway is somehow altered in our digenic model (DcKO), and that this mechanism is different in the cyst formation in kidney and liver concerning also different thresholds of functional protein in both tissues. Future experiments will be required to validate this hypothesis.

CONCLUSIONS

USC UNIVERSIDADE DE SANTIAGO DE COMPOSTELA

CONCLUSIONS

1. We have developed CystAnalyser as a software tool for the quantitative analysis of histological images from cystic kidney and liver mice samples, in order to quantify their cystic index reliably and accurately, cyst number and cyst size in preclinical studies. Also, CystAnalyser has proven to be significantly more sensitive and reliable, and less subjective, in quantifying the cystic area, cyst number and size, than the most used software in cystic disease research (ImageJ).

2. We reported a novel proteomic quantitative study based on SWATH MS technology comparing proteomes of *Wild Type* and polycystic livers. Several and novel pathways and targets were identified expanding the knowledge about molecular mechanisms in PLD field and highlighting the fibrinogen-cluster as a new possible therapeutic target.

3. Our findings reported here highlighted the pathogenic role of ECM and MMPs in the progression of renal and hepatic cystogenesis. In the same way, the MMPs inhibitor Marimastat was tested in two PKD orthologous murine models showing an amelioration of renal disease with a specific inhibition of cysts derived from collecting ducts and an inhibition of hepatic cystogenesis. In addition, we demonstrated that this pharmacological intervention based on inhibition of MMPs controls fibrosis progression and it is a plausible therapeutic approach for PKD and PLD. Finally, in combination with Tolvaptan, Marimastat delayed renal and hepatic cystic disease showing a mutual synergist effect.

4. We found that the TWEAK/Fn14 axis is upregulated in human ADPKD and both rapidly and slowly progressive murine models, where it promotes cyst initiation and progression in an orthologous *Pkd1* mutant murine mice model. Furthermore, anti-TWEAK treatment effectively slows cyst growth decreasing pro-proliferative, pro-inflammatory markers and macrophage recruitment. These results suggest that inhibition of TWEAK/Fn14 axis and the pro-inflammatory component can be an effective therapeutic approach for ADPKD.

5. We generated and characterized two different and novel genetic interactions between *Pkhd1* and *Pkd1* genes in mice models. Our study highlighted the central role of *Pkd1*/PC1 for cystogenesis, the PKD as a gene-functional protein dosage-dependent disorder and the possibility of different thresholds for both genes and both kidney and liver. Finally, these double knockout models may improve knowledge of key pathways related with cyst formation in PKD.

USC UNIVERSIDADE DE SANTIAGO DE COMPOSTELA

BILIOGRAPHY

BIBLIOGRAPHY

1. Wilson, P. D. Polycystic Kidney Disease. *N. Engl. J. Med.* 151–164 (2004).
2. Harris, P. C. & Torres, V. E. V. E. Polycystic kidney disease. *Annu Rev Med* **60**, 321–337 (2009).
3. Song, X. *et al.* Prevalence Estimates of Polycystic Kidney and Liver Disease by Population Sequencing. *J. Am. Soc. Nephrol.* **29**, 2593–2600 (2018).
4. Suwabe, T. *et al.* Epidemiology of autosomal dominant polycystic kidney disease in Olmsted county. *Clin. J. Am. Soc. Nephrol.* **15**, 69–79 (2020).
5. Cordido, A., Besada-Cerecedo, L. & García-González, M. A. M. A. M. A. The Genetic and Cellular Basis of Autosomal Dominant Polycystic Kidney Disease—A Primer for Clinicians. *Front. Pediatr* **5**, 279 (2017).
6. Cornec-Le Gall, E., Alam, A. & Perrone, R. D. Autosomal dominant polycystic kidney disease. *Lancet* **393**, 919–935 (2019).
7. Bergmann, C. *et al.* Polycystic kidney disease. *Nat. Rev. Dis. Prim.* **4**, 50 (2018).
8. Loftus, H. & Ong, A. C. M. Cystic kidney diseases: Many ways to form a cyst. *Pediatr. Nephrol.* **28**, 33–49 (2013).
9. Torres, V. E., Harris, P. C. & Pirson, Y. Autosomal dominant polycystic kidney disease. *Lancet* **369**, 1287–1301 (2007).
10. Harris, P. C. & Rossetti, S. Molecular diagnostics for autosomal dominant polycystic kidney disease. *Nat. Rev. Nephrol.* **6**, 197–206 (2010).
11. Bergmann, C. ARPKD and early manifestations of ADPKD: the original polycystic kidney disease and phenocopies. *Pediatr. Nephrol.* **30**, 15–30 (2015).
12. Zerres, K. *et al.* Prenatal diagnosis of autosomal recessive polycystic kidney disease (ARPKD): Molecular genetics, clinical experience, and fetal morphology. *Am. J. Med. Genet.* **76**, 137–144 (1998).
13. Igarashi, P. & Somlo, S. Genetics and Pathogenesis of Polycystic Kidney Disease. *J. Am. Soc. Nephrol.* **13**, 2384–2398 (2002).
14. Adeva, M. *et al.* Clinical and molecular characterization defines a broadened spectrum of autosomal recessive polycystic kidney disease (ARPKD). *Medicine (Baltimore).* **85**, 1–21 (2006).
15. Cnossen, W. R. & Drenth, J. P. Polycystic liver disease: an overview of pathogenesis, clinical manifestations and management. *Orphanet J. Rare Dis.* **9**, 69 (2014).

16. Santos-Laso, A. *et al.* New Advances in Polycystic Liver Diseases. *Semin. Liver Dis.* **37**, 045–055 (2017).
17. Gunay-Aygun, M. Liver and kidney disease in ciliopathies. *Am. J. Med. Genet. Part C Semin. Med. Genet.* **151**, 296–306 (2009).
18. Reeders, S. T. *et al.* Regional localization of the autosomal dominant polycystic kidney disease locus. *Genomics* **3**, 150–155 (1988).
19. Germino, G. G. *et al.* The gene for autosomal dominant polycystic kidney disease lies in a 750-kb CpG-rich region. *Genomics* **13**, 144–151 (1992).
20. Somlo, S. *et al.* Fine genetic localization of the gene for autosomal dominant polycystic kidney disease (PKD1) with respect to physically mapped markers. *Genomics* **13**, 152–158 (1992).
21. Burn, T. C. *et al.* Analysis of the genomic sequence for the autosomal dominant polycystic kidney disease (PKD1) gene predicts the presence of a leucine-rich repeat: The AMERICAN pkd1 consortium (apkd1 consortium). *Hum. Mol. Genet.* **4**, 575–582 (1995).
22. Bogdanova, N. *et al.* Homologues to the first gene for autosomal dominant polycystic kidney disease are pseudogenes. *Genomics* **74**, 333–341 (2001).
23. Van Raay, T. J. *et al.* A 2.5 kb polypyrimidine tract in the PKD1 gene contains at least 23 H-DNA-forming sequences. *Microb. Comp. Genomics* **1**, 317–327 (1996).
24. Daoust, M. C., Reynolds, D. M., Bichet, D. G. & Somlo, S. Evidence for a third genetic locus for autosomal dominant polycystic kidney disease. *Genomics* **25**, 733–736 (1995).
25. Lens, X. M. *et al.* An integrated genetic and physical map of the autosomal recessive polycystic kidney disease region. *Genomics* **41**, 463–466 (1997).
26. Lu, H. *et al.* Mutations in DZIP1L, which encodes a ciliary-transition-zone protein, cause autosomal recessive polycystic kidney disease. *Nat. Genet.* **49**, 1025–1034 (2017).
27. Nagasawa, Y. *et al.* Identification and Characterization of Pkhd1, the Mouse Orthologue of the Human ARPKD Gene. *J. Am. Soc. Nephrol.* **13**, 2246–2258 (2002).
28. Hartung, E. A. & Guay-Woodford, L. M. Polycystic kidney disease: DZIP1L defines a new functional zip code for autosomal recessive PKD. *Nat. Rev. Nephrol.* **13**, 519–520 (2017).
29. Li, A. *et al.* Mutations in PRKCSH cause isolated autosomal dominant polycystic liver disease. *Am. J. Hum. Genet.* **72**, 691–703 (2003).
30. Drenth, J. P. H., Te Morsche, R. H. M., Smink, R., Bonifacino, J. S. & Jansen, J. B. M. J. Germline mutations in PRKCSH are associated

with autosomal dominant polycystic liver disease. *Nat. Genet.* **33**, 345–347 (2003).
31. Davila, S. *et al.* Mutations in SEC63 cause autosomal dominant polycystic liver disease. *Nat. Genet.* **36**, 575–577 (2004).
32. Cnossen, W. R. *et al.* Whole-exome sequencing reveals LRP5 mutations and canonical Wnt signaling associated with hepatic cystogenesis. *Proc. Natl. Acad. Sci.* **111**, 5343–5348 (2014).
33. Porath, B. *et al.* Mutations in GANAB, Encoding the Glucosidase IIα Subunit, Cause Autosomal-Dominant Polycystic Kidney and Liver Disease. *Am. J. Hum. Genet.* **98**, 1193–1207 (2016).
34. Besse, W. *et al.* Isolated polycystic liver disease genes define effectors of polycystin-1 function. *J. Clin. Invest.* (2017) doi:10.1172/JCI90129.
35. Besse, W. *et al.* ALG9 Mutation Carriers Develop Kidney and Liver Cysts. *J. Am. Soc. Nephrol.* ASN.2019030298 (2019) doi:10.1681/ASN.2019030298.
36. Lee-Law, P. Y., van de Laarschot, L. F. M., Banales, J. M. & Drenth, J. P. H. Genetics of polycystic liver diseases. *Curr. Opin. Gastroenterol.* **35**, 65–72 (2019).
37. Perugorria, M. J. & Banales, J. M. Genetics: Novel causative genes for polycystic liver disease. *Nat. Rev. Gastroenterol. Hepatol.* **14**, 391–392 (2017).
38. Qian, F. *et al.* PKD1 interacts with PKD2 through a probable coiled-coil domain. *Nat. Genet.* **16**, 179–183 (1997).
39. Hughes, J. *et al.* The polycystic kidney disease 1 (PKD1) gene encodes a novel protein with multiple cell recognition domains. *Nat. Genet.* **10**, (1995).
40. Onuchic, L. F. *et al.* PKHD1, the polycystic kidney and hepatic disease 1 gene, encodes a novel large protein containing multiple immunoglobulin-like plexin-transcription-factor domains and parallel beta-helix 1 repeats. *Am. J. Hum. Genet.* **70**, 1305–17 (2002).
41. Ward, C. J. *et al.* The gene mutated in autosomal recessive polycystic kidney disease encodes a large, receptor-like protein. *Nat. Genet.* **30**, 259–269 (2002).
42. Grieben, M. *et al.* Structure of the polycystic kidney disease TRP channel Polycystin-2 (PC2). *Nat. Struct. Mol. Biol.* **24**, 114–122 (2016).
43. Torres, V. E. & Harris, P. C. Autosomal dominant polycystic kidney disease: The last 3 years. *Kidney Int.* **76**, 149–168 (2009).
44. Hanaoka, K. *et al.* Co-assembly of polycystin-1 and -2 produces unique cation-permeable currents. *Nature* **408**, 990–994 (2000).
45. Su, Q. *et al.* Structure of the human PKD1 / PKD2 complex. *Science*

(80-.). **9819**, 1–21 (2018).
46. Douguet, D., Patel, A. & Honoré, E. Structure and function of polycystins: insights into polycystic kidney disease. *Nat. Rev. Nephrol.* (2019) doi:10.1038/s41581-019-0143-6.
47. Kaimori, J. ya *et al.* Polyductin undergoes notch-like processing and regulated release from primary cilia. *Hum. Mol. Genet.* **16**, 942–956 (2007).
48. Ward, C. J. *et al.* Cellular and subcellular localization of the ARPKD protein; fibrocystin is expressed on primary cilia. *Hum. Mol. Genet.* **12**, 2703–2710 (2003).
49. Zhang, M.-Z. *et al.* PKHD1 protein encoded by the gene for autosomal recessive polycystic kidney disease associates with basal bodies and primary cilia in renal epithelial cells. *Proc. Natl. Acad. Sci.* **101**, 2311–2316 (2004).
50. Grantham, J. J. Autosomal Dominant Polycystic Kidney Disease. *N. Engl. J. Med.* **359**, 1477–1485 (2008).
51. Hwang, Y. H. Y.-H. *et al.* Refining Genotype-Phenotype Correlation in Autosomal Dominant Polycystic Kidney Disease. *J. Am. Soc. Nephrol.* **27**, 1861–1868 (2016).
52. Pei, Y. A 'two-hit' model of cystogenesis in autosomal dominant polycystic kidney disease? *Trends Mol. Med.* **7**, 151–6 (2001).
53. Lu, W. *et al.* Perinatal lethality with kidney and pancreas defects in mice with a targetted pkd1 mutation. *Nature Genetics* vol. 17 179–181 (1997).
54. Wu, G. *et al.* Somatic inactivation of Pkd2 results in polycystic kidney disease. *Cell* **93**, 177–188 (1998).
55. Paterson, A. D., Wang, K. R., Lupea, D., St. George-Hyslop, P. & Pei, Y. Recurrent fetal loss associated with bilineal inheritance of type 1 autosomal dominant polycystic kidney disease. *Am. J. Kidney Dis.* **40**, 16–20 (2002).
56. Qian, F., Watnick, T. J., Onuchic, L. F. & Germino, G. G. The molecular basis of focal cyst formation in human autosomal dominant polycystic kidney disease type I. *Cell* **87**, 979–987 (1996).
57. Watnick, T. J. *et al.* Somatic mutation in individual liver cysts supports a two-hit model of cystogenesis in autosomal dominant polycystic kidney disease. *Mol. Cell* **2**, 247–251 (1998).
58. Pei, Y. *et al.* Somatic PKD2 mutations in individual kidney and liver cysts support a 'two-hit' model of cystogenesis in type 2 autosomal dominant polycystic kidney disease. *J. Am. Soc. Nephrol.* **10**, 1524–1529 (1999).
59. Janssen, M. J. *et al.* Secondary, somatic mutations might promote cyst formation in patients with autosomal dominant polycystic liver

disease. *Gastroenterology* **141**, 2056-2063.e2 (2011).
60. Janssen, M. J. *et al.* Somatic loss of polycystic disease genes contributes to the formation of isolated and polycystic liver cysts. *Gut* **64**, 688–690 (2015).
61. Saigusa, T. & Darwin Bell, P. Molecular pathways and therapies in autosomal-dominant polycystic kidney disease. *Physiology* **30**, 195–207 (2015).
62. Torres, V. E. *et al.* Cyst Number but Not the Rate of Cystic Growth Is Associated with the Mutated Gene in Autosomal Dominant Polycystic Kidney Disease. *J. Am. Soc. Nephrol.* **17**, 3013–3019 (2006).
63. Bae, K. T. *et al.* Growth Pattern of Kidney Cyst Number and Volume in Autosomal Dominant Polycystic Kidney Disease. *Clin. J. Am. Soc. Nephrol.* **14**, 823–833 (2019).
64. Hoevenaren, I. A. *et al.* Polycystic liver: clinical characteristics of patients with isolated polycystic liver disease compared with patients with polycystic liver and autosomal dominant polycystic kidney disease. *Liver Int.* **28**, 264–270 (2010).
65. Bae, K. T. *et al.* Magnetic resonance imaging evaluation of hepatic cysts in early autosomal-dominant polycystic kidney disease: the Consortium for Radiologic Imaging Studies of Polycystic Kidney Disease cohort. *Clin. J. Am. Soc. Nephrol.* **1**, 64–69 (2006).
66. Grantham, J. J. *et al.* Determinants of renal volume in autosomal-dominant polycystic kidney disease. *Kidney Int.* **73**, 108–116 (2007).
67. Happé, H. & Peters, D. J. M. Translational research in ADPKD: lessons from animal models. *Nat. Rev. Nephrol.* **10**, 587–601 (2014).
68. Piontek, K. B. *et al.* A Functional Floxed Allele of Pkd1 that Can Be Conditionally Inactivated In Vivo. *J. Am. Soc. Nephrol.* **15**, 3035–3043 (2004).
69. Garcia-Gonzalez, M. A. *et al.* Genetic interaction studies link autosomal dominant and recessive polycystic kidney disease in a common pathway. *Hum. Mol. Genet.* **16**, 1940–1950 (2007).
70. Piontek, K., Menezes, L. F., Garcia-Gonzalez, M. A., Huso, D. L. & Germino, G. G. A critical developmental switch defines the kinetics of kidney cyst formation after loss of Pkd1. *Nat. Med.* **13**, 1490–1495 (2007).
71. Hopp, K. *et al.* Functional polycystin-1 dosage governs autosomal dominant polycystic kidney disease severity. *J. Clin. Invest.* **122**, 1–17 (2012).
72. Menezes, L. F. *et al.* Network Analysis of a Pkd1-Mouse Model of Autosomal Dominant Polycystic Kidney Disease Identifies HNF4α as a Disease Modifier. *PLoS Genet.* **8**, (2012).

73. Williams, S. S. *et al.* Tissue-specific regulation of the mouse Pkhd1 (ARPKD) gene promoter. *Am. J. Physiol. Renal Physiol.* **307**, F356-68 (2014).
74. Urribarri, A. D. *et al.* Inhibition of metalloprotease hyperactivity in cystic cholangiocytes halts the development of polycystic liver diseases. *Gut* **63**, 1658–1667 (2014).
75. Lee, K., Boctor, S., Barisoni, L. M. C. & Gusella, G. L. Inactivation of Integrin- 1 Prevents the Development of Polycystic Kidney Disease after the Loss of Polycystin-1. *J. Am. Soc. Nephrol.* **26**, 888–895 (2015).
76. Lakhia, R. *et al.* MicroRNA-21 Aggravates Cyst Growth in a Model of Polycystic Kidney Disease. *J. Am. Soc. Nephrol.* **27**, 2319–30 (2015).
77. Rogers, K. A. *et al.* Differences in the timing and magnitude of Pkd1 gene deletion determine the severity of polycystic kidney disease in an orthologous mouse model of ADPKD. *Physiol. Rep.* **4**, e12846 (2016).
78. Warner, G. *et al.* Food Restriction Ameliorates the Development of Polycystic Kidney Disease. *J. Am. Soc. Nephrol.* **27**, 1437–1447 (2016).
79. Chiaravalli, M. *et al.* 2-Deoxy-D-Glucose Ameliorates PKD Progression. *J. Am. Soc. Nephrol.* **27**, 1958–1969 (2016).
80. Cebotaru, L. *et al.* Inhibition of histone deacetylase 6 activity reduces cyst growth in polycystic kidney disease. *Kidney Int.* **90**, 90–99 (2016).
81. Hajarnis, S. *et al.* MicroRNA-17 family promotes polycystic kidney disease progression through modulation of mitochondrial metabolism. *Nat. Commun.* **8**, 1–15 (2017).
82. Cassini, M. F. *et al.* Mcp1 Promotes Macrophage-Dependent Cyst Expansion in Autosomal Dominant Polycystic Kidney Disease. *J. Am. Soc. Nephrol.* ASN.2018050518 (2018) doi:10.1681/ASN.2018050518.
83. Kraus, A. *et al.* HIF-1α promotes cyst progression in a mouse model of autosomal dominant polycystic kidney disease. *Kidney Int.* **94**, 887–899 (2018).
84. Irazabal, M. V. *et al.* Imaging Classification of Autosomal Dominant Polycystic Kidney Disease: A Simple Model for Selecting Patients for Clinical Trials. *J. Am. Soc. Nephrol.* **26**, 160–172 (2015).
85. Guay-Woodford, L. M. Autosomal recessive polycystic kidney disease: the prototype of the hepato-renal fibrocystic diseases. *J Pediatr Genet* **3**, 89–101 (2014).
86. Bergmann, C. Spectrum of Mutations in the Gene for Autosomal

Recessive Polycystic Kidney Disease (ARPKD/PKHD1). *J. Am. Soc. Nephrol.* **14**, 76–89 (2003).

87. Gansevoort, R. T. *et al.* Recommendations for the use of tolvaptan in autosomal dominant polycystic kidney disease: A position statement on behalf of the ERA-EDTA Working Groups on Inherited Kidney Disorders and European Renal Best Practice. *Nephrol. Dial. Transplant.* **31**, 337–348 (2016).
88. Baur, B. P. & Meaney, C. J. Review of tolvaptan for Autosomal dominant polycystic kidney disease. *Pharmacotherapy* **34**, 605–616 (2014).
89. Chebib, F. T. *et al.* A Practical Guide for Treatment of Rapidly Progressive ADPKD with Tolvaptan. *J. Am. Soc. Nephrol.* **29**, (2018).
90. Harris, P. C. & Torres, V. E. Genetic mechanisms and signaling pathways in autosomal dominant polycystic kidney disease. *J. Clin. Invest.* **124**, 2315–2324 (2014).
91. Riella, C., Czarnecki, P. G. & Steinman, T. I. Therapeutic advances in the treatment of polycystic kidney disease. *Nephron - Clin. Pract.* **128**, 297–302 (2014).
92. Parrish, A. R. *Matrix Metalloproteinases in Kidney Disease: Role in Pathogenesis and Potential as a Therapeutic Target*. *Matrix Metalloproteinases and Tissue Remodeling in Health and Disease: Target Tissues and Therapy* vol. 148 (Elsevier Inc., 2017).
93. Norman, J. Fibrosis and progression of Autosomal Dominant Polycystic Kidney Disease (ADPKD). *Biochim. Biophys. Acta - Mol. Basis Dis.* **1812**, 1327–1336 (2011).
94. Perugorria, M. J. *et al.* Polycystic liver diseases: advanced insights into the molecular mechanisms. *Nat. Rev. Gastroenterol. Hepatol.* **11**, 750–61 (2014).
95. Wilson, P. D., Hreniuk, D. & Gabow, P. A. Abnormal extracellular matrix and excessive growth of human adult polycystic kidney disease epithelia. *J. Cell. Physiol.* **150**, 360–369 (1992).
96. Ebihara, I. *et al.* Altered extracellular matrix component gene expression in murine polycystic kidney. *Ren. Physiol. Biochem.* **18**, 73–80 (1995).
97. Wilson, P. D., Norman, J. T., Kuo, N. T. & Burrow, C. R. Abnormalities in extracellular matrix regulation in autosomal dominant polycystic kidney disease. *Contrib. Nephrol.* **118**, 126–134 (1996).
98. Murray, S. L. *et al.* Matrix metalloproteinase activity in human intrahepatic biliary epithelial cell lines from patients with autosomal dominant polycystic kidney disease. *Connect. Tissue Res.* **33**, 249–

256 (1996).
99. Ramasubbu, K., Gretz, N. & Bachmann, S. Increased Epithelial Cell Proliferation and Abnormal Extracellular Matrix in Rat Polycystic Kidney Disease. *J. Am. Soc. Nephrol.* **9**, (1998).
100. Seeger-Nukpezah, T. & Golemis, E. A. The extracellular matrix and ciliary signaling. *Curr. Opin. Cell Biol.* **24**, 652–61 (2012).
101. Short, K. M. & Smyth, I. M. The contribution of branching morphogenesis to kidney development and disease. *Nature Reviews Nephrology* vol. 12 754–767 (2016).
102. Pohl, M., Sakurai, H., Bush, K. T. & Nigam, S. K. Matrix metalloproteinases and their inhibitors regulate in vitro ureteric bud branching morphogenesis. *Am. J. Physiol. - Ren. Physiol.* **279**, (2000).
103. Jackson, B. C., Nebert, D. W. & Vasiliou, V. Update of human and mouse matrix metalloproteinase families. *Hum. Genomics* **4**, 194–201 (2010).
104. Jabłońska-Trypuć, A., Matejczyk, M. & Rosochacki, S. Matrix metalloproteinases (MMPs), the main extracellular matrix (ECM) enzymes in collagen degradation, as a target for anticancer drugs. *J Enzym. Inhib Med Chem* **31**, 177–183 (2016).
105. Khokha, R., Murthy, A. & Weiss, A. Metalloproteinases and their natural inhibitors in inflammation and immunity. *Nat. Rev. Immunol.* **13**, 649–665 (2013).
106. Catania, J. M., Chen, G. & Parrish, A. R. Role of matrix metalloproteinases in renal pathophysiologies. *Am J Physiol Ren. Physiol* **292**, 905–911 (2007).
107. Schaefer, L. *et al.* Tubular gelatinase A (MMP-2) and its tissue inhibitors in polycystic kidney disease in the Han:SPRD rat. *Kidney Int.* **49**, 75–81 (1996).
108. Rankin, C. A. *et al.* Matrix metalloproteinases and TIMPS in cultured C57BL/6J-cpk kidney tubules. *Kidney Int.* **50**, 835–844 (1996).
109. Rankin, C. A. *et al. Matrix Metalloproteinase-2 in a Murine Model of Infantile-Type Polycystic Kidney Disease*. (1999).
110. Nakamura, T. *et al.* Elevation of Serum Levels of Metalloproteinase-1, Tissue Inhibitor of Metalloproteinase-1 and Type IV Collagen, and Plasma Levels of Metalloproteinase-9 in Polycystic Kidney Disease. *Am. J. Nephrol.* **20**, 32–36 (2000).
111. Stroope, A. *et al.* Hepato-renal pathology in Pkd2ws25/- mice, an animal model of autosomal dominant polycystic kidney disease. *Am. J. Pathol.* **176**, 1282–1291 (2010).
112. Garcia-Irigoyen, O. *et al.* Matrix metalloproteinase-10 expression is induced during hepatic injury and plays a fundamental role in liver

tissue repair. *Liver Int.* **34**, 257–270 (2014).
113. Ta, M. H. T. T., Harris, D. C. H. H. & Rangan, G. K. Role of interstitial inflammation in the pathogenesis of polycystic kidney disease. *Nephrology* **18**, 317–330 (2013).
114. Kurbegovic, A. & Trudel, M. Acute kidney injury induces hallmarks of polycystic kidney disease. *Am. J. Physiol. - Ren. Physiol.* **311**, F740–F751 (2016).
115. Swenson-Fields, K. I. *et al.* Macrophages promote polycystic kidney disease progression. *Kidney Int.* **83**, 855–864 (2013).
116. Karihaloo, A. *et al.* Macrophages Promote Cyst Growth in Polycystic Kidney Disease. *J. Am. Soc. Nephrol.* **22**, 1809–1814 (2011).
117. Gardner, K. D., Burnside, J. S., Elzinga, L. W. & Locksley, R. M. Cytokines in fluids from polycystic kidneys. *Kidney Int.* **39**, 718–724 (1991).
118. Merta M, Tesar V, Zima T, Jirsa M, Rysavá R, Z. J. Cytokine profile in autosomal dominant polycystic kidney disease. *Biochem Mol Biol Int.* **41**, 619–624 (1997).
119. Nichols, M. T. *et al.* Secretion of cytokines and growth factors into autosomal dominant polycystic kidney disease liver cyst fluid. *Hepatology* **40**, 836–846 (2004).
120. Amura, C. R. *et al.* CXCR2 agonists in ADPKD liver cyst fluids promote cell proliferation. *Am. J. Physiol. - Cell Physiol.* **294**, C786 (2008).
121. Yang, Y. *et al.* Interactions between Macrophages and Cyst-Lining Epithelial Cells Promote Kidney Cyst Growth in Pkd1 -De fi cient Mice. *J Am Soc Nephrol* **29**, 2310–2325 (2018).
122. Winkles, J. A. The TWEAK-Fn14 cytokine-receptor axis: Discovery, biology and therapeutic targeting. *Nature Reviews Drug Discovery* (2008) doi:10.1038/nrd2488.
123. Sanz, A. B., Sanchez-Nĩo, M. D. & Ortiz, A. TWEAK, a multifunctional cytokine in kidney injury. *Kidney Int.* **80**, 708–718 (2011).
124. Poveda, J. *et al.* TWEAK/Fn14 and non-canonical NF-kappaB signaling in kidney disease. *Front. Immunol.* **4**, 1–7 (2013).
125. Sanz, A. B. *et al.* TWEAK and the progression of renal disease: clinical translation. *Nephrol. Dial. Transplant.* **29**, i54–i62 (2014).
126. Cherry, E. M., Lee, D. W., Jung, J. U. & Sitcheran, R. Tumor necrosis factor-like weak inducer of apoptosis (TWEAK) promotes glioma cell invasion through induction of NF-κB-inducing kinase (NIK) and noncanonical NF-κB signaling. *Mol. Cancer* **14**, (2015).
127. Wisniacki, N. *et al.* Safety, tolerability, pharmacokinetics, and pharmacodynamics of anti-TWEAK monoclonal antibody in patients

with rheumatoid arthritis. *Clin. Ther.* **35**, 1137–1149 (2013).
128. Hildebrandt, F., Benzing, T. & Katsanis, N. Ciliopathies. *N. Engl. J. Med.* **364**, 1533–1543 (2011).
129. Ma, M. Cilia and polycystic kidney disease. *Semin. Cell Dev. Biol.* 0–1 (2020) doi:10.1016/j.semcdb.2020.05.003.
130. Ma, M., Tian, X., Igarashi, P., Pazour, G. J. & Somlo, S. Loss of cilia suppresses cyst growth in genetic models of autosomal dominant polycystic kidney disease. *Nat. Genet.* **45**, 1004–1012 (2013).
131. Retailleau, K. & Duprat, F. Polycystins and partners: proposed role in mechanosensitivity. *J. Physiol.* **592**, 2453–2471 (2014).
132. Ma, M., Gallagher, A. R. & Somlo, S. Ciliary mechanisms of cyst formation in polycystic kidney disease. *Cold Spring Harb. Perspect. Biol.* **9**, (2017).
133. Köttgen, M. *et al.* TRPP2 and TRPV4 form a polymodal sensory channel complex. *J. Cell Biol.* **182**, 437–447 (2008).
134. Boehlke, C. *et al.* Primary cilia regulate mTORC1 activity and cell size through Lkb1. *Nat. Cell Biol.* **12**, 1115–1122 (2010).
135. Delling, M. *et al.* Primary cilia are not calcium-responsive mechanosensors. *Nature* **531**, 656–660 (2016).
136. Hofherr, A. & Köttgen, M. Polycystic kidney disease: Cilia and mechanosensation revisited. *Nat. Rev. Nephrol.* **12**, 318–319 (2016).
137. Fedeles, S. V. *et al.* A genetic interaction network of five genes for human polycystic kidney and liver diseases defines polycystin-1 as the central determinant of cyst formation. *Nat. Genet.* **43**, 639–647 (2011).
138. Olson, R. J. *et al.* Synergistic Genetic Interactions between Pkhd1 and Pkd1 Result in an ARPKD-Like Phenotype in Murine Models. *J. Am. Soc. Nephrol.* ASN.2019020150 (2019) doi:10.1681/ASN.2019020150.
139. Gallagher, A. R. & Somlo, S. Loss of cilia does not slow liver disease progression in mouse models of autosomal recessive polycystic kidney disease. *Kidney360* 1–14 (2020) doi:10.34067/KID.0001022019.
140. Ong, A. C. M. & Harris, P. C. A polycystin-centric view of cyst formation and disease: The polycystins revisited. *Kidney Int.* **88**, 699–710 (2015).
141. Harris, P. C. & Hopp, K. The Mutation, a Key Determinant of Phenotype in ADPKD. *J. Am. Soc. Nephrol.* **24**, 868–870 (2013).
142. Gall, E. C. Le *et al.* Type of PKD1 Mutation Influences Renal Outcome in ADPKD. *J. Am. Soc. Nephrol.* **24**, 1006–1013 (2013).
143. Rossetti, S. *et al.* Incompletely penetrant PKD1 alleles suggest a role for gene dosage in cyst initiation in polycystic kidney disease. *Kidney*

Int. **75**, 848–855 (2009).
144. Fedeles, S. V., Gallagher, A. R. & Somlo, S. Polycystin-1: A master regulator of intersecting cystic pathways. *Trends Mol. Med.* **20**, 251–260 (2014).
145. Krappitz, M., Gallagher, A.-R. & Fedeles, S. Is it Time to Fold the Cysts Away? *Trends Mol. Med.* **22**, (2016).
146. Cai, Y. *et al.* Altered trafficking and stability of polycystins underlie polycystic kidney disease. *J. Clin. Invest.* **124**, 5129–5144 (2014).
147. Lantinga-van leeuwen, I. S. *et al.* Kidney-specific inactivation of the Pkd1 gene induces rapid cyst formation in developing kidneys and a slow onset of disease in adult mice. *Hum. Mol. Genet.* **16**, 3188–3196 (2007).
148. Bangor, A., Kortum, P. & Miller, J. *Determining What Individual SUS Scores Mean: Adding an Adjective Rating Scale*. *Journal of Usability Studies* vol. 4 http://uxpajournal.org/wp-content/uploads/sites/8/pdf/JUS_Bangor_May2009.pdf (2009).
149. Brooke, J. *SUS: A Retrospective*. vol. 8 http://uxpajournal.org/wp-content/uploads/sites/8/pdf/JUS_Brooke_February_2013.pdf (2013).
150. Sauro, J. *A practical guide to the system usability scale : background, benchmarks & best practices*.
151. Shevchenko, A. *et al.* A strategy for identifying gel-separated proteins in sequence databases by MS alone. in *Biochemical Society Transactions* vol. 24 893–896 (Portland Press Ltd, 1996).
152. Shilov, I. V. *et al.* The paragon algorithm, a next generation search engine that uses sequence temperature values sequence temperature values and feature probabilities to identify peptides from tandem mass spectra. *Mol. Cell. Proteomics* **6**, 1638–1655 (2007).
153. del Pilar Chantada-Vázquez, M. *et al.* Proteomic investigation on bio-corona of Au, Ag and Fe nanoparticles for the discovery of triple negative breast cancer serum protein biomarkers. *J. Proteomics* **212**, 103581 (2020).
154. Varela-Rodríguez, B. M. *et al.* Beneficial Effects of Bariatric Surgery-Induced by Weight Loss on the Proteome of Abdominal Subcutaneous Adipose Tissue. *J. Clin. Med.* **9**, 213 (2020).
155. Hermida-Nogueira, L. *et al.* Proteomic analysis of extracellular vesicles derived from platelet concentrates treated with Mirasol® identifies biomarkers of platelet storage lesion. *J. Proteomics* **210**, (2020).
156. Tamara, C. *et al.* Vesicles shed by pathological murine adipocytes spread pathology: Characterization and functional role of insulin resistant/hypertrophied adiposomes. *Int. J. Mol. Sci.* **21**, (2020).
157. Víctor Álvarez, J. *et al.* Proteomic analysis in morquio a cells treated

with immobilized enzymatic replacement therapy on nanostructured lipid systems. *Int. J. Mol. Sci.* **20**, (2019).
158. Meyer, J. G. & Schilling, B. Clinical applications of quantitative proteomics using targeted and untargeted data-independent acquisition techniques. *Expert Review of Proteomics* vol. 14 419–429 (2017).
159. Luo, Y. *et al.* SWATH-based proteomics identified carbonic anhydrase 2 as a potential diagnosis biomarker for nasopharyngeal carcinoma. *Sci. Rep.* **7**, 1–11 (2017).
160. Ortea, I., Ruiz-Sánchez, I., Cañete, R., Caballero-Villarraso, J. & Cañete, M. D. Identification of candidate serum biomarkers of childhood-onset growth hormone deficiency using SWATH-MS and feature selection. *J. Proteomics* **175**, 105–113 (2018).
161. Tan, H. T. & Chung, M. C. M. Label-Free Quantitative Phosphoproteomics Reveals Regulation of Vasodilator-Stimulated Phosphoprotein upon Stathmin-1 Silencing in a Pair of Isogenic Colorectal Cancer Cell Lines. *Proteomics* **18**, 1–13 (2018).
162. Lambert, J. P. *et al.* Mapping differential interactomes by affinity purification coupled with data-independent mass spectrometry acquisition. *Nat. Methods* **10**, 1239–1245 (2013).
163. Narasimhan, M., Kannan, S., Chawade, A., Bhattacharjee, A. & Govekar, R. Clinical biomarker discovery by SWATH-MS based label-free quantitative proteomics: Impact of criteria for identification of differentiators and data normalization method. *J. Transl. Med.* **17**, 1–15 (2019).
164. Chutipongtanate, S. & Greis, K. D. Multiplex Biomarker Screening Assay for Urinary Extracellular Vesicles Study : A Targeted Label-Free Proteomic Approach. *Sci. Rep.* **8**, 1–8 (2018).
165. Warnes, G. R. *et al.* gplots: Various R Programming Tools for Plotting Data. R package version 3.0.1.1. *gplots Var. R Program. Tools Plotting Data* (2019).
166. Shao, X. Epithelial-Specific Cre/lox Recombination in the Developing Kidney and Genitourinary Tract. *J. Am. Soc. Nephrol.* **13**, 1837–1846 (2002).
167. Traykova-Brauch, M. *et al.* An efficient and versatile system for acute and chronic modulation of renal tubular function in transgenic mice. *Nat. Med.* **14**, 979–984 (2008).
168. Sanz, A. B. *et al.* The Cytokine TWEAK Modulates Renal Tubulointerstitial Inflammation. *J. Am. Soc. Nephrol.* **19**, 695–703 (2008).
169. Sanz, A. B. *et al.* Tweak induces proliferation in renal tubular epithelium: A role in uninephrectomy induced renal hyperplasia. *J.*

Cell. Mol. Med. **13**, 3329–3342 (2009).
170. Moreno, J. A. *et al.* The inflammatory cytokines TWEAK and TNFα reduce renal klotho expression through NFκB. *J. Am. Soc. Nephrol.* **22**, 1315–1325 (2011).
171. Izquierdo, M. C. *et al.* TWEAK (tumor necrosis factor-like weak inducer of apoptosis) activates CXCL16 expression during renal tubulointerstitial inflammation. *Kidney Int.* **81**, 1098–1107 (2012).
172. Ucero, A. C. *et al.* TNF-related weak inducer of apoptosis (TWEAK) promotes kidney fibrosis and Ras-dependent proliferation of cultured renal fibroblast. *Biochim. Biophys. Acta - Mol. Basis Dis.* **1832**, 1744–1755 (2013).
173. Sanchez-Niño, M. D. *et al.* Fn14 in podocytes and proteinuric kidney disease. *Biochim. Biophys. Acta - Mol. Basis Dis.* **1832**, 2232–2243 (2013).
174. Cordido, A., Cernadas, E., Fernández-Delgado, M. & García-González, M. A. M. A. CystAnalyser: A new software tool for the automatic detection and quantification of cysts in Polycystic Kidney and Liver Disease, and other cystic disorders. *PLoS Comput. Biol.* **16**, (2020).
175. Haverty, T. P. *et al.* Characterization of a renal tubular epithelial cell line which secretes the autologous target antigen of autoimmune experimental interstitial nephritis. *J. Cell Biol.* **107**, 1359–1368 (1988).
176. Moriwaki, K. *et al.* The Necroptosis Adaptor RIPK3 Promotes Injury-Induced Cytokine Expression and Tissue Repair. *Immunity* **41**, 567–578 (2014).
177. Sonka, M., Hlavac, V. & Boyle, R. *Image Processing, Analysis, and Machine Vision*. *Thomson-Engineering* (Springer US, 2007). doi:10.1007/978-1-4899-3216-7_1.
178. Duda, R. O., Hart, P. E. (Peter E. & Stork, D. G. *Pattern classification*. (Wiley, 2001).
179. Suzuki, S. & be, K. Topological structural analysis of digitized binary images by border following. *Comput. Vision, Graph. Image Process.* **30**, 32–46 (1985).
180. Fernández-Delgado, M., Cernadas, E., Barro, S., Amorim, D. & Fernández-Delgado, A. *Do we Need Hundreds of Classifiers to Solve Real World Classification Problems? Journal of Machine Learning Research* vol. 15 http://www.mathworks.es/products/neural-network. (2014).
181. Chang, C. C. & Lin, C. J. LIBSVM: A Library for support vector machines. *ACM Trans. Intell. Syst. Technol.* **2**, 1–27 (2011).
182. Ojala, T., Pietika, M. & Maenpaa, T. Multiresolution Gray-Scale and

Rotation Invariant Texture Classification with Local Binary Patterns. *IEEE Trans. Pattern Anal. Mach. Intell.* **24**, 971–987 (2002).
183. Pintor, J. M. *et al.* Govocitos: A software tool for estimating fish fecundity based on digital analysis of histological images. *Comput. Electron. Agric.* **125**, 89–98 (2016).
184. González-Rufino, E., Carrión, P., Cernadas, E., Fernández-Delgado, M. & Domínguez-Petit, R. Exhaustive comparison of colour texture features and classification methods to discriminate cells categories in histological images of fish ovary. *Pattern Recognit.* **46**, 2391–2407 (2013).
185. Chang, R. Y. K., Etheridge, N., Nouwens, A. S. & Dodd, P. R. SWATH analysis of the synaptic proteome in Alzheimer's disease. *Neurochem. Int.* **87**, 1–12 (2015).
186. Ludwig, C. *et al.* Data-independent acquisition-based SWATH-MS for quantitative proteomics: a tutorial. *Mol. Syst. Biol.* **14**, e8126 (2018).
187. Gillet, L. C. *et al.* Targeted data extraction of the MS/MS spectra generated by data-independent acquisition: A new concept for consistent and accurate proteome analysis. *Mol. Cell. Proteomics* **11**, (2012).
188. Mi, H. & Thomas, P. PANTHER pathway: an ontology-based pathway database coupled with data analysis tools. *Methods Mol. Biol.* **563**, 123–140 (2009).
189. von Mering, C. *et al.* STRING: A database of predicted functional associations between proteins. *Nucleic Acids Research* vol. 31 258–261 (2003).
190. Fabregat, A. *et al.* Reactome pathway analysis: A high-performance in-memory approach. *BMC Bioinformatics* **18**, (2017).
191. Mayer, G., Poirier, S. & Seidah, N. G. Annexin A2 is a C-terminal PCSK9-binding protein that regulates endogenous low density lipoprotein receptor levels. *J. Biol. Chem.* **283**, 31791–31801 (2008).
192. Kopec, A. K. & Luyendyk, J. P. Role of Fibrin(ogen) in Progression of Liver Disease: Guilt by Association? *Semin. Thromb. Hemost.* **42**, 397–407 (2016).
193. Brown, P. D. & Giavazzi, R. Matrix metalloproteinase inhibition: A review of anti-tumour activity. *Ann. Oncol.* **6**, 967–974 (1995).
194. Steward, W. P. Marimastat (BB2516): Current status of development. in *Cancer Chemotherapy and Pharmacology, Supplement* vol. 43 S56–S60 (Springer, 1999).
195. Song, C. J., Kurt A. Zimmerman;, Scott J. Henke; & Bradley K. Yoder. Inflammation and Fibrosis in Polycystic Kidney Disease. in *Molecular Biology* vol. 60 1–9 (2017).

196. Torres, V. E. *et al.* Tolvaptan in patients with autosomal dominant polycystic kidney disease. *N. Engl. J. Med.* **367**, 2407–2418 (2012).
197. Torres, V. E. *et al.* Tolvaptan in Later-Stage Autosomal Dominant Polycystic Kidney Disease. *N. Engl. J. Med.* **377**, 1930–1942 (2017).
198. Mancinelli, R. *et al.* Vasopressin regulates the growth of the biliary epithelium in polycystic liver disease. *Lab. Investig.* **96**, 1147–1155 (2016).
199. Song, X. *et al.* Systems biology of autosomal dominant polycystic kidney disease (ADPKD): Computational identification of gene expression pathways and integrated regulatory networks. *Hum. Mol. Genet.* **18**, 2328–2343 (2009).
200. Chen, W. C., Tzeng, Y. S. & Li, H. Gene expression in early and progression phases of autosomal dominant polycystic kidney disease. *BMC Research Notes* vol. 1 (2008).
201. Dweep, H., Sticht, C., Kharkar, A., Pandey, P. & Gretz, N. Parallel Analysis of mRNA and microRNA Microarray Profiles to Explore Functional Regulatory Patterns in Polycystic Kidney Disease: Using PKD/Mhm Rat Model. *PLoS One* **8**, (2013).
202. Pandey, P. *et al.* Microarray-based approach identifies microRNAs and their target functional patterns in polycystic kidney disease. *BMC Genomics* **9**, 3–5 (2008).
203. Rahimmanesh, I. & Fatehi, R. Systems biology approaches toward autosomal dominant polycystic kidney disease (ADPKD). *Clin. Transl. Med.* **9**, 1–8 (2020).
204. Li, X. *et al.* A tumor necrosis factor-alpha-mediated pathway promoting autosomal dominant polycystic kidney disease. *Nat. Med.* **14**, 863–868 (2008).
205. Gao, H.-X. *et al.* TNF-like weak inducer of apoptosis (TWEAK) induces inflammatory and proliferative effects in human kidney cells. *Cytokine* **46**, 24–35 (2009).
206. Sanz, A. B. *et al.* TWEAK activates the non-canonical NFκB pathway in murine renal tubular cells: Modulation of CCL21. *PLoS One* **5**, (2010).
207. Yamaguchi, T. *et al.* cAMP stimulates the in vitro proliferation of renal cyst epithelial cells by activating the extracellular signal-regulated kinase pathway. *Kidney Int.* **57**, 1460–1471 (2000).
208. Omori, S. *et al.* Extracellular signal-regulated kinase inhibition slows disease progression in mice with polycystic kidney disease. *J. Am. Soc. Nephrol.* **17**, 1604–1614 (2006).
209. Joly, D. *et al.* The polycystin 1-C-terminal fragment stimulates ERK-dependent spreading of renal epithelial cells. *J. Biol. Chem.* **281**, 26329–26339 (2006).

210. Wahl, P. R. *et al.* Inhibition of mTOR with sirolimus slows disease progression in Han:SPRD rats with autosomal dominant polycystic kidney disease (ADPKD). *Nephrol. Dial. Transplant.* **21**, 598–604 (2006).
211. Shillingford, J. M. *et al.* The mTOR pathway is regulated by polycystin-1, and its inhibition reverses renal cystogenesis in polycystic kidney disease. *Proc. Natl. Acad. Sci.* **103**, 5466–5471 (2006).
212. Novalic, Z. *et al.* Dose-Dependent Effects of Sirolimus on mTOR Signaling and Polycystic Kidney Disease. *J. Am. Soc. Nephrol.* **23**, 842–853 (2012).
213. Ravichandran, K. *et al.* An mTOR anti-sense oligonucleotide decreases polycystic kidney disease in mice with a targeted mutation in Pkd2. *Hum. Mol. Genet.* **23**, 4919–4931 (2014).
214. Justo, P. *et al.* Cytokine cooperation in renal tubular cell injury: The role of TWEAK. *Kidney Int.* **70**, 1750–1758 (2006).
215. Berzal, S. *et al.* TNF-related weak inducer of apoptosis (TWEAK) regulates junctional proteins in tubular epithelial cells via canonical NF-kB pathway and ERK activation. *J. Cell. Physiol.* **230**, 1580–1593 (2015).
216. Belliere, J. *et al.* Specific macrophage subtypes influence the progression of rhabdomyolysis-induced kidney injury. *J. Am. Soc. Nephrol.* **26**, 1363–1377 (2015).
217. Fedeles, S. V. *et al.* Sec63 and Xbp1 regulate IRE1α activity and polycystic disease severity. *J. Clin. Invest.* **125**, 1955–1967 (2015).
218. Abu-Wasel, B., Walsh, C., Keough, V. & Molinari, M. Pathophysiology, epidemiology, classification and treatment options for polycystic liver diseases. *World J. Gastroenterol.* **19**, 5775–5786 (2013).
219. Zhang, L. *et al.* Subcellular proteome analysis unraveled annexin A2 related to immune liver fibrosis. *J. Cell. Biochem.* **110**, 219–228 (2010).
220. Yang, M. *et al.* Annexin A2 promotes liver fibrosis by mediating von Willebrand factor secretion. *Dig. Liver Dis.* **49**, 780–788 (2017).
221. Bugge, T. H. *et al.* Loss of fibrinogen rescues mice from the pleiotropic effects of plasminogen deficiency. *Cell* **87**, 709–719 (1996).
222. Fernández, G. C. *et al.* Galectin-3 and soluble fibrinogen act in concert to modulate neutrophil activation and survival: Involvement of alternative MAPK pathways. *Glycobiology* **15**, 519–527 (2005).
223. Tang, M. *et al.* Increased expression of Fibrinogen-Like Protein 2 is associated with poor prognosis in patients with clear cell renal cell

carcinoma. *Sci. Rep.* **7**, (2017).
224. Hantgan, R. R., Stahle, M. C. & Lord, S. T. Dynamic regulation of fibrinogen: Integrin αiIbβ3 binding. *Biochemistry* **49**, 9217–9225 (2010).
225. Riera, M., Burtey, S. & Fontés, M. Transcriptome analysis of a rat PKD model: Importance of genes involved in extracellular matrix metabolism. *Kidney Int.* **69**, 1558–1563 (2006).
226. Du, X. *et al.* Involvement of matrix metalloproteinase-2 in the development of renal interstitial fibrosis in mouse obstructive nephropathy. *Lab. Investig.* **92**, 1149–1160 (2012).
227. Ślusarz, A. *et al.* Overexpression of MMP-7 increases collagen 1A2 in the aging kidney. *Physiol. Rep.* **1**, 90 (2013).
228. Wang, Z. *et al.* TIMP2 and TIMP3 have divergent roles in early renal tubulointerstitial injury. *Kidney Int.* **85**, 82–93 (2014).
229. Kassiri, Z. *et al.* Loss of TIMP3 enhances interstitial nephritis and fibrosis. *J. Am. Soc. Nephrol.* **20**, 1223–1235 (2009).
230. Kim, H. *et al.* TIMP-1 Deficiency Does Not Attenuate Interstitial Fibrosis in Obstructive Nephropathy. *J Am Soc Nephrol* **12**, 736–748 (2001).
231. Liu, B., Li, C., Liu, Z., Dai, Z. & Tao, Y. Increasing extracellular matrix collagen level and MMP activity induces cyst development in polycystic kidney disease. *BMC Nephrol.* **13**, 1–8 (2012).
232. Obermüller, N., Morente, N., Kränzlin, B., Gretz, N. & Witzgall, R. A possible role for metalloproteinases in renal cyst development. *Am. J. Physiol. Renal Physiol.* **280**, F540-50 (2001).
233. Danielsen, H. *et al.* Expansion of Extracellular Volume in Early Polycystic Kidney Disease. *Acta Med. Scand.* **219**, 399–405 (1986).
234. Seeman, T. *et al.* Renal Concentrating Capacity is Linked to Blood Pressure in Children with Autosomal Dominant Polycystic Kidney Disease. *Physiol. Res* **53**, 629–634 (2004).
235. Cowley, B. D., Ricardo, S. D., Nagao, S. & Diamond, J. R. Increased renal expression of monocyte chemoattractant protein-1 and osteopontin in ADPKD in rats. *Kidney Int.* **60**, 2087–2096 (2001).
236. Choe, J. Y. & Kim, S. K. Serum TWEAK as a biomarker for disease activity of systemic lupus erythematosus. *Inflamm. Res.* **65**, 479–488 (2016).
237. Yilmaz, M. I. *et al.* Soluble TWEAK plasma levels as a novel biomarker of endothelial function in patients with chronic kidney disease. *Clin. J. Am. Soc. Nephrol.* **4**, 1716–1723 (2009).
238. Bastos, A. P. *et al.* Pkd1 haploinsufficiency increases renal damage and induces microcyst formation following ischemia/reperfusion. *J. Am. Soc. Nephrol.* **20**, 2389–2402 (2009).

239. Bell, P. D. *et al.* Loss of primary cilia upregulates renal hypertrophic signaling and promotes cystogenesis. *J. Am. Soc. Nephrol.* **22**, 839–848 (2011).
240. Patel, V. *et al.* Acute kidney injury and aberrant planar cell polarity induce cyst formation in mice lacking renal cilia. *Hum. Mol. Genet.* **17**, 1578–1590 (2008).
241. Takakura, A. *et al.* Renal injury is a third hit promoting rapid development of adult polycystic kidney disease. *Hum. Mol. Genet.* **18**, 2523–2531 (2009).
242. Happé, H. *et al.* Toxic tubular injury in kidneys from Pkd1-deletion mice accelerates cystogenesis accompanied by dysregulated planar cell polarity and canonical Wnt signaling pathways. *Hum. Mol. Genet.* **18**, 2532–2542 (2009).
243. Hotta, K. *et al.* Direct targeting of fibroblast growth factor-inducible 14 protein protects against renal ischemia reperfusion injury. *Kidney Int.* **79**, 179–88 (2011).
244. Zhao, Z. *et al.* TWEAK/Fn14 Interactions Are Instrumental in the Pathogenesis of Nephritis in the Chronic Graft-versus-Host Model of Systemic Lupus erythematosus. *J. Immunol.* **179**, 7949–7958 (2007).
245. Vincent, C. *et al.* Pro-inflammatory cytokines TNF-related weak inducer of apoptosis (TWEAK) and TNFalpha induce the mitogen-activated protein kinase (MAPK)-dependent expression of sclerostin in human osteoblasts. *J. Bone Miner. Res.* **24**, 1434–49 (2009).
246. Tao, Y., Kim, J., Schrier, R. W. & Edelstein, C. L. Rapamycin markedly slows disease progression in a rat model of polycystic kidney disease. *J. Am. Soc. Nephrol.* **16**, 46–51 (2005).
247. Zafar, I., Ravichandran, K., Belibi, F. A., Doctor, R. B. & Edelstein, C. L. Sirolimus attenuates disease progression in an orthologous mouse model of human autosomal dominant polycystic kidney disease. *Kidney Int.* **78**, 754–761 (2010).
248. Boca, M. *et al.* Polycystin-1 Induces Resistance to Apoptosis through the Phosphatidylinositol 3-Kinase/Akt Signaling Pathway. *J. Am. Soc. Nephrol.* **17**, 637–647 (2006).
249. Li, L. X. *et al.* Lysine methyltransferase SMYD2 promotes cyst growth in autosomal dominant polycystic kidney disease. *J. Clin. Invest.* **127**, 2751–2764 (2017).
250. Rowe, I. *et al.* Defective glucose metabolism in polycystic kidney disease identifies a new therapeutic strategy. *Nat. Med.* **19**, 488–493 (2013).
251. Huang, J. L. *et al.* Vascular Endothelial Growth Factor C for Polycystic Kidney Diseases. *J. Am. Soc. Nephrol.* **27**, 69–77 (2016).
252. Zheng, D. *et al.* Urinary excretion of monocyte chemoattractant

protein-1 in autosomal dominant polycystic kidney disease. *J. Am. Soc. Nephrol.* **14**, 2588–2595 (2003).
253. Grantham, J. J. *et al.* Tolvaptan suppresses monocyte chemotactic protein-1 excretion in autosomal-dominant polycystic kidney disease. *Nephrol. Dial. Transplant.* gfw060 (2016) doi:10.1093/ndt/gfw060.
254. Messchendorp, A. L. *et al.* Urinary Biomarkers to Identify Autosomal Dominant Polycystic Kidney Disease Patients With a High Likelihood of Disease Progression. *Kidney Int. Reports* **3**, 291–301 (2017).
255. Wang, S. *et al.* Fibrocystin / Polyductin , Found in the Same Protein Complex with Polycystin-2 , Regulates Calcium Responses in Kidney Epithelia. *Mol. Cell. Biol.* **27**, 3241–3252 (2007).
256. Kaimori, J. & Germino, G. G. ARPKD and ADPKD: first cousins or more distant relatives? *J. Am. Soc. Nephrol.* **19**, 416–8 (2008).
257. Wu, G. *et al.* Trans-heterozygous Pkd1 and Pkd2 mutations modify expression of polycystic kidney disease. *Hum. Mol. Genet.* **11**, 1845–54 (2002).
258. Pei, Y. *et al.* Bilineal disease and trans-heterozygotes in autosomal dominant polycystic kidney disease. *Am. J. Hum. Genet.* **68**, 355–363 (2001).
259. Gainullin, V. G., Hopp, K., Ward, C. J., Hommerding, C. J. & Harris, P. C. Polycystin-1 maturation requires polycystin-2 in a dose-dependent manner. *J. Clin. Invest.* **125**, 607–620 (2015).
260. Cornec-Le Gall, E. *et al.* Monoallelic Mutations to DNAJB11 Cause Atypical Autosomal-Dominant Polycystic Kidney Disease. *Am. J. Hum. Genet.* **102**, 832–844 (2018).
261. Lin, F. *et al.* Kidney-specific inactivation of the KIF3A subunit of kinesin-II inhibits renal ciliogenesis and produces polycystic kidney disease. **100**, (2003).
262. Davenport, J. R. *et al.* Report Disruption of Intraflagellar Transport in Adult Mice Leads to Obesity and Slow-Onset Cystic Kidney Disease. 1586–1594 (2007) doi:10.1016/j.cub.2007.08.034.
263. Jonassen, J. A., Agustin, J. S., Follit, J. A. & Pazour, G. J. Deletion of IFT20 in the mouse kidney causes misorientation of the mitotic spindle and cystic kidney disease. *J. Biol. Chem.* **183**, 377–384 (2008).
264. Jonassen, J. A., Sanagustin, J., Baker, S. P. & Pazour, G. J. Disruption of IFT Complex A Causes Cystic Kidneys without Mitotic Spindle Misorientation. (2012) doi:10.1681/ASN.2011080829.
265. Tran, P. V *et al.* Downregulating Hedgehog Signaling Reduces Renal Cystogenic Potential of Mouse Models Pamela. *J Am Soc Nephrol* **25**, 2201–12 (2014).

266. Li, Y. *et al.* Deletion of ADP Ribosylation Factor-Like GTPase 13B Leads to Kidney Cysts. 3628–3638 (2016) doi:10.1681/ASN.2015091004.
267. Legué, E. & Liem, K. F. Tulp3 Is a Ciliary Trafficking Gene that Regulates Polycystic Kidney Disease. *Curr. Biol.* **29**, 803-812.e5 (2019).
268. Shao, L. *et al.* Genetic reduction of cilium length by targeting intraflagellar transport 88 protein impedes kidney and liver cyst formation in mouse models of autosomal polycystic kidney disease. *Kidney Int.* **98**, 1225–1241 (2020).

USC UNIVERSIDADE DE SANTIAGO DE COMPOSTELA

SUPPLEMENTAL MATERIAL

USC UNIVERSIDADE DE SANTIAGO DE COMPOSTELA

SUPPLEMENTAL MATERIAL

1. SUPPLEMENTAL INFORMATION

1.1. Author contributions

The vast majority of results presented in this thesis were performed by the author of the same. Adrián Cordido performed and designed most experiments and statistical analysis, interpreted them, and wrote the results and discussions, as well as the manuscripts for the results published and futures publications. But, specifically, some results showed in the present thesis were performed in the context of a scientific collaboration:

- Chapter 1: software construction and the algorithm for the automatic image recognition were elaborated by Dra. Eva Cernadas and Dr. Manuel Fernández-Delgado, from CiTIUS-USC.
- Chapter 2 and 3: SWATH-MS quantitative proteomic protocol were performed by the Proteomic unit of IDIS, leaded by Dra. Susana Bravo. Data accurate from the proteomic raw data were performed by Dr. Alberto Molares from Bioinformatic unit of IDIS.
- Chapter 4: characterization of TWEAK/Fn14 axis (RT-qPCR, *Western Blotting* and immunohistochemistry analysis), TUNEL, F4/80 IHQs and *in vitro* experiments were performed by Dr. Ana Belen Sanz and Prof. Alberto Ortiz laboratories from IIS-Fundación Jiménez Díaz. Also, *Pkd1^{cond};Pax8;TET-OCre* mouse samples was kindly provided by Dra. Patricia Outeda and Prof. Terry Watnick from Baltimore PKD Core Center (Maryland, USA), and samples of slowly progressive *Pkd1$^{cond/cond}$;Tam-Cre* and *Pkd1$^{cond/cond}$Tam-KSP-Cre* mouse models were kindly provided by Dra. Alessandra Boletta (San Raffaele Scientific Institute, Milan, Italy).
- Chapter 5: all results presented were performed by the thesis author.

1.2. Competing interests

The intellectual property of the CystAnalyser (SC-208/19) was protected by a software registration: 2/3 USC (50% Eva Cernadas; 50% Manuel Fernández Delgado) and 1/3 FIDIS (50% Adrián Cordido; 50% Miguel Ángel García González).

The author has nothing to disclosure with the rest of content of the present thesis.

2. SUPPLEMENTAL FIGURES

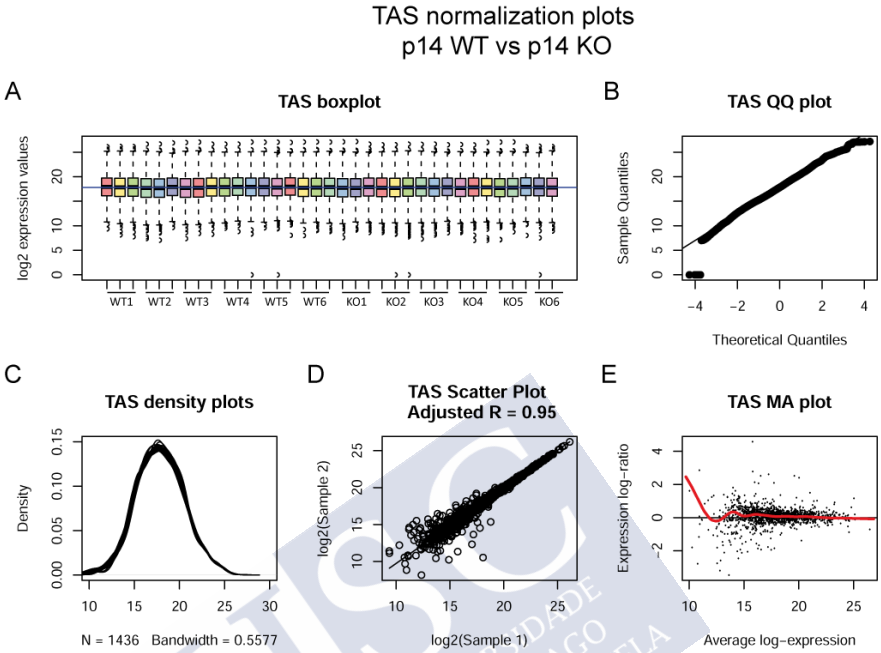

Supplemental Figure 1. TAS (Total Area Sums) normalization plots p14 data. (A) TAS (Total Area Sums) boxplots show a graphical representation of log2 protein expression values (after TAS normalization). All samples, with its triplicates, are aligned with reference line. (B) TAS QQ plot comparing independent normal data on the vertical axis to a standard normal population on the horizontal axis. The linearity of points suggests that the data follows normal distribution. (C) TAS density plots are represented. The approximate representation of a Gaussian "bell" suggests that the data are normally distributed. Next, in order to determine the dispersion or distribution of our data we have performed two different analysis. (D) TAS scatter plot and correlation coefficient. Points dispersion and adjusted R with a value ≥0.95 (near to 1) suggest low dispersion. (E) TAS MA plot is shown. The slope of the line around 1 suggest good distribution of the analyzed data. In summary, these results show that data of p14 study follow a normal distribution and with a good distribution.

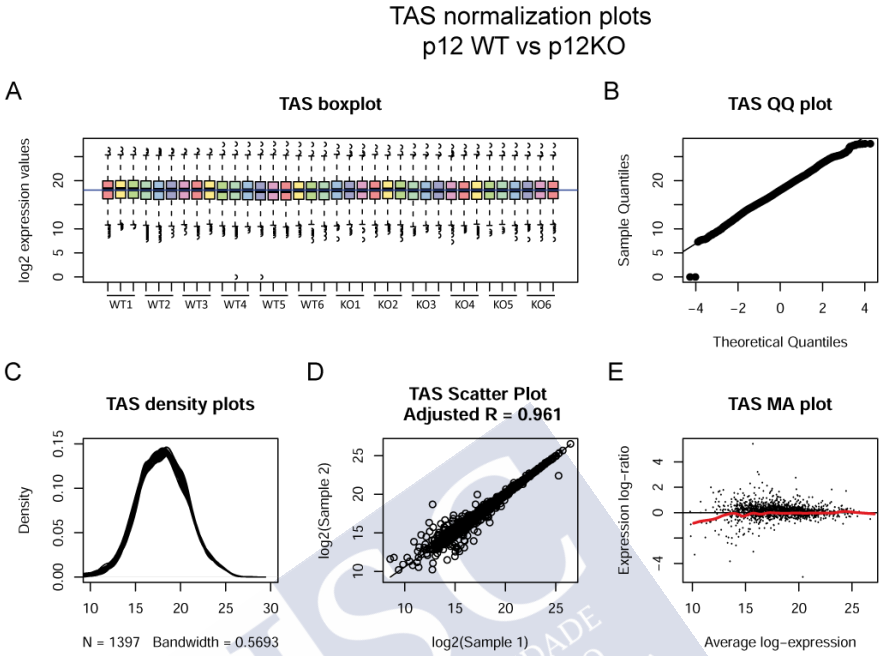

Supplemental Figure 2. TAS (Total Area Sums) normalization plots of p12 data. (A) TAS boxplots show a graphical representation of log2 protein expression values (after TAS normalization). All samples, with its triplicates, are aligned with reference line. (B) The linearity of points in the TAS QQ plot suggests that the data follows normal distribution. (C) TAS density plots are represented. The approximate representation of a Gaussian "bell" suggests that the data are normally distributed. (D) TAS scatter plot and correlation coefficient. Points dispersion and adjusted R with a value ≥0.95 (near to 1) suggest a good distribution. (E) TAS MA plot is represented. The slope of the line around 1 suggest normalization of data. In conclusion, these results show that data of p12 study follow a normal distribution and with a good data dispersion.

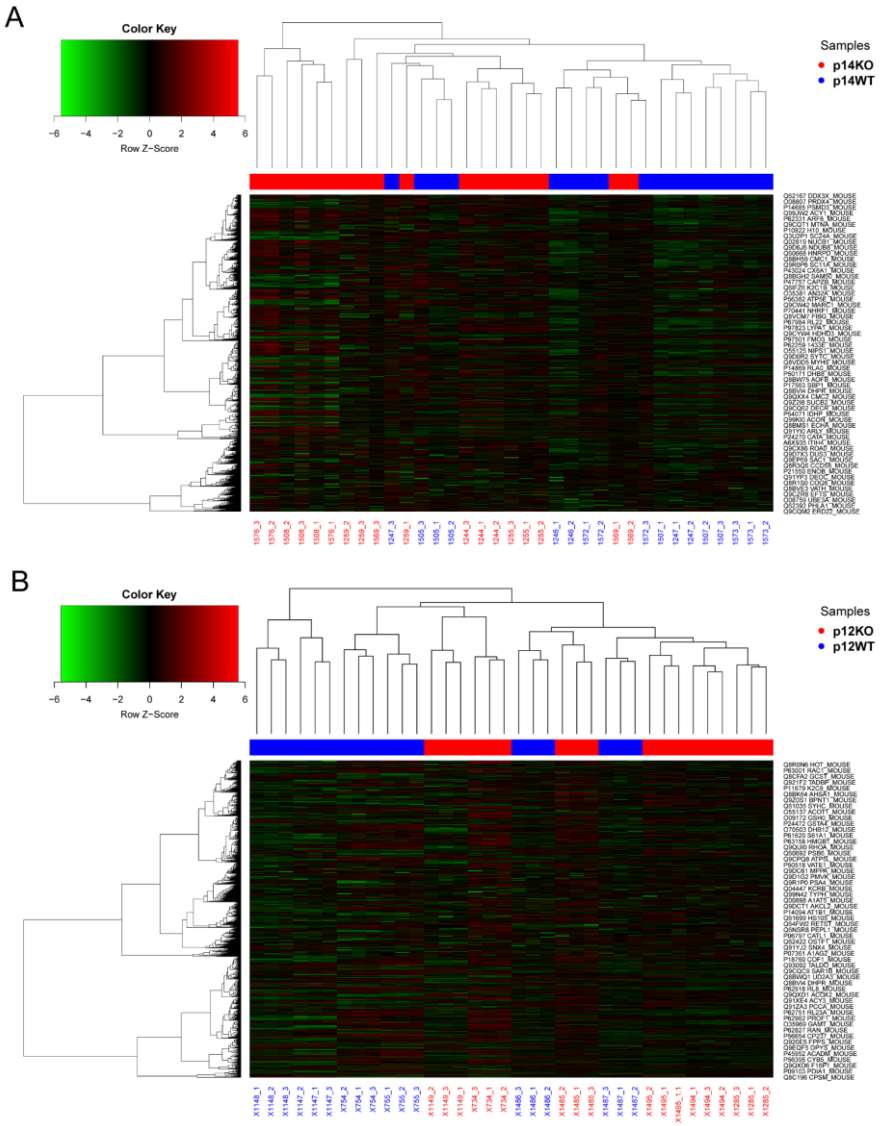

Supplemental Figure 3. Unsupervised heatmap Cluster analysis of all proteins detected by SWATH-MS. Heatmap figure of cluster analysis of all proteins identified by SWATH MS. (A-B) Cluster of results corresponding to postnatal day 14 (p14) (A) and postnatal day 12 (p12) (B). Samples from the *Wild Types* (WT p12 and WT p14) and mutant (KO p12 and KO p14) groups are shown in blue and red, respectively. Color gradient is determined by the RowZ-score, where red and green represent increase and decrease, respectively, of protein abundance.

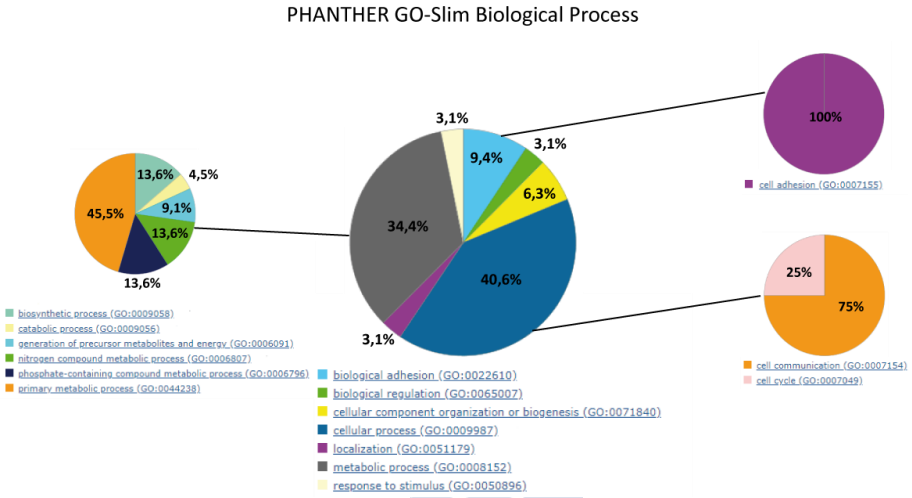

Supplemental Figure 4. Go analysis using PANTHER classification system according to Biological Process Ontologies. Pie charts showed that the most of the proteins are involved in cell adhesion, cell communication and metabolic process

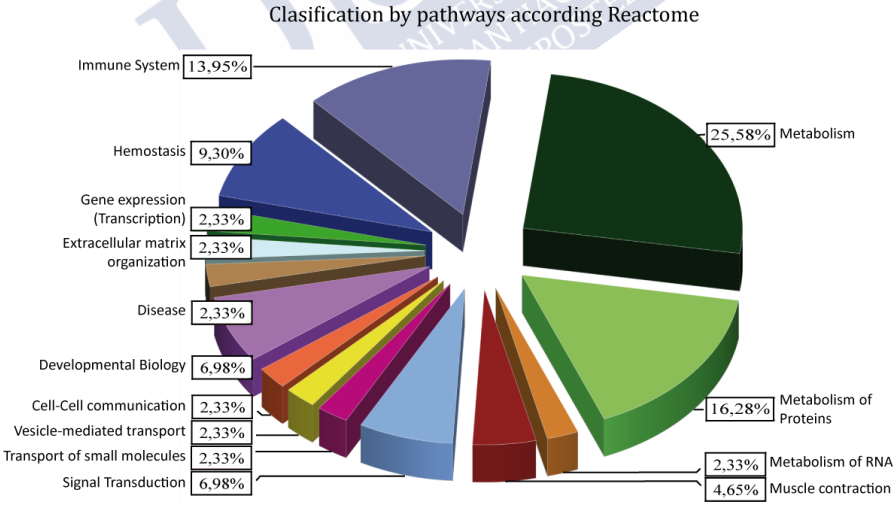

Supplemental Figure 5. Pathway enrichment proteins with statistical significance according to Reactome data base. Classification of significantly expressed proteins identified by SWATH-MS approach according to Reactome data base. Important to note that 4 proteins (Q71KU9, Q64464, Q8R1F5, Q00898) are not detected by Reactome data base, and therefore it could not be classified.

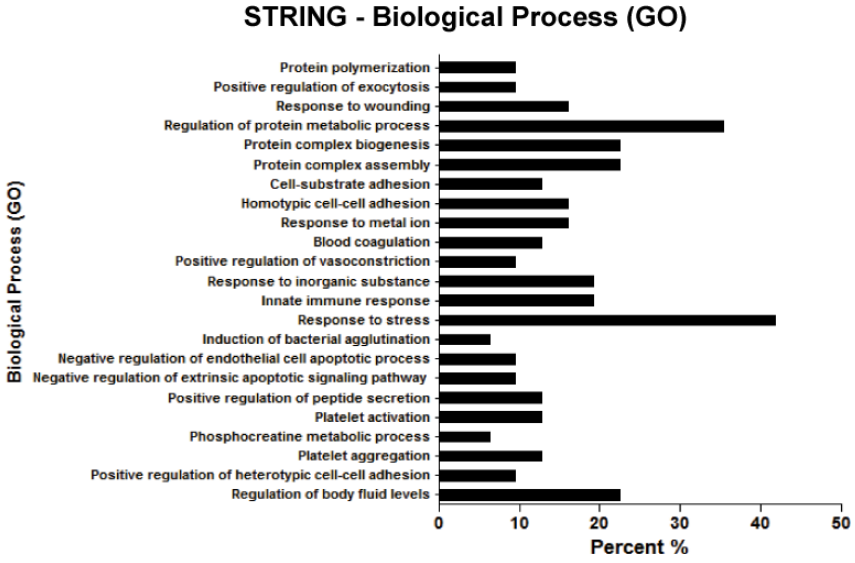

Supplemental Figure 6. Representation of most representative Biological Process and Cellular Components according to Gene Ontology (GO). We represent the biological process of SWATH MS data. Proteins with significant differences in abundance (increase and decrease) at p12 and p14 identified by SWATH MS analysis were uploaded into String software. Interestingly, pathways related with response to stress, cell adhesion and regulation of several process appear enriched.

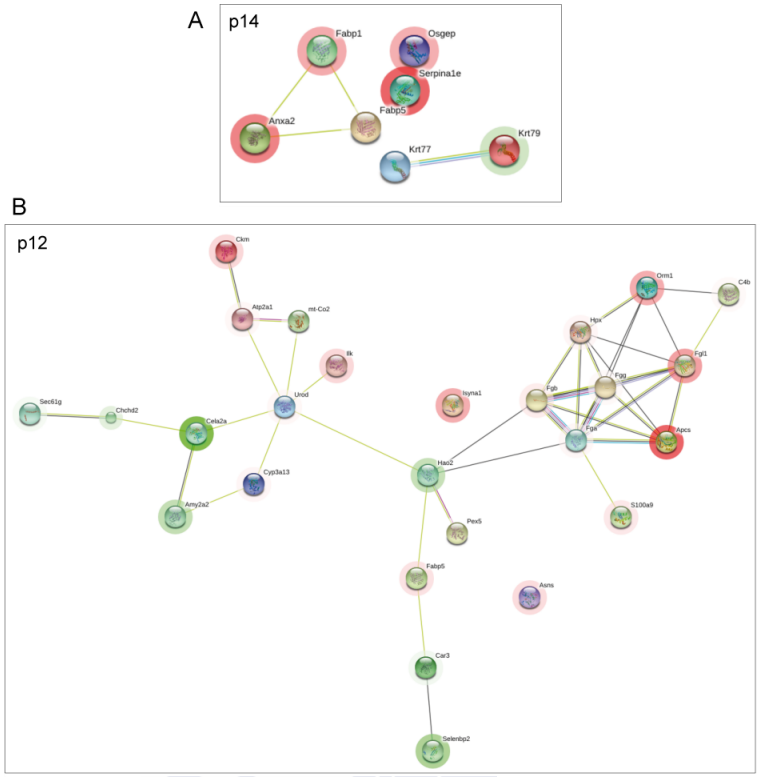

Supplemental Figure 7. Full protein-protein interaction map according String. Proteins with significant increase and decrease protein abundance were submitted to String analysis. (A) and (B) Represents protein-protein interaction analysis of p14 and p12 data, respectively. Proteins are represented as nodules, which are colored red or green imply increase or decrease in protein abundance. Specifically, important selected clusters of proteins are represented in **Figure 24**.

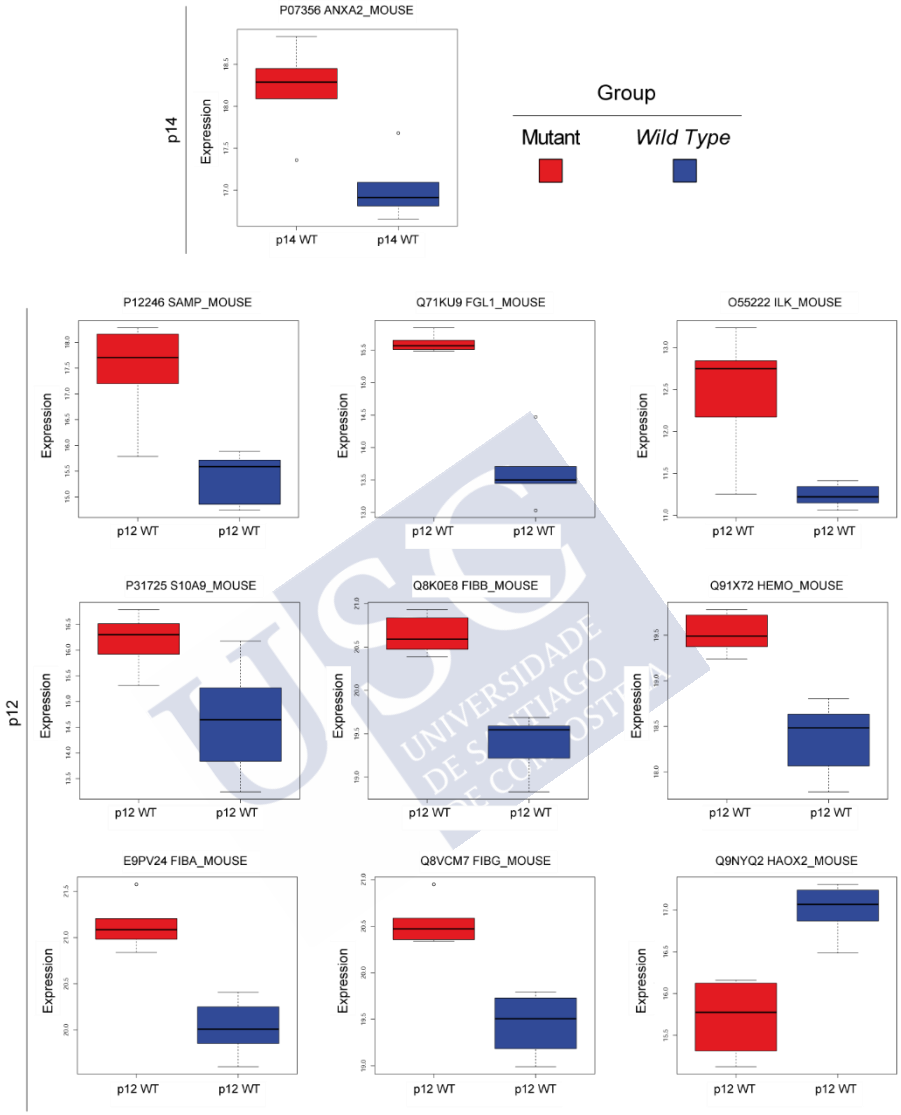

Supplemental Figure 8. SWATH MS data box-plot of the selected targets for validation. Box-plots of quantitative proteomic SWATH MS data of selected targets for validation. Box-plots represents protein abundance. The lower and upper ends of the box define the 25% and 75% quantiles, respectively, the middle line in the box is the median of the values and the whiskers are the 0% and 100% quantiles. Specific fold-change and adjusted p-value data in **Table 4** and **Table 5**.

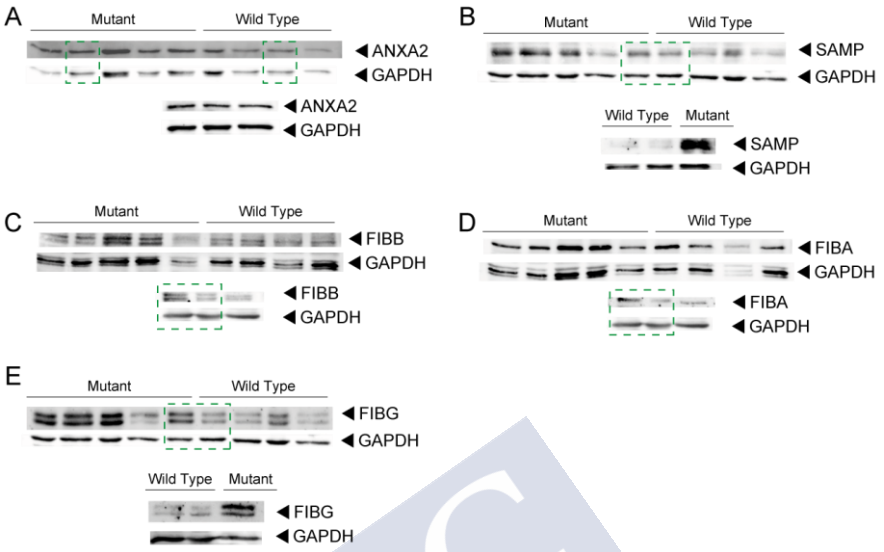

Supplemental Figure 9. Full Western Blots of protein validations. Full WBs are shown of up-regulated selected p14 target annexin A2 (ANXA2) (A); up-regulated p12 targets amyloid P Component, Serum (SAMP) (B), Fibrinogen Beta Chain (FIBB) (C), Fibrinogen Alpha Chain (FIBA) (D), Fibrinogen Gamma Chain (FGG) (E). Green boxes indicate plots used by **Figure 26**.

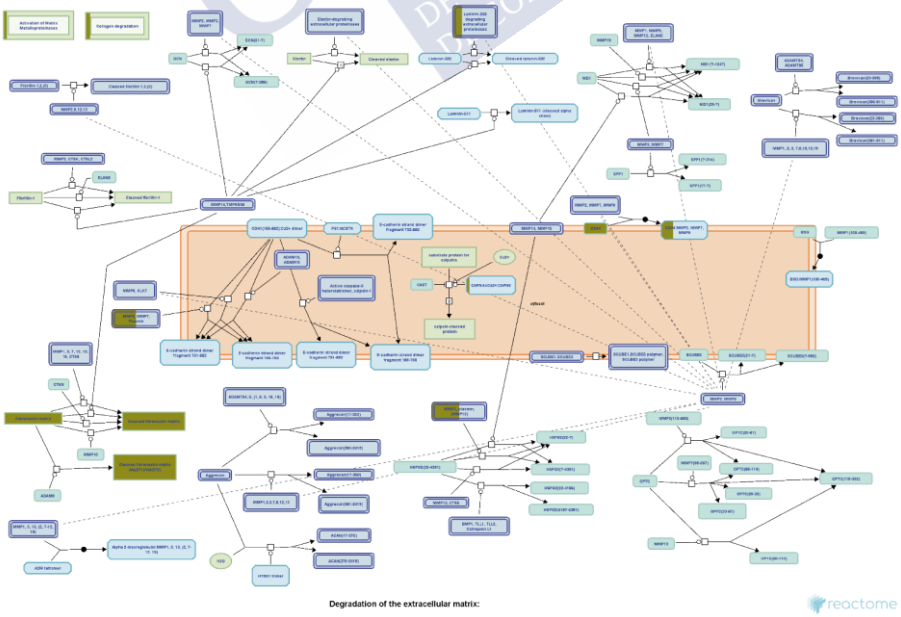

Supplemental Figure 10. Degradation of the extracellular matrix subpathway from Reactome®. A snapshot of "Degradation of the extracellular matrix" subpathway is showed. After "Muscle contraction", "Extracellular matrix organization" was the pathway with most matched/total number of molecules of our significantly differentially proteins set (kidney and liver) and with highest FDR value (1,08E-01) according to Reactome®. "Degradation of the extracellular matrix" was the subpathway with most entities found (p value=3,2E-3) and total interactors. Green color overlay indicates the matching interactors. Several MMPs and Fibronectin were direct matches and had interactors that match our significantly differentially proteins set. FDR: False Discovery Rate. FDR indicates the corrected over-representation probability, and p-value indicates the result of the statistical test for over-representation, for molecules of the results type selected.

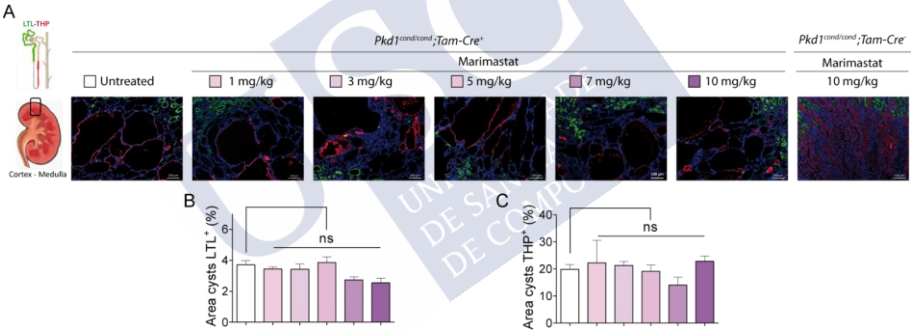

Supplemental Figure 11. Marimastat does not cause slowing of cystic growth in proximal tubule and thick ascending limb of the loop of Henle. Characterization of cyst origin by immunofluorescences in renal cortex-medulla. Green marks the cysts from proximal tubules (LTL^+) and red marks cyst that derived from thick ascending limb of the loop of Henle (THP^+). (B-C) Quantification of immunofluorescence LTL+ (B) and THP+ (C) cysts. No effect detected in LTL^+ or THP^+ cysts with Marimastat treatment. Scale bar, 100µm.

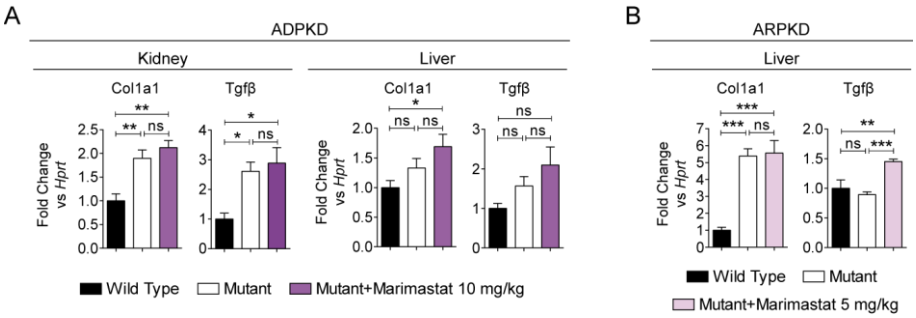

Supplemental Figure 12. Gene expression of *Col1a1* and *Tgfβ* were not altered after Marimastat treatment. (A-B) RT-qPCR of Collagen-1a1 (*Col1a1*) and Transforming growth factor-beta (*Tgfβ*), two markers of fibrosis in kidneys (A, left) and liver (A, right) in Wild Types (*Pkd1*$^{cond/cond}$*;Tam-Cre*$^{-}$ n=4), Mutants (*Pkd1*$^{cond/cond}$*;Tam-Cre*$^{-}$ n=5) and Mutants treated with Marimastat 10mg/kg (*Pkd1*$^{cond/cond}$*;Tam-Cre*$^{-}$ n=5) (A); and Wild Type (C57BL/6 mouse n=5), mutant (*Pkhd1*$^{del3\text{-}4/del3\text{-}4}$ n=6) and treated (Marimastat 5 mg/kg) mutant (n=6) groups (B). *Hprt* gene was used as housekeeping. Bars represent means±SEM. Two-way ANOVA was used and a value of P<0.05 was considered significant. ns: not significant (p≥0.05), * p<0.05, ** p<0.01, *** p<0.001.

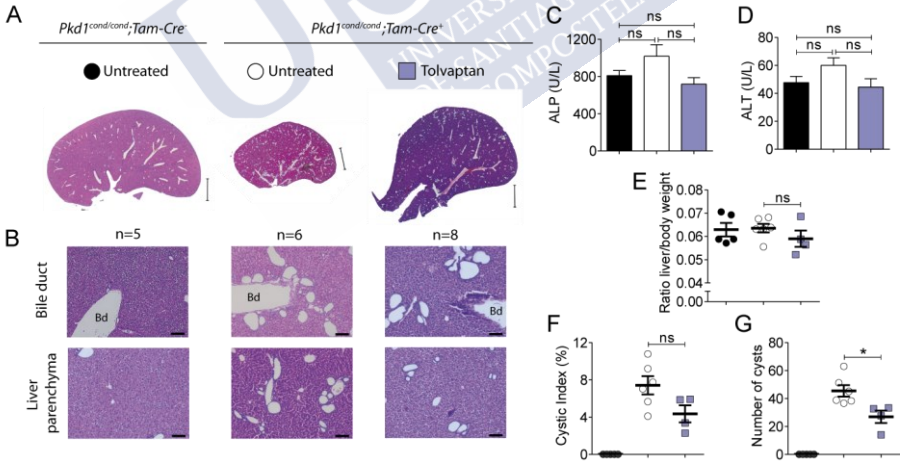

Supplemental Figure 13. Effect of Tolvaptan in hepatic cystogenesis in ADPKD. (A-B) Representative images of Hematoxylin-Eosin (HE) stained from livers of *Pkd1-CKO* mouse. Images of biggest lobule slide (A), and cysts from hepatic parenchyma (B, Up) and bile duct (C, down) are showed. Scale bars, 2mm (A) 50µm (B). (C-D) ALP (C) and ALT (D) values of serum hepatic function. (E) Ratio of liver weight to total body weight. (F-G) Hepatic cystic index (F) and total number of cysts (G). Bars represent means±SEM. Two-way ANOVA was used and a value of P<0.05 was considered significant. ns: not significant (p≥0.05), * p<0.05.

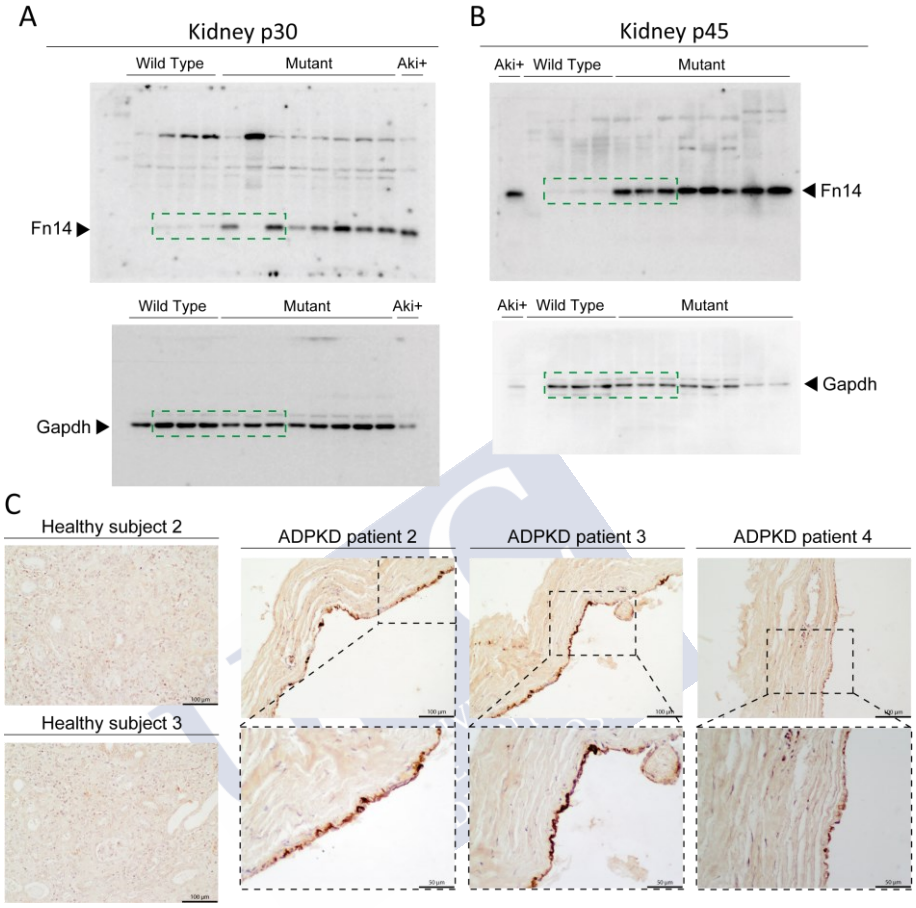

Supplemental Figure 14. Western Blots and IHQ for Fn14 and GAPDH. All Western Blots (WBs) of Fn14 and GAPDH (used as housekeeping) used for Figure 1. WBs for kidney samples (A-B) at postnatal day p30 (A) and p45 (B) are shown. Green boxes represent the cutouts used for Figure 1. (C) Immunohistochemistry of human ADPKD kidneys showed specific staining of FN14 at the cyst epithelium (x100 and x200 magnification). Negative control, original magnification x200.

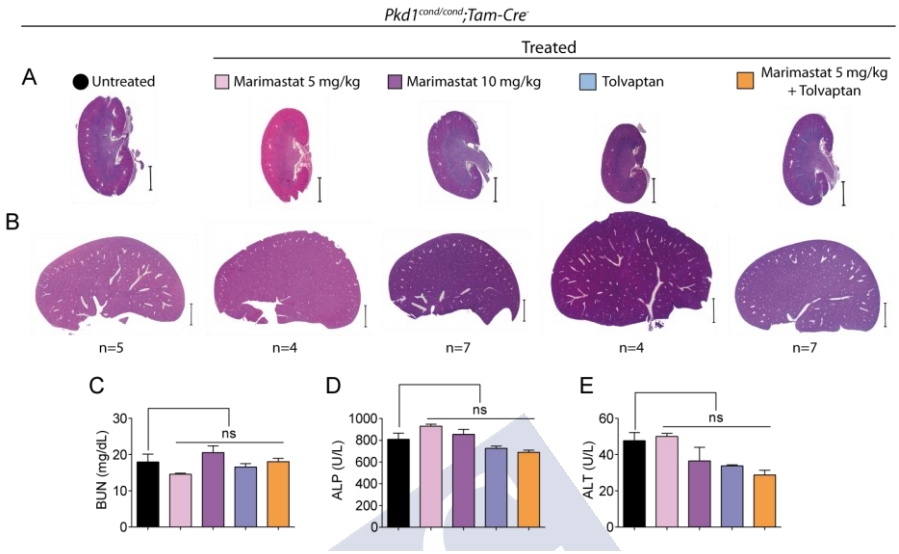

Supplemental Figure 15. Marimastat not alter normal histology and serum values in *Wild Type* mice. Kidney (A) and liver (B) slides of untreated (n=5), Marimastat (5 and 10 mg/kg, n= 4 and 7 respectively), Tolvaptan (n=4) and Marimastat plus Tolvaptan (n=7) treated groups in *Wild Type* (*Pkd1*$^{cond/cond}$;*Tam-Cre*$^{-}$) mice. Scale bars: 2mm. (C-E) Serum values of renal function based on BUN (C), and hepatic function based on ALP (D) and ALT (E). Bars represent means±SEM. Two-way ANOVA was used and a value of $P<0.05$ was considered significant. ns: not significant ($p\geq0.05$).

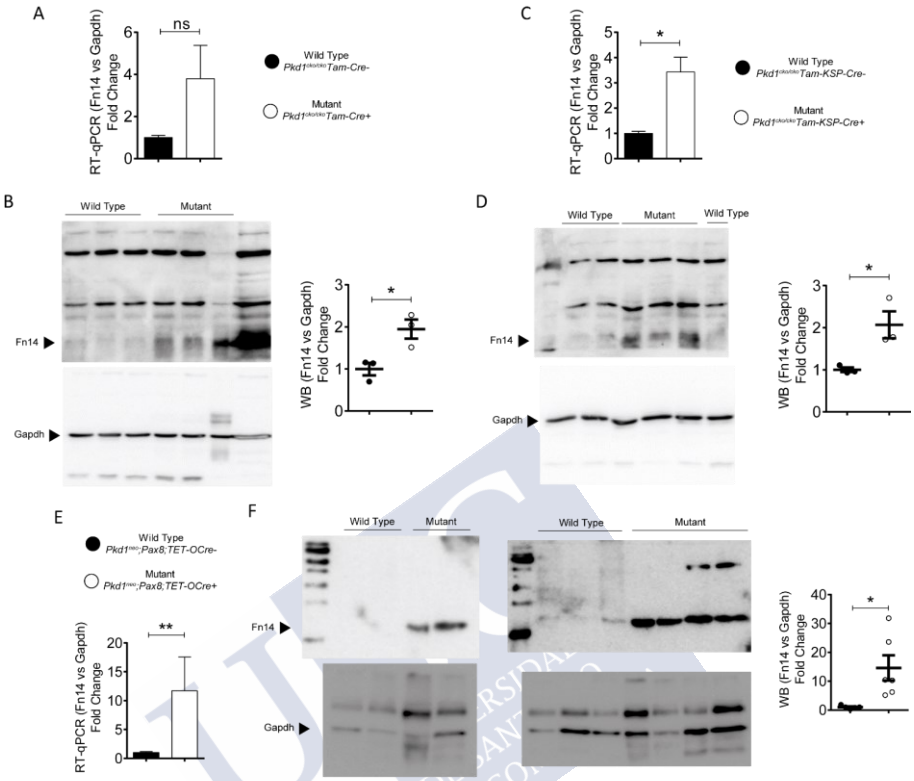

Supplemental Figure 16. Fn14 is upregulated in other murine ADPKD model. (A-B) Fn14 is upregulated in a slowly progressive orthologous ADPKD model. In *Pkd1*$^{cond/cond}$*Tam-Cre* ADPKD orthologous mice, *Pkd1* was inactivated on postnatal day 45, mice were sacrificed >14 weeks and kidneys were recollected. *Fn14* gene expression assessed by RT-qPCR (A), and Fn14 protein level by Western Blot (B) in *Wild Type* (n=3) and Mutant samples (n=3). (C-D) Upregulation of Fn14 was also observed in murine *Pkd1*$^{cond/cond}$*Tam-KSP-Cre* ADPKD which has a kidney epithelial cell promoter. Pkd1 was inactivated on postnatal days 10-11, mice were sacrificed at p38-p39 and kidneys collected from. *Fn14* gene expression assessed by RT-qPCR (C), and Fn14 protein level by Western Blot (D) in *Wild Type* (n=3) and Mutant samples (n=3). (E-F) Finally, Fn14 was assessed status in murine ADPKD model with a kidney tubular-cell-specific promoter. *Pkd1* was inactivated from *Pkd1*^{cond}*;Pax8;TET-OCre+* mice at p27 and then sacrificed at p150-p160. Fn14 is significantly upregulated in mutant kidneys. *Fn14* gene expression assessed by RT-qPCR (E), and Fn14 protein level by Western Blot (F) in *Wild Type* (n=4) and Mutant samples (n=6). *Gapdh* was used as housekeeping control in all cases. pX: postnatal day X. Bars represent means ± SEM. ns: not significant ($p \geq 0.05$), * $p < 0.05$, ** $p < 0.01$.

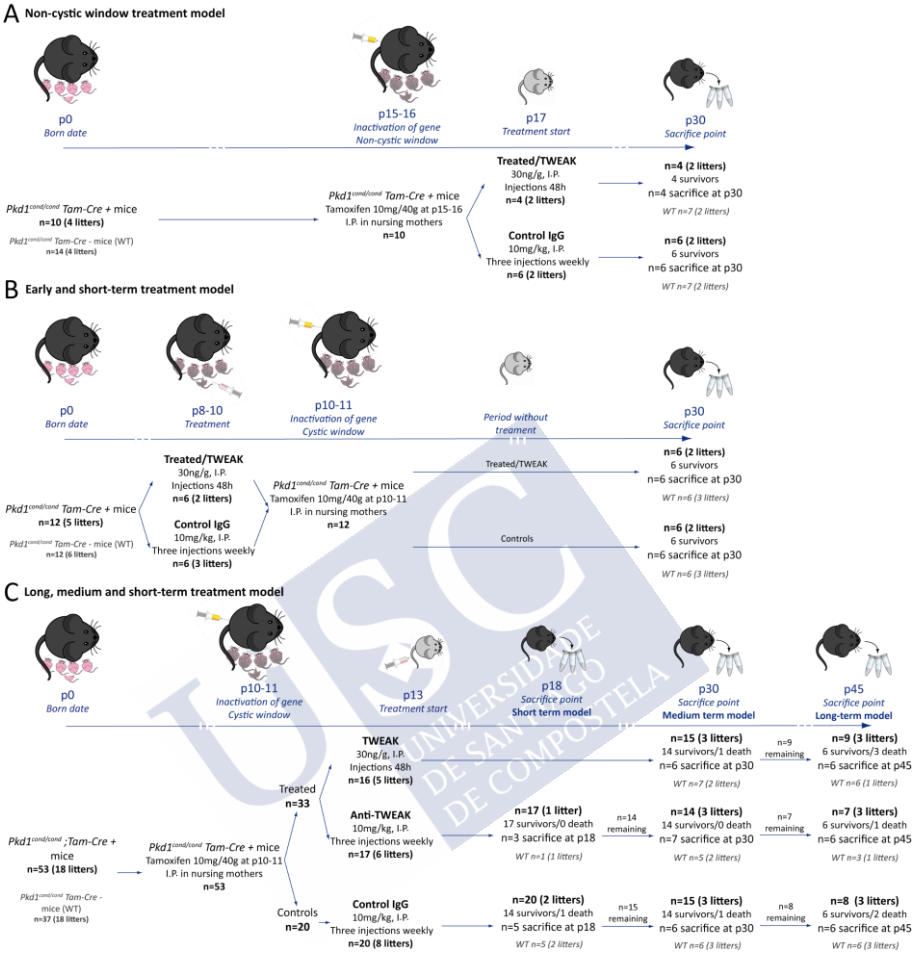

Supplemental Figure 17. Schematic representation of the different experimental designs performed in the study. (A) Non-cystic window treatment model. Pkd1 inactivation in *Pkd1*$^{cond/cond}$*;Tam-Cre*$^{+}$ was induced with tamoxifen at day p15 and p16 (non-cystic window). TWEAK administration started at day p17, until sacrifice, and tissues were recollected at postnatal day 30 (p30). (B) Early and short-term TWEAK treatment model. Pkd1 inactivation in *Pkd1*$^{cond/cond}$*;Tam-Cre*$^{+}$ was induced at days p10 and p11 (cystic window). TWEAK administered from day p8 to p10 and tissues collected at p30. (C) Medium- and long-term treatment model. Pkd1 inactivation in *Pkd1*$^{cond/cond}$*;Tam-Cre*$^{+}$ was induced at days p10 and p11. TWEAK and anti-TWEAK administration started at day 13 and continued until sacrifice, when kidneys were collected at p30 (mid-term model) and p45 (long-term model). p(x): postnatal day; I.P: intraperitoneal injection; n: number.

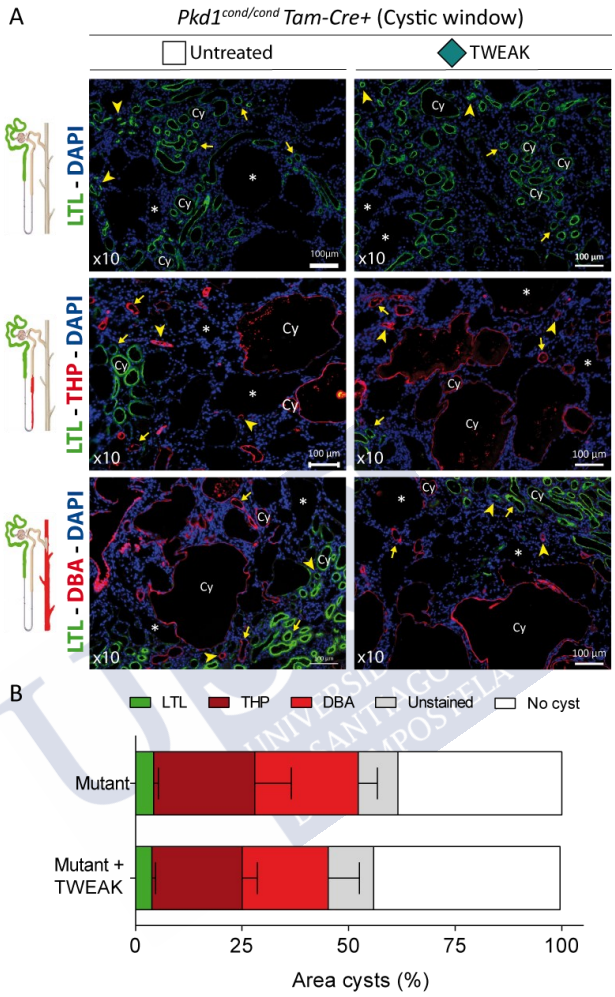

Supplemental Figure 18. Tubule specific markers in cysts in the short treatment model of TWEAK administration. (A) Immunofluorescence of specific markers from proximal tubules (LTL, Lotus Tetragonolobus Lectin. Green, up), ascending limb of the loop of Henle (THP, Tamm-Horsfall Protein. Red, medium) and collecting ducts (DBA, Dolichos Biflorus Agglutinin. Red, down), in control and TWEAK-exposed groups according the experimental design shown in **Supplemental Figure 17B**. Cy: cyst; * cyst without specific marking; yellow arrow: dilated tubule; yellow arrowhead: tubule. Scale bars: 50 µm (upper panel) and 100µm (center and lower panel). (B) Quantification of immunofluorescence cystic area. TWEAK had not effect on cystic area of LTL^+, DBA^+ and THP^+ cysts

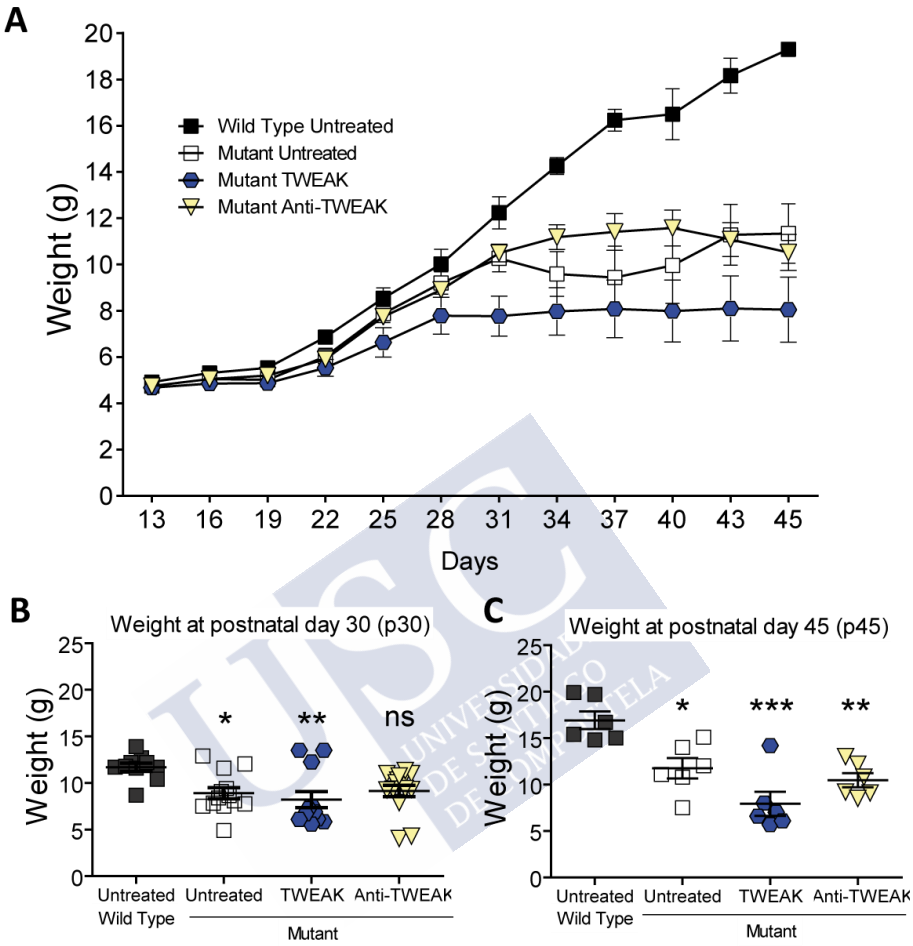

Supplemental Figure 19. Evolution of weight over time of different mice groups. *Pkd1* mutant mice administered TWEAK grow more slowly, however this was not the case when treated with anti-TWEAK. (A) Evolution of weight along the time of Wild Type, mutant untreated, TWEAK-exposed and anti-TWEAK treated mice, respectively. Graphs present weights at postnatal days p30 (B) and p45 (C), the two outcome time points for medium- and long-term experiments, respectively (**Supplemental Figure 17**). Bars represent means±SEM. ns: non-significant; * $p<0.05$; ** $p<0.01$; *** $p<0.001$.

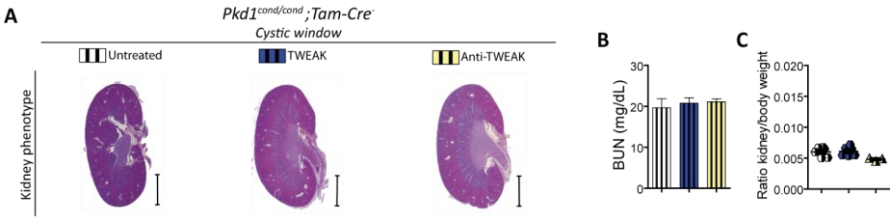

Supplemental Figure 20. TWEAK or anti-TWEAK treatment did not alter kidney histology o related serum biochemistry values in *Wild Type* control mice. (A) Representative kidney images from untreated, TWEAK-exposed and anti-TWEAK treated *Wild Type* mice at p45 according of experimental scheme in **Supplemental Figure 17C** (long-term model treatment). Markers of renal function and liver injury present standard values. (B) Serum Blood Urea Nitrogen (BUN). (C) Body weight ratio for kidney. p(x): postnatal day. Bars represent means±SEM.

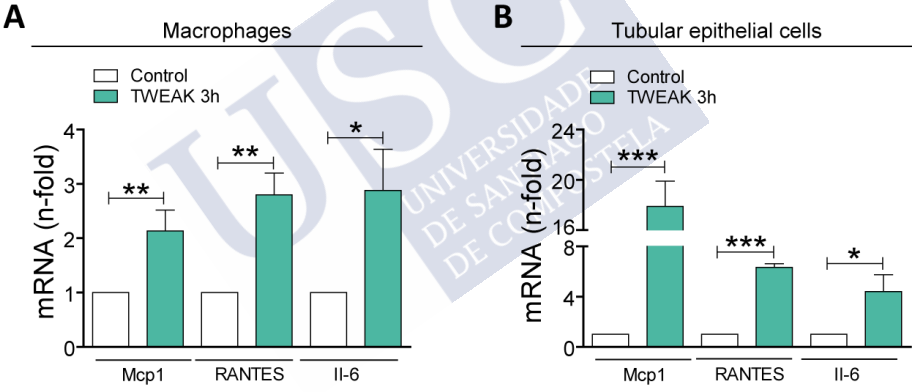

Supplemental Figure 21. TWEAK promotes an inflammatory status in macrophages and tubular epithelial cells. (A-B) Gene expression of *Mcp1*, RANTES and *Il-6* by RT-qPCR in macrophages (A) and tubular epithelial cells (B). An n=3 was performed for each experiment. Exposure to 100 ng/mL TWEAK for 3 h increased the proinflammatory status of macrophages and tubular epithelial cells for the three inflammatory markers assessed. Bars represent means ± SEM. ns: not significant ($p \geq 0.05$), * $p<0.05$, ** $p<0.01$, *** $p<0.001$.

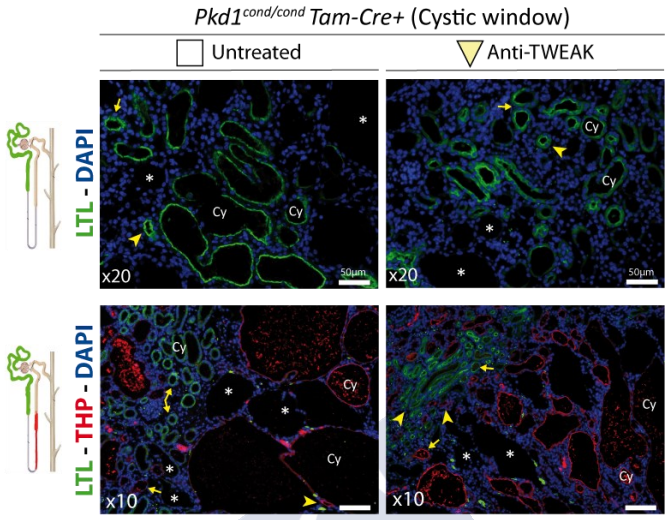

Supplemental Figure 22. Cyst origin characterization in control and anti-TWEAK-treated *Pkd1*-deficient mice, cystic window. Immunofluorescence of specific markers from proximal tubules (LTL, Lotus Tetragonolobus Lectin. Green, upper panel) and ascending limb of the loop of Henle (THP, Tamm-Horsfall Protein. Red, lower panel). Cy: cyst; * cyst without specific marking; yellow arrow: dilated tubule; yellow arrowhead: tubule. Scale bars: 50 µm (upper panel) and 100 µm (lower panel).

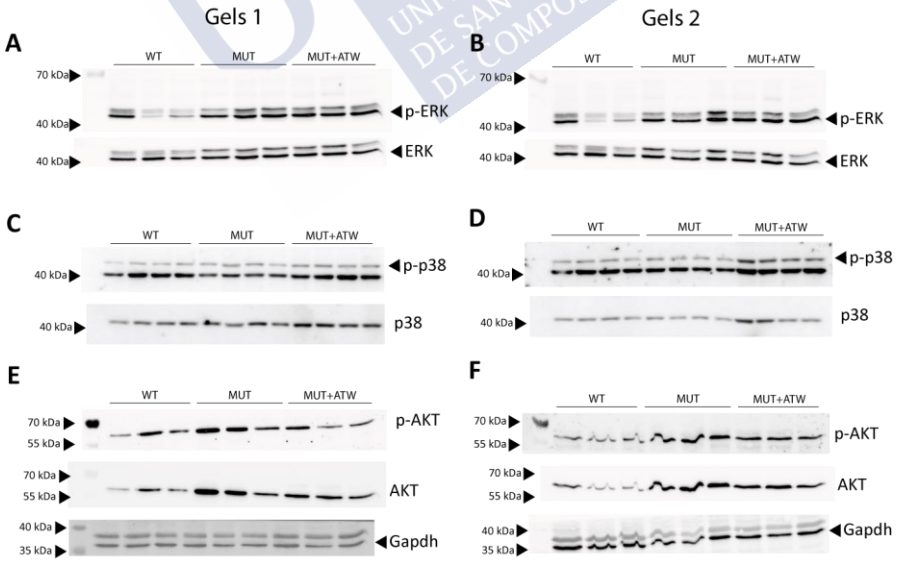

Supplemental Figure 23. Western Blots for p-ERK and ERK, p-p38 and p38, p-AKT and AKT and GAPDH. All Western Blots (WBs) used for **Figure 40** are shown. For each protein, two WBs were performed (here represented as Gels 1 and 2).WBs for (A-B) p-ERK and ERK, (C-D) p-p38 and p38, (E-F) p-AKT, AKT and GAPDH.

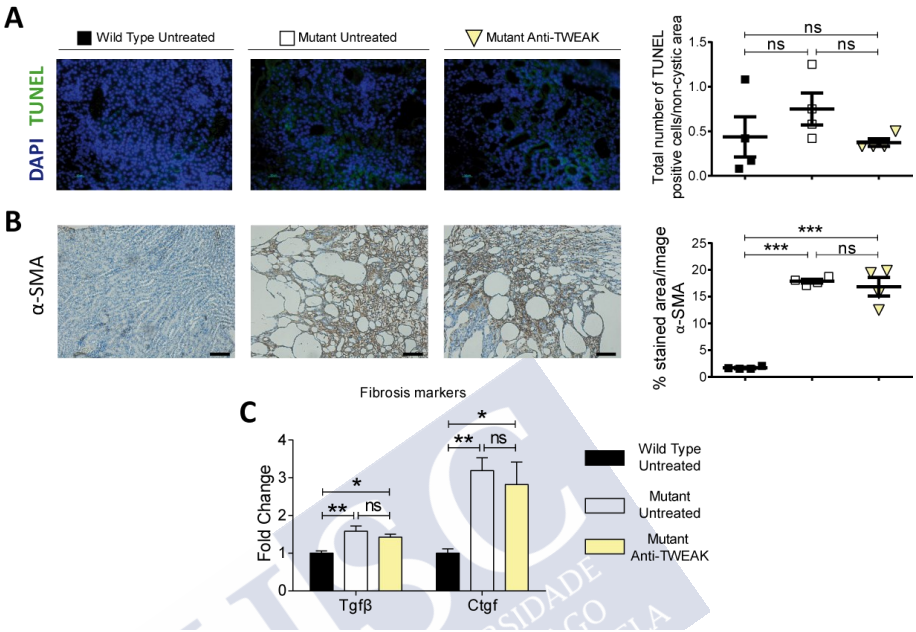

Supplemental Figure 24. Anti-TWEAK did not reduce fibrosis. (A) α-SMA staining in Wild Types, Mutant and Mutant anti-TWEAK treated (n=4 each group) kidneys. Representative images are shown (left) and quantification (right) of staining. Scale bars: 100 μm. (B) Gene expression measured by RT-qPCR of Tgfβ and Ctgf in Wild Type (n=6), Mutant (n=6) and Mutant mice treated with anti-TWEAK (n=6). Mice were sacrificed at postnatal day p30, according to the scheme shown in Supplemental Figure 2C (medium-term model). Bars represent means±SEM. ns: non-significant; *** $p<0.001$.

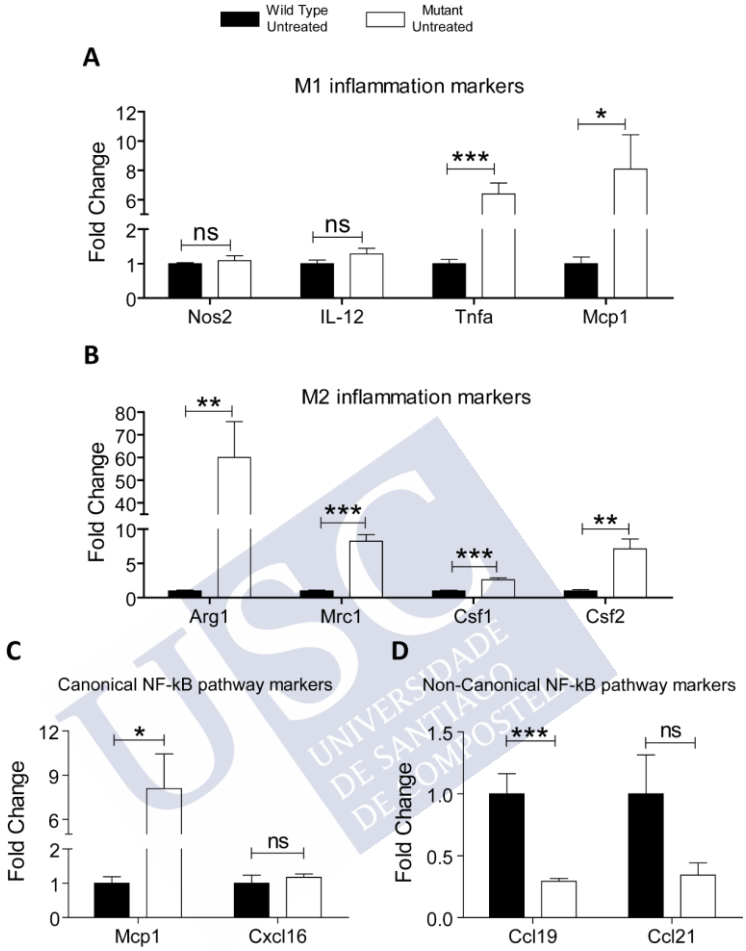

Supplemental Figure 25. M1 and M2 inflammatory markers, and NF-κB pathways in Pkd1 mutant mice. RT-qPCR of (A) of *Nos2*, *IL-12*, *Tnfa* and *Mcp1* (M1 markers); and (B) *Argl*, *Mrc1*, *Csf1* and *Csf2* (M2 markers). M1 is the predominant proinflammatory pathway, although the M2 pathway is also upregulated. Gene expression assessed by RT-qPCR of (C) *Mcp1* and *Cxcl16*; and (D) *Ccl19* and *Ccl21*, markers of canonical and non-canonical NF-κB pathway activation, respectively. Interestingly, whereas the expression of *Mcp1*, regulated by the canonical NF-κB pathway is upregulated, genes regulated by the non-canonical pathway are downregulated in ADPKD. Wild Type (n=5) and Mutant (n=5) mice were sacrificed at postnatal day 30. *Hprt* was used as housekeeping gene in all cases. Bars represent means±SEM. Mice were sacrificed at postnatal day p30, according of the scheme shown in **Supplemental Figure 17C** (medium-term model). Bars represent means±SEM. ns: non-significant; * p<0.05; ** p<0.01; *** p<0.001.

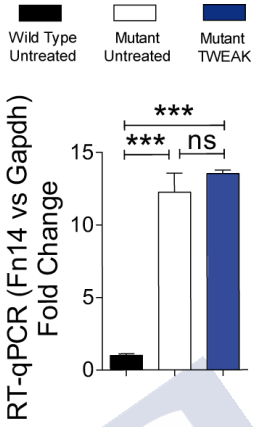

Supplemental Figure 26. TWEAK did not further increase Fn14 expression. Gene expression assessed by RT-qPCR of Fn14 in Wild Type (n=6), Mutant (n=6) and Mutant mice administrated with TWEAK (n=5). Mice were sacrificed at postnatal day p30, according of the scheme shown in **Supplemental Figure 17C** (long-term model). Bars represent means±SEM. ns: non-significant; *** $p<0.001$.

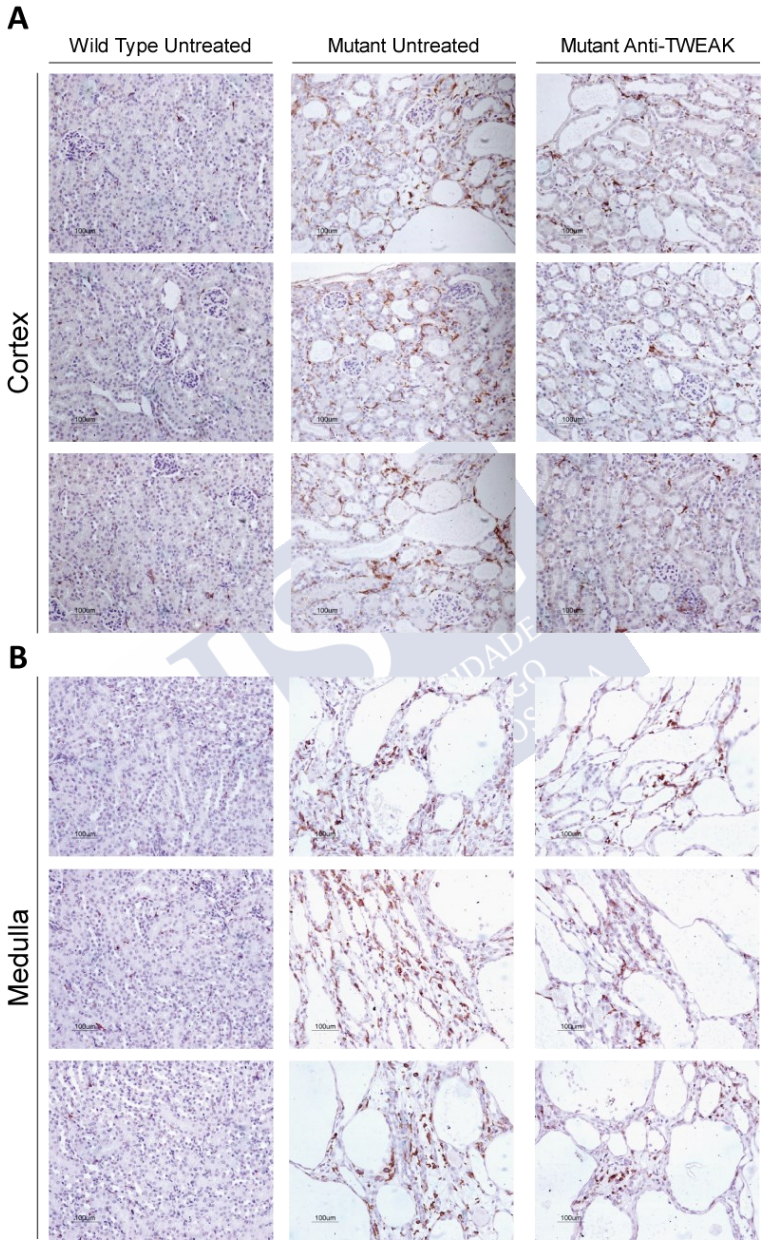

Supplemental Figure 27. Macrophage infiltration of kidneys. F4/80 staining in kidney tissue of Wild Type (n=4), mutant untreated (n=4) and mutant Pkd1 mutant mice treated with anti-TWEAK (n=3). Mice were sacrificed at postnatal day p30, according of the scheme shown in **Supplemental Figure 17C** (medium-term model).

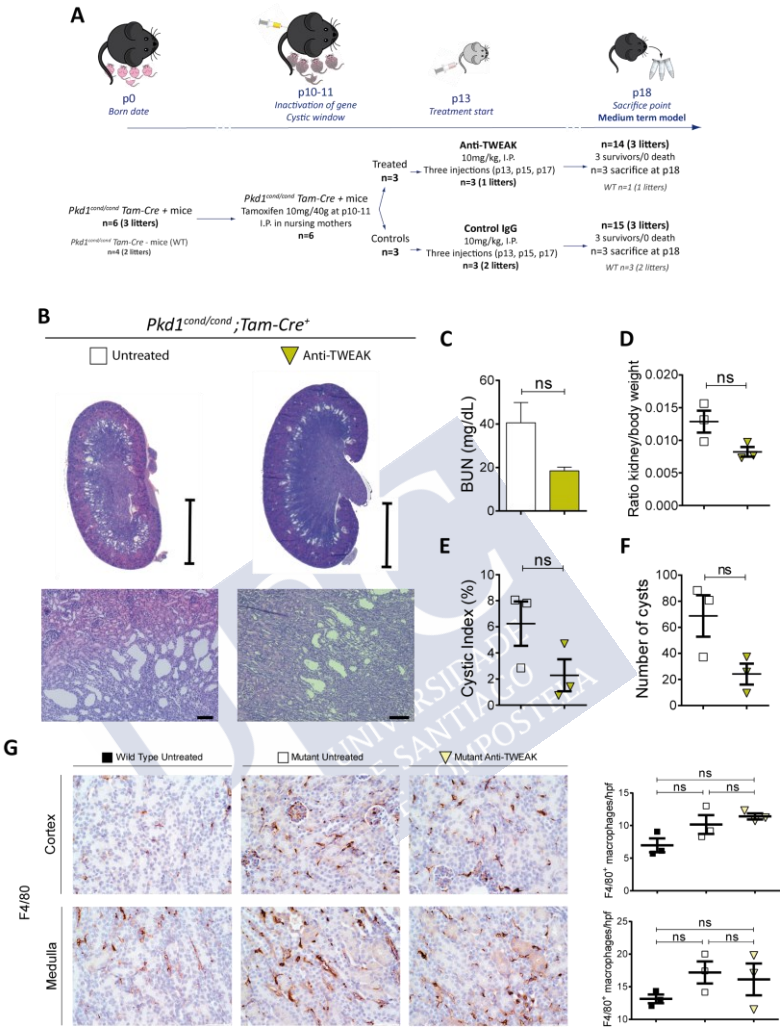

Supplemental Figure 28. Anti-TWEAK ameliorated cyst progression in early stages but did not reduce macrophage recruitment. (A) Schematic representation of the experiment. *Pkd1* inactivation in *Pkd1*$^{cond/cond}$*;Tam-Cre*$^{+}$ was induced at days p10 and p11. Anti-TWEAK was administered at p13, p15 and p17. Kidneys were collected at p18 (sacrifice point). p(x): postnatal day; I.P: intraperitoneal injection; n: number.(B) Hematoxylin-Eosin stained sagittal cross-sections of kidneys treated with anti-TWEAK (n=3) and control kidneys (n=3), sacrifice at postnatal day p18. Scale bars: 2 mm (upper panel); 100 µm (lower panel). In anti-TWEAK treated mice, there was a numerical decrease in Blood Urea Nitrogen (BUN) (C), kidney weight to total body weight ratio (D), cystic index (E) and number of cysts (F), although significance differences were not found, likely because of low mice number. (G) F4/80 staining in kidney tissue. There were no numerical nor significant differences in numbers of positive F4/80 macrophages in cortex and medulla (upper and lower panels, respectively) in mutant mice treated with anti-TWEAK (n=3) versus untreated mutant mice (n=3). p(x): postnatal day. Bars represent means±SEM. ns: not significant

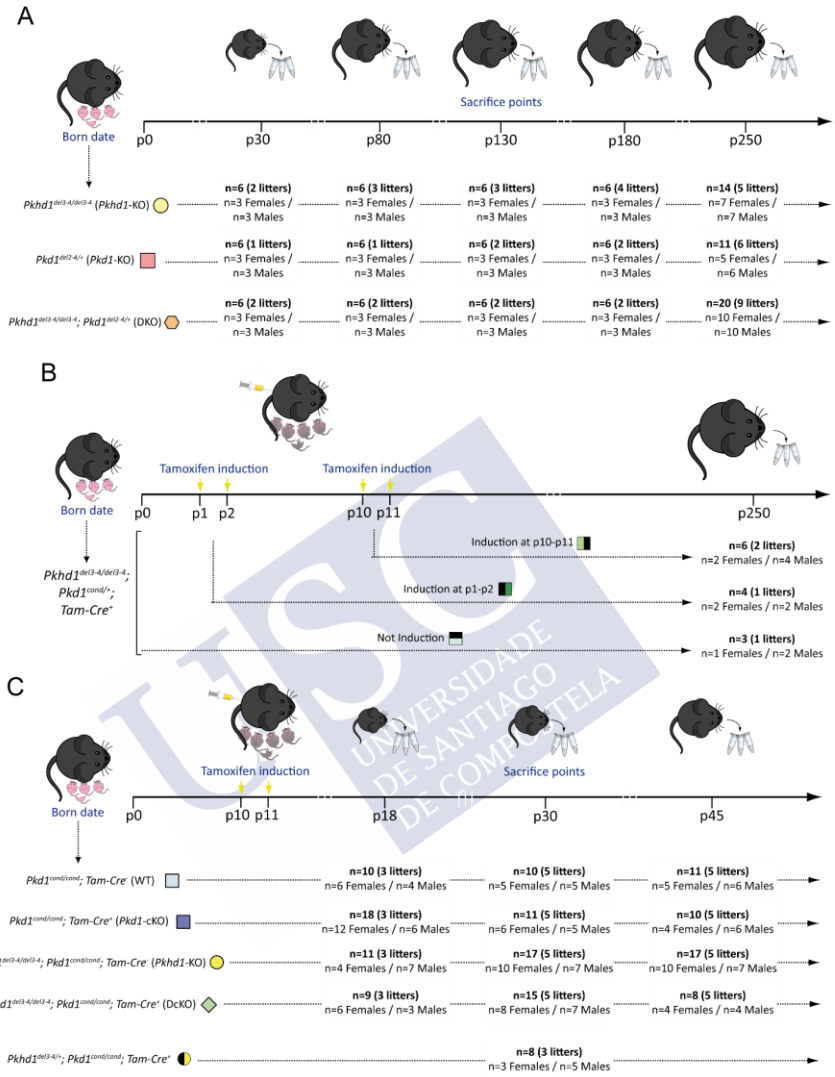

Supplemental Figure 29. Scheme with experimental designs performed in Chapter 5. In the figure we represented three visual schemes with litters and mice used for the study. (A) Litters and mice sacrificed at p30, p80, p130, p180 and p250 of *Pkhd1*$^{del3\text{-}4/del3\text{-}4}$ (*Pkhd1*-KO), *Pkd1*$^{del2\text{-}4/+}$ (*Pkd1*-KO) and *Pkhd1*$^{del3\text{-}4/del3\text{-}4}$; *Pkd1*$^{del2\text{-}4/+}$ (DKO) groups. (B) Deletion of Pkd1 gene of *Pkhd1*$^{del3\text{-}4/del3\text{-}4}$; *Pkd1*$^{cond/+}$ mice was performed at p1-2 and p10-11 (with the administration of tamoxifen) and then sacrificed at p250. (C) *Pkd1* inactivation in *Pkd1*$^{cond/cond}$;*Tam-Cre*$^{-/+}$ (WT and *Pkd1*-cKO, respectively) and *Pkhd1*$^{del3\text{-}4/del3\text{-}4}$;*Pkd1*$^{cond/cond}$;*Tam-Cre*$^{-/+}$ (Pkhd1-KO and DcKO, respectively) was induced at days p10 and p11. Tissues were collected at p18, p30 and p45. p(x): postnatal day; I.P: intraperitoneal injection; n: number.

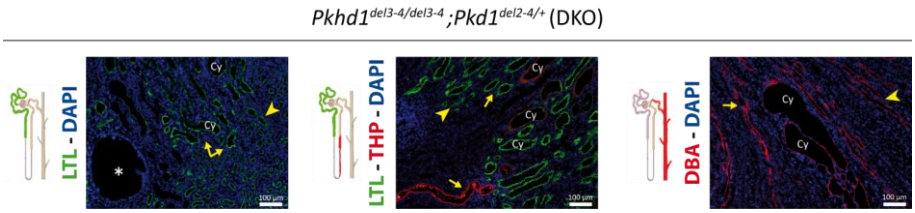

Supplemental Figure 30. Cystic origin characterization of DKO mice. Representative immunofluorescences pictures of specific markers from proximal tubules (LTL, Lotus Tetragonolobus Lectin. Green, up), ascending limb of the loop of Henle (THP, Tamm-Horsfall Protein. Red, medium) and collecting ducts (DBA, Dolichos Biflorus Agglutinin. Red, down), in DKO mice group at postnatal day 180 (**Supplemental Figure 29A**). Cy: cyst; * cyst without specific marking; yellow arrow: dilated tubule; yellow arrowhead: tubule. Scale bars: 100µm.

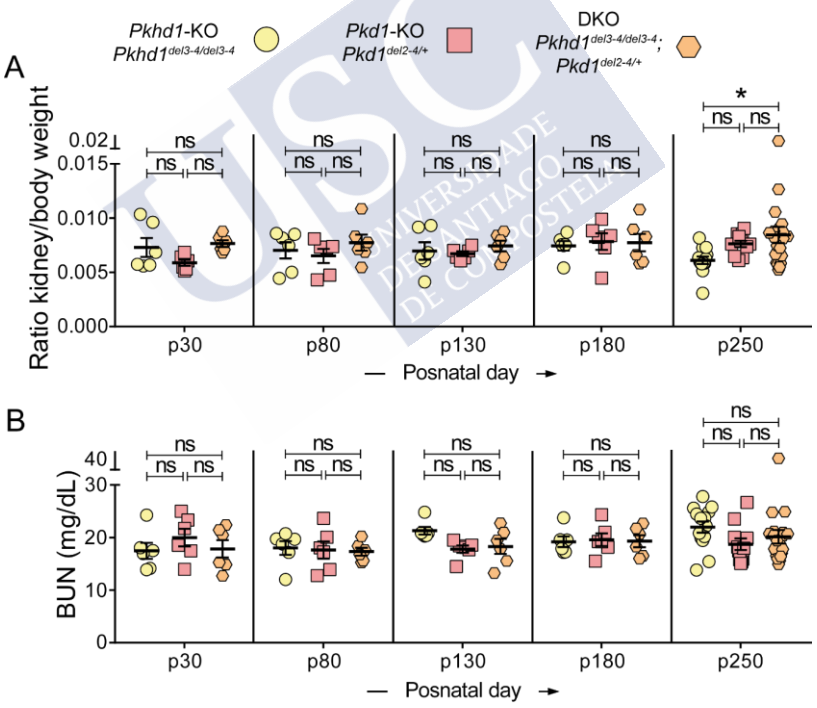

Supplemental Figure 31. (A) Ratio of kidney to body weight and (B) BUN (Blood Urea Nitrogen) values of *Pkhd1*$^{del3-4/del3-4}$ (*Pkhd1*-KO), *Pkd1*$^{del2-4/+}$ (*Pkd1*-KO) and *Pkhd1*$^{del3-4/del3-4}$*; Pkd1*$^{del2-4/+}$ (DKO) mice groups at p30, p80, p130, p180 and p250. DKO mice not present loss of renal function. p(x): postnatal day. Bars represent means±SEM. ns: non-significant; * p<0,05.

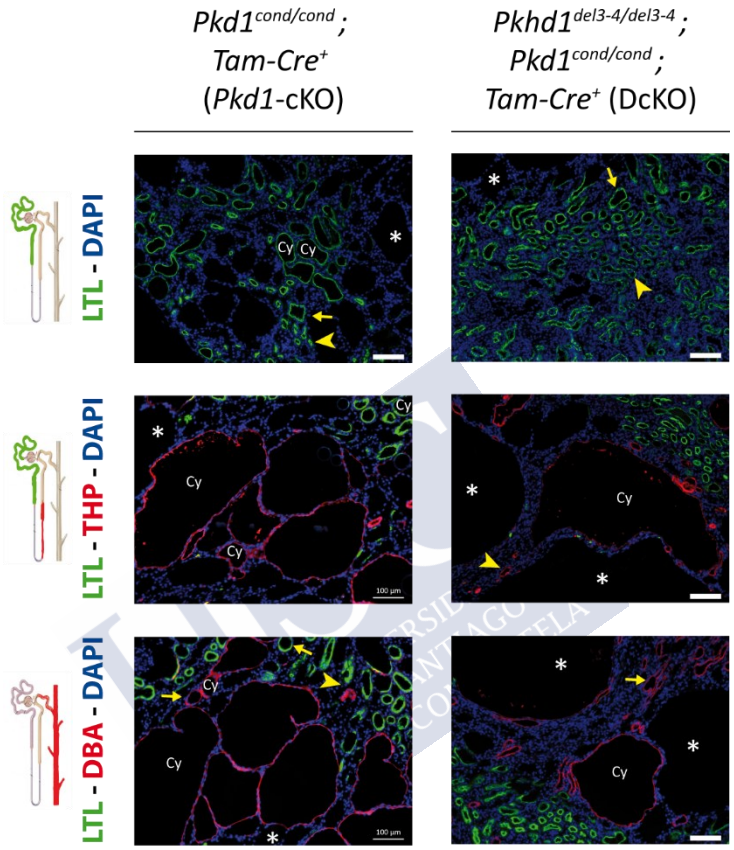

Supplemental Figure 32. Cyst growth amelioration in DcKO mice is not nephron segment specific. Immunofluorescence analysis of *Pkd1*-cKO (*Pkd1*$^{cond/cond}$;*Tam-Cre*$^{+}$) and DcKO (*Pkhd1*$^{del3\text{-}4/del3\text{-}4}$; *Pkd1*$^{cond/cond}$;*Tam-Cre*$^{+}$) mice groups. Representative images from (LTL, Lotus Tetragonolobus Lectin. Green, up, medium and down), ascending limb of the loop of Henle (THP, Tamm-Horsfall Protein. Red, medium) and collecting ducts (DBA, Dolichos Biflorus Agglutinin. Red, down) are shown. Mice scarified at p30 were used, according to **Supplemental Figure 29C**. Cy: cyst; *: cyst without specific marking; yellow arrow: dilated tubule; yellow arrowhead: tubule. Scale bars: 100µm.

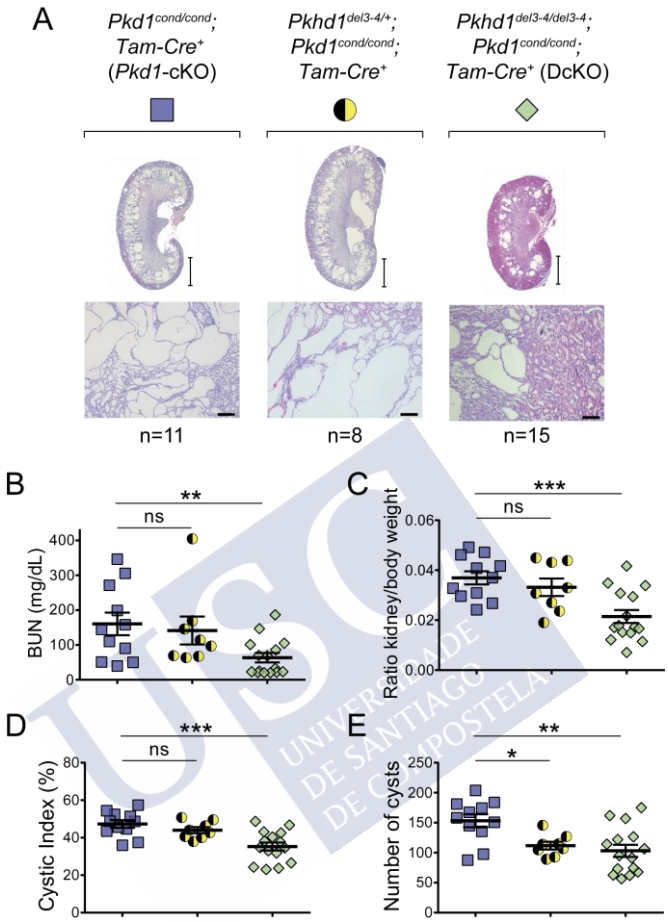

Supplemental Figure 33. *Pkhd1* Dosage did not affect to renal cyst progression. Mutations in heterozygosis of *Pkdh1* not alter renal phenotype of *Pkd1*-cKO mice. (A) Representative Hematoxylin-Eosin images of kidneys from *Pkd1*$^{cond/cond}$;*Tam-Cre*$^{+}$ (*Pkd1*-cKO), *Pkhd1*$^{del3-4/+}$;*Pkd1*$^{cond/cond;}$*Tam-Cre*$^{+}$ and *Pkhd1*$^{del3-4/del3-4}$;*Pkd1*$^{cond/cond;}$*Tam-Cre*$^{+}$ (DcKO) mice groups. Schematic representation of the experimental design in **Supplemental Figure 29C**. The n listed under kidney slides represents the number of mice analyzed for group. Scale bars: 2 mm (upper panel); 100 µm (lower panel). (B-E) Ratio of kidney to body weight (B), renal function based on BUN (C), cystic index (D) and number of cysts (E). p(x): postnatal day. Bars represent means±SEM. ns: not significant; ** p<0.01; *** p<0.001.

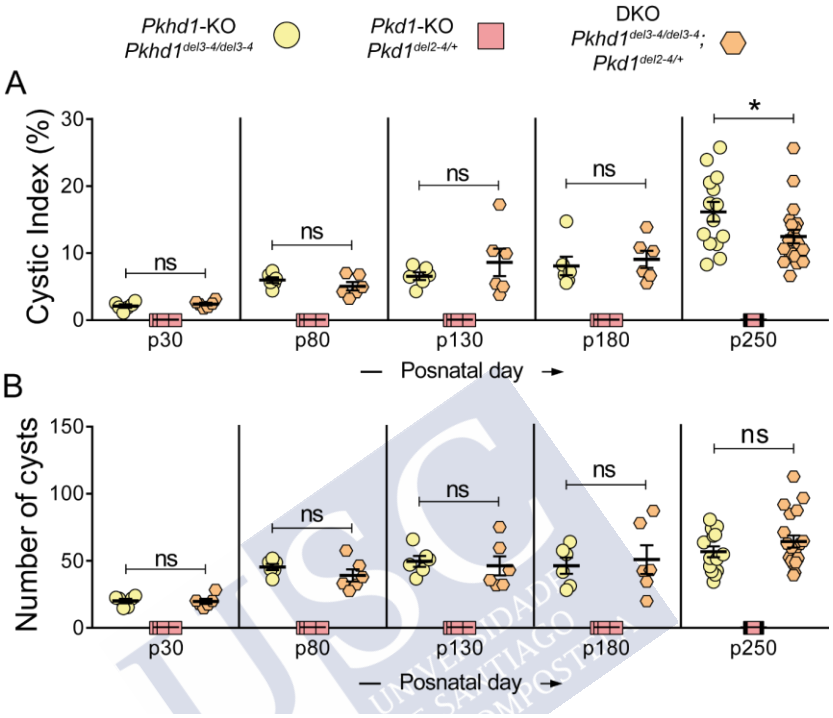

Supplemental Figure 34. Liver cystic index and number of cysts were not altered in DKO mice. (A-B) Cystic index (A) and number of cysts (B) of *Pkhd1*$^{del3\text{-}4/del3\text{-}4}$ (*Pkhd1*-KO), *Pkd1*$^{del2\text{-}4/+}$ (*Pkd1*-KO) and *Pkhd1*$^{del3\text{-}4/del3\text{-}4}$; *Pkd1*$^{del2\text{-}4/+}$ (DKO) mice groups at p30, p80, p130, p180 and p250. p(x): postnatal day. Bars represent means±SEM. ns: non-significant; * p<0,05.

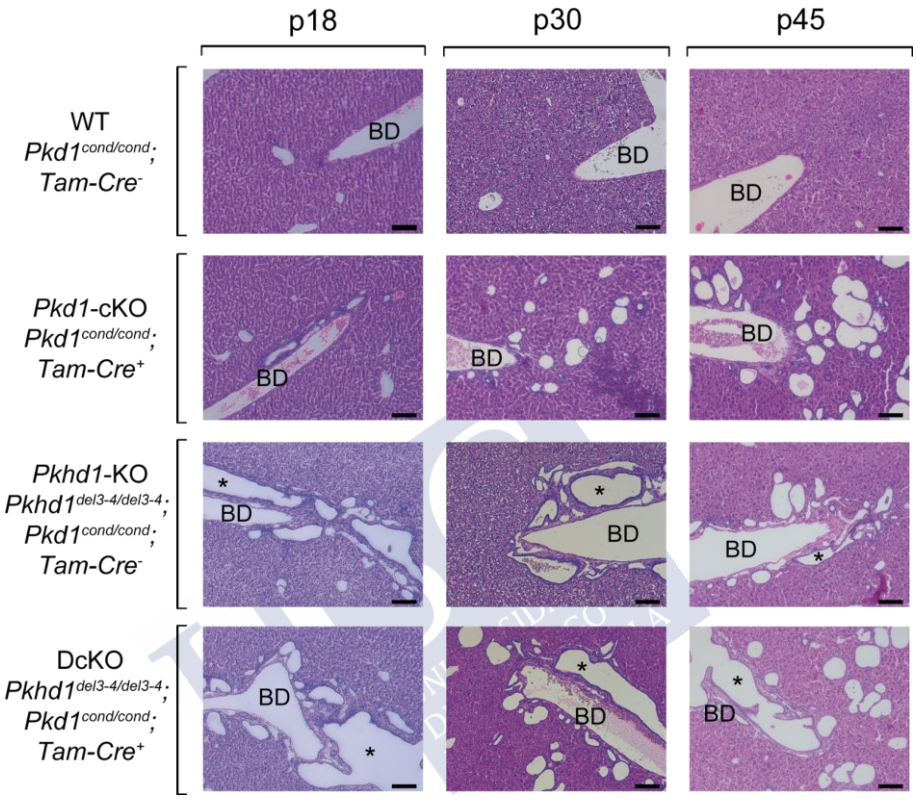

Supplemental Figure 35. DcKO mice presented higher enlargement of branches of bile ducts. One of the hepatic phenotypes of PLD that develop *Pkhd1*-KO mice is the enlargement of dilation of the small branches of bile ducts, which is aggravated with *Pkd1* genetic interaction in DcKO mice. BD: bile duct; *: dilation of branch of bile duct. Cy: cyst; *: cyst without specific marking. Scale bars: 100 µm.

3. SUPPLEMENTAL TABLES

Supplemental Table 1. Analyzed samples with its ID and distribution in each group, and the samples pooling for the acquisition of shotgun runs to build the spectral library.

Sample ID	Group	Pool for shotgun runs
1246_1,2,3	WT p14	A
1246_1,2,3	WT p14	A
1505_1,2,3	WT p14	A
1507_1,2,3	WT p14	A
1572_1,2,3	WT p14	A
1573_1,2,3	WT p14	A
1244_1,2,3	KO p14	B
1255_1,2,3	KO p14	B
1259_1,2,3	KO p14	B
1508_1,2,3	KO p14	B
1569_1,2,3	KO p14	B
1576_1,2,3	KO p14	B
754_1,2,3	WT p12	C
755_1,2,3	WT p12	C
1147_1,2,3	WT p12	C
1148_1,2,3	WT p12	C
1486_1,2,3	WT p12	C
1487_1,2,3	WT p12	C
734_1,2,3	KO p12	D
1149_1,2,3	KO p12	D
1285_1,2,3	KO p12	D
1485_1,2,3	KO p12	D
1494_1,2,3	KO p12	D
1494_1,2,3	KO p12	D

Supplemental Table 2. Animals of *Pkd1*$^{cond/cond}$*;Tam-Cre*, ADPKD orthologous mouse model, used in Chapter 3. From left to right, treatment group, precise genotype, phenotype (classified in *Wild Type* or non-cystic and mutant or cystic), genre and n (number) of each animal, and finally a summary.

Treatment	Litter	Genotyping	Phenotype	Genre	n	Summary
Un-treatment	A	*Pkd1-CKO-Cre*$^{-}$	*Wild Type*	Female	1	Litters n=3 Wild Types n=5 Mutants n=6
		Pkd1-CKO-Cre^{+}	Mutant	Female	1	
	B	*Pkd1-CKO-Cre*$^{-}$	*Wild Type*	Female	2	
		Pkd1-CKO-Cre^{-}	*Wild Type*	Male	2	
		Pkd1-CKO-Cre^{+}	Mutant	Female	2	
		Pkd1-CKO-Cre^{+}	Mutant	Male	1	
	C	*Pkd1-CKO-Cre*$^{+}$	Mutant	Male	2	
Marimastat 1 mg/kg	A	*Pkd1-CKO-Cre*$^{-}$	*Wild Type*	Female	1	Litters n=1 Wild Types n=3 Mutants n=3
		Pkd1-CKO-Cre^{-}	*Wild Type*	Male	2	
		Pkd1-CKO-Cre^{+}	Mutant	Male	3	
Marimastat 3 mg/kg	A	*Pkd1-CKO-Cre*$^{-}$	*Wild Type*	Female	2	Litters n=2 Wild Types n=4 Mutants n=5
		Pkd1-CKO-Cre^{+}	Mutant	Female	3	
		Pkd1-CKO-Cre^{+}	Mutant	Male	2	
	B	*Pkd1-CKO-Cre*$^{--}$	*Wild Type*	Female	1	
		Pkd1-CKO-Cre^{-}	*Wild Type*	Male	1	
Marimastat 5 mg/kg	A	*Pkd1-CKO-Cre*$^{-}$	*Wild Type*	Female	2	Litters n=3 Wild Types n=4 Mutants n=6
		Pkd1-CKO-Cre^{-}	*Wild Type*	Male	2	
		Pkd1-CKO-Cre^{+}	Mutant	Female	2	
	B	*Pkd1-CKO-Cre*$^{+}$	Mutant	Female	2	
	C	*Pkd1-CKO-Cre*$^{+}$	Mutant	Female	2	

Marimastat 7 mg/kg	A	*Pkd1-CKO-Cre⁻*	*Wild Type*	Male ♂	1	Litters n=1 Wild Types n=1 Mutants n=3
		Pkd1-CKO-Cre⁺	Mutant	Female ♀	2	
		Pkd1-CKO-Cre⁺	Mutant	Male ♂	1	

Treatment	Litter	Genotyping	Phenotype	Genre	n	Summary
Marimastat 10 mg/kg	A	*Pkd1-CKO-Cre⁻*	Wild Type	Female ♀	2	Litters n=3 Wild Types n=7 Mutants n=8
		Pkd1-CKO-Cre⁺	Mutant	Female ♀	2	
		Pkd1-CKO-Cre⁺	Mutant	Male ♂	2	
	B	*Pkd1-CKO-Cre⁻*	Wild Type	Male ♂	2	
	C	*Pkd1-CKO-Cre⁻*	Wild Type	Female ♀	1	
		Pkd1-CKO-Cre⁻⁻	Wild Type	Male ♂	2	
		Pkd1-CKO-Cre⁺	Mutant	Female ♀	2	
		Pkd1-CKO-Cre⁺	Mutant	Male ♂	1	
Tolvaptan	A	*Pkd1-CKO-Cre⁻*	*Wild Type*	Female ♀	3	Litters n=2 Wild Types n=4 Mutants n=4
		Pkd1-CKO-Cre⁻	*Wild Type*	Male ♂	1	
		Pkd1-CKO-Cre⁺	Mutant	Female ♀	1	
		Pkd1-CKO-Cre⁺	Mutant	Male ♂	2	
	B	*Pkd1-CKO-Cre⁺*	Mutant	Male ♂	1	
Marimastat 5 mg/kg + Tolvaptan	A	*Pkd1-CKO-Cre⁻⁻*	*Wild Type*	Male ♂	4	Litters n=3 Wild Types n=7 Mutants n=8
		Pkd1-CKO-Cre⁺	Mutant	Female ♀	3	
		Pkd1-CKO-Cre⁺	Mutant	Male ♂	1	
	B	*Pkd1-CKO-Cre⁺*	Mutant	Female ♀	2	
	C	*Pkd1-CKO-Cre⁻*	*Wild Type*	Female ♀	2	
		Pkd1-CKO-Cre⁻	*Wild Type*	Male ♂	1	
		Pkd1-CKO-Cre⁺	Mutant	Female ♀	1	
		Pkd1-CKO-Cre⁺	Mutant	Male ♂	1	

Supplemental Table 3. Animals of *Pkhd1*$^{del3\text{-}4/del3\text{-}4}$, ARPKD orthologous mouse model, used in Chapter 3. From left to right, treatment group, precise genotype, phenotype (classified in *Wild Type* or non-cystic and mutant or cystic), genre and n (number) of each animal, and finally a summary.

Treatment	Litter	Genotyping	Phenotype	Genre	n	Summary
Un-treatment	A	C57BL/6 mouse	*Wild Type*	Female	2	Litters n=7 Wild Types n=5 Mutants n=14
	B	C57BL/6 mouse	*Wild Type*	Male	3	
	C	*Pkhd1*$^{del3\text{-}4/del3\text{-}4}$	Mutant	Female	1	
		Pkhd1$^{del3\text{-}4/del3\text{-}4}$	Mutant	Male	1	
	D	*Pkhd1*$^{del3\text{-}4/del3\text{-}4}$	Mutant	Female	2	
	E	*Pkhd1*$^{del3\text{-}4/del3\text{-}4}$	Mutant	Male	1	
	F	*Pkhd1*$^{del3\text{-}4/del3\text{-}4}$	Mutant	Female	4	
	G	*Pkhd1*$^{del3\text{-}4/del3\text{-}4}$	Mutant	Male	5	
Marimastat 5 mg/kg	A	*Pkhd1*$^{del3\text{-}4/del3\text{-}4}$	Mutant	Male	3	Litters n=2 Mutants n=6
	B	*Pkhd1*$^{del3\text{-}4/del3\text{-}4}$	Mutant	Male	3	
Marimastat 5mg/kg + Tolvaptan	A	*Pkhd1*$^{del3\text{-}4/del3\text{-}4}$	Mutant	Female	3	Litters n=3 Mutants n=5
	B	*Pkhd1*$^{del3\text{-}4/del3\text{-}4}$	Mutant	Female	2	

Supplemental Table 4. Primers sequence list used in Chapter 2. *Gapdh* (Glyceraldehyde 3-phosphate dehydrogenase); *Anxa2* (Annexin A2); *Apcs* (Amyloid P Component, Serum); *Fgl1* (Fibrinogen Like 1); *Ilk* (Integrin Linked Kinase); *S100a* (S100 Calcium Binding Protein A1); *Fgb* (Fibrinogen Beta Chain); *Hpx* (Hemopexin); *Fga* (Fibrinogen Alpha Chain); *Fgg* (Fibrinogen Gamma Chain); *Hao2* (Hydroxyacid Oxidase 2).

Gene name		Primer sequence (5'-3')
Housekeeping		
Gapdh	Forward	5'-ATTTGCCGTGAGTGGAGTCAT-3'
	Reverse	5'-GCAAAGTGGAGATTGTTGCCA-3'
p14 group		
Anxa2	Forward	5'-ACGAAATCCTGTGCAAGCTC-3'
	Reverse	5'-TCTCAGCATCGAAGTTGGTG-3'
p12 group		
Apcs	Forward	5'-TGTTTGTCTTCACCAGCCTTC-3'
	Reverse	5'-GATGTGGGATCAGCTTCACA-3'
Fgl1	Forward	5'-CCCTCGAGAGTGAGAACTGC-3'
	Reverse	5'-GCTGTGCAATCATGGTCTGT-3'
Ilk	Forward	5'-TGGAGCACGGATTAATGTGA-3'
	Reverse	5'-TGCATTGATGTCAGCCTTGT-3'
S100a	Forward	5'-AGGACCTGGACACAAACCAG-3'
	Reverse	5'-GGGTTGTTCTCATGCAGCTT-3'
Fgb	Forward	5'-AAGGCTACTGCCAACCAGAA-3'
	Reverse	5'-CCCGTAGGACACAACACTCC-3'
Hpx	Forward	5'-CCGAACACTGCTTGGATACC-3'
	Reverse	5'-AGTGACCCCTCCACACAAAC-3'
Fga	Forward	5'-GTACGTGGCCCAAGAGTTGT-3'
	Reverse	5'-CTGAAGGGCATTTGTGGTTC-3'
Fgg	Forward	5'-TTCGGTAGTTTCTGCCCAAC-3'
	Reverse	5'-TTTCAGCCCGGAATAAGATG-3'
Hao2	Forward	5'-CAATGACAACTTGGCAGCAT-3'
	Reverse	5'-ATCTCCTGCCCTTGGATTGT-3'

Supplemental Table 5. Primers sequence list used in Chapter 3. *Hprt* (Hypoxanthine Phosphoribosyltransferase); *Mmpx* (Matrix metalloprotease x); *Timpx* (Tissue inhibitor of metalloproteases X); *Cxcl1* (Chemokine (C-X-C motif) ligand 1); *Il6* (Interleukin 6); *Ctgf* (connective tissue growth factor); *Col1a1* (Collagen-1a1); *TgfB* (Transforming growth factor-beta).

Gene name		Primer sequence (5'-3')
Housekeeping		
Hprt	Forward	5'-CAATGCAAACTTTGCTTTCCC-3'
	Reverse	5'-TCCTTTTCACCAGCAAGCTTG-3'
Mmps - Collagenases		
Mmp1	Forward	5'-CGGCAAAATGTGGAGACAGT-3'
	Reverse	5'-TCAGCCATCATCTCCTTGC-3'
Mmp8	Forward	5'-TGCCTTCCCAGTACCTGAAC-3'
	Reverse	5'-AGACCGGAATTGATTGCTTG-3'
Mmp13	Forward	5'-TGAGGAAGACCTTGTGTTTGC-3'
	Reverse	5'-TTTCTCGGAGCCTGTCAACT-3'
Mmps - Gelatinases		
Mmp2	Forward	5'-GATGTCGCCCCTAAAACAGA-3'
	Reverse	5'-TTGAGGGTATCTTTCAGCACAA-3'
Mmp9	Forward	5'-CCCCAAAGACCTGAAAACCT-3'
	Reverse	5'-GCTTCTCTCCCATCATCTGG-3'
Mmps - Stromelysins		
Mmp3	Forward	5'-TGTGGTTGTGTGCTCATCCT-3'
	Reverse	5'-GCTTCACATCTTTTGCAAGG-3'
Mmp11	Forward	5'-CTCTGCTGCTCCTGTTGCT-3'
	Reverse	5'-CCCTTTCTTCACAGGGTGAT-3'
Mmps - Matrilysins		
Mmp7	Forward	5'-AGGAAGCTGGAGATGTGAGC-3'
	Reverse	5'-TCCACTAGACTATTGACCTTCTTTG-3'
Mmps - Membrane-type Transmembrane		
Mmp14	Forward	5'-CCGCCATGCAAAAGTTCTAT-3'
	Reverse	5'-CCCAAACTTATCCGGAACAC-3'
Mmp15	Forward	5'-TGGTGCTTCTGGACTGTCTG-3'
	Reverse	5'-GGCTGGGGTAGGTAGCCATA-3'
Mmp16	Forward	5'-CGTTCGGGTGTGTTTTTCTT-3'
	Reverse	5'-GTCAGTCGGTGGAAGGTAGC-3'
Mmp24	Forward	5'-AGTCCGCGGTCTCCACTAT-3'
	Reverse	5'-CTCAAGTGGGGATGATCAGG-3'

GPI			
	Mmp17	Forward	5'-CACCCACTTTGATGACGATG-3'
		Reverse	5'-ACCAATGGCATGACCAAACT-3'
	Mmp25	Forward	5'-CTGGCGCTTCTGTTGGTT-3'
		Reverse	5'-GCAGGTAGCCATAGCGAGTC-3'
Timps			
	Timp1	Forward	5'-ATCTGGCATCCTCTTGTTGC-3'
		Reverse	5'-GGGAACCCATGAATTTAGCC-3'
	Timp2	Forward	5'-CGTTTTGCAATGCAGACGTA-3'
		Reverse	5'-GAATCCTCTTGATGGGGTTG-3'
	Timp3	Forward	5'-GTGGGAAAGAAGCTGGTGAA-3'
		Reverse	5'-AGAGGCTTCCGTGTGAATGT-3'
	Timp4	Forward	5'-TTTGCTCTTCCCTCTGTGGT-3'
		Reverse	5'-GGGCTCAATGTAGTTGCACA-3'
Inflammation markers			
	Cxcl1 (Il8 homolog)	Forward	5'-GCACCCAAACCGAAGTCATA-3'
		Reverse	5'-TGGGGACACCTTTTAGCATC-3'
	Il6	Forward	5'-CCCAACAGACCTGTCTATACCA-3'
		Reverse	5'-CAGAATTGCCATTGCACAAC-3'
Fibrotic markers			
	Ctgf	Forward	5'-AGTGTGCACTGCCAAAGATG-3'
		Reverse	5'-CCAGGCAAGTGCATTGGTAT-3'
	Col1a1	Forward	5'-TGTTCAGCTTTGTGGACCTC-3'
		Reverse	5'- GGACCCTTAGGCCATTGTGT-3'
	TgfB1	Forward	5'-AGCCCGAAGCGGACTACTAT-3'
		Reverse	5'-TGTGTGAGATGTCTTTGGTTTTC-3'

Supplemental Table 6. PCR primers used for Real-Time quantitative PCR (RT-qPCR) in Chapter 4. *Hprt* (Hypoxanthine Phosphoribosyltransferase); *Akt1* (AKT serine/threonine kinase 1); *Nos2* (Nitric oxide synthase 2, inducible); *Il12* (Interleukin 12); *Tnfa* (Tumor necrosis factor alpha); *Ccl2/Mcp1* (Monocyte chemoattractant protein-1); *Arg1* (Arginase 1); *Mrc1* (Mannose receptor, C type 1); *Csf1/MCSF* (Colony stimulating factor 1 (macrophage)); *Csf2/Gmcf* (Colony stimulating factor 2 (granulocyte-macrophage)); *Cxcl16* (Chemokine (C-X-C motif) ligand 16); *Ccl21* (Chemokine (C-C motif) ligand21); *Ccl19* (Chemokine(C-C motif) ligand 19); *TgfB* (Transforming growth factor beta); Ctgf (Connective tissue growth factor).

Gene name		Primer sequence (5'-3')
Housekeeping		
Hprt	Forward	5'-CAATGCAAACTTTGCTTTCCC-3'
	Reverse	5'-TCCTTTTCACCAGCAAGCTTG-3'
Proliferative way		
Akt1 (PKB/Akt)	Forward	5'-GGATGTGGATCAGCGAGAGT-3'
	Reverse	5'-GCAGCGGATGATAAAGGTGT-3'
Macrophage polarization		
M1	Forward	5'-GATCAAAAACTGGGGCAGTG-3'
Nos2	Reverse	5'-ACTCTTGGGGTTCATGATGG-3'
Il12b	Forward	5'-TGTGGGAGCTGGAGAAAGAC-3'
	Reverse	5'-CATCTTCTTCAGGCGTGTCA-3'
Tnfa	Forward	5'-GGATGTGGATCAGCGAGAGT-3'
	Reverse	5'-GCAGCGGATGATAAAGGTGT-3'
Ccl2 (Mcp-1)	Forward	5'-CATCCACGTGTTGGCTCA-3'
	Reverse	5'-TTGTAGCTCTCCAGCCTACTCA-3'
Macrophage polarization		
M2	Forward	5'-AAAGCTGGTCTGCTGGAAAA-3'
Arg1	Reverse	5'-CCGTGGGTTCTTCACAATTT-3'
Mrc1	Forward	5'-TTCTCCTGCTTCTGGCTTTT-3'
	Reverse	5'-ATGGCACTTAGAGCGTCCAC-3'
Csf1	Forward	5'-GCAGGAGTATTGCCAAGGAG-3'
	Reverse	5'-AAAGGCAATCTGGCATGAAG-3'
Csf2	Forward	5'-GGGCAATTTCACCAAACTCA-3'
	Reverse	5'-ATGAAATCCGCATAGGTGGT-3'

Canonical NF-κB			
	Cxcl16	Forward	5'-GACCCTTGTCTCTTGCGTTC-3'
		Reverse	5'-GGGTGCCAGAAGAAATGGTA-3'
Non-Canonical NF-κB			
	Ccl21	Forward	5'-TCCGAGGCTATAGGAAGCAA-3'
		Reverse	5'-CTTCCTCAGGGTTTGCACAT-3'
	Ccl19	Forward	5'-TGCTGGTTCTCTGGACCTTC -3'
		Reverse	5'-GGAAGGCTTTCACGATGTTC -3'
Fibrosis			
	TgfB	Forward	5'-AGCCCGAAGCGGACTACTAT-3'
		Reverse	5'-TGTGTGAGATGTCTTTGGTTTTC-3'
	Ctgf	Forward	5'-AGTGTGCACTGCCAAAGATG -3'
		Reverse	5'-CCAGGCAAGTGCATTGGTAT -3'

Supplemental Table 7. Clinical characteristics of ADPKD patients in Chapter 4. Median (interquartile range). eGFR: estimated glomerular filtration rate, UACR: urinary albumin: creatinine ratio, UPCR: urinary protein: creatinine ratio; TKV: total kidney volume.

Women n, (%)	Age (years)	eGFR (mL/min/1.73 m^2)	UACR (mg/g)	UPCR (mg/g)	TKV (ml)
44 (56%)	53(42-66)	65.5 (40.7-98)	20 (8-70)	68 (44-132)	1547.5 (603.2-2562.2)

ANNEXS

USC UNIVERSIDADE DE SANTIAGO DE COMPOSTELA

ANNEXS

Annex 1. Cordido A, Cernadas E, Fernandez- Delgado M, Garcıa-Gonzalez MA. (2020). CystAnalyser: A new software tool for the automatic detection and quantification of cysts in Polycystic Kidney and Liver Disease, and other cystic disorders. PLoS Comput Biol 16(10): e1008337. https://doi.org/10.1371/journal. pcbi.1008337.

Annex 2. Certificate of use of experimental animals. Functions B and C.

Annex 3. Certificate of use of experimental animals. Function D.

Annex 4. ARRIVE checklists.

USC UNIVERSIDADE DE SANTIAGO DE COMPOSTELA

CONSEJERÍA DE MEDIO AMBIENTE,
ADMINISTRACIÓN LOCAL
Y ORDENACIÓN DEL TERRITORIO

Comunidad de Madrid

Certificado de reconocimiento de la capacitación para manejar animales utilizados, criados o suministrados con fines de experimentación y otros fines científicos, incluyendo la docencia. Orden ECC/566/2015, de 20 de marzo

D./Dña. ADRIÁN CORDIDO EIJO, con DNI/NIE 35590045Y ha obtenido el reconocimiento de la capacitación para realizar las funciones de:

EUTANASIA DE LOS ANIMALES

REALIZACIÓN DE LOS PROCEDIMIENTOS

en los siguientes grupos de especies animales:

ROEDORES

Nº de certificado: CAP-1368-18

ORGANISMO QUE EXPIDE EL CERTIFICADO

Dirección General de Agricultura y Ganadería. Consejería de Medio Ambiente y Ordenación del Territorio. Comunidad de Madrid

El reconocimiento de la capacitación para la realización de las funciones relacionadas en este certificado surtirá efecto en todo el territorio nacional.

Fecha 1 de junio de 2018	**Sello**

COMUNIDAD DE MADRID - CONSEJERÍA DE MEDIO AMBIENTE, ADMINISTRACIÓN LOCAL Y ORDENACIÓN DEL TERRITORIO - DIRECCIÓN GENERAL DE AGRICULTURA Y GANADERÍA

EL DIRECTOR GENERAL DE AGRICULTURA Y GANADERÍA

(P.D.F Resolución de 2 de noviembre de 2015)

EL SUBDIRECTOR GENERAL DE RECURSOS AGRARIOS

Fdo: Jesús Carpintero Hervás

CONSEJERÍA DE MEDIO AMBIENTE,
ADMINISTRACIÓN LOCAL
Y ORDENACIÓN DEL TERRITORIO

Comunidad de Madrid

Certificado de reconocimiento de la capacitación para manejar animales utilizados, criados o suministrados con fines de experimentación y otros fines científicos, incluyendo la docencia. Orden ECC/566/2015, de 20 de marzo

D./Dña. ADRIÁN CORDIDO EIJO, con DNI/NIE 35590045Y ha obtenido el reconocimiento de la capacitación para realizar las funciones de:

DISEÑO DE LOS PROYECTOS Y PROCEDIMIENTOS

en los siguientes grupos de especies animales:

SIN LIMITACIÓN DE ESPECIES

Nº de certificado: CAP-1288-18

ORGANISMO QUE EXPIDE EL CERTIFICADO

Dirección General de Agricultura y Ganadería. Consejería de Medio Ambiente, Administración Local y Ordenación del Territorio. Comunidad de Madrid

El reconocimiento de la capacitación para la realización de las funciones relacionadas en este certificado surtirá efecto en todo el territorio nacional.

Fecha 25 de abril de 2018	**Sello**

COMUNIDAD DE MADRID - DIRECCIÓN GENERAL DE AGRICULTURA Y GANADERÍA - CONSEJERÍA DE MEDIO AMBIENTE, ADMINISTRACIÓN LOCAL Y ORDENACIÓN DEL TERRITORIO

EL DIRECTOR GENERAL DE AGRICULTURA Y GANADERÍA

(P.D.F Resolución de 2 de noviembre de 2015)

EL SUBDIRECTOR GENERAL DE RECURSOS AGRARIOS

Fdo: Jesús Carpintero Hervás

Lista de verificación de recomendacións para **Teses EDI saúde. XERAL**

Sí-Non-N/A		Páxina
Para todas as Teses		
Si	Declaración de potenciais conflitos de interés por parte do autor	151
Si	Declaración sobre a orixe e copyright das figuras non orixinais e permiso en caso necesario. Incluílos no pe de cada figura no orixinal.	4-22
N/A	Lista de adecuación estatística no caso de non cubrir ningunha das outras tres checklist específicas.	
Para Teses que implican a seres humáns, a súas mostras ou os seus datos de carácter persoal		
	Declaración sobre a súa aprobación polo comité de ética da investigación	
	Código de rexistro do estudo	
	Copia do informe favorable	
	Declaración de que os datos baséanse en información anónima e polo tanto non se necesita aprobación do comité de ética da investigación	
	Se o estudo é observacional, checklist STROBE	
Para Teses que describen un ensaio clínico		
	Declaración sobre a súa autorización pola Axencia Española de Medicamentos e produtos sanitarios.	
	Copia da autorización	
	Checklist CONSORT	
Para Teses que usan células troncais humanas, embrionarias ou inducidas		
	Declaración sobre a súa autorización	
	Referencia da autorización	
	Copia da autorización	
Para Teses que inclúen estudos con animais de experimentación		
Si	Declaración da súa autorización	33-34
Si	Número da autorización do proxecto de experimentación animal	34
Si	Rexistro do centro de usuario autorizado se é español	34
Si	Copia do certificado de capacitación se os experimentos foron feitos polo doutorando	215
Si	Indicación da persoa, empresa ou servizo que levou a cabo o experimento no seu caso	34
Si	Checklist ARRIVE	212-215

Firma doutorando

Lista de verificación para Tese con animais de experimentación. **EXPERIMENTACIÓN ANIMAL ARRIVE**

Si/non/NA		**páxina**
	Título	
Si	Proporcionar unha descrición tan exacta e concisa como sexa posible sobre o contido do traballo.	1
	Resumo	
Si	Proporcionar un resumo preciso dos antecedentes, os obxectivos da investigación, incluíndo detalles da especie e cepa dos animais utilizados, métodos relevantes, achados principais e conclusións do estudo.	10-13
	Antecedentes	
Si	Incluír suficientes antecedentes científicos (incluíndo as referencias pertinentes ao traballo anterior) a fin de comprender a motivación e o contexto para o estudo, e explicar as bases e o enfoque experimental.	24, 44-112
Si	Explicar como e por que a especie e o modelo animal utilizados permiten abordar os obxectivos científicos e, cando sexa apropiado, a relevancia do estudo para a bioloxía humana.	114-126
	Obxectivos	
Si	Describir claramente os obxectivos primarios e secundarios do estudo, ou as hipóteses específicas que se van a probar.	24
	Declaración Ética	
Si	Indicar o permiso do comité ético, e as leis ou decretos pertinentes para o coidado e uso de animais, baixo as que se realiza a investigación.	34
	Deseño do estudo	
Si	Número de grupos experimentais e control.	26-27, 33-34
Si	Calquera medida adoptada para minimizar os efectos de sesgo subxectivo ao asignar os animais aos grupos de tratamento (por ex., procedemento aleatorio) e ao avaliar os resultados (por ex., si faise, describir quen eran cegos e cando).	33
Si	A unidade experimental (por ex., un só animal, grupos ou gaiolas de animais). Un diagrama cronolóxico ou de fluxo poden ser útiles para ilustrar como se realizaron os deseños de estudo complexos.	33, 75, 76, 165, 175, 182-184
	Procedementos experimentais	
Si	Como (por ex., formulación e dose do tratamento, o sitio e a vía de administración, anestesia e analxesia utilizadas [incluíndo a monitorización], procedemento cirúrxico, o método de eutanasia). Proporcionar detalles de calquera equipo especializado utilizado, incluíndo provedor(é).	33-35
Si	Cando (por ex., a hora do día).	75, 76, 165, 175, 182-184
N/A	Onde (por ex., gaiola de aloxamento, laboratorio, proba do labirinto acuático).	
Si	Por que (por ex., fundamentos para a elección do anestésico específico, a vía de administración, dose do fármaco utilizado).	33-34
	Animais de experimentación	

Si	Proporcionar detalles dos animais utilizados, incluíndo especie, cepa, sexo, etapa de desenvolvemento (por ej., idade media ou mediana de idade e rango) e peso (por ex., media ou mediana máis rango de peso).	33-35, 75, 76, 165, 175, 182-184
Si	Proporcionar outra información pertinente, como a procedencia dos animais, nomenclatura internacional da cepa, modificación xenética (por ex., animal deficiente ou transxénico), xenotipo, estado de saúde/inmune, si os animais foron incluídos en estudos ou recibido tratamentos anteriormente, procedementos previos, etc.	33, 34
	Animais	
Si	Aloxamento (tipo de instalación por ex., libre de patóxenos específicos [SPF], tipo de gaiola ou habitáculo, material do leito, número de animais por gaiola, forma e material do tanque, etc. para peces).	33, 34
Si	Condicións de cría (por ex., programa de reprodución, ciclo de luz/escuridade, temperatura, calidade de auga, etc. para peixes, o tipo de alimentación, o acceso aos alimentos e ao auga, enriquecemento ambiental).	33
N/A	Avaliacións e intervencións relacionadas co benestar que se levaron a cabo antes, durante ou despois do experimento	
	Tamaño da mostra	
Si	Especificar o número total de animais utilizados en cada experimento, e o número de animais en cada grupo experimental.	33-35, 75, 76, 165, 175, 182-184
N/A	Explicar como se determinou o número de animais. Proporcionar detalles do cálculo do tamaño da mostra utilizado.	
N/A	Indicar o número de repeticións independentes de cada experimento, si é pertinente.	
	Asignación de animais a grupos experimentais	
Si	Proporcionar detalles completos da forma en que os animais foron asignados a grupos experimentais, incluíndo distribución aleatoria ou asignación específica, si así se fixo.	33
Si	Describir a orde no que os animais nos diferentes grupos experimentais foron tratados e avaliados.	33
Si	Resultados experimentais	44-112
Si	Definir claramente os resultados primarios e secundarios avaliados (por ex., morte celular, marcadores moleculares, cambios de comportamento).	44-112
	Métodos estatísticos	
Si	Proporcionar detalles sobre os métodos estatísticos utilizados para cada análise.	42
Si	Especificar a unidade de análise para cada grupo de datos (por ex., un só animal, grupo de animais, neurona individual).	33-34
Si	Describir os métodos utilizados para avaliar si os datos corroboran as suposicións do método estatístico.	42
	Datos basais	
N/A	Para cada grupo experimental, indicar as características relevantes e estado de saúde dos animais (por ex., peso, estado microbiolóxico, se os animais foron incluídos en estudos ou recibido drogas anteriormente) antes de iniciar o tratamento ou proba. (Esta información pode ser a miúdo tabulada).	

	Cantidades analizadas	
Si	Indicar o número de animais en cada grupo incluído en cada análise. Presentar números absolutos (por ex., 10/20, non 50 %).	75, 76, 165, 175, 182-184
N/A	Se algún dos animais ou datos non foi incluído na análise, explicar por que.	
	Resultados e Discusión	
Si	Indicar os resultados de cada análise levada a cabo, cunha medida de precisión (por ex., erro estándar ou intervalo de confianza).	44-112
	Eventos adversos	
N/A	Dar detalles de todos os eventos adversos importantes en cada grupo experimental.	
N/A	Describir as modificacións aos protocolos experimentais realizadas para reducir os eventos adversos.	
	Interpretación /implicacións científicas	
Si	Interpretar os resultados, tendo en conta os obxectivos e as hipóteses do estudo, a teoría actual e outros estudos pertinentes na literatura.	44-126
Si	Comentar as limitacións do estudo incluíndo calquera fonte potencial de sesgo, calquera limitación do modelo animal e a imprecisión asociada cos resultados	114-126
Si	Describir calquera implicación dos métodos experimentais ou achados para o remplazo, refinamento ou redución (as 3 R) do uso dos animais en investigación.	26
	Capacidade de xeneralización/aplicabilidade	
Si	Comentar se, e de que forma, os achados deste estudo son aplicables a outras especies ou sistemas, incluíndo calquera relevancia para a bioloxía humana.	114-126
	Financiamento	
N/A	Listar todas as fontes de financiamento (incluíndo o número do proxecto) e o papel da fonte(s) de financiamento no estudo.	

Baseado en The ARRIVE guidelines: Animal Research: Reporting of In vivo Experiments.

Sinatura Doutorando